Semiconductors, Vol. 36, No. 5, 2002, pp. 481–486. Translated from Fizika i Tekhnika Poluprovodnikov, Vol. 36, No. 5, 2002, pp. 513–518.

ELECTRONIC AND OPTICAL PROPERTIES OF SEMICONDUCTORS

Nonlinear Photoluminescence of Graded-Gap $Al_xGa_{1-x}As$ Solid Solutions

V. F. Kovalenko, A. Yu. Mironchenko, and S. V. Shutov

Institute of Semiconductor Physics, National Academy of Sciences of Ukraine, Kherson, 73008 Ukraine

Submitted July 2, 2001; accepted for publication September 13, 2001

Abstract—Dependences of photoluminescence (PL) intensity for undoped and doped graded-gap $Al_xGa_{1-x}As$ ($x \lesssim 0.36$) solid solutions on the excitation level J (10^{19} photon cm^{-2} s^{-1} $\lesssim J \lesssim 10^{22}$ photon cm^{-2} s^{-1}) were investigated for various built-in electric fields $E = e^{-1}\nabla E_g$ (85 V/cm $\lesssim E \lesssim$ 700 V/cm). It was found that the accelerating effect of the field E gives rise to a complex dependence of intensity of the edge PL (I) on the excitation level. The nonlinearity of the $I(J)$ dependence is attributed to the contribution of the two-photon absorption of PL emission when the latter is reemitted. An optimal range of E values exists (120 V/cm $\lesssim E \lesssim$ 200 V/cm). In this range, the contribution of two-photon absorption to the reemission process in undoped solid solutions is largest.

1. INTRODUCTION

Generally, emission characteristics of graded-gap semiconductors under the accelerating effect of the built-in electric field $E = e^{-1}\nabla E_g$ are determined by the drift of nonequilibrium charge carriers and the photon drift, which is associated with the reemission of recombination radiation. Here, the ∇E_g quantity is the band gap gradient. The contribution of these factors to the formation of luminescence properties is determined by parameters of semiconductors [1]. Thus, for low E values, the photon drift of nonequilibrium charge carriers, which determines the formation of both the spectrum and the intensity of radiative recombination, is dominant [2–5]. Luminescent properties of semiconductors with intermediate and large ∇E_g, in which the drift of nonequilibrium charge carriers dominates in their transport, are determined by the joint action of the drift of nonequilibrium charge carriers in the field E and reemission. Much attention was paid to the investigation of the contribution of the former factor to the formation of the emission spectrum for such semiconductors [1, 6, 7]. However, the influence of reemission on their luminescence characteristics has been inadequately investigated. It is known [8, 9] that reemission with drift of nonequilibrium charge carriers in the field E leads to an increase in the external photon yield of luminescence. However, the mechanism of reemission in such semiconductors has hardly been studied.

In this study, the specific features of reemission in graded-gap $Al_xGa_{1-x}As$ solid solutions with the drift mechanism of transport of nonequilibrium charge carriers are considered. These features were found from measurements of the dependence of their PL spectra on the photoexcitation level.

2. EXPERIMENTAL

Undoped ($n \lesssim 10^{16}$ cm^{-3}) and Te-doped ($n \simeq 10^{18}$ cm^{-3}) epilayers of $Al_xGa_{1-x}As$ solid solutions grown on GaAs substrates from a limited volume of solution–melt were investigated. The composition of the layers varied along the growth axis. Specifically, the Al content was highest at the layer–substrate interface ($x \simeq 0.36$) and decreased to the surface, where $x = 0$. The layer composition varied linearly over the thickness in the region adjoining the substrate. This region makes approximately 80% of the contribution to the total thickness d. For various undoped structures, ∇E_g varied within the range of 85 eV/cm $\lesssim \nabla E_g \lesssim$ 700 eV/cm. An increase in ∇E_g was attained by decreasing the thickness of the layers grown with the same Al content at the substrate–layer interface. The thickness of the solid-solution layers investigated varied within the range of 16 μm $\lesssim d \lesssim$ 70 μm. For doped layers, the ∇E_g values were 150–170 eV/cm.

The photoluminescence (PL) at 77 and 300 K was excited from the wide- and narrow-gap sides of the epilayer (i.e., from the $E_g^{\max}$ and $E_g^{\min}$ sides, as is shown in the inset to Fig. 1) using the angle laps of the structure [1]. The excitation was carried out using the optical beam of an argon (λ = 0.488–0.514 μm) laser; the beam diameter was ~30 μm. The intensity of PL excitation J varied in the range of 10^{19} photon cm^{-2} s^{-1} $\lesssim J \lesssim$ 10^{22} photon cm^{-2} s^{-1}. The PL spectra were recorded using a Ge photodiode according to the conventional procedure [1]. The external PL photon yield was estimated using a calibrated Si photodiode. The effective shift of nonequilibrium charge carriers l_+ was determined from the slope of the low-energy falloff of the edge emission band [1].

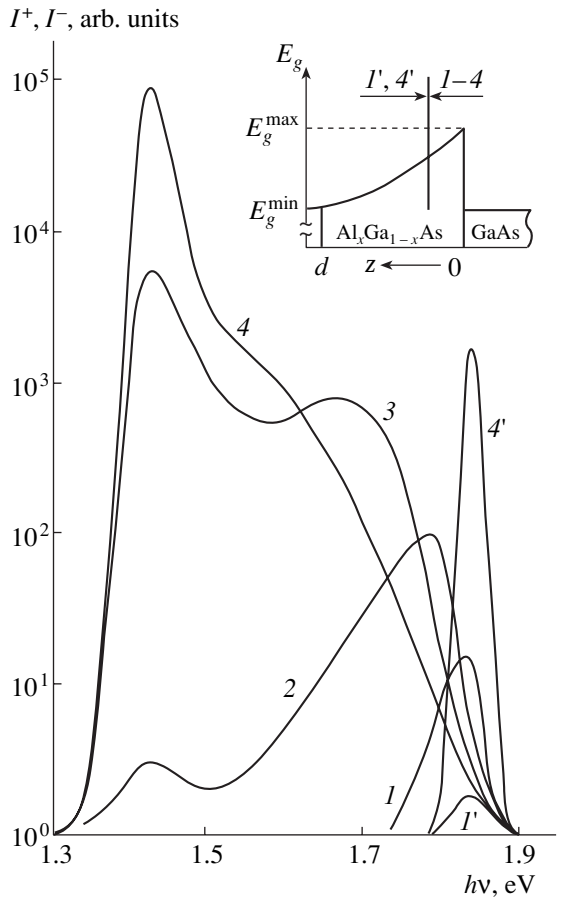

Fig. 1. Variation in the shape of the edge photoluminescence spectrum for the undoped epilayer with $eE = \nabla E_g = 160$ eV/cm in relation to the excitation level with the excitation from the E_g^{max} side (*1*–*4*) and from the E_g^{min} side (*1*', *4*') at T = 300 K. J: (*1*, *1*') 10^{19}; (*2*) 10^{20}; (3) 2.5×10^{21}; and (*4*, *4*') 10^{22} photon cm^{-2} s^{-1}. The variation in the band gap over the epilayer thickness for undoped solid solutions and the experimental layout are shown in the inset. The arrows indicate the direction of photoluminescence excitation. Numbering of arrows corresponds to numbering of the spectra (*1*–*4*, *1*', *4*').

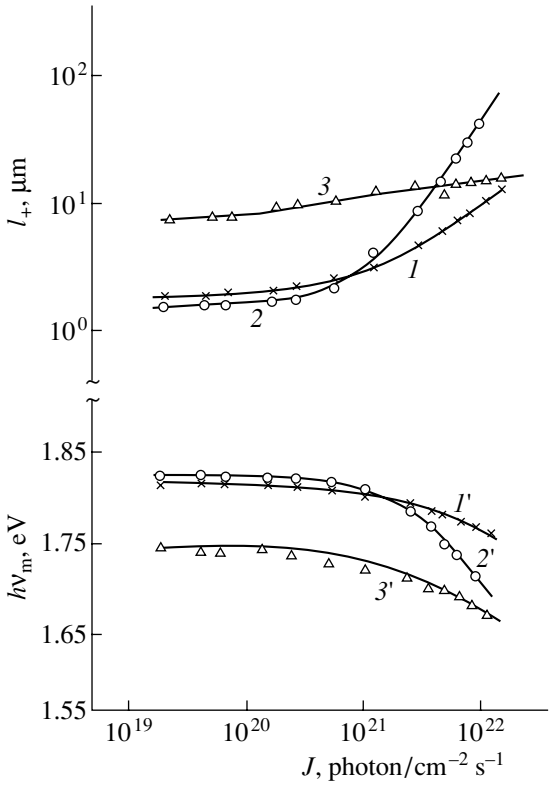

Fig. 2. Effective shift of nonequilibrium charge carriers (*1*–*3*) and location of the short-wavelength peak in the photoluminescence spectra (*1*'–*3*') for undoped epilayers in relation to the excitation intensity at T = 300 K. The built-in field E = (*1*, *1*') 89, (*2*, *2*') 160, and (*3*, *3*') 256 V/cm.

3. RESULTS

The PL spectra of undoped solid solutions included the edge emission band only. With the PL excitation from the E_g^{max} side, i.e., with the accelerating effect of the field E, the shape of PL spectra depended on the magnitude of this field and excitation level J. For the edge emission, the E dependence of its shape for a low PL excitation level ($J \lesssim 2 \times 10^{20}$ photon cm^{-2} s^{-1}) was considered by us in [6]. The variation in the shape of the edge emission band for one of the undoped layers, depending on the excitation level, with the illumination both from the E_g^{max} side (I^+, curves *1*–*4*) and from the E_g^{min} side (I^-, curves *1*', *4*') is shown in Fig. 1. It can be seen that, as J increases, the band is broadened to a low-energy region and the radiative recombination region shifts from the wide-gap region to the narrow-gap region of the layer. This shift manifests itself in the shift of the short-wavelength peak $h\nu_m$ to the long-wavelength region. The variation in the spectrum shape is caused by an increase in the effective shift of nonequilibrium charge carriers l_+ with increasing J. The magnitude of the shift of $h\nu_m$ to the short-wavelength region is proportional to l_+. These characteristics also depend on the built-in field E (Fig. 2). For high excitation intensities, the magnitude l_+ in the layers with $E \approx 160$–260 V/cm is largest.

If the E_g^{max} side is illuminated, the integrated intensity of the edge PL band I_Σ^+ side increases with increasing J. The increase in I_Σ^+ follows the power law

$$I_\Sigma^+ = CJ^m. \quad (1)$$

Here, C is the proportionality coefficient, which accounts for the experimental layout, the angular distribution of the PL intensity, the refractive index of the semiconductor, the interaction of excitation radiation with the semiconductor, the recombination rate, the

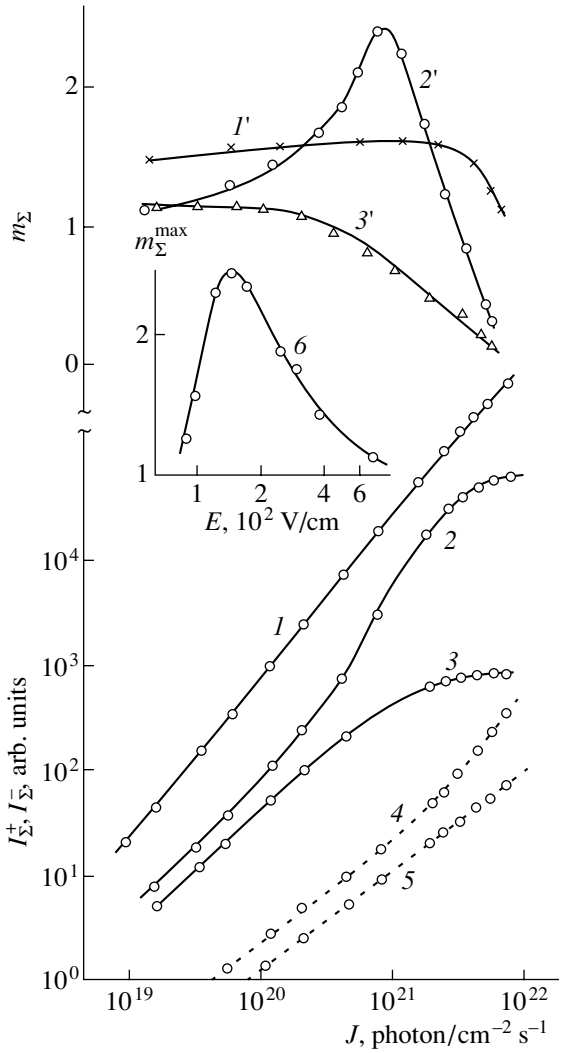

Fig. 3. Dependences of the integrated intensity of edge emission (*1*–*5*), of the exponent m_Σ in relationship (1) on the excitation level (*1*'–*3*'), as well as of the largest value of the exponent m_Σ^{max} on the built-in field (*6*) for undoped solid solutions with the excitation from the E_g^{max} side (*1*–*3*, *1*'–*3*', *6*) and from the E_g^{min} side (*4*, *5*) at T = 300 K. E = (*1*, *1*') 89, (*2*, *2*') 160, (*3*, *3*') 700, (*4*) ≲160, and (*5*) > 200 V/cm.

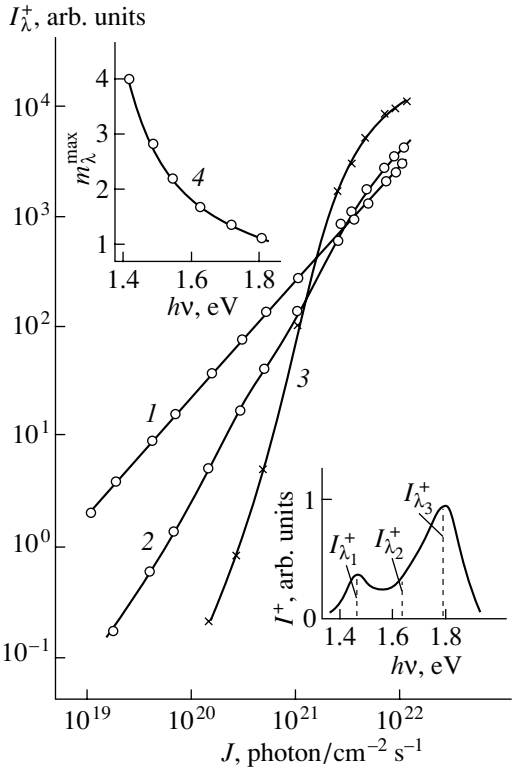

Fig. 4. Spectral dependences of photoluminescence intensity I_λ^+ on the excitation level for various sections of the edge photoluminescence band, as is shown in the inset, for the undoped layer of the solid solution with $E \simeq 180$ V/cm, and the dependence of the largest exponent m_λ^{max} in relationship (1) as a function of energy of photons emitted in the edge photoluminescence band at T = 300 K (curve *4*). Intensities $I_{\lambda_1}^+$, $I_{\lambda_2}^+$, and $I_{\lambda_3}^+$ correspond to their dependences on J represented by curves *1*–*3*.

internal PL photon yield, and the lifetime of nonequilibrium charge carriers.

For low and medium intensities $J \lesssim 10^{21}$ photon cm^{-2} s^{-1}, an increase in intensity I_Σ^+ is superlinear ($m = m_\Sigma > 1$). The degree of superlinearity of dependence (1), i.e., the magnitude of exponent m_Σ, is proportional to the shift of the short-wavelength peak of the edge emission band. With increasing E, m_Σ passes through a maximum (Fig. 3). In the PL spectra of the layers with the most significant shift of $h\nu_m$, the parameter m_Σ increases with increasing J and attains the values $m_\Sigma > 2$ for medium excitation levels (10^{20} photon cm^{-2} s^{-1} ≲ J ≲ 10^{21} photon cm^{-2} s^{-1}). In this case, the degree of superlinearity, i.e., the m value, varies with the intensity I_λ^+ for different wavelengths λ of the same emission band. In the region of the short-wavelength peak, the quantity m is smallest, increases with increasing emission wavelength, and attains the largest values ($m_\Sigma \lesssim 4$) for the low-energy peak (see the inset in Fig. 4).

For high excitation levels ($J > 10^{21}$ photon cm^{-2} s^{-1}), dependence (1) becomes sublinear ($m < 1$). In this case, the exponent m decreases with increasing J, E, and excitation wavelength λ (Fig. 3). With the excitation from the E_g^{max} side, the external photon yield η_{ex} increases with an increase in the excitation level from 0.5–1% for $J = 10^{19}$ photon cm^{-2} s^{-1} to 3–10 % for $J \simeq 10^{22}$ photon cm^{-2} s^{-1} depending on E. The largest values of η_{ex} are observed for the layers with the lowest fields and decrease with increasing E.

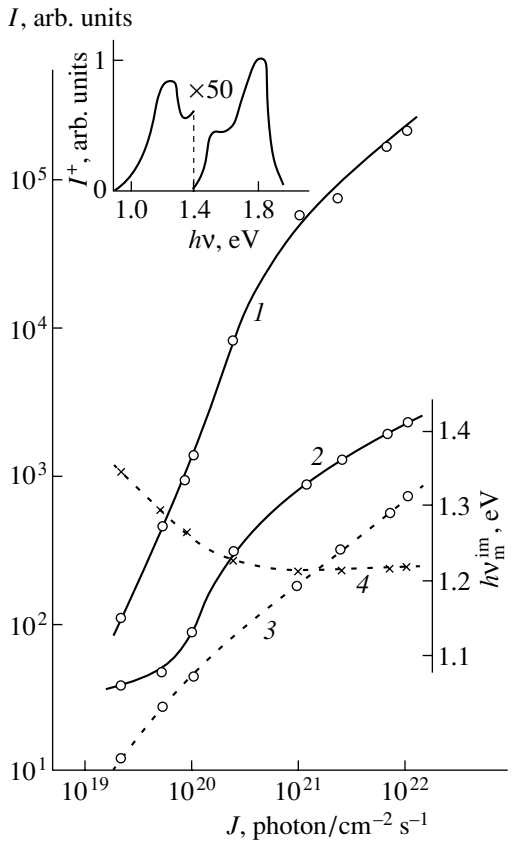

Fig. 5. Dependences of integrated intensity of the edge photoluminescence (*1*), impurity emission (*2*, *3*), and energy of the peak of the edge photoluminescence band (*4*) on the excitation level for one of the doped layers with $E = 154$ V/cm for the excitation from the $E_g^{\max}$ side (*1*, *2*, *4*) and the $E_g^{\min}$ side (*3*) at $T = 77$ K. The shape of the spectrum for this layer of solid solution with the excitation from the $E_g^{\max}$ side is shown in the inset ($J = 10^{21}$ photon cm^{-2} s^{-1}).

The J dependences of the integrated intensity of the edge (I_Σ^+) and impurity ($I_{\Sigma\text{im}}^+$) emission in the PL spectra of doped layers are shown in Fig. 5. It can be seen that the quantities $I_{\Sigma\text{im}}^+(J)$ also depend nonlinearly on the excitation intensity J. Specifically, with increasing J, they pass from sublinear dependences for $J \lesssim 10^{20}$ photon cm^{-2} s^{-1} to superlinear ones with an increase in the exponent m_Σ. This variation in $I_{\Sigma\text{im}}^+(J)$ is accompanied by a shift of the impurity-band peak $h\nu_m^{\text{im}}$ to the longer wavelength. For $J > 5 \times 10^{20}$ photon cm^{-2} s^{-1}, the dependence $I_{\Sigma\text{im}}^+(J)$ becomes sublinear again. The region of stabilization of $h\nu_m^{\text{im}}$ corresponds to this portion of the dependence (Fig. 5).

With the PL excitation from the $E_g^{\min}$ side, i.e., with the decelerating effect of the field, the shape of the edge PL band is typical of direct-gap semiconductors with a constant composition (Fig. 1, curves *1'*, *4'*). The location of the intensity peak of this band (I^-) is determined by the composition of the excited region of the solid solution and is independent of the excitation level. The band shape remains unchanged. The integrated PL intensity I_Σ^- for undoped layers with $E < 200$ V/cm increases linearly for low and medium excitation levels ($m_\Sigma = 1$). For high J values ($J \lesssim 2 \times 10^{21}$ photon cm^{-2} s^{-1}), an increase is superlinear ($m_\Sigma \simeq 1.8$). For undoped layers with $E \gtrsim 200$ V/cm and doped ones, the linear dependence $I_\Sigma^-(J)$ is observed in the entire range in variation of the J quantity (Fig. 3). In this case, the external photon yield of the edge PL remains constant and does not exceed 0.3–0.8% for various layers of solid solutions.

With increasing J, both the shape of the impurity emission band and the J dependence of $h\nu_m^{\text{im}}$ do not vary. However, the intensity I_Σ^- increases linearly with the excitation level for $J < 10^{20}$ photon cm^{-2} s^{-1} and sublinearly for higher J (Fig. 5).

4. DISCUSSION

For the one-photon absorption of the excitation light, dependence (1) can be linear with the proviso that $\Delta n < n_0$. Here, Δn and n_0 are the nonequilibrium and equilibrium carrier densities, respectively. In this case, the exponent $m_{(1)} = 1$, where the subscript (1) indicates the one-photon absorption. Alternatively, dependence (1) can be quadratic when $\Delta n > n_0$. In this case, $m_{(1)} = 2$ [10]. For the two-photon absorption, the intensity of band-to-band PL I_{PL} is also the power-law function of the excitation level J. The exponent $m_{(2)}$, in which subscript (2) indicates the two-photon absorption, exceeds the exponent for the one-photon absorption by a factor of 2 [11]:

$$I_{\text{PL}} = C_{(2)}J^{m_{(2)}} = C_{(2)}J^{2m_{(1)}}. \qquad (2)$$

Thus, for $\Delta n < n_0$, dependence (2) is quadratic.

On the other hand, if the concentration of nonequilibrium charge carriers $\Delta n > n_0$, the exponent in the J dependence of I_{PL} is equal to 4.

Thus, if we have the one-photon or two-photon absorption only, and with the proviso $\Delta n < n_0$, the exponent m in dependence (1) takes the values of 1 or 2. With the proviso $\Delta n > n_0$, it takes the values of 2 or 4, respectively. Obviously the realization of the one-photon and two-photon PL mechanisms should simultaneously (for $\Delta n < n_0$ and $\Delta n > n_0$) determine continuous series of m values in the range of $1 \le m \le 4$ depending on the contribution of one or another excitation mechanism and excitation intensity.

The specific features observed in the dependences $I_\Sigma^+(J)$ and $I_\lambda^+(J)$ are characteristic of the two-photon excitation. These are the superlinearity and superquadratic behavior with various values of the exponent m ($1 < m_\Sigma \le 2.5$; $1 < m_\lambda \le 4$). This permits one to make the following conclusion. With the excitation of graded-gap $Al_xGa_{1-x}As$ solid solutions from the E_g^{max} side, the emission contributes to the measured intensity of the edge PL, which emerges as a result of recombination of nonequilibrium charge carriers. These can be generated both with the one-photon surface absorption of excitation laser radiation and with the one-photon and two-photon absorption in the crystal bulk during repeated reemission. The role of reemission in the formation of the PL intensity is shown by the values of the external photon yield η_{ex} for medium and high excitation levels. These values far exceed the largest theoretical value $\eta_{ex} \simeq 1.5\%$ for homogeneous (homogeneous-gap) III–V semiconductors with the internal emission photon yield $\eta_{in} = 100\%$ and emission output through a flat polished surface in the absence of reemission.

The joint effect of the following phenomena is observed: the drift of nonequilibrium charge carriers in the built-in field E; a coordinate dependence of probability of the radiative recombination, which is determined by the field; broadening of the excitation region with increasing J; and reemission. These phenomena lead to the situation where various mechanisms of recombination (linear, quadratic) and PL absorption (one-photon and two-photon) can occur in different regions of the solid-solution layer. Their combination and role in each of the regions can vary with varying J. The I_Σ^+ quantity is the superposition of intensities I_λ^+ from regions with different compositions. These regions are characterized by various combinations of mechanisms of recombination of nonequilibrium charge carriers and PL absorption. For this reason, the dependence $I_\Sigma^+(J)$ has a variable degree of superlinearity and superquadratic behavior of m for various J.

An increase in the exponent m_λ along the direction of the drift of nonequilibrium charge carriers is apparently associated with an increase in the coefficient of the two-photon absorption $K_{(2)}$. The latter is described for allowed transitions by the expression [10]

$$K_{(2)}(h\nu) = a_1[h(\nu_1 + \nu_2) - E_g]^{1/2}\rho. \quad (3)$$

Here, a_1 is the coefficient, which depends on the orientation of the polarization vectors of photons $h\nu_1$ and $h\nu_2$; and ρ is the density of the primary PL emission. It can be seen from relationship (3) that, for the same values of $h\nu_1$, $h\nu_2$, and $\rho = \text{const}$, the value of $K_{(2)}$ increases with decreasing E_g.

The dependence of the parameter m_Σ^{max} on the built-in field E is apparently controlled by the following factors.

On the one hand, an increase in the field for $E <$ 200 V/cm leads to an increase in the coefficient of the one-photon PL absorption $K_{(1)}$, which is described by the expression [12]

$$K_{(1)}(z) = A[h\nu_1(z_1) - E_g(z_2) + E_g(z - z_2)]^{1/2}. \quad (4)$$

Here, $z > z_2 > z_1$ are the coordinates along the direction of decreasing E_g, $h\nu(z_1)$ is the energy of the photon emitted along the coordinate z_1, and $E_g(z_2)$ is the band gap at the coordinate z_2 ($E_g(0) = E_g^{max} > h\nu(z_1) > E_g(z_2)$). On the other hand, an increase in E broadens the region of radiative recombination to the narrow-gap regions of the layer, in which the role of two-photon absorption increases. This is a result of an increase in both the drift rate and the effective shift of nonequilibrium charge carriers l_+. Both these factors increase the contribution of reemission to the generation of nonequilibrium charge carriers, which leads to increasing m_Σ^{max} with an increase in the field E in the above range of its variation.

For $E >$ 200 V/cm, the l_+ quantity becomes comparable with the thickness of the layers under investigation or exceeds it. In this case, with increasing E, a progressively larger fraction of nonequilibrium charge carriers, which are generated by external excitation at the wide-gap surface, reaches the rear narrow-gap surface, where the carriers recombine nonradiatively. This is shown by transformation of the superlinear and superquadratic dependences $I_\Sigma^+(J)$ and $I_\lambda^+(J)$ into sublinear ones upon reaching saturation in the layers with the larger E values at higher excitation levels. As a result, with increasing E, the fraction of nonequilibrium charge carriers, which recombine radiatively in the bulk, decreases; the contribution of reemission to the generation of nonequilibrium charge carriers reduces; the fulfillment of the condition $\Delta n > n_0$ becomes hampered or impossible; and, consequently, the degree of superlinearity of dependences $I_\Sigma^+(J)$ and $I_\lambda^+(J)$ decreases.

Upon excitation from the E_g^{min} side, the character of the $I_\Sigma^-(J)$ dependence points to linear recombination in undoped layers with $E >$ 200 V/cm over the entire range of variation in J. For undoped layers with $E <$ 200 V/cm, the linear recombination at low and medium excitation levels gives way to the quadratic one at $J > 10^{21}$ photon cm^{-2} s^{-1}. This is caused by an increase in the diffusion length of nonequilibrium charge carriers and, consequently, by an increase in the lifetime of nonequilibrium charge carriers with decreasing ∇E_g [13]. Low values of η_{ex} point to large

nonradiative losses, mainly at the surface illuminated, and to the absence of reemission with deceleration of nonequilibrium charge carriers by the field E.

Let us consider the specific features of the excitation-level dependence of the impurity PL intensity I_{im}. For doped layers, the impurity PL band originates owing to transitions with the involvement of $Te_{As}V_{Ga}$ centers, which introduce a deep level into the lower part of the band gap [14]. It is known that, for a homogeneous n-type semiconductor, the intensity of radiative transitions to such a level at small J values, which ensure the fulfillment of the condition $\Delta n < n_0$, is equal to [15]

$$I_{im} \simeq \eta_{in} C_n n_0 \Delta p. \quad (5)$$

Here, η_{in} is the internal emission photon yield in the centers, C_n is the coefficient of electron capture at the center, and Δp is the concentration of nonequilibrium holes ($\Delta p = \Delta n$). When $\Delta p < N_r$, where N_r is the density of centers, I_{im} increases linearly with the excitation level with the proviso that $\Delta p \propto J$. With increasing J, when $\Delta p > N_r$ and $\Delta n < n_0$, all centers are occupied with holes. In this case, either leveling off (for η_{in} = const) or a sublinear increase (with increasing η_{in} with increasing J) of the I_{im} quantity takes place, which is accompanied by a linear increase in the edge PL intensity. In this case, I_{im} can be represented as

$$I_{im} \simeq \eta_{in} C_n n_0 N_r. \quad (6)$$

For high excitation levels ($\Delta n > n_0$, $\Delta n = \Delta p > N_r$), the intensity of the impurity PL band I_{im}, which is described by the expression

$$I_{im} \cong \eta_{in} C_n N_r \Delta n, \quad (7)$$

increases with increasing J. In this case, the dependence $I_{im}(J)$ is governed mainly by the character of the variation in Δn with increasing excitation level, with the J dependence of the edge emission intensity [15] being quadratic.

For the doped solid solutions investigated, the $I_{im}(J)$ dependence described by expressions (5) and (6) is realized with excitation from the E_g^{min} side, whereas with excitation from the E_g^{max} side, the dependence is described by expression (7). In fact, the intensity of the edge emission I_Σ^+ increases superlinearly with increasing J in the latter case, whereas $I_{\Sigma im}^+$ increases sublinearly. This indicates that the condition $\Delta n > n_0$ is satisfied for $J < 10^{20}$ photon cm^{-2} s^{-1}. For $J > 10^{20}$ photon cm^{-2} s^{-1}, the increase in $I_{\Sigma im}^+$ is superlinear. This is associated with the superlinear increase in the nonequilibrium charge-carrier density Δn due to the two-photon absorption of the edge PL, as shown by the superquadratic dependence $I_\Sigma^+(J)$. The shift of the impurity PL region to the narrow-gap side of the layer and its localization at the rear surface for high excitation levels, the cause of which was considered previously [7], lead to substantial nonradiative losses on this surface. This gives rise to the sublinear dependence $I_{\Sigma im}^+(J)$ for $J \gtrsim 10^{21}$ photon cm^{-2} s^{-1} similarly to that for the dependence of the edge PL $I_\Sigma^+(J)$.

REFERENCES

1. G. P. Peka, V. F. Kovalenko, and A. N. Smolyar, *Varib-and Semiconductors* (Vishcha Shkola, Kiev, 1989).
2. G. V. Tsarenkov, Fiz. Tekh. Poluprovodn. (Leningrad) **13** (6), 1095 (1979) [Sov. Phys. Semicond. **13**, 641 (1979)].
3. R. I. Roedel and V. G. Keramidas, J. Appl. Phys. **50** (10), 6353 (1979).
4. A. S. Volkov and A. L. Lipko, Fiz. Tekh. Poluprovodn. (Leningrad) **16** (3), 412 (1982) [Sov. Phys. Semicond. **16**, 262 (1982)].
5. A. S. Volkov, A. L. Lipko, S. A. Nikishin, *et al.*, Pis'ma Zh. Tekh. Fiz. **5** (11–12), 655 (1979) [Sov. Tech. Phys. Lett. **5**, 269 (1979)].
6. A. I. Bazyk, V. F. Kovalenko, A. Yu. Mironchenko, and S. V. Shutov, Fiz. Tekh. Poluprovodn. (St. Petersburg) **35** (1), 53 (2001) [Semiconductors **35**, 54 (2001)].
7. V. F. Kovalenko, A. Yu. Mironchenko, and S. V. Shutov, Fiz. Tekh. Poluprovodn. (St. Petersburg) **36** (2), 192 (2002) [Semiconductors **36**, 185 (2002)].
8. A. I. Bazyk, V. F. Kovalenko, and G. P. Peka, Ukr. Fiz. Zh. **27** (7), 1007 (1982).
9. A. I. Bazyk, V. F. Kovalenko, G. P. Peka, and O. D. Tokalin, Zh. Prikl. Spektrosk. **42** (10), 441 (1985).
10. *Radiative Recombination in Semiconductors*, Ed. by Ya. E. Pokrovskiĭ (Nauka, Moscow, 1972).
11. V. P. Gribkovskiĭ, *The Theory of Absorption and Emission of Light in Semiconductors* (Nauka i Tekhnika, Minsk, 1975).
12. M. Konagai and K. Takahashi, J. Appl. Phys. **46**, 3542 (1975).
13. F. P. Kesamanly, V. F. Kovalenko, I. E. Maronchuk, *et al.*, Fiz. Tekh. Poluprovodn. (Leningrad) **12** (7), 1318 (1978) [Sov. Phys. Semicond. **12**, 780 (1978)].
14. N. K. Dryapiko, V. F. Kovalenko, and G. P. Peka, Fiz. Tekh. Poluprovodn. (Leningrad) **17** (5), 863 (1983) [Sov. Phys. Semicond. **17**, 541 (1983)].
15. K. D. Glinchuk, A. V. Prohorovich, V. E. Rodionov, and V. I. Vovnenko, Phys. Status Solidi A **48**, 593 (1978).

Translated by N. Korovin

Semiconductors, Vol. 36, No. 5, 2002, pp. 487–492. Translated from Fizika i Tekhnika Poluprovodnikov, Vol. 36, No. 5, 2002, pp. 519–524.

ELECTRONIC AND OPTICAL PROPERTIES OF SEMICONDUCTORS

Features of Determination of Shallow-Level Impurity Concentrations in Semiconductors from Analysis of the Exciton Luminescence Spectrum

K. D. Glinchuk* and A. V. Prokhorovich

Institute of Semiconductor Physics, National Academy of Sciences of Ukraine, Kiev, 03028 Ukraine

**e-mail: ria@isp.kiev.ua*

Submitted January 10, 2001; accepted for publication September 26, 2001

Abstract—The range of applicability of the method for the determination of the shallow-level donor and acceptor content in semiconductors from the ratio of low-temperature (T = 1.8–4.2 K) intensities of exciton-luminescence bands was analyzed; these bands are caused, in particular, by the radiative annihilation of excitons bound to impurities and free excitons. It is shown that the correct data on the concentrations of shallow-level acceptors and donors and on changes in these concentrations under various effects can be obtained if the occupancy of the defects under consideration by electrons and holes is independent of the luminescence excitation intensity and external factors. The procedures for verifying the fulfillment of conditions for applicability of the method are outlined. An example of using the method for determination of thermally stimulated changes in concentrations of shallow-level acceptors and donors in gallium arsenide is given. © *2002 MAIK "Nauka/Interperiodica".*

1. INTRODUCTION

It is known that intense luminescence bands are observed at low temperatures (T = 1.8–4.2 K) in the edge emission spectrum of semiconductors (henceforth, the emitted-photon energy is denoted by $h\nu$). These bands are caused by the radiative annihilation of free excitons X (reaction $X \longrightarrow h\nu$, its probability is α_X, and the emission intensity is I_X) as well as of excitons bound to shallow impurities, i.e., neutral acceptors A^0 (hereafter, bound excitons A^0X, reaction $A^0X \longrightarrow A^0 + h\nu$, its probability is α_{A^0X}, and the emission intensity is I_{A^0X}), and those bound at ionized (D^+) and neutral (D^0) donors (hereafter, bound excitons D^+X and D^0X, reactions $D^+X \longrightarrow D^+ + h\nu$ and $D^0X \longrightarrow D^0 + h\nu$, the corresponding probabilities are α_{D^+X} and α_{D^0X}, and the emission intensities are I_{D^+X} and I_{D^0X} [1]).[1] Previously (see, e.g., [4–13]), the analysis of the ratio of intensities of exciton luminescence bands in semiconductors was widely used for the determination of the impurity composition. Thus, measurements of the intensity ratio of luminescence bands caused by annihilation of bound and free excitons were used for the determination of shallow-level acceptor N_A and donor N_D concentrations in various semiconductors (e.g., in Si [4–7], GaAs [8, 9], and InP [9]) and the changes in concentrations induced by various external factors F, in particular, by doping and heating (e.g., in GaAs [10, 11]). In addition, measurements in GaAs of the intensity ratio of luminescence bands caused by the annihilation of excitons bound to shallow acceptors and donors were used to determine the concentration ratio N_A/N_D [12] and its change under external factor F (variations in the growth conditions of epitaxial layers) [13]. However, in this case, insufficient attention was paid to the consideration of the method's physical grounds, in particular, to conditions that, when satisfied, make it possible to use this method to obtain reliable data on the quantities N_A, N_D, N_A/N_D, and on their dependences on F.

Below, we will consider in detail the physical conditions under which the correct determination of shallow acceptor and donor concentrations in a semiconductor, as well as the changes in the concentrations caused by various factors, is possible. We will show that the use of normalized intensities of exciton luminescence bands for the determination of the quantities N_A, N_D, and N_A/N_D and their changes caused by variations in F has certain restrictions; we will outline the criteria that, when fulfilled, make it possible to reliably determine the above quantities by analyzing the experimental data. We will also illustrate the proper use of the luminescence method under consideration by the example of the determination of thermally stimulated changes in the shallow acceptor and donor concentrations in semi-insulating GaAs.

[1] Note that, in particular, in the bound excitons A^0X, D^+X, and D^0X, not only radiative but also nonradiative electron transitions (with probabilities α'_{A^0X} α'_{D^+X}, and α'_{D^0X}, respectively) can take place [2, 3].

2. METHOD BASICS

2.1. General Expression for the Luminescence Intensity Ratio

We consider a semiconductor containing acceptors and donors both isolated (i.e., those without bound excitons) and bound with excitons. We define the normalized intensities of exciton luminescence I_{A^0X}/I_X, I_{D^+X}/I_X, I_{D^0X}/I_X, I_{A^0X}/I_{D^+X}, I_{A^0X}/I_{D^0X}, and I_{D^+X}/I_{D^0X} in this semiconductor at low temperatures T = 1.8–4.2 K.[2] Obviously, under the conditions indicated, the intensities of the exciton luminescence bands are defined as follows:

$$I_{A^0X} = \alpha_{A^0X} n_{A^0X} = B_{A^0X} N_{A^0} n_X,$$
$$I_{D^+X} = \alpha_{D^+X} n_{D^+X} = B_{D^+X} N_{D^+} n_X,$$
$$I_{D^0X} = \alpha_{D^0X} n_{D^0X} = B_{D^0X} N_{D^0} n_X,$$

where B_{A^0X}, B_{D^+X}, and B_{D^0X} are the proportionality factors dependent on the nature of acceptors and donors; n_X, n_{A^0X}, n_{D^+X}, and n_{D^0X} are the concentrations of free (X) and bound (A^0X, D^+X, and D^0X) excitons; and N_{A^0}, N_{D^+}, and N_{D^0} are concentrations of neutral acceptors and ionized and neutral donors, respectively.[3] Then, the normalized intensities of the exciton luminescence bands under consideration are given by

$$\frac{I_{A^0X}}{I_X} \propto \varphi_{A^0} N_A, \quad \frac{I_{D^+X}}{I_X} \propto \varphi_{D^+} N_D, \quad \frac{I_{D^0X}}{I_X} \propto \varphi_{D^0} N_D; \quad (1)$$

$$\frac{I_{A^0X}}{I_{D^+X}} \propto \frac{\varphi_{A^0}}{\varphi_{D^+}} \frac{N_A}{N_D}, \quad \frac{I_{A^0X}}{I_{D^0X}} \propto \frac{\varphi_{A^0}}{\varphi_{D^0}} \frac{N_A}{N_D}; \quad (2)$$

$$\frac{I_{D^+X}}{I_{D^0X}} \propto \frac{\varphi_{D^+}}{\varphi_{D^0}} \propto \frac{\delta p}{\delta n}, \quad (3)$$

where concentrations $N_{A^0} = \varphi_{A^0} N_A$, $N_{D^+} = \varphi_{D^+} N_D$, and $N_{D^0} = \varphi_{D^0} N_D$ are expressed in terms of the probabilities of the acceptor occupation with holes (φ_{A^0}), donor occupation with holes (φ_{D^+}), and electrons (φ_{D^0}); i.e.,

$$\varphi_{A^0} = \frac{c^-_{pA}\delta p}{c^-_{pA}\delta p + c^0_{nA}\delta n}, \quad \varphi_{D^+} = \frac{c^0_{pD}\delta p}{c^0_{pD}\delta p + c^+_{nD}\delta n}, \quad (4)$$

$$\varphi_{D^0} = \frac{c^+_{nD}\delta n}{c^0_{pD}\delta p + c^+_{nD}\delta n}, \quad (5)$$

where c^-_{pA} and c^0_{nA} are the coefficients of hole capture by ionized acceptors and of electron capture by neutral acceptors, and c^0_{pD} and c^+_{nD} are the coefficients of hole capture by neutral donors and of electrons capture by ionized donors.[4] Thus, formulas (4) and (5) define the probabilities of finding an acceptor in the neutral state A^0 and a donor in the state D^+ or in the neutral state D^0.

2.2. Determination of the Dependences N_A, N_D = f(F) from Analysis of Exciton Luminescence Spectra

As was mentioned above, the determination of dependences of N_A and N_D on the magnitude of the external factor F is based on measurements of intensity ratios I_{A^0X}/I_X, I_{D^+X}/I_X, and I_{D^0X}/I_X under the effect of various external factors F at low temperatures (T = 1.8–4.2 K) [10, 11]. However, it can be seen from formulas (1), (4), and (5) that, in the general case, the variations in these ratios due to changes in F are defined not only by the dependences of shallow acceptor and donor concentrations on F but also by quantities φ_{A^0}, φ_{D^+}, and φ_{D^0}, i.e., by dependences of the ratio of the excess electron and hole concentrations ($\delta n/\delta p$) together with the dependences of the capture rates of carriers by acceptors ($c^0_{nA}\delta n/c^-_{pA}\delta p$) and donors ($c^+_{nD}\delta n/c^0_{pD}\delta p$) on the magnitude of F.

[2] It is assumed that at these temperatures, first, conductivity of the semiconductor (due to freezing of equilibrium charge carriers) is controlled by the excess electrons (their concentration is δn and their lifetime is τ_n) and holes (their concentration is δp and their lifetime is τ_p) and, second, the thermal dissociation of excitons can be ignored.

[3] It is assumed in defining the relations I_{A^0X}, I_{D^+X}, and I_{D^0X} that, first, the concentration of acceptors and donors, to which the excitons are bound, is low, i.e., $n_{A^0X} \ll N_{A^0}$, $n_{D^+X} \ll N_{D^+}$, and $n_{D^0X} \ll N_{D^0}$ (the conditions indicated are one of the main conditions for the applicability of the method under consideration; see below and also [6]). Second, it is assumed that the nonradiative annihilation of bound excitons A^0X, D^+X, and D^0X (if its role is important, i.e., if $\alpha'_{A^0X} \geq \alpha_{A^0X}$, $\alpha'_{D^+X} \geq \alpha_{D^+X}$, and $\alpha'_{D^0X} \geq \alpha_{D^0X}$) is not caused by their interaction with free charge carriers; in particular, the dissociation of exciton–impurity complexes A^0X, D^+X, and D^0X due to transitions of free electrons and holes at acceptors or donors can be ignored.

[4] It is implied in relations (4) and (5) that the probabilities φ_{A^0}, φ_{D^+}, and φ_{D^0} are defined only by transitions of free electrons and holes to the neutral and ionized acceptors and donors [14, 15], i.e., the generation and annihilation of bound excitons A^0X, D^+X, and D^0X do not affect the quantities N_{A^0}, N_{D^+}, and N_{D^0}. Obviously, this assumption is valid if the annihilation of exciton–impurity complexes A^0X, D^+X, and D^0X is accompanied mainly by the appearance of isolated acceptors A^0 and donors D^+ and D^0, i.e., the Auger recombination of bound excitons A^0X, D^+X, and D^0X can be ignored [15]).

Obviously, formulas (1) can be transformed into

$$\frac{I_{A^0X}}{I_X} \propto N_A, \tag{6}$$

if $\varphi_{A^0} \neq f(L, F)$, where L is the intensity of luminescence excitation;

$$\frac{I_{D^+X}}{I_X} \propto N_D, \tag{7}$$

if $\varphi_{D^+} \neq f(L, F)$; and

$$\frac{I_{D^0X}}{I_X} \propto N_D, \tag{8}$$

if $\varphi_{D^0} \neq f(L, F)$; (on the conditions for φ_{A^0}, φ_{D^+}, $\varphi_{D^0} \neq f(L, F)$, see below).

Expressions (6)–(8) are essential using the exciton luminescence spectra for the determination of dependences N_A, $N_D = f(F)$. They represent a linear relation (necessary for the correctness of the method) between the normalized intensities of bound-exciton luminescence and concentrations of shallow impurities.[5] Consequently, the correct use of the method considered for the determination of variations in shallow acceptor concentrations induced by external factors is possible if $\varphi_{A^0} \neq f(L, F)$; similarly, we can determine variations in shallow donor concentrations if φ_{D^+} or φ_{D^0} are independent of L and F, because only in these cases I_{A^0X}/I_X increases linearly with N_A and ratios I_{D^+X}/I_X and I_{D^0X}/I_X increase linearly with the increase in N_D. Otherwise, the method considered yields an incorrect dependence of N_A and N_D on the external factors; i.e., its form will be different for dissimilar values of L (in particular, if φ_{A^0}, φ_{D^+}, $\varphi_{D^0} = f(L)$; this apparently takes place when the form of dependences of I_{A^0X}, I_{D^+X}, and I_{D^0X} on L is different; see, e.g., [9, 16]).

[5] The method under consideration is valid if only a small fraction of acceptors and donors are bound with excitons, i.e., $n_{A^0X} \ll N_A$ and $n_{D^+X} + n_{D^0X} \ll N_D$. In this case, the luminescence intensities I_{A^0X}, I_{D^+X}, and I_{D^0X} are proportional to L^m, where m can change from 1.5 to 2 [16], and the normalized intensities of the exciton luminescence bands are possibly independent of L (see below). Otherwise, if, e.g., $n_{A^0X} \approx N_A$, intensity $I_{A^0X} \approx \alpha_{A^0X} N_A$ is independent of L, whereas the intensity ratio $I_{A^0X}/I_X \propto N_A/n_X = f(L)$ for any L.

The aforementioned independence of φ_{A^0}, φ_{D^+}, and φ_{D^0} on L and F can take place under the following conditions, as follows from relations (4) and (5):

(i) $\delta p \simeq \delta n$ or $\delta p/\delta n \neq f(L, F)$, then φ_{A^0}, φ_{D^+}, $\varphi_{D^0} \neq f(L, F)$;

(ii) $c^-_{pA}\,\delta p \gg c^0_{nA}\,\delta n$, then $\varphi_{A^0} \simeq 1$, i.e., $\varphi_{A^0} \neq f(L, F)$;

(iii) $c^+_{nD}\,\delta n \gg c^0_{pD}\,\delta p$, then $\varphi_{D^0} \simeq 1$, i.e., $\varphi_{D^0} \neq f(L, F)$;

(iv) $c^0_{pD}\,\delta p \gg c^0_{nD}\,\delta n$, then $\varphi_{D^+} \simeq 1$, i.e., $\varphi_{D^+} \neq f(L, F)$.

Obviously, experimentally, the independence of intensity ratios I_{A^0X}/I_X, I_{D^+X}/I_X, and I_{D^0}/I_X from L is indicative of the fulfillment of the conditions φ_{A^0}, φ_{D^+}, $\varphi_{D^0} \neq f(L)$. Undoubtedly, the independence of the intensity ratio $I_{D^+X}/I_{D^0X} \propto \delta p/\delta n$ on L and F also confirms the fulfillment of relations φ_{A^0}, φ_{D^+}, $\varphi_{D^0} \neq f(L, F)$ in experiment [see expression (3)].

The fulfillment of the above conditions defining the limits of the independence of quantities φ_{A^0}, φ_{D^+}, and φ_{D^0} from L and F appreciably restrict the domain of the applicability of the method under consideration. Their fulfillment in the experiments involves certain difficulties. Therefore, in the relevant experiment, it is very likely that the normalized intensities I_{A^0X}/I_X, I_{D^+X}/I_X, and I_{D^0X}/I_X and ratios I_{A^0X}/I_{D^+X} and I_{A^0X}/I_{D^0X} depend on L, and, consequently, the method under consideration cannot be used for the determination of changes of N_A, N_D, and N_A/N_D when F is varied. Thus, condition $\delta p \simeq \delta n$ can be fulfilled only for fairly large values of L (not necessarily attainable experimentally); the values of L depend on the parameters of recombination centers [14, 15]. Condition $\delta p/\delta n \neq f(L)$ can be fulfilled only for a certain scheme of the recombination transitions in semiconductors [14, 15]. Condition $\delta p/\delta n \neq f(F)$ can be met only if the external factors have a small magnitude and if they affect the quantities δp and δn only slightly; then, δp, $\delta n \neq f(F)$) or affect the quantities δp and δn in a similar way. The latter can occur only for specific recombination parameters of local levels [14, 15]. At the same time, due to a large difference between the coefficients c^-_{pA} and c^0_{nA} ($c^-_{pA} \gg c^0_{nA}$), c^+_{nD} and c^0_{pD} ($c^+_{nD} \gg c^0_{pD}$) and a somewhat lesser difference between δp and δn, the fulfillment of conditions $c^-_{pA}\,\delta p \gg c^0_{nA}\,\delta n$ and $c^+_{nD}\,\delta n \gg c^0_{pD}\,\delta p$ experimentally is highly probable. Actually, e.g., in GaAs, the coefficients c^-_{pA} and c^0_{nA}, c^+_{nD} and c^0_{pD} differ by about five orders of

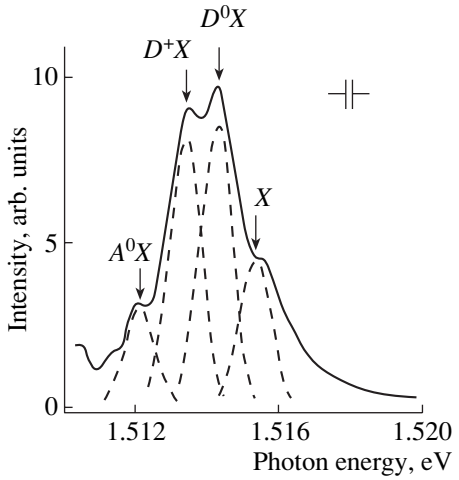

Fig. 1. Luminescence spectrum of the original semi-insulating GaAs at the temperature $T = 4.2$ K and intensity of the luminescence excitation $L = 10^{18}$ photon cm^{-2} s^{-1}.

magnitude (c^-_{pA}/c^0_{nA}, $c^+_{nD}/c^0_{pD} \simeq 10^5$) [17]. At the same time, depending on the technology of GaAs fabrication, the type and magnitude of its conductivity, as well as the excitation intensity used L (in measurements of luminescence spectra, usually $L \gtrsim 10^{18}$ photon cm^{-2} s^{-1}), the values of δn and δp (obviously, $\delta p/\delta n = \tau_p/\tau_n$) can be of the same order of magnitude (see, e.g., [18, 19]) or differ by no more than two to three orders of magnitude (see, e.g., [19–21]).

2.3. Determination of Dependences $N_A/N_D = f(F)$ from the Analysis of the Exciton Luminescence Spectra

As was mentioned above, the determination of dependences N_A/N_D on F is based on the low-temperature (T = 1.8–4.2 K) measurements of the intensity ratios I_{A^0X}/I_{D^+X} or I_{A^0X}/I_{D^0X} for various F [13]. As follows from expression (2),

$$\frac{I_{A^0X}}{I_{D^+X}} \propto \frac{N_A}{N_D}, \tag{9}$$

if $\varphi_{A^0}/\varphi_{D^+} \neq f(L, F)$, and

$$\frac{I_{A^0X}}{I_{D^0X}} \propto \frac{N_A}{N_D}, \tag{10}$$

if $\varphi_{A^0}/\varphi_{D^0} \neq f(L, F)$. It is obvious that conditions for the independence of $\varphi_{A^0}/\varphi_{D^+}$ and $\varphi_{A^0}/\varphi_{D^0}$ from L and F are similar to those considered in Subsection 2.2.

Consequently, the correct use of the luminescence method considered for the determination of the change of N_A/N_D with F is possible when $\varphi_{A^0}/\varphi_{D^+}$ or $\varphi_{A^0}/\varphi_{D^0}$ are independent of L and F. In this case, ratios I_{A^0X}/I_{D^+X} or I_{A^0X}/I_{D^0X} are independent of L and increase linearly with increasing N_A/N_D. In the opposite case, the intensity ratios I_{A^0X}/I_{D^+X} and I_{A^0X}/I_{D^0X} depend on L and turn out to be related nonlinearly to the ratio of shallow acceptor and donor concentrations N_A/N_D.

2.4. Determination of N_A, N_D, and N_A/N_D from Analysis of the Exciton Luminescence Spectra

The method under consideration is based on the calculation of ratios I_{A^0X}/I_X, I_{D^0X}/I_X, and I_{A^0X}/I_{D^0X} from the low-temperature (T = 1.8–4.2 K) luminescence spectra of test crystals (films). Then, using the known calibration dependences $I_{A^0X}/I_X = f(N_A)$, $I_{D^0X}/I_X = f(N_D)$, and $I_{A^0X}/I_{D^0X} = f(N_A/N_D)$ (apparently, they have a linear form if φ_{A^0}, $\varphi_{D^0} \neq f(L, N_A, N_D)$, we can determine the concentrations N_A and N_D as well as their ratio [4–9, 12]. Undoubtedly, as follows from Subsections 2.2 and 2.3, for such a procedure of determination, these quantities can be obtained if the probabilities φ_{A^0} and φ_{D^0} [see relations (1) and (2)] are independent (or depend similarly, which is unlikely) of L, N_A, and N_D, both for the test structure and for the reference crystals. In this case, I_{A^0X}/I_X, I_{D^0X}/I_X, and $I_{A^0X}/I_{D^0X} \neq f(L)$.

3. EXAMPLE: EMPLOYMENT OF THE METHOD FOR THE DETERMINATION OF THERMALLY STIMULATED CHANGES IN SHALLOW ACCEPTOR AND DONOR CONCENTRATIONS IN GaAs.

We illustrate the proper use of the method under consideration by the example of studies of variations in shallow acceptor and donor concentrations in semi-insulating GaAs; these variations are induced by thermal annealing (at the annealing temperature T_a = 900°C) of various durations t (the annealing time t varied from 20 to 90 min). At T = 4.2 K, the GaAs conductivity is caused by excess electrons and holes. For simplicity, we restrict ourselves to the presentation of the luminescence spectra and dependences I_{A^0X}/I_X, I_{D^+X}/I_X, I_{D^0X}/I_X, and $I_{D^+X}/I_{D^0X} = f(L)$ for the fixed external effect in the absence of thermal treatment, and dependences I_{A^0X}/I_X, I_{D^+X}/I_X, I_{D^0X}/I_X, and $I_{D^+X}/I_{D^0X} = f(t)$ for the fixed excitation intensity L. This is associated with the following fact: the dependences of the intensity ratio on L, given below, are independent of the thermal treatment duration t, and the dependences on the annealing time are independent of L.

A typical spectrum of the exciton luminescence of GaAs at T = 4.2 K (the luminescence was excited by

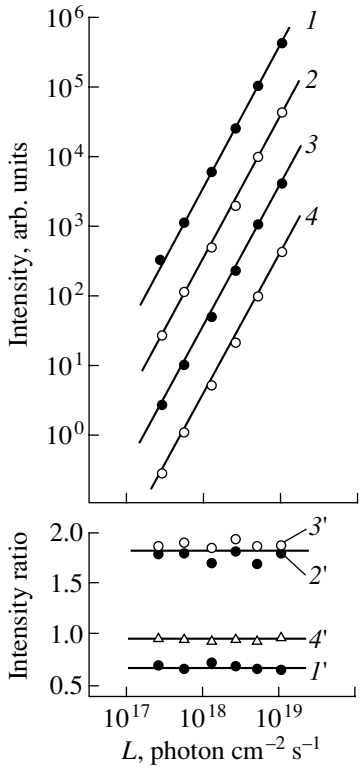

Fig. 2. Dependences of intensities of the exciton luminescence bands (*1*) I_{A^0X}, (*2*) I_{D^+X}, (*3*) I_{D^0X}, and (*4*) I_X as well as their ratio I_{A^0X}/I_X (*1'*), I_{D^+X}/I_X (*2'*), I_{D^0X}/I_X (*3'*), and I_{D^+X}/I_{D^0X} (*4'*) on the intensity L of the luminescence excitation in the original semi-insulating GaAs at $T = 4.2$ K. Ratios between quantities I_{A^0X}, I_{D^+X}, I_{D^0X}, and I_X are arbitrary; the real ratios can be deduced from Fig. 1.

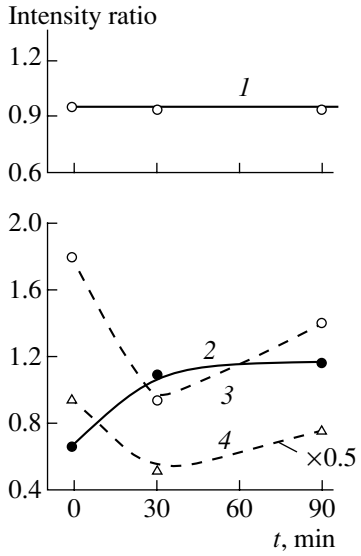

Fig. 3. Dependences of the intensity ratios of luminescence bands (*1*) I_{D^+X}/I_{D^0X}, (*2*) I_{A^0X}/I_X, (*3*) I_{D^+X}/I_X, and (*4*) I_{D^0X}/I_X on the thermal treatment duration t of the semi-insulating GaAs at the temperature $T_a = 900$°C. The measurements were carried out at $T = 4.2$ K and luminescence excitation intensity $L = 10^{18}$ photon cm^{-2} s^{-1}.

He–Ne-laser radiation with the quantum energy $h\nu_e$ = 1.96 eV). The luminescence bands caused by annihilation of bound (A^0X, D^+X, and D^0X) and free (X) excitons are observed in the spectrum. The position of the emission peaks are $h\nu_m = 1.512$, 1.5133, 1.541, and 1.5153 eV, respectively [8–13, 22]. As was mentioned above, the shape of the luminescence spectrum is independent of the excitation intensity L and the duration of thermal treatment of crystals t; i.e., the intensities of various bands in the spectrum change similarly with L. Only the ratios between the band intensities in the spectrum change if the annealing duration t is varied.

The typical dependences of intensities I_{A^0X}, I_{D^+X}, I_{D^0X}, and I_X (lines *1–4*), as well as their ratio (lines *1'–4'*), on the excitation intensity are shown in Fig. 2. The luminescence band intensities increase superlinearly with increasing L ($\propto L^2$), and their ratios are independent of L. A similar independence of intensity ratios from L, as was mentioned above, was observed in GaAs heated for various time periods (t = 30 and 90 min).

The dependences of intensity ratios I_{D^+X}/I_{D^0X}, as well as I_{A^0X}/I_X, I_{D^+X}/I_X, and I_{D^0X}/I_X, on the heat treatment duration of GaAs at $T_a = 900$°C are shown in Fig. 3. The shape of these dependences are retained as L is changed. As can be seen from Fig. 3, the intensity ratio I_{D^+X}/I_{D^0X} is independent of time t, and the ratios I_{A^0X}/I_X, I_{D^+X}/I_X, and I_{D^0X}/I_X change nonmonotonically with t.

It follows from the experimental quadratic dependences of luminescence intensities I_{A^0X}, I_{D^+X}, and I_{D^0X} on L, as well as from the independence of the intensity ratios I_{A^0X}/I_X, I_{D^+X}/I_X, I_{D^0X}/I_X, and I_{D^+X}/I_{D^0X} from L and t, that, in the GaAs studied, $n_{A^0X} \ll N_A$, $n_{D^+X} + n_{D^0X} \ll N_D$, and $\delta p/\delta n \neq f(L, F)$; i.e., the necessary condition $\varphi_{A^0}, \varphi_{D^+}, \varphi_{D^0} \neq f(L, F)$ for the correct use of the method under consideration for the determination of N_A and N_D variations under thermal effect is fulfilled (see, Subsection 2.2).[6] The variations in N_A and

[6] It is highly probable that the independence of the intensity ratios I_{A^0X}/I_X and I_{D^0X}/I_X from L is also caused by the fact that, in the GaAs studied, the relations $c^-_{pA}\delta p \gg c^0_{nA}\delta n$ and $c^+_{nD}\delta n \gg c^0_{pD}\delta p$ are fulfilled (see Subsection 2.2.).

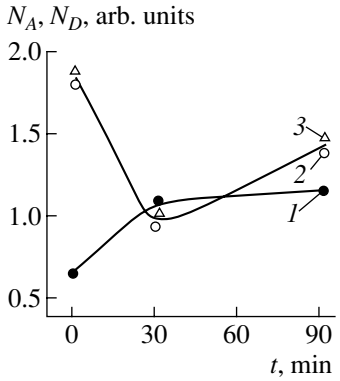

Fig. 4. The dependence of shallow (*1*) acceptor N_A and (*2*, *3*) donor N_D concentrations on the thermal treatment duration t of the semi-insulating GaAs at T_a = 900°C.

N_D obtained by this method, with the change in the annealing duration t and in semi-insulating GaAs heat treated at T_a = 900°C, are shown in Fig. 4. The concentration of shallow acceptors N_A (*1*) is obtained from the data on $I_{A^0X}/I_X = f(t)$ (see Fig. 3); the donor concentration N_D (*2*, *3*) was determined from dependences I_{D^+X}/I_X, $I_{D^0X}/I_X = f(t)$.

CONCLUSION

The measurements at T = 1.8–4.2 K of the intensity ratio of the luminescence bands caused by annihilation of bound and free excitons are widely used for the determination of shallow acceptor N_A and donor N_D concentrations in semiconductors. The same method is used for the determination of changes in these concentrations induced by external factors. However, one should keep in mind that this method yields correct values of N_A, N_D, and N_A/N_D and their dependences on various factors F only if, for the values of L and F used, the "limiting" (independent of L and F) occupancy of acceptors with holes and donors with holes and electrons takes place. This happens if concentrations of excess holes δp and electrons δn are almost the same or if their ratio $\delta p/\delta n$ is independent of L and F, i.e., if there is a significant difference in the capture rates of electrons and holes by the defects considered. In the opposite case, the use of the method under consideration results in incorrect values of N_A, N_D, and N_A/N_D and their dependences on external factors.

REFERENCES

1. V. I. Gavrilenko, A. M. Grekhov, D. V. Korbutyak, and V. G. Litovchenko, *Optical Properties of Semiconductors* (Naukova Dumka, Kiev, 1987).
2. T. Taguchi, J. Shiraruji, and Y. Inuishi, Phys. Status Solidi B **68**, 727 (1975).
3. T. Shmidt, K. Lischka, and W. Zulehner, Phys. Rev. B **45**, 8989 (1992).
4. M. Tajima, Appl. Phys. Lett. **32**, 719 (1978).
5. H. Nakayama, T. Nishino, and Y. Hamakawa, Jpn. J. Appl. Phys. **19**, 501 (1980).
6. A. S. Kaminskiĭ, L. I. Kolesnik, B. M. Leĭferov, and Ya. E. Pokrovskiĭ, Zh. Prikl. Spektrosk. **36**, 745 (1982).
7. B. M. Leĭferov and A. G. Libinson, Vysokochist. Veshchestva, No. 1, 147 (1987).
8. S. Ambros, W. Kamp, K. Wolter, *et al.*, J. Appl. Phys. **64**, 5098 (1988).
9. H. F. Pen, F. A. Driessen, S. M. Olsthoorn, and L. J. Giling, Semicond. Sci. Technol. **7**, 1400 (1992).
10. K. D. Glinchuk, N. M. Litovchenko, O. N. Stril'chuk, and A. V. Prokhorovich, Fiz. Tekh. Poluprovodn. (St. Petersburg) **34** (5), 530 (2000) [Semiconductors **34**, 514 (2000)].
11. K. D. Glinchuk, N. M. Litovchenko, O. N. Stril'chuk, and A. V. Prokhorovich, Fiz. Tekh. Poluprovodn. (St. Petersburg) **34** (11), 1311 (2000) [Semiconductors **34**, 1259 (2000)].
12. Z. H. Lu, M. C. Hanna, D. M. Szmyd, *et al.*, Appl. Phys. Lett. **56**, 177 (1990).
13. K. S. Zhuravlev, A. K. Kalagin, N. T. Meshegov, *et al.*, Fiz. Tekh. Poluprovodn. (St. Petersburg) **30**, 1704 (1996) [Semiconductors **30**, 891 (1996)].
14. S. M. Ryvkin, *Photoelectric Effects in Semiconductors* (Fizmatgiz, Moscow, 1963; Consultants Bureau, New York, 1964).
15. V. E. Lashkarev, A. V. Lyubchenko, and M. K. Sheĭnkman, *Nonequilibrium Processes in Photoconductors* (Naukova Dumka, Kiev, 1981).
16. K. D. Glinchuk, N. M. Litovchenko, O. N. Stril'chuk, and A. V. Prokhorovich, Optoélektron. Poluprovodn. Tekh. **35**, 176 (2000).
17. J. I. Pankove, *Optical Processes in Semiconductors* (Prentice-Hall, Englewood Cliffs, 1971; Mir, Moscow, 1973).
18. M. J. Papastamatiou and G. J. Papaioannou, J. Appl. Phys. **68**, 1094 (1990).
19. I. A. Karpovich and M. V. Stepikhova, Fiz. Tekh. Poluprovodn. (St. Petersburg) **30**, 1785 (1996) [Semiconductors **30**, 934 (1996)].
20. V. Kazukauskas, Appl. Phys. A **60**, 509 (1995).
21. N. M. Litovchenko and L. G. Shepel', Optoélektron. Poluprovodn. Tekh. **29**, 108 (1995).
22. K. D. Glinchuk, N. M. Litovchenko, O. N. Stril'chuk, and A. V. Prokhorovich, Fiz. Tekh. Poluprovodn. (St. Petersburg) **35**, 537 (2001) [Semiconductors **35**, 516 (2001)].

Translated by T. Galkina

Semiconductors, Vol. 36, No. 5, 2002, pp. 493–495. Translated from Fizika i Tekhnika Poluprovodnikov, Vol. 36, No. 5, 2002, pp. 525–527.

ELECTRONIC AND OPTICAL PROPERTIES OF SEMICONDUCTORS

Deep Level Spectra of MBE-Grown ZnTe:Cr^{2+} Layers

Yu. G. Sadofyev^* and M. V. Korshkov**

** Lebedev Physical Institute, Russian Academy of Sciences, Leninskiĭ pr. 53, Moscow, 117924 Russia*

*** Ryazan State Academy of Radio Engineering, Ryazan, 391000 Russia*

^ e-mail: sadofyev@sci.lebedev.ru

Submitted September 25, 2001; accepted for publication October 17, 2001

Abstract—ZnTe:Cr^{2+} layers grown by molecular beam epitaxy on (001) GaAs substrates and doped with chromium from a metallic source or CrI_3 compound have been studied by current deep level transient spectroscopy (I-DLTS). The spectra of the layers show the presence of a deep level with an activation energy of (1.09 ± 0.03) eV, related to a center originating from an electric-field-induced Cr^{2+}–Cr^{+} transition. Doping with chromium from CrI_3 compound eliminates a number of point defects characteristic of ZnTe epitaxial layers, but leads to pronounced contamination of the grown films with iodine. *© 2002 MAIK "Nauka/Interperiodica".*

Cr-doped II–VI compounds have been studied since the 1960s. In the last five years, the increased interest in these materials is due to a number of specific features of the absorption and emission spectra of Cr^{2+} ions substituting cations with tetrahedral symmetry of chemical bonds, which is characteristic of crystal lattices of sphalerite and wurtzite. The given type of crystal field symmetry gives rise to only a single radiative transition ^5E–$^5T_2$ between the lower excited (^5E) and ground ($^5T_2$) states of the Cr^{2+} ion. The Stokes shift between the absorption and emission bands exceeds 1000 cm^{-1}, with the result that the self-absorption loss in these materials is low. The quantum yield of luminescence is close to 100%. The emission band extends over the range from 1.9 to 3 μm. These, and some other features, allow for the creation of compact tunable IR lasers that can effectively operate at room temperature [1]. To date, much success has been achieved in fabricating lasers of this kind [2]. Samples cut from a single-crystal material with the Cr concentration in the range 10^{18}–10^{19} cm^{-3} were used as the active element of the lasers.

Data on the properties of the Cr impurity in II–VI materials have been obtained mainly by optical techniques (transmission, photoluminescence, and optically induced electron spin resonance). Of interest in this connection is to study the influence exerted by chromium atoms incorporated into II–VI compounds on the deep level spectrum by means of electrical techniques.

This communication presents the results obtained in studying ZnTe:Cr^{2+} epitaxial layers grown by molecular beam epitaxy on (100) n^+-GaAs substrates. The growth technique was described in [3]. For comparison, an undoped ZnTe layer was grown. The thickness of the epitaxial layers was within 3–9 μm. The temperatures used for zinc and tellurium evaporation (and also the substrate temperature) were 800–900° lower than the evaporation temperature of metallic chromium. Additional heating by the chromium source leads to difficulties in maintaining constant the substrate temperature in the course of epitaxy. Therefore, a representative of the class of volatile chromium halides—the chemical compound CrI_3—was also used as a dopant source. As shown by element distribution profiles obtained by secondary ion mass spectrometry (SIMS) (Fig. 1), additional doping of the grown layers with iodine occurs in the latter case.

The deep level parameters were studied by current deep level current transient spectroscopy (I-DLTS). Owing to the high resistance of the obtained epitaxial layers, the capacitance of the structures is voltage-independent, similarly to the case of a plane capacitor. This rules out the using of the conventional capacitance DLTS. The contacts to the structures were fabricated by

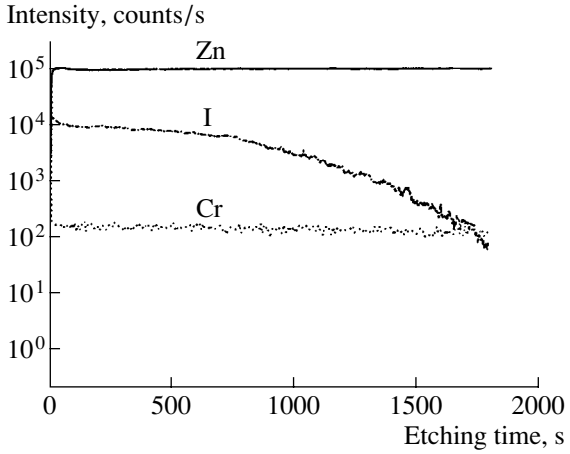

Fig. 1. SIMS distribution profiles of some elements in ZnTe epitaxial layer doped from the CrI_3 compound.

1063-7826/02/3605-0493$22.00 © 2002 MAIK "Nauka/Interperiodica"

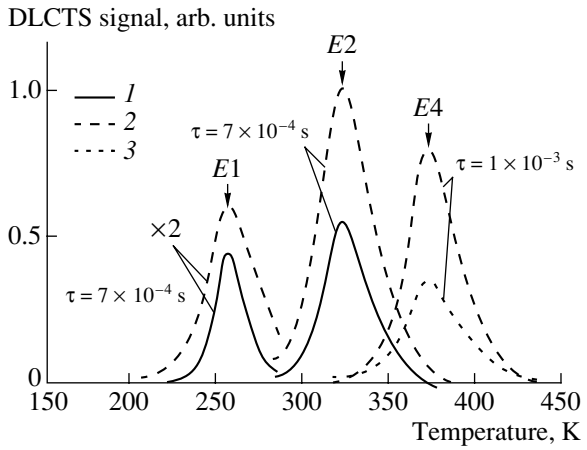

Fig. 2. I-DLTS spectra of (*1*) undoped and (*2, 3*) Cr-doped ZnTe epitaxial layers. Doping with the use of (*2*) metallic chromium and (*3*) CrI_3. Curve numbers correspond to sample numbers. τ is pulse duration.

depositing Ni onto the surface of ZnTe layers through a mask with openings 0.8 mm in diameter by vacuum evaporation and a solid In layer onto the back side of the GaAs substrates.

The parameters of the layers under study (chromium concentration N_{Cr}) and the detected deep levels (activation energy ΔE_t, capture cross-section σ, concentration N_t) are presented in the table. An I-DLTS spectrum of undoped ZnTe (sample no. 1) contains two peaks due to deep centers (Fig. 2). Their activation energies ΔE_t are 0.21 ± 0.01 eV (*E*1) and 0.58 ± 0.02 eV (*E*2). These same centers were found in sample no. 2, doped by evaporation of metallic chromium (see table). The first center is associated with a trap related to zinc vacancies V_{Zn} [4], and the second, with the presence in the material of tellurium vacancies or interstitial zinc atoms [5, 6]. The problem of temperature stabilization in epitaxy and also the large size of chromium atoms lead to different capture cross-sections of *E*1 and E2 deep levels in samples nos. 1 and 2. In sample no. 2, one more deep level (*E*4) was observed with an activation energy of 1.09 ± 0.03 eV. The same deep level was found in sample no. 3, doped by evaporation of CrI_3 in ZnTe epitaxy.

Previous studies of ESR in ZnTe:Cr^{2+} single crystals revealed the presence of metastable singly ionized Cr^+ ions formed by optical excitation. The thermal activation energy was found to be 1.14 eV for the Cr^{2+}–C^+ transition. Within experimental error, this value virtually coincides with 1.09 ± 0.03 eV, obtained in this study for *E*4, which relates the observed deep level to a singly charged chromium ion. The concentration of Cr^+ ions is 10^{-5} of the total amount of dopant. Mention should also be made of the gigantic capture cross-section for the revealed deep centers, close to 10^{-10} cm^2.

Measuring the capture cross-section by varying the duration of the filling pulse gives a value on the order of 10^{-13} cm^2 for the *E*4 deep center, whereas for the *E*2 center this value is 10^{-16} cm^2. The difference between the deep center capture cross-sections determined in trap depletion and filling is not surprising for DLTS. In both these cases, the capture cross-section of the *E*4 deep center greatly exceeds (by three orders of magnitude or more) the capture cross-sections of the other observed deep centers.

No *E*1 or *E*2 deep centers, present in other samples, were observed in the epitaxial layer doped by CrI_3 evaporation. Presumably, iodine ions incorporated in the host lattice act as gettering centers with respect to other defects. The forming complexes are electrically neutral and cannot be revealed by I-DLTS. At low temperatures, samples nos. 2 and 3 also showed a deep level *E*3 with an activation energy of ~90 meV. The related center is formed irrespective of the type of source used for doping with chromium, and its concentration is four orders of magnitude lower than the concentration of iodine ions found in sample no. 3 by SIMS. Moreover, the concentration of *E*3 centers in sample no. 2 exceeds that in sample no. 3 by nearly two orders of magnitude. Consequently, this deep level is not related to the iodine impurity.

Thus, I-DLTS with electrical excitation revealed in ZnTe:Cr^{2+} epitaxial layers a deep level with an activation energy of (1.09 ± 0.03) eV and a capture cross-sec-

Parameters of ZnTe epitaxial layers under study and deep levels revealed by I-DLTS

Sample no.	Chromium source	N_{Cr}, cm^{-3}	Level	ΔE_t, eV	Capture cross-section σ, cm^2	N_t, cm^{-3}
1	None	None	*E*1	0.21 ± 0.01	4.0×10^{-16}	1.8×10^{13}
			*E*2	0.58 ± 0.02	8.6×10^{-17}	3.8×10^{13}
2	Cr	10^{18}	*E*3	0.09 ± 0.01	2.7×10^{-18}	9.1×10^{12}
			*E*1	0.22 ± 0.01	2.1×10^{-18}	2.0×10^{13}
			*E*2	0.60 ± 0.02	2.1×10^{-13}	1.0×10^{14}
			*E*4	1.09 ± 0.03	7.8×10^{-11}	7.2×10^{13}
3	CrI_3	10^{17}	*E*3	0.08 ± 0.01	3.9×10^{-16}	1.3×10^{11}
			*E*4	1.09 ± 0.03	4.2×10^{-11}	2.9×10^{13}

tion close to 10^{-10} cm^2, with the concentration of related centers on the order of 10^{-5} of the concentration of dopant chromium atoms. This level is related, in our opinion, to the Cr^{2+}–C^+ transition in ZnTe:Cr^{2+} under the action of an electric field. Doping with chromium from the CrI_3 compound eliminates a number of point defects characteristic of ZnTe epitaxial layers, presumably because of the gettering action of iodine ions, with, however, strong contamination of the obtained layers with iodine. A possible reason for this is the incomplete dissociation of CrI_3 in its evaporation from a molecular source.

REFERENCES

1. L. D. De Loach, R. H. Page, *et al.*, IEEE J. Quantum Electron. **32**, 885 (1996).
2. G. J. Wagner, T. J. Carrig, R. H. Page, *et al.*, Opt. Lett. **24**, 19 (1999).
3. Yu. G. Sadofyev, V. F. Pevtsov, E. M. Dianov, *et al.*, in *Papers from the 19th North American Conference on Molecular Beam Epitaxy, Tempe, 2000*, p. 42.
4. H. Tubota, J. Appl. Phys. **1**, 259 (1973).
5. C. B. Norris, J. Appl. Phys. **53**, 5172 (1982).
6. P. S. Kireev, A. G. Kornitskiĭ, V. N. Martynov, *et al.*, Fiz. Tekh. Poluprovodn. (Leningrad) **4**, 900 (1970) [Sov. Phys. Semicond. **4**, 762 (1970)].
7. M. Godlewsky and M. Kaminska, J. Phys. C **13**, 6537 (1980).

Translated by M. Tagirdzhanov

Semiconductors, Vol. 36, No. 5, 2002, pp. 496–500. Translated from Fizika i Tekhnika Poluprovodnikov, Vol. 36, No. 5, 2002, pp. 528–532.

ELECTRONIC AND OPTICAL PROPERTIES OF SEMICONDUCTORS

Band Structure of Mg_2Si and Mg_2Ge Semiconducting Compounds with a Strained Crystal Lattice

A. V. Krivosheeva, A. N. Kholod, V. L. Shaposhnikov, A. E. Krivosheev, and V. E. Borisenko

Belarussian State University of Information Science and Radio Engineering, ul. Brovki 17, Minsk, 220013 Belarus'

e-mail anna@nano.bsuir.edu.by

Submitted September 19, 2001; accepted for publication October 18, 2001

Abstract—The effect of isotropic and uniaxial deformation of a lattice on the electronic band structure of the indirect band gap Mg_2Si and Mg_2Ge semiconductors was investigated using the method of linear augmented plane waves. The reduction of the lattice constant down to 95% results in a linear increase in the energy gap for the direct transition in magnesium silicide by 48%. In contrast, the indirect band gap decreases and tends to overlap with the valence band, which is typical of the zero-gar semiconductors. The stresses arising under uniaxial deformation not only shift the bands but also split the degenerate states. The changes in the interband transitions under the uniaxial deformation are found to be nonlinear. © *2002 MAIK "Nauka/Interperiodica".*

INTRODUCTION

Silicides belong to the most promising materials for modern solid-state electronics because of their high chemical and technological compatibility with silicon, high thermal stability, resistance to oxidizing and aggressive media, and chemical inertness. The majority of silicides exhibit metallic properties; however, the most urgent problem consists of studying the semiconducting compounds such as the two isostructural compounds magnesium silicide Mg_2Si and germanide Mg_2Ge [1].

The first calculations of the band structures of these semiconductors were made in the early 1960s. It has been reliably established now that both Mg_2Si and Mg_2Ge are direct gap semiconductors, although there is a considerable spread in the values of their band gaps. The values of the energy gap obtained theoretically for Mg_2Si fall within the range of 0.37–1.3 eV, and the energies of the first direct transition at the Γ point are within the range of 1.8–2.84 eV [2–9], while the optical data yield 0.6–0.74 eV and 2.17 eV, respectively [2–4]. The values of the basic energy gap in Mg_2Ge, according to various data, fall within 0.57–0.74 eV; the direct transition, according to calculations, corresponds to 1.6 eV, while the photoconductivity data yield 1.8 eV [2–4, 8, 9]. Almost all theoretical calculations, except for the latest studies, were performed in terms of the semiempirical pseudopotential method. In [8, 9], a more precise Green function method was used taking into account the screened coulomb interaction in the context of the project or-augmented wave method.

All studies of the electronic properties of magnesium silicide and germanide made hitherto were restricted to the determination of their band structure for ideal conditions without considering the effect of external factors. The complexity of the formation of magnesium silicide films did not make it possible to study this compound adequately. Nevertheless, the results obtained recently in [10] demonstrated the possibility of obtaining Mg_2Si films by molecular-beam epitaxy on silicon substrate using the codeposition of Mg and Si. However, the mismatch of the lattice parameters of a substrate material and the growing epilayer inevitably results in the occurrence of stresses in such structures and deforms their lattice. Such deformations may be both isotropic and anisotropic, inevitably resulting in a change in the basic electronic properties of the material.

The aim of this study is the theoretical simulation of the changes in the structures of electron energy bands in Mg_2Si and Mg_2Ge compounds under the effect of the isotropic uniaxial deformation of their crystal lattices.

DETAILS OF SIMULATION

The structure of electron energy bands was calculated using the linear augmented plane waves method in the context of the generalized gradient approximation. This is one of the most powerful methods in terms of the local density functional (LDF) used nowadays. It allows for satisfactory agreement between the experimental and theoretical data to be reached not only for the eigenvalues of energy, but also for the lattice parameters and optical functions [11]. This is an *ab initio* method because it does not imply parametrization of the Hamiltonian using the experimental data. The method is available as the WIEN97[12] software package, which we used in all required calculations.

1063-7826/02/3605-0496$22.00

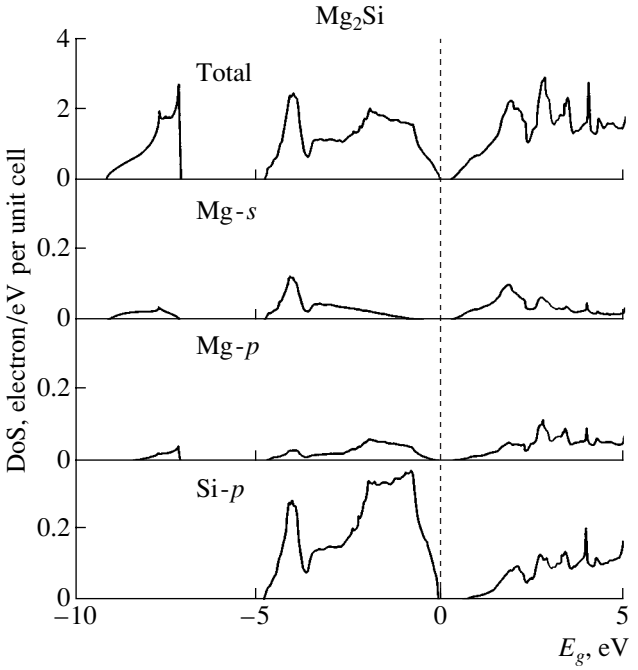

Fig. 1. Total and partial densities of states (DoS) in magnesium silicide.

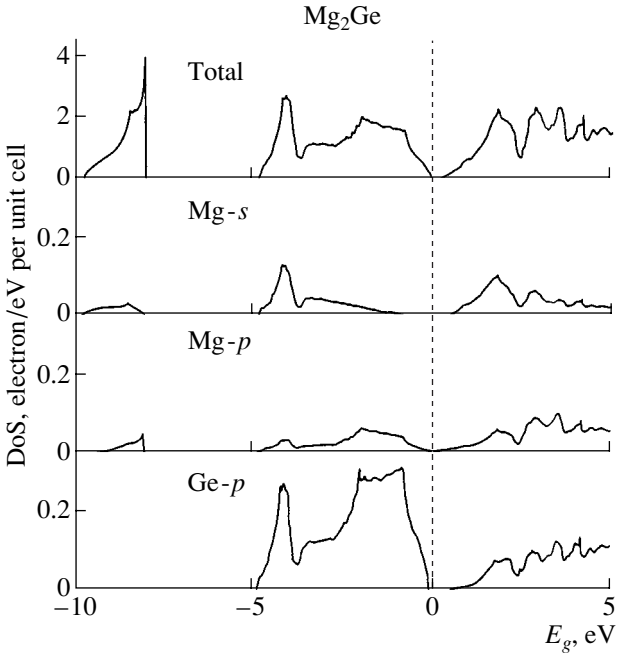

Fig. 2. Total and partial densities of states (DoS) in magnesium germanate.

This is the first time this method has been used for the magnesium compounds under consideration. In order to verify the adequacy of the results, we performed test calculations for silicon, which showed good qualitative and quantitative consistency with other theoretical calculations in terms of LDF, but revealed a certain underestimation of the energy values in comparison with the experimental data [13].

The matching procedure was performed using 244 k points in the irreducible region of the Brillouin zone. The radius of muffin-tin spheres was equal to 2.0 au, the $R_{MT}K_{max}$ parameter, which controls the convergence, was taken to be equal to 9, and the expansion of wave functions in lattice harmonics for partial waves inside atomic spheres was performed up to $l = 10$.

Crystallized Mg_2Si and Mg_2Ge belong to the antifluorite structural type with an fcc lattice and the space group $Fm\bar{3}m$. The atoms of Si or Ge are located at the (0, 0, 0) sites in a primitive cell, and two equivalent Mg atoms occupy the (a/4) (1, 1, 1) and (3a/4) (1, 1, 1) sites, where a is the lattice constant [14]. The lattice constants used in the calculations were equal to 0.6338 and 0.6388 nm for Mg_2Si and Mg_2Ge, respectively [15].

The simulation of the isotropic deformation effect was obtained by reducing the lattice constant a by 5% with a step of 1% and retaining the crystal lattice unchanged. The effect of uniaxial deformation, in its turn, results in the lowering of the symmetry group of a crystal and in the transformation of the cubic lattice into a tetragonal one [16]. We studied the effect of the uniaxial deformation along the [100] direction, which is the most widely used in the epitaxial growth of silicide films on the substrates of other materials. In this case, the lattice constant $a_\parallel$ in the (100) plane of a silicide replicates the lattice constant of a substrate, and the change in the lattice constant along the direction normal to this plane $a_\perp$ can be described in terms of the elasticity theory [17]; i.e.,

$$a_\perp = a\left(1 - 2\frac{C_{12}}{C_{11}}\left(\frac{a_\parallel}{a} - 1\right)\right),$$

where C_{11} and C_{12} are the elastic constants determining the crystal response to the external action. The experimental values of these constants for Mg_2Si [18] and Mg_2Ge [19] are given in the table. The value of $a_\parallel$ was varied within ±2% around the equilibrium value of a and also with a step of 1%.

RESULTS AND DISCUSSION

We consider first the structures of ideal Mg_2Si and Mg_2Ge crystals. The calculated total and partial densities of states (DoS) for these materials are shown in Figs. 1 and 2. Their shapes are qualitatively consistent

Elastic constants for Mg_2Si [18] and Mg_2Ge [19] at room temperature (in 10^{11} dyn/cm^2)

Material	C_{11}	C_{12}
Mg_2Si	12.1 ± 0.2	2.2 ± 0.2
Mg_2Ge	11.79 ± 0.15	2.3 ± 0.5

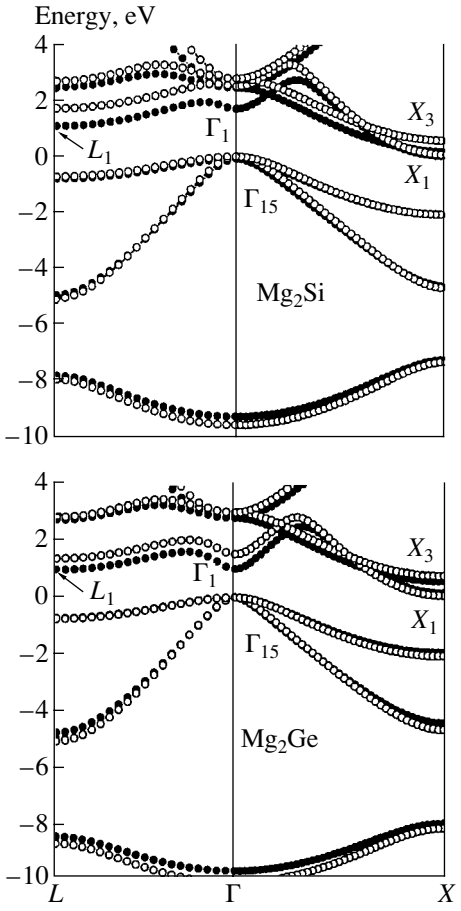

Fig. 3. Electron band structure in Mg_2Si and Mg_2Ge. Filled and open circles are the unstressed and isotropically compressed by 3% structures, respectively.

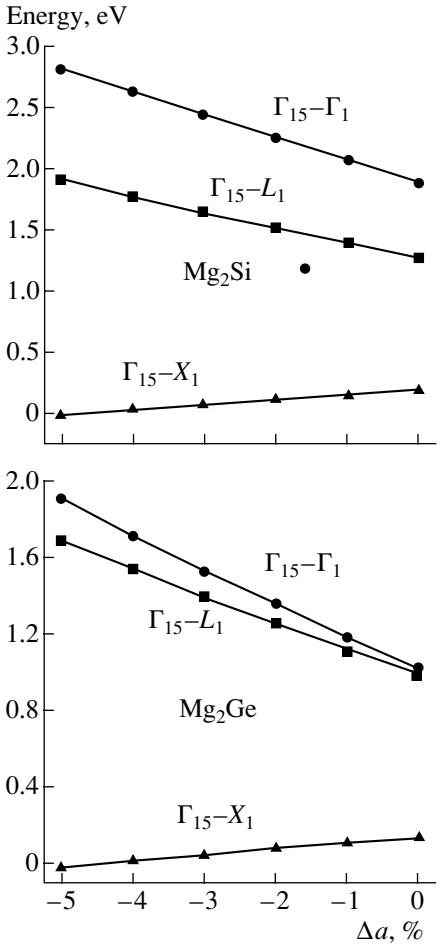

Fig. 4. Changes in the energies of the basic electron transitions in Mg_2Si and Mg_2Ge under the isotropic compression of their lattices.

with the Dos reported in [20]. According to the calculations, the *s* states of Si and Ge have a pronounced effect only on the first valence band, whereas their effect near the Fermi level is minor; therefore their spectra are excluded from consideration. The densities of states for both materials are almost the same. The dominant contribution to the valence band in both compounds are made by the *s* and *p* states of Mg hybridized with *p* states of Si or Ge. The lower conduction band is characterized by the hybridization of all states of Si (Ge) and Mg, the total contribution of Mg states being greater than the total contribution of Si (Ge).

The calculated energy band diagrams for Mg_2Si and Mg_2Ge are shown in Fig. 3, where the valence-band top corresponds to zero on the energy scale. The filled and open circles correspond respectively to the states in unstressed crystals and in the crystals subjected to isotropic deformation with a reduced lattice constant. It is possible to see a qualitative similarity between the band diagrams in the unstressed state for the semiconductors studied. The direct transition occurs between the fourth and fifth bands at the center of the Brillouin zone (at the Γ point). This point corresponds to the maximum of the valence band for the compounds under study. The energy minimum of the conduction band is located at the point *X*, which is consistent with the results of previous calculations [2–6]; correspondingly, the basic indirect transition occurs between the Γ and *X* points. The specific feature of the Mg_2Si structure is the close location of bands at the points with a high symmetry X_1 and X_3, which hampers the precise determination of the index of a conduction band minimum for the Γ–*X* transition. According to our calculations, this minimum is located at the point X_1. The upper valence bands correspond to the unfilled *p*-electron shells of Si with a fraction of *s* and *p* electrons of Mg.

We obtained the following energies of the transitions: approximately 1.9 and 1.02 eV for the direct Γ_{15}–Γ_1 transition in Mg_2Si and Mg_2Ge, respectively. The energies for the indirect Γ_{15}–L_1 and Γ_{15}–X_1 transitions are equal to 1.29 and 0.19 eV for Mg_2Si, and 1.0 and 0.15 eV for Mg_2Ge, respectively.

There is an obvious discrepancy between our results and the data for energy gaps obtained experimentally

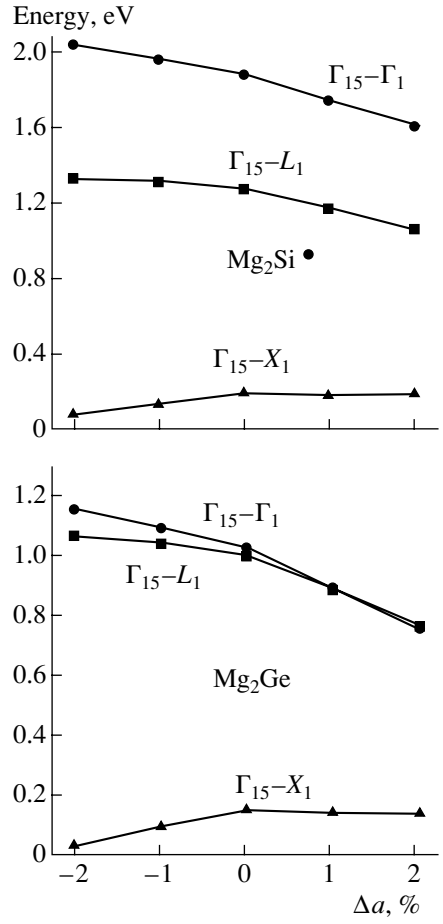

Fig. 5. Changes in the energies of the basic electron transitions in Mg_2Si and Mg_2Ge under the uniaxial compression of their lattices.

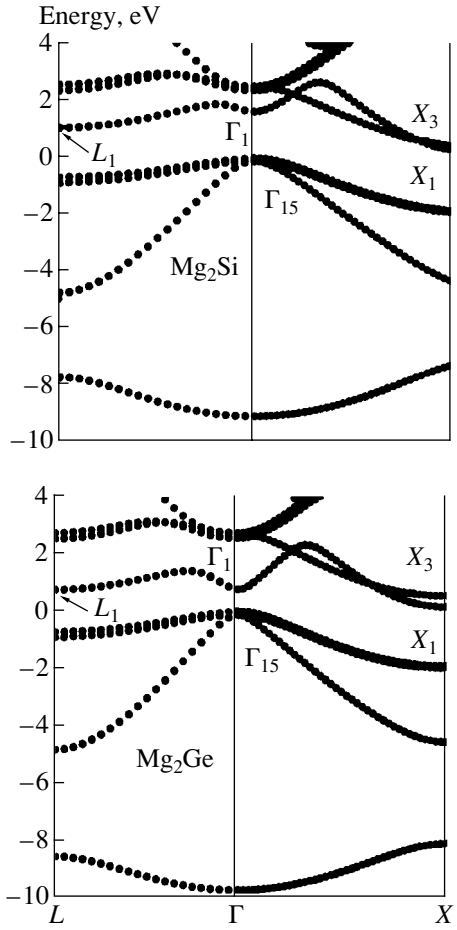

Fig. 6. Electron band structure in Mg_2Si and Mg_2Ge under the uniaxial compression of their lattices by 2%.

and by semiempirical calculations. This can be attributed to the so-called correlation effects. It is well known that the methods based on the electron density functional underestimate the energy gaps in the semiconductors having a band gap formed by the hybridization of the *s*- and *p*-electron states of atoms, to which the compounds under study belong. At the same time, the calculations performed in terms of LDF for iron disilicide β-$FeSi_2$ [21] showed a reasonable agreement between the experimental and theoretically calculated values of the energy gap (the difference was found to be equal to about 40 meV). This result can be explained by the fact that the corresponding wave functions at the band extrema are controlled mainly by the *d*-electron states of iron atoms and are susceptible to almost the same correlation shift.

The change in the energy of the basic transition under the lattice deformation at the isotropic compression is shown in Fig. 4. Isotropic compression reduces the interatomic distances. This usually widens the energy gap in semiconductors, which is observed in our case. The increase of pressure both for Mg_2Si and Mg_2Ge results in the increase in the direct-transition energy at the point Γ. The energy gap in the Γ_{15}–L_1 direction also increases, but at a somewhat lower rate. In contrast, the indirect Γ_{15}–X_1 transition energy decreases at a rate comparable to the rate of increase of the Γ_1–Γ_{15} transition energy. It is interesting that the above behavior for Mg_2Si and Mg_2Ge is qualitatively in accordance with the results for the isotropic compression of Si and Ge also having an fcc lattice [22, 23].

Dependences of the energies of basic interband transitions in Mg_2Si and Mg_2Ge semiconductors on the lattice parameter under the effect of uniaxial compression/tension are shown in Fig. 5. It is obvious that the main tendencies in these dependences remained the same as under isotropic deformations; however, isotropic compression produced an almost linear change in the energies of the Γ_{15}–L_1 and Γ_{15}–Γ_1 transitions, whereas the effect of the tetragonal (uniaxial) deformation can be approximated linearly only for certain portions of the curves. The cause of such behavior is the simultaneous occurrence of tensile and compressive stresses. Since the minima in the conduction band in the

compounds with an fcc lattice are located in several valleys, the compression along a certain axis under the effect of uniaxial deformation reduces the band gap in this direction. At the same time, this compression produces simultaneous tension in the plane normal to the direction of compression, which results in the shift of some minima in the conduction zone to higher energies [24]. Apart from this feature, uniaxial compression results in another interesting effect consisting in the splitting of degenerate states both in the valence and conduction bands. The splitting of states for the lattice uniaxially compressed by 2% is shown in Fig. 6.

CONCLUSION

The method of a linear augmented plane waves was used for the calculation and analysis of band structures in Mg_2Si and Mg_2Ge as a function of isotropic and uniaxial deformations of their crystal lattices. It is established that the changes in the energies of basic interband transitions with a lattice deformation are the same for both compounds. Isotropic deformation results in a linear increase in the energy gap for the direct Γ_{15}–Γ_1 and indirect Γ_{15}–L_1 transitions, while the indirect band gap Γ_{15}–X_1 reduces. Similar tendencies also take place under uniaxial deformation; however, in the latter case, the dependence of the energy gap on the lattice parameter is nonlinear. The most pronounced effect associated with crystal lattice deformation is the shift of the energy bands. Isotropic compression results only in the shift of energy levels both in the valence and conduction bands, whereas uniaxial deformation results also in the splitting of degenerate states. The compression of the crystal lattices of Mg_2Si and Mg_2Ge down to 95% does not transform these nondirect-gap semiconductors into direct-gap ones. In contrast, there can arise a situation typical of zero-gap semiconductors when the top of the valence band lies higher then the conduction-band bottom. However, this effect requires consideration of the correction to the interband-transition energies which are underestimated in terms of the local density approximation used in calculations.

REFERENCES

1. *Semiconducting Silicides*, Ed. by V. E. Borisenko (Springer-Verlag, Berlin, 2000).
2. W. J. Scouler, Phys. Rev. **178**, 1353 (1969).
3. F. Vazquez, R. A. Forman, and M. Cardona, Phys. Rev. **176**, 905 (1968).
4. Y. Au-Yang and M. L. Cohen, Phys. Rev. **178**, 1358 (1969).
5. P. M. Lee, Phys. Rev. **135**, A1110 (1964).
6. F. Aymerich and G. Mula, Phys. Status Solidi **42**, 697 (1970).
7. D. M. Wood and A. Zunger, Phys. Rev. B **34**, 4105 (1986).
8. B. Arnaud and M. Alouani, Phys. Rev. B **62**, 4464 (2000).
9. B. Arnaud and M. Alouani, Phys. Rev. B **64**, 033202 (2001).
10. A. Vantomme, G. Langouche, J. E. Mahan, and J. P. Becker, Microelectron. Eng. **50**, 237 (2000).
11. L. Hsu, G. Y. Guo, J. D. Denlinger, and J. W. Allen, Phys. Rev. B **63**, 155105 (2001).
12. P. Blaha, K. Schwarz. and J. Luitz, *WIEN 97* (Vienna Univ. of Technology, Vienna, 1997); P. Blaha, K. Schwarz, P. Sorantin, and S. B. Trickey, Comput. Phys. Commun. **59**, 399 (1990).
13. C. S. Wang and B. M. Klein, Phys. Rev. B **24**, 3393 (1981).
14. N. O. Folland, Phys. Rev. **158**, 764 (1967).
15. R. J. LaBotz, D. R. Mason, and D. F. O'Kane, J. Electrochem. Soc. **110**, 127 (1963).
16. G. L. Bir and G. G. Pikus, *Symmetry and Strain-Induced Effects in Semiconductors* (Nauka, Moscow, 1972; Wiley, New York, 1975).
17. M. M. Rieger and P. Vogl, Phys. Rev. B **48**, 14276 (1993).
18. W. B. Whitten, P. L. Chung, and G. C. Danielson, J. Phys. Chem. Solids **26**, 49 (1965).
19. P. L. Chung, W. B. Whitten, and G. C. Danielson, J. Phys. Chem. Solids **26**, 1753 (1965).
20. A. L. Ivanovskiĭ, Izv. Akad. Nauk SSSR, Neorg. Mater. **26**, 1226 (1990).
21. A. B. Filonov, D. B. Migas, V. L. Shaposhnikov, *et al.*, J. Appl. Phys. **79**, 7708 (1996).
22. M. Alouani and J. M. Wills, Phys. Rev. B **54**, 2480 (1996).
23. A. R. Goni, K. Syassen, and M. Cardona, Phys. Rev. B **41**, 10104 (1990).
24. J. I. Pankove, *Optical Processes in Semiconductors* (Prentice-Hall, Englewood Cliffs, 1971; Mir, Moscow, 1973).

Translated by A. Zalesskiĭ

Semiconductors, Vol. 36, No. 5, 2002, pp. 501–504. Translated from Fizika i Tekhnika Poluprovodnikov, Vol. 36, No. 5, 2002, pp. 533–536.

ELECTRONIC AND OPTICAL PROPERTIES OF SEMICONDUCTORS

Localized States in $Hg_3In_2Te_6$: Cr Compounds

P. N. Gorleĭ, O. G. Grushka, and V. M. Frasunyak

Chernovtsy National University, Chernovtsy, 58012 Ukraine

Submitted May 14, 2001; accepted for publication October 23, 2001

Abstract—The effect of chromium doping on the energy spectrum of the density of states $N(E)$ in the band gap of the $Hg_3In_2Te_6$ semiconductor compound was studied. Although the chromium impurity has no significant effect on the electrical properties and the Fermi level position, it increases the band tail extent and the density of localized states within the band gap E_g. Comparison of the data on the field effect and on light absorption for photon energies $h\nu$ lower than E_g made it possible to ascertain that the density of states is distributed continuously and rapidly increases near the edges of the valence and conduction bands. The obtained spectra are discussed on the assumption that the chromium content growth increases the structure disorder and the random potential, which increases $N(E)$. It is shown that localized states control the screening length and pin the Fermi level near the midgap and are also responsible for the compensation of impurity ion charges. © *2002 MAIK "Nauka/Interperiodica".*

Interest in the $Hg_3In_2Te_6$ semiconductor compound is due to the following reasons. First, $Hg_3In_2Te_6$ is a candidate for electronic engineering devices [1]. Second, its crystallochemical and physical properties have a number of features untypical of IV, II–VI, and III–V semiconductors. The principal difference is a high concentration (about 10^{21} cm^{-3}) of electroneutral stoichiometric vacancies (SV) in the sphalerite-type $Hg_3In_2Te_6$ structure, which causes the electrical inactivity of introduced impurities and a high resistance of the crystal parameters to ionizing radiation. As was shown in [2], sp^3-hybridization clouds extend from tellurium atoms to SVs. These clouds are chemically inert, unshared electron pairs with antiparallel spins, which causes chemical inertness of both the bulk and surfaces of crystals with SVs. The high efficiency of short-wavelength photoconduction of direct-gap $Hg_3In_2Te_6$ crystals away from the fundamental absorption edge is attributed to a special feature of the surface bonds (see [3]). Photodiodes based on $Hg_3In_2Te_6$ have almost a 100% quantum efficiency due to the absence of recombination losses at the heterojunction interface [4]. A distinguishing feature of $Hg_3In_2Te_6$ is also the fact that the Fermi level is located near the midgap (E_g = 0.74 eV at 300 K) and is not appreciably shifted by introduced impurities. This causes a high bipolar conductivity of $Hg_3In_2Te_6$, similar to intrinsic semiconductors, in a wide temperature range.

Continuation of the 3*d*-impurity behavior studies begun in [5] may provide deeper insight into the impurity self-compensation processes in semiconductors with specific intrinsic defects, i.e., stoichiometric vacancies.

In this paper, we report the results of studying the radical changes in the spectrum of $Hg_3In_2Te_6$ localized states caused by the chromium impurity.

The $Hg_3In_2Te_6$ semiconductor is an easily producible material due to congruent melting and a rather narrow homogeneity region, which facilitates the Bridgman–Stockbarger melt growth of ingots with a uniform distribution of basic components along the ingot axis. At the same time, incorporation of impurity atoms into the host depends on the impurity type.

A chromium impurity (5×10^{19} cm^{-3}) was added to the $Hg_3In_2Te_6$ blend before synthesis. The studied samples were prepared from different parts of a grown ingot cut into disks. Electrical measurements showed that the carrier concentration (about ~10^{13} cm^{-3}) and the Hall mobility (250–300 cm^2(V s)$^{-1}$ at 300 K) in the ingot, except for its tail part, are virtually equal to those of an undoped crystal. Magnetic susceptibility (MS) studies showed no carrier contribution; therefore, the temperature-independent MS of the undoped crystal was set equal to the lattice MS ($\chi_L = -2.75 \times 10^{-7}$ cm^3/g). The impurity MS χ_{Cr} of paramagnetic ions in a diamagnetic host was defined as $\chi_{Cr} = \chi - \chi_L$, where χ is the measured MS. The obtained distribution of χ_{Cr} along the ingot axis at 77 K is shown Fig. 1, where sample numbers are also given along the horizontal axis. The temperature dependences of χ_{Cr} for samples 1–6 cut from the starting and central ingot parts obey the Curie law, $\chi_{Cr} = C/T$, where $C = N_{Cr}\mu^2/3k$, N_{Cr} is the concentration of impurity ions, μ is their magnetic moment, and k is the Boltzmann constant. As a certain chromium concentration is exceeded, a deviation from the Curie law is observed. For samples 7 and 8 from the ingot end, the MS is described by the Curie–Weiss law, $\chi_{Cr} = C/(T - \theta)$, with positive θ in the temperature range of 120–300 K, while at $T < 120$ K, the dependences $\chi_{Cr}^{-1} = f(T)$ tend to the coordinate origin. As follows from the dependences shown in Fig. 1, the impurity is pushed into the melt

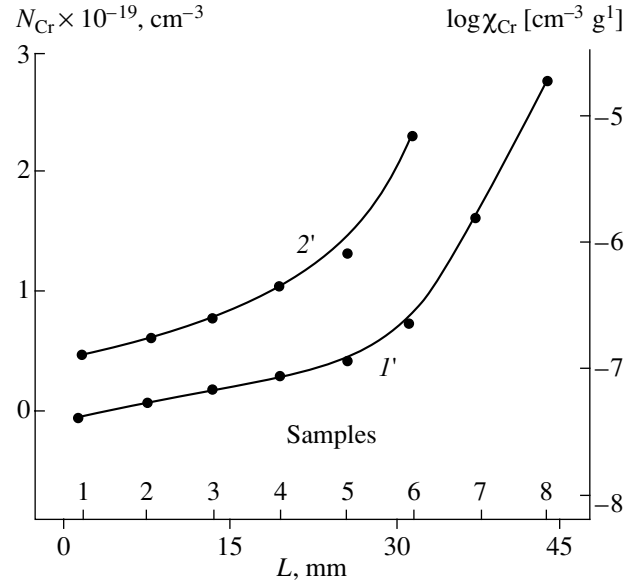

Fig. 1. Distribution of (*1*') the impurity paramagnetic susceptibility χ at 77 K and (*2*') the Cr^{+2} ion concentration *N* along the $Hg_3In_2Te_6$ ingot axis. The sample numbers are also given at the length axis *L*.

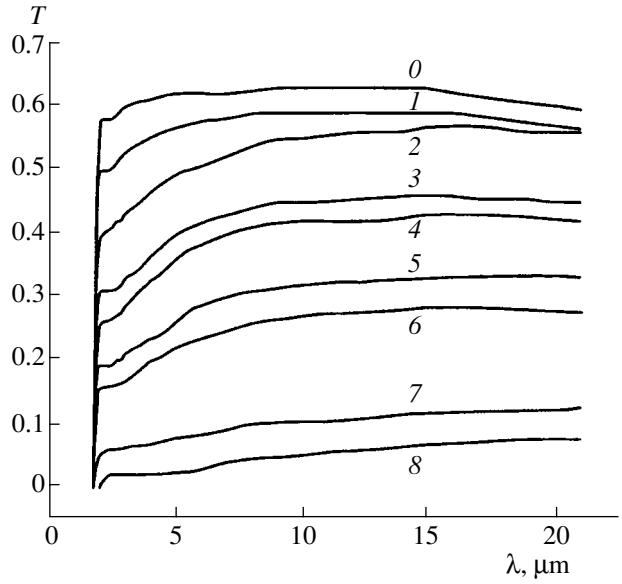

Fig. 2. Transmission *T* spectra of the $Hg_3In_2Te_6$ samples undoped (*0*) and doped with chromium. Sample numbers from *1* to *8* corresponds to increasing chromium concentration.

during crystallization, since the effective coefficient of the distribution is smaller than unity. Therefore, the highest chromium concentration was found in samples 7 and 8. As is known [6, 7], compared with other impurities of transition elements, chromium produces a greater number of charge states (up to four) in semiconductors. It is not improbable that the chromium impurity in our case can be found in more than one state. However, to estimate the Cr concentration N_{Cr} in the samples (Fig. 1), we assumed that chromium is in the charge state Cr^{+2} in the range of the Curie law validity.

The fundamental-absorption studies showed that chromium doping decreases the absorption edge steepness and correspondingly shifts it to lower energies. At the photon energy $h\nu < E_g = 0.74$ eV, the absorptivity α exponentially depends on $h\nu$, obeying the Uhrbach rule $\alpha \sim \exp(h\nu/E_0)$, where the characteristic energy E_0 increases with doping, which indicates enhancement of $Hg_3In_2Te_6$ structural disordering by the chromium impurity. At $h\nu < 0.67$ eV, the dependence of α on $h\nu$ weakens and becomes flat at $h\nu < 0.62$ eV.

Undoped $Hg_3In_2Te_6$ crystals in the transparency range of 2–20 μm (0.62–0.062 eV) are characterized by transmittances of 58–62% and the absence of both absorption structure and absorption caused by free carriers. One can see from Fig. 2 that the chromium impurity decreases the transparency correlating with the doping level. However, the electrical parameters remain relatively unchanged in samples with transmittances exceeding 10%. The transparency decrease is caused by an increase in the density of defect states in the $Hg_3In_2Te_6$ band gap. These states can be caused by perturbations introduced by chromium ions into the tetrahedral compound lattice. It should be taken into account that Cr^{+2} and Cr^{+3} tend to form octahedral bonds. In the strong-absorption range down to $h\nu = 0.062$ eV, two types of optical transitions are involved: those between localized states with the density $N(E)$ and delocalized states with $N(E + h\nu)$ of the conduction band, as well as the transitions from delocalized states of the valence band to localized states with corresponding densities. Correspondingly, the absorptivity is the sum of two components, $\alpha = \alpha_1 + \alpha_2$. In $Hg_3In_2Te_6$ with the Fermi level near the midgap, contributions of both transition types to the absorptivity are comparable, i.e., $\alpha_1 \approx \alpha_2$.

We determined the density of localized states separately for α_1 and α_2 using the approximation (see [8])

$$\alpha(h\nu) = (A/h\nu) \times \int N(E) f(E) N(E + h\nu)[1 - f(E + h\nu)]dE, \quad (1)$$

where $\alpha(h\nu)$ is the absorptivity at the photon energy $h\nu$, $N(E)$ is the density of initial states with the energy E, $N(E + h\nu)$ is the density of final states, and $f(E)$ is the Fermi function.

Using the coefficient $A = 4 \times 10^{-38}$ cm^5 eV^2 [9] and the condition for parabolicity of the valence and conduction bands, integration was carried out over all the pairs of initial and final states separated by the energy $h\nu$.

The obtained distributions of the total density of states $N(E)$, shown in Fig. 3 by solid lines, are similar for all the samples. Receding from the midgap, an initially insignificant increase in the density of states $N(E)$

drastically grows as the band edges are approached. As the doping level increases, the spectra $N(E)$ are shifted upwards in accordance with the additional density of states. One can see from Fig. 3 that the Cr impurity uniformly increases the density of states over the entire band gap. The absence of a structure in the energy spectra counts in favor of the quasi-continuous distribution of the density of states. Such spectra are conventionally described within the theory of unordered systems [10], according to which local levels can arise due to potential fluctuations caused by microinclusions of charged centers [11]. The energy band modulation in undoped $Hg_3In_2Te_6$, caused by intrinsic structural defects, is enhanced by impurity defects, which gives rise to an additional potential.

The obtained data indicate that there are two systems of density of states in the band gap, corresponding to the continuous spectra of defect levels of two types differing in their charge states (donor and acceptor). Figure 3 (dots) illustrates separation of the distribution $N(E)$ into two components. This representation conforms with the Cohen–Fritzsche–Ovshinsky model [12], where the overlapping of two such systems of density of states maintains self-compensation and pins the Fermi level near the midgap.

To gain additional data on the density of localized states, we studied the field effect, which yields data on the total density of states, irrespective of the charge state.

All the samples were subjected to identical mechanical and chemical treatment to produce a relief-free surface with a low density of surface electron states. The dark quasi-surface conductance was measured by the technique [12] at room temperature depending on the transverse electric field applied to the sample through a thin (10–20 μm) mica plate.

The transverse field bends the bands and shifts the local levels in the surface region with respect to the Fermi level. Therefore, a change of the localized state population affects the quasi-surface conductance.

The obtained dependences of the quasi-surface conductance ΔG on the induced charge $\pm Q$ are typical of an intrinsic semiconductor with a pronounced minimum near $Q = 0$, which separates the electron and hole branches. The minimum position with respect to the abscissa axis (Q) is independent of doping. However, the quantity ΔG decreases as the Cr impurity content grows, reaching values comparable to the measurement error for samples 7 and 8.

The data on quasi-surface conductance were approximated as (see [13])

$$\frac{\Delta G}{G_0} = \frac{L}{d}\left[\frac{b}{1+b}F(-Y_s) + \frac{1}{1+b}F(Y_s)\right],$$
$$F(Y_s) = \int_0^{Y_s}\frac{e^{-Y}-1}{Y}dY, \qquad (2)$$

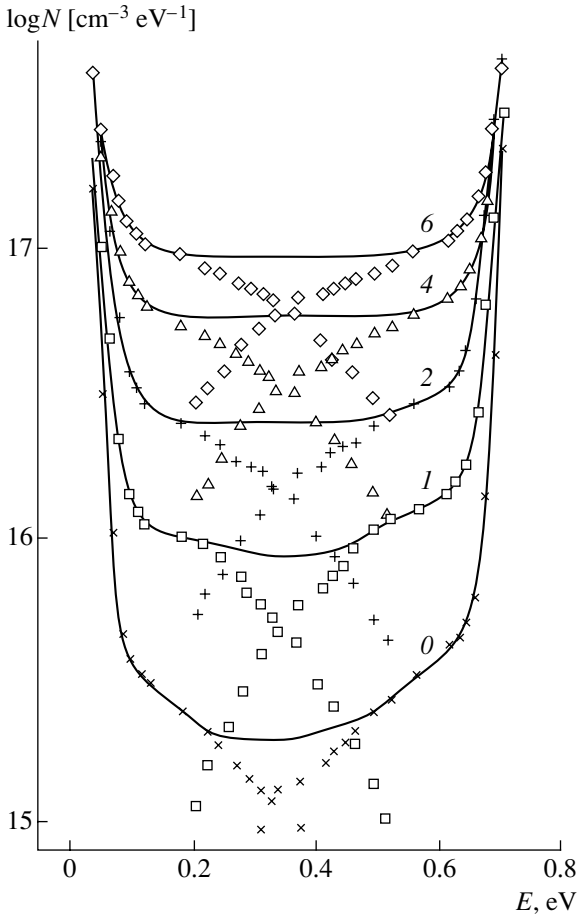

Fig. 3. Energy spectra of the density of localized states of the $Hg_3In_2Te_6$ samples without (*0*) impurity and with increasing chromium concentration (*1–6*). The energy is measured from the conduction band bottom.

where G_0 is the surface conductance in the absence of transverse field, $Y = V(x)/kT$ is the reduced potential, $Y_s = V_s/kT$, V_s is the potential at the surface, L is the screening length, d is the sample thickness, and b is the ratio of electron and hole mobilities.

Expression (2) was derived on the assumption of the exponential decrease of the electrostatic potential V with the distance x from the semiconductor surface into the depth, $V(x) = V_s\exp(-x/L)$ [13]. In this case, the charge per unit area for the final densities of states $N(E_F)$ at the Fermi level is given by

$$Q = \varepsilon\varepsilon_0\left(\frac{dV}{dx}\right)_{x=0} = \frac{\varepsilon\varepsilon_0 kTY_s}{L}, \qquad (3)$$

where ε is the relative dielectric constant, ε_0 is the dielectric constant of free space, and the screening length is written as

$$L = \sqrt{\frac{\varepsilon\varepsilon_0}{eN(E_F)}}. \qquad (4)$$

Table

N_{sam}	N_F^{opt}, cm^{-3} eV^{-1}	N_F^{fe}, cm^{-3} eV^{-1}	L, cm
0	2.1×10^{15}	8.6×10^{14}	1.1×10^{-4}
1	9.4×10^{15}	2.5×10^{15}	6.4×10^{-5}
2	2.8×10^{16}	7.4×10^{15}	3.7×10^{-5}
4	6.5×10^{16}	1.7×10^{16}	2.4×10^{-5}
6	1.2×10^{17}	3.1×10^{16}	1.8×10^{-5}

Using the experimental data on $\Delta G/G_0$ and Q, we determined the surface potential Y_s and screening length L from formulas (2) and (3), while the density of states $N(E_F)$ at the Fermi level was determined from (4). The obtained values L and N_F^{fe} for the field effect are listed in the table. One can see that the screening length decreases and the density of states at the Fermi level correspondingly grows as the doping level increases (samples 1–6). Hence, the localized states control the screening length and quasi-surface conductance. As follows from the table, the values of N_F^{fe} obtained using the field effect are significantly smaller than N_F^{opt} determined from the optical absorption data. The latter can be overestimated since the density of states $N(E)$ was determined on the assumption that the total transparency decrease is caused by intraband optical transitions with participation of localized states. In this case, the contribution of light scattering by inhomogeneities caused by the interaction between intrinsic and impurity defects was ignored. If microinclusions with an electron concentration differing from that of the host are formed, the light-scattering intensity is independent of wavelength but proportional to the concentration of inclusions and to the squared difference of the dielectric constants of inclusions and the host. Determination of the latter quantities seems to be impossible. However, the obtained variations in the energy spectra of the density of states give insight into the contribution of localized states to optical absorption processes and screening, as well as account for the self-compensation of charged defects.

REFERENCES

1. G. G. Grushka, A. P. Bakhtinov, and Z. M. Grushka, J. Adv. Mater. **4** (1), 36 (1997).
2. L. S. Palatnik, V. M. Koshkin, and Yu. F. Komnik, *Chemical Bonding in Semiconductors and Solids* (Nauka i Tekhnika, Minsk, 1965), p. 301.
3. D. B. Anan'ina, V. L. Bakumenko, and L. N. Kurbatov, Fiz. Tekh. Poluprovodn. (Leningrad) **10**, 2373 (1976) [Sov. Phys. Semicond. **10**, 1405 (1976)].
4. A. I. Malik and G. G. Grushka, Zh. Tekh. Fiz. **60** (10), 188 (1990) [Sov. Phys. Tech. Phys. **35**, 1227 (1990)].
5. O. G. Grushka, Z. M. Grushka, and V. M. Frasunyak, Fiz. Tekh. Poluprovodn. (St. Petersburg) **33**, 1416 (1999) [Semiconductors **33**, 1272 (1999)].
6. V. I. Fistul', *Amphoteric Impurities in Semiconductors* (Metallurgiya, Moscow, 1992).
7. V. F. Masterov, Fiz. Tekh. Poluprovodn. (Leningrad) **18**, 3 (1984) [Sov. Phys. Semicond. **18**, 1 (1984)].
8. *Advances in Disordered Semiconductors*, Vol. 1: *Amorphous Silicon and Related Materials*, Ed. by H. Fritzsche (World Scientific, Singapore, 1989; Mir, Moscow, 1991).
9. L. A. Balagurov, É. M. Omel'yanovskiĭ, and T. N. Pinsker, Fiz. Tekh. Poluprovodn. (Leningrad) **19**, 48 (1985) [Sov. Phys. Semicond. **19**, 28 (1985)].
10. V. L. Bonch-Bruevich, I. P. Zvyagin, R. Kapper, A. G. Mironov, and R. Enderlein, *Electronic Theory of Unordered Semiconductors* (Nauka, Moscow, 1981).
11. E. Rosencher and R. Coppard, J. Appl. Phys. **55**, 971 (1984).
12. A. Madan and M. Shaw, *The Physics and Applications of Amorphous Semiconductors* (Academic, Boston, 1988; Mir, Moscow, 1991).
13. N. F. Mott and E. A. Davis, *Electronic Processes in Non-Crystalline Materials* (Clarendon, Oxford, 1979; Mir, Moscow, 1982), Vol. 1.

Translated by A. Kazantsev

Semiconductors, Vol. 36, No. 5, 2002, pp. 505–510. Translated from Fizika i Tekhnika Poluprovodnikov, Vol. 36, No. 5, 2002, pp. 537–542.

SEMICONDUCTOR STRUCTURES, INTERFACES, AND SURFACES

Control of Charge Transport Mode in the Schottky Barrier by δ-Doping: Calculation and Experiment for Al/GaAs

V. I. Shashkin*, A. V. Murel, V. M. Daniltsev, and O. I. Khrykin

Institute for Physics of Microstructures, Russian Academy of Sciences, Nizhny Novgorod, 603950 Russia

**e-mail: sha@ipm.sci-nnov.ru*

Submitted October 15, 2001; accepted for publication October 30, 2001

Abstract—The possibility of controlling the effective barrier height in Schottky diodes by introducing a δ-doped layer near the metal–semiconductor contact is considered. A decrease in the effective barrier height is caused by the increased role of carrier tunneling through the barrier. A complete quantum-mechanical numerical simulation of the effect of the δ-layer parameters (concentration and depth) on the current–voltage characteristics of modified diodes was carried out for the Schottky barrier contacts to *n*-GaAs. The simulation results were found to fit well the experimental characteristics of diodes produced by metal-organic chemical vapor epitaxy. The studies carried out made it possible to choose the optimal δ-layer parameters to produce low-barrier (about 0.2 eV) diodes with a reasonable nonideality factor ($n \le 1.5$). Such structures can be employed to fabricate microwave detector diodes without bias. © *2002 MAIK "Nauka/Interperiodica".*

INTRODUCTION

Transport characteristics of metal–semiconductor contacts produced under clean epitaxial or ultrahigh-vacuum conditions are reproducible and have been studied adequately [1]. The charge transport is mainly controlled by the parameters of the Schottky potential barrier in the semiconductor near the interface with metal. In particular, for gallium arsenide with a moderate electron density (lower than 10^{18} cm^{-3}), the Schottky barrier height is within 0.6–1.0 eV for more than 40 metals [1–3]. Within certain limits, the barrier height can be varied by additional heavy doping of the semiconductor subsurface region [1, 2]. Nonepitaxial methods based on impurity implantation or alloying are characterized by a narrow range of barrier height control or lead to inhomogeneities and poor reproducibility [2, 4]. Precision doping during epitaxy was found to be more efficient for the controlled decrease of the effective barrier height in *n*-GaAs (100) [5, 6]. The difference in the approaches was related to the δ-doping technique in [5] and uniform doping in [6]. In both cases, the decrease in the effective barrier height is obviously caused by the appearence of a current thermal-field component. In the case of heavier doping, the current becomes a tunneling one; in the limit, the ohmic contact can be attained [7–9]. As for the doping method, as early as in [10], it was indicated that δ-doping is equivalent to an ultrahigh level of volume doping in the problems under consideration. This is caused by the obvious fact that the distance between the metal and the δ-layer, which completely screens the contact electric field, should be two times shorter than in the case of uniform doping at identical surface concentrations of doping donors. Therefore, the δ-doping approach appears to be more promising also in the problems of attaining a low effective barrier (0.2–0.25 eV) with low nonideality factors ($n \lesssim 1.5$) being preserved. It is also important that the surface concentration N_{2D} of charged donors (e.g., Si) in the δ-layer in GaAs can exceed 10^{13} cm^{-2}. In this case, the barrier height is decreased by 0.6–0.8 eV at distances x_0 = 4–6 nm from the metal boundary to the doping plane. Figure 1 displays this practically important range of doping parameters as an N_{2D}–x_0 plot. The curve corresponds to the δ-layer depletion edge at zero bias, and the initial barrier ϕ^0 = 0.7 eV according to the dependence (see [7])

$$\phi^0 = q/\varepsilon\varepsilon_0 N_{2D} x_0, \quad (1)$$

where q is the electron charge, ε is the relative dielectric constant of the semiconductor, and $\varepsilon_0 = 8.85 \times 10^{-14}$ F cm^{-1}. The insets illustrate the behavior of the conduction band edge on each side from the interface. At volume doping with silicon up to about $\sim 6 \times 10^{18}$ cm^{-3}, which is close to the limiting density of electrically active Si impurity atoms in GaAs, a much thicker ($x_0 \sim$ 17 nm) layer is required to attain the same surface density of about 10^{13} cm^{-2} of charged donors. This can result in a decrease in the tunnel transparency together with strengthening of its dependence on the bias voltage, which brings about an increase in the nonideality factor n [6, 11].

In this study (continuing [5, 12]), we demonstrate the possibility of producing low-barrier contacts to *n*-GaAs (100) while retaining a low nonideality factor. We present the results of detailed numerical calculations, beginning with the determination of the band profile and finishing with calculations of current–voltage

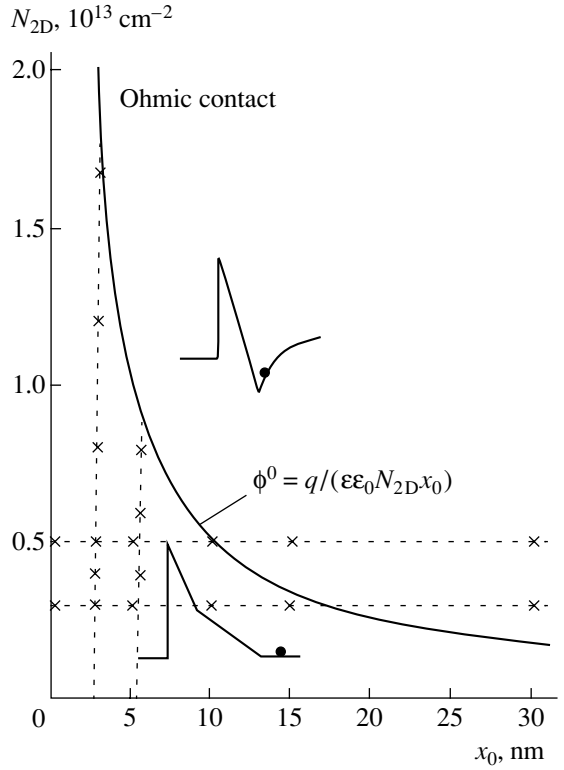

Fig. 1. Range of the δ-doping parameters for a structure with the Schottky barrier. The curve corresponds to the δ-layer depletion boundary at a zero bias and $\phi^0 = 0.7$ eV. The insets above and below this curve schematically show the conduction band E_C edge. The dots are the experimentally attained parameters. The range of the parameters for ohmic contact formation is also indicated.

(*I–V*) characteristics compared to the experimental ones. The practical significance of this study is evident due to the need for low-barrier diodes for microwave detectors that do not require a constant bias [12, 13]. Other applications, based on the potential of the technology of nonalloyed ohmic contacts [5, 7, 8], which can be important for devices with nanometer-scale active regions, are also possible.

CALCULATIONS

The transport characteristics of the modified metal–semiconductor contact were numerically calculated in two stages. At the first stage, the depth (axis *x*) profile of the conduction band edge was calculated at various bias voltages *V* by solving the one-dimensional Poisson equation (see, e.g., [14]). The doping profile was considered as known, and the doping impurity was assumed to be completely ionized. The layer sequence in the structure was chosen close to the experimental one: a heavily doped substrate with the electron density $n^+ = 2 \times 10^{18}$ cm^{-3}, a lightly doped epitaxial layer with $n^- = 2 \times 10^{16}$ cm^{-3} 100 nm thick, a δ-layer of silicon atoms with the surface concentration N_{2D}, a cover GaAs layer with a thickness of x_0, and a metal contact. The δ-layer spread along *x* is approximated by the Gaussian

$$n(x) = \frac{N_{2D}}{\Delta x}\exp\left[-\frac{1}{2}\left(\frac{x - x_0}{\Delta x}\right)^2\right], \qquad (2)$$

where Δx is the standard deviation taken as 0.5 nm [7] in the calculations. Furthermore, the barrier height decrease due to the image forces was taken into account. The temperature was supposed to be 295 K. We neglected the quantization effects in the potential well of the δ-layer, since the basic results of this study concern the case of its total depletion.

Examples of calculations of the potential barrier of the metal–semiconductor contact without external bias at two x_0 and N_{2D} combinations are given in Figs. 2a and 2b, respectively. One can see that the sharp triangular spike arises at the barrier top due to δ-doping; it is the barrier tunnel transparency that leads to a decrease of the effective barrier height for electrons. A simultaneous increase in N_{2D} and x_0 near its bottom gives rise to a potential well filled with electrons.

At the next stage, the Schrödinger equation is solved by the transfer matrix method [11] for the calculated potential barrier. The electron transmittance $\tilde{T}$ is calculated in relation to the electron energy *E* and the bias *V*, which controls the potential barrier shape. Subsequent integration of the transmittance $\tilde{T}(E, V)$ over all the occupied electron states in the semiconductor and all the free electron states in the metal yields the carrier current density j_{S-M} from semiconductor to metal. Similarly, the metal-to-semiconductor current density j_{M-S} is calculated. Their difference yields the total current density in the Schottky diode,

$$j(V) = j_{S-M} - j_{M-S}$$
$$= \frac{2q}{h^3}\int_{E_C}^{\infty}\tilde{T}(E, V)[F_{E_F}(E) - f_{E_F - qV}(E)]dE, \qquad (3)$$

where $f_{E_F}(E)$ and $f_{E_F - qV}(E)$ are the Fermi distribution functions in the semiconductor and metal, respectively. The transmittance is assumed to be independent of the electron momentum parallel to the metal–semiconductor interface. Therefore, the expression for current can be integrated in transverse directions, which yields the following expression for current (see [9]):

$$j(V) = \frac{A^*T}{k_B}\int_{E_C}^{\infty}\tilde{T}(E_x, V)$$
$$\times \ln\left\{\frac{1 + \exp[(E_x - E_F^S)/k_BT]}{\exp(-qV/k_BT) + \exp[(E_x - E_F^S)/k_BT]}\right\}dE_x. \qquad (4)$$

Here, E_x is the electron energy fraction corresponding to its motion along axis x, E_F^S is the Fermi energy in the semiconductor, T is the temperature, and k_B is the Boltzmann constant. Calculating the integral numerically at various biases, the I–V characteristics of a specific structure can be obtained. It is noteworthy that these characteristics were calculated ignoring the series and with shunt resistances always existing in actual diode structures. The inclusion of the resistances (as was done, e.g., in [6]) allows for a better fit of experimental I–V characteristics.

EXPERIMENTAL

The GaAs epitaxial structures were grown by vapor-phase epitaxy from metal-organic compounds (MOVPE) at temperatures of 600–650°C. The layer parameters were the same as in the preceding section. The values of N_{2D} and x_0 were varied during the experiments (see crosses in dashed lines in Fig. 1). The MOVPE and δ-layer diagnostic techniques are described in [15]. The values N_{2D} were estimated by measurements at test structures where similar δ-layers were grown at a depth of 0.15–0.2 μm, which allows for their characterization by the Hall method and capacitance–voltage characteristics. It was shown that the sheet carrier concentration n_s coincides with the MOVPE-introduced donor concentration N_{2D} up to 6×10^{12} cm^{-2} and then levels off.

After completion of GaAs growth, the growth chamber temperature was lowered to 160–200°C and an aluminum layer about 100 nm thick was grown without opening the reactor and, thus, violating the growth conditions. Additional aftergrowth evaporation of aluminum was carried out in a number of cases. Diodes with a metal contact diameter of 10–500 μm and a mesa depth of 0.2 μm were formed by photolithography and chemical etching. A rear ohmic contact was produced by electrochemical deposition of GeNi + Au followed by firing-in.

The diode I–V characteristics were measured at room temperature. The effective barrier heights ϕ^{eff} were determined from the measured characteristics in the conventional way, assuming the dependence to be close to the first approximation of the theory of thermal-field emission (see [12]),

$$j_{TE} = A^* T^2 \exp\left(-\frac{\phi^{\text{eff}}(V)}{k_B T}\right)\left\{\exp\left(\frac{qV}{k_B T}\right) - 1\right\}, \quad (5)$$

where A^* is the modified Richardson constant. The dependence of the effective barrier height ϕ^{eff} on the bias defines the nonideality factor of the metal–semiconductor contact. In the absence of δ-doping, the barrier height is about 0.7 eV (n = 1.04– 1.06).

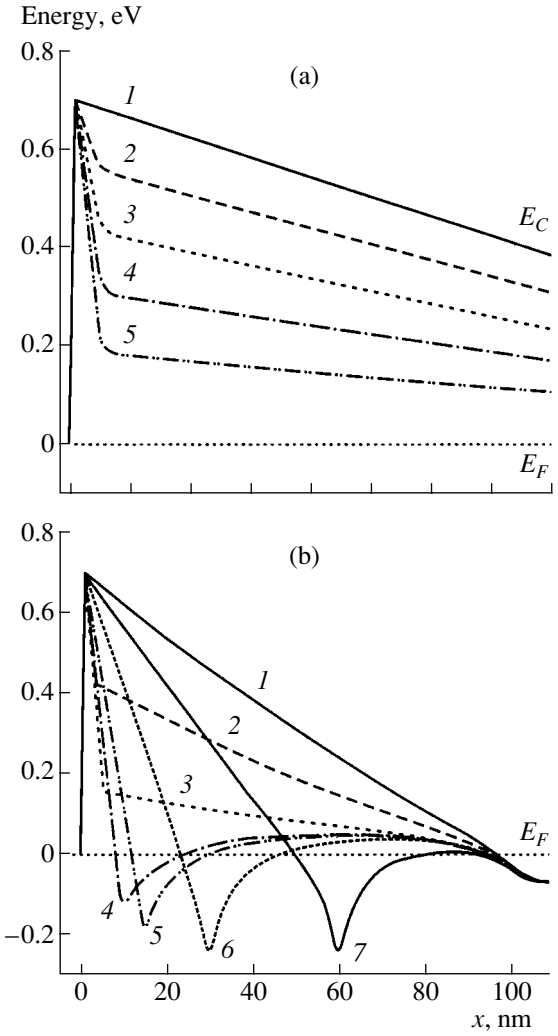

Fig. 2. Calculation of the potential of the modified Schottky barrier at (a) x_0 = 2.5 nm and N_{2D} = (*1*) 0, (*2*) 4×10^{12}, (*3*) 8×10^{12}, (*4*) 1.2×10^{13}, and (*5*) 1.6×10^{13} cm^{-2}; (b) $N_{2D} = 8 \times 10^{12}$ cm^{-2} and x = (*1*) 0, (*2*) 2.5, (*3*) 5, (*4*) 10, (*5*) 15, (*6*) 30, and (*7*) 60 nm.

DISCUSSION

The effect of control of the effective barrier height is illustrated by Fig. 3 showing the measured and calculated I–V characteristics of diodes with δ-doping within $(4–16) \times 10^{12}$ cm^{-2} in the plane spaced from the metal by 2.5 nm. One can see that the calculated characteristics fit well with the experimental ones. Similar calculations and experiments were carried out for a deeper (5 nm) doping plane. The effective barrier heights were determined in all the cases and are shown in Fig. 4 versus the surface (2D) concentration. One can see that the effective barrier height linearly decreases as the surface concentration increases. This means that the concept of the tunneling-transparent spike above a nontransparent classical pedestal is a good physical idealization. The deeper the δ-layer, the greater the effective barrier

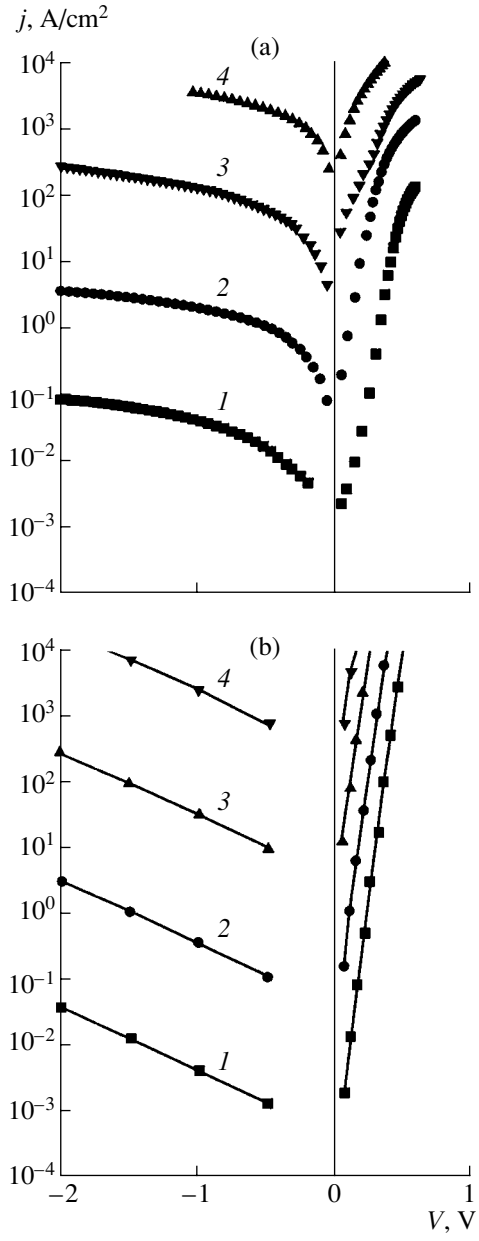

Fig. 3. Experimental (a) and calculated (b) current–voltage characteristics of modified Schottky diodes at $x_0 = 2.5$ nm and N_{2D} = (*1*) 4×10^{12}, (*2*) 8×10^{12}, (*3*) 1.2×10^{13}, and (*4*) 1.6×10^{13} cm^{-2}.

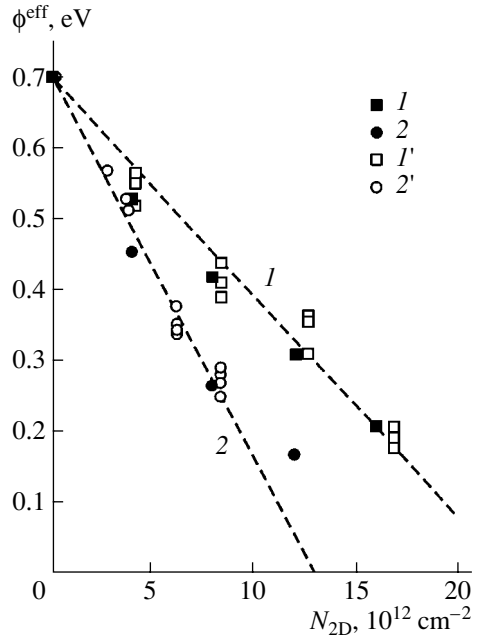

Fig. 4. Effective barrier height versus the δ-doping level at the two distances between the δ-layer and the metal–semiconductor contact, x_0 = (*1*, *1*') 2.5 and (*2*, *2*') 5 nm; (*1*, *2*) calculation and (*1*', *2*') experiment.

height decrease (Fig. 4, curve *2*), however, only under the condition of a sufficiently high tunneling transparency of the triangular barrier.

The second experimental series was dedicated to processes taking place when the above condition ceases to be met. The donor surface density N_{2D} was fixed, and the depth x_0 was varied within 2.5–60 nm. The experimental and calculated *I–V* characteristics at $N_{2D} = 4 \times 10^{12}$ cm^{-2} are displayed in Figs. 5a and 5b, respectively. One can see that the effective barrier height ϕ^{eff} initially decreases (as x_0 increases) and then increases, which is caused by a decrease in the tunneling transparency of the potential barrier between the metal and the δ-layer. The minimum attainable value $\phi^{eff} \approx 0.33$ eV (curve *2*) at $N_{2D} = 4 \times 10^{12}$ cm^{-2} corresponds to $x_0 \approx 10$ nm. It is evident that the calculation satisfactorily predicts the features of the *I–V* characteristics, e.g., the two saturation regions in the reverse portion, which is caused by a change in the total surface charge in the δ-layer during its filling with electrons as the external bias is changed. The nonmonotonic dependence of the effective barrier height ϕ^{eff} on the δ-layer depth x_0 for two values of N_{2D} is shown in Fig. 6a. Processing of the calculated *I–V* characteristics for the same surface impurity concentrations in the δ-layer yields very close results, as is shown in Fig. 6a. As N_{2D} increases, the $\phi^{eff}(x_0)$ is attained at a closer proximity of the δ-layer to the metal–semiconductor contact. Figure 6b shows the calculated nonideality factor versus the δ-layer depth x_0 for two values of N_{2D}. It is noteworthy that the nonideality factor n increases near $x_0 \approx 10$ nm, i.e., at such a depth when the probability of electron tunneling through the barrier begins to decrease. As x_0 further increases, the thermoelectron component of the current begins to prevail, and the nonideality factor decreases. Thus, the most adverse situation is when the δ-layer depth is 8–15 nm. The same effect, manifesting itself in the case of high uniform doping near the metal–semiconductor contact, was observed in [6] at a heavily doped δ-layer thicker than 10 nm, which drastically limits the possibility of

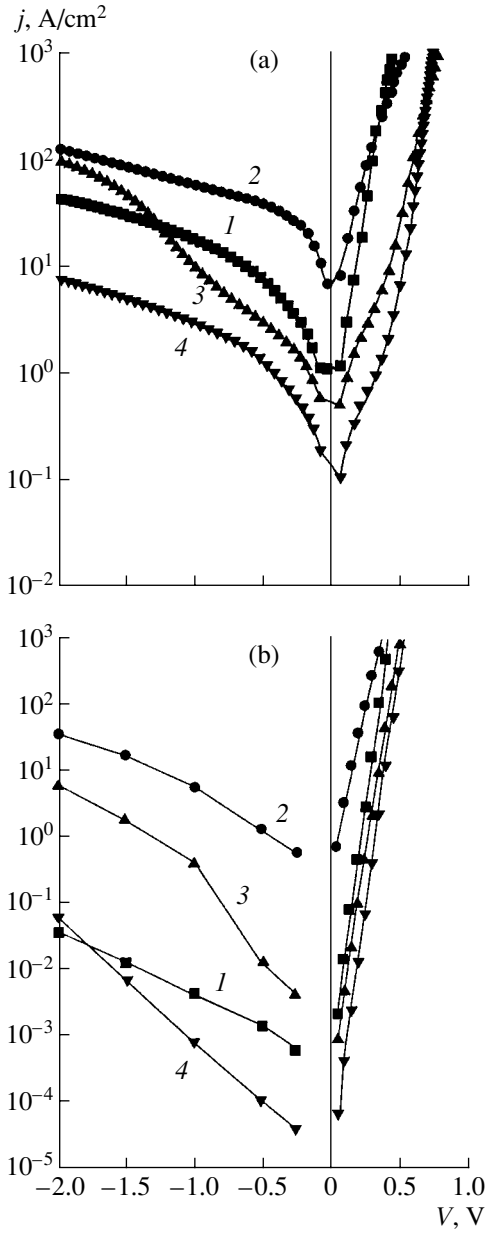

Fig. 5. (a) Experimental and (b) calculated current–voltage characteristics of the modified Schottky diodes at $N_{2D} = 4 \times 10^{12}$ cm^{-2} and x_0 = (*1*) 2.5, (*2*) 10, (*3*) 30, and (*4*) 60 nm.

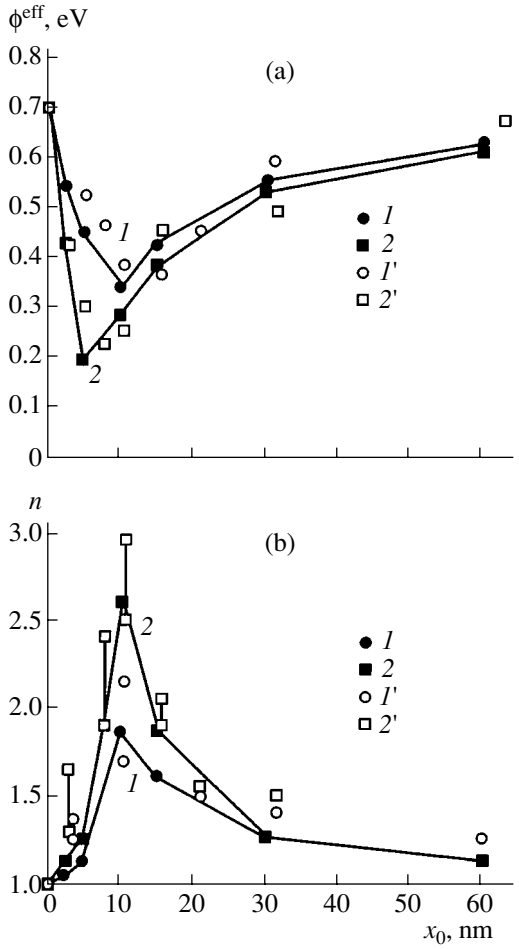

Fig. 6. Dependence of (a) the effective barrier height ϕ^{eff} and (b) the nonideality factor n on the δ-layer depth x_0 at N_{2D} = (*1*, *1*') 4×10^{12} and (*2*, *2*') 8×10^{12} cm^{-2}; (*1*, *2*) calculation and (*1*', *2*') experiment.

producing diodes with a low barrier height using such a method. A practically achieved (see [6]) decrease of the barrier height was 0.6 eV at a nonideality factor up to 1.3 (the volume doping concentration was 5×10^{18} cm^{-3}). Therefore, the use of the δ-doped plane seems preferable. The joint analysis of the data of Figs. 6a and 6b shows that diodes with a low barrier (about 0.2 eV) and the nonideality factor $n \le 1.5$ can be developed at δ-layer depths not exceeding 5 nm. This is confirmed experimentally (see Fig. 6b). The nonideality factors that are somewhat larger than the theoretically predicted ones at distances $x_0 \le 5$ nm can be caused by deep charged states of donors in the δ-layer. As was shown in [15], an extended tail of the density of donor states begins to be formed in the GaAs band gap even at $N_{2D} > 5 \times 10^{12}$ cm^{-2}; their depth reaches 100 meV. As N_{2D} increases, the effect becomes more pronounced. At small ϕ^{eff} (<0.2 eV) and (or) large forward biases, this causes recharging of deep donor states in the δ-layer. Therefore, the effective barrier height ϕ^{eff} in (4) acquires an additional dependence on the bias, and the nonideality factor increases. It is evident that this effect at static measurements complicates the pattern and, in principle, can lead to different ϕ^{eff} and n for forward and reverse portions of *I–V* characteristics. At $N_{2D} = 1.6 \times 10^{13}$ cm^{-2} and $x_0 = 2.5$ nm, the calculations yield $\phi^{eff} \approx 0.2$ eV and $n \le 1.5$, which are confirmed experimentally. Based on these structures, efficient microwave diode detectors operating without bias were produced [13].

CONCLUSION

The studies carried out show the possibility of controlling the effective height of the Schottky barrier using subsurface δ-doping, which enhances the role of the thermal-field (tunnel) component of the conduction current. Numerical simulation of charge transport with a rather wide variation in the doping parameters made it possible to reveal basic laws and determine the most acceptable parameters of GaAs-based diodes with a lowered barrier height. The MOVPE method was used to produce Al/*n*-GaAs⟨δ(*n*)⟩ diode structures. Their parameters were shown to be in a good agreement with the numerical simulation data. In particular, the possibility of forming a barrier contact to *n*-GaAs, having a height of about 0.2 eV and an nonideality factor $n < 1.5$, was demonstrated.

ACKNOWLEDGMENTS

We are grateful to V.Ya. Aleshkin, I.M. Nefedov, and I.A. Shereshevsky for their participation in discussions and their help with the development of programs and calculations.

This study was supported by the Russian Foundation for Basic Research, project no. 01-02-16451, as well as the program "Physics of Solid-State Nanostructures".

REFERENCES

1. E. H. Rhoderick, *Metal–Semiconductor Contacts* (Claredon, Oxford, 1978; Radio i Svyaz', Moscow, 1982).
2. S. Sze, *Physics of Semiconductor Devices* (Wiley, New York, 1981; Mir, Moscow, 1984), Part 1.
3. G. Myburg, F. D. Auret, W. E. Meyer, *et al.*, Thin Solid Films **325**, 181 (1998).
4. T. A. Bryantseva, V. E. Lyubchenko, and E. O. Yunevich, Radiotekh. Élektron. (Moscow) **40** (8), 1306 (1995).
5. V. I. Shashkin, A. V. Murel', Yu. N. Drozdov, *et al.*, Mikroélektronika **26**, 57 (1997).
6. S. Sassen, B. Witzigmann, C. Wolk, and H. Brugger, IEEE Trans. Electron Devices **47**, 24 (2000).
7. E. F. Schubert, J. E. Cunnighum, W. S. Tsang, and T. H. Chiu, Appl. Phys. Lett. **49**, 292 (1986).
8. M. Missous and T. Taskin, Semicond. Sci. Technol. **8**, 1848 (1993).
9. R. K. Kupka and W. A. Anderson, J. Appl. Phys. **69**, 3623 (1991).
10. J. M. Geraldo, W. N. Podrigues, G. Medeiros-Ribeiro, and A. G. de Oliveira, J. Appl. Phys. **73**, 820 (1993).
11. *Tunneling Phenomena in Solids*, Ed. by E. Burstein and S. Lundqvist (Plenum, New York, 1969; Mir, Moscow, 1973).
12. V. I. Shashkin, V. M. Daniltsev, O. I. Khrykin, *et al.*, in *Proceedings of the International Semiconductor Device Research Symposium (ISDRS), Charlottseville, USA, 1997*, p. 147.
13. V. I. Shashkin, V. L. Vaks, E. A. Vopilkin, in *Proceedings of the 7th Russia Conference "Gallium Arsenide", Tomsk, 1999*, p. 175.
14. I. H. Tan, G. L. Snider, and E. L. Hu, J. Appl. Phys. **68**, 4071 (1990).
15. V. Ya. Aleshkin, V. M. Danil'tsev, A. V. Murel', *et al.*, Fiz. Tekh. Poluprovodn. (St. Petersburg) **32**, 733 (1998) [Semiconductors **32**, 659 (1998)].

Translated by A. Kazantsev

Semiconductors, Vol. 36, No. 5, 2002, pp. 511–518. Translated from Fizika i Tekhnika Poluprovodnikov, Vol. 36, No. 5, 2002, pp. 543–549.

LOW-DIMENSIONAL SYSTEMS

Electrons, Holes, and Excitons in a Superlattice Composed of Cylindrical Quantum Dots with Extremely Weak Coupling between Quasiparticles in Neighboring Layers of Quantum Dots

N. V. Tkach*, A. M. Makhanets*, and G. G. Zegrya**

** Chernovtsy National University, Chernovtsy, 58012 Ukraine*

*** Ioffe Physicotechnical Institute, Russian Academy of Sciences, Politekhnicheskaya ul. 26, St. Petersburg, 194021 Russia*

e-mail: Zegrya@theory.ioffe.rssi.ru

Submitted July 3, 2001; accepted for publication August 28, 2001

Abstract—The spectrum of electrons, holes, and excitons in a superlattice composed of cylindrical quantum dots with extremely weak coupling between quasiparticles in neighboring layers of quantum dots was studied theoretically. Calculations were performed for the example of cylindrical β-HgS quantum dots embedded in β-CdS in the form of a superlattice. It is shown that electrons and holes in such a system form quasi-two-dimensional energy minibands, whereas excitons can be described in terms of the Shinoda–Sugano model. The dependence of the quasiparticle spectra on geometric parameters of a superlattice with cylindrical quantum dots was studied. It is shown that the positions of minibands for all quasiparticles are very sensitive to the height of quantum dots, which should manifest itself in the experimental excitonic absorption spectrum.

1. INTRODUCTION

The spectra and interaction of quasiparticles in quantum dots (QDs), quantum wires, and quantum wells (QWs) have been studied in detail for years both theoretically [1–4] and experimentally [5, 6]. Periodic structures formed of planar QWs [the so-called superlattices (SLs)] have also been investigated thoroughly [7, 8]. However, the periodic structures consisting of semiconductor quantum dots–wells arranged in a semiconductor medium have been produced only recently [7, 8] and, therefore, have been studied inadequately.

The general theory of quasiparticle spectra and interactions in periodic QD structures (the QD SLs) has not been developed to date, although several particular cases have been studied [9].

As is well known, there are periodic structures with semiconductor QDs (among those structures already produced experimentally) in which the distances between the QD layers in different planes are much larger than the inter-QD distances in an individual layer; as a result, the coupling between the quasiparticles residing in different layers is very weak.

The objective of this study was to investigate theoretically the electron, hole, and (mainly) exciton spectra in a semiconductor SL composed of cylindrical QDs with extremely weak coupling between quasiparticles in different layers and with inter-QD distances in the layers such that the quasiparticles (electrons, holes, and excitons) are translated over the entire SL composed of cylindrical QDs, rather than localized in an individual QD. We will show that the quasi-two-dimensional (quasi-2D) Shinoda–Sugano excitons are likely to be generated in such a system.

2. THE ELECTRON AND HOLE SPECTRA IN A SUPERLATTICE COMPOSED OF CYLINDRICAL QUANTUM DOTS WITH WEAK COUPLING BETWEEN QUASIPARTICLES IN NEIGHBORING LAYERS

We consider a semiconductor SL composed of cylindrical QDs (or QWs) embedded in the host medium in the way illustrated in Fig. 1a. We assume that the following geometric parameters of the system are known: the QD base radius (a), the QD height (L), the distances between the QD bases in the adjacent layers (h), and the distances between the boundaries of the two neighboring QDs in the same layer (b) (we assume that $h \gg b$). In what follows, we intend to calculate the electron and hole spectra in the effective-mass approximation and use the dielectric-continuum model in calculating the exciton spectrum. To this end, we require that geometric parameters of the QD and the spatial domain between two nearest QDs be much larger than the sizes of unit cells for the crystals in the QD (a_d) and the medium (a_m); i.e.,

$$\sqrt[3]{a^2L} \approx \sqrt[3]{b^2L} \gg a_d \approx a_m. \quad (1)$$

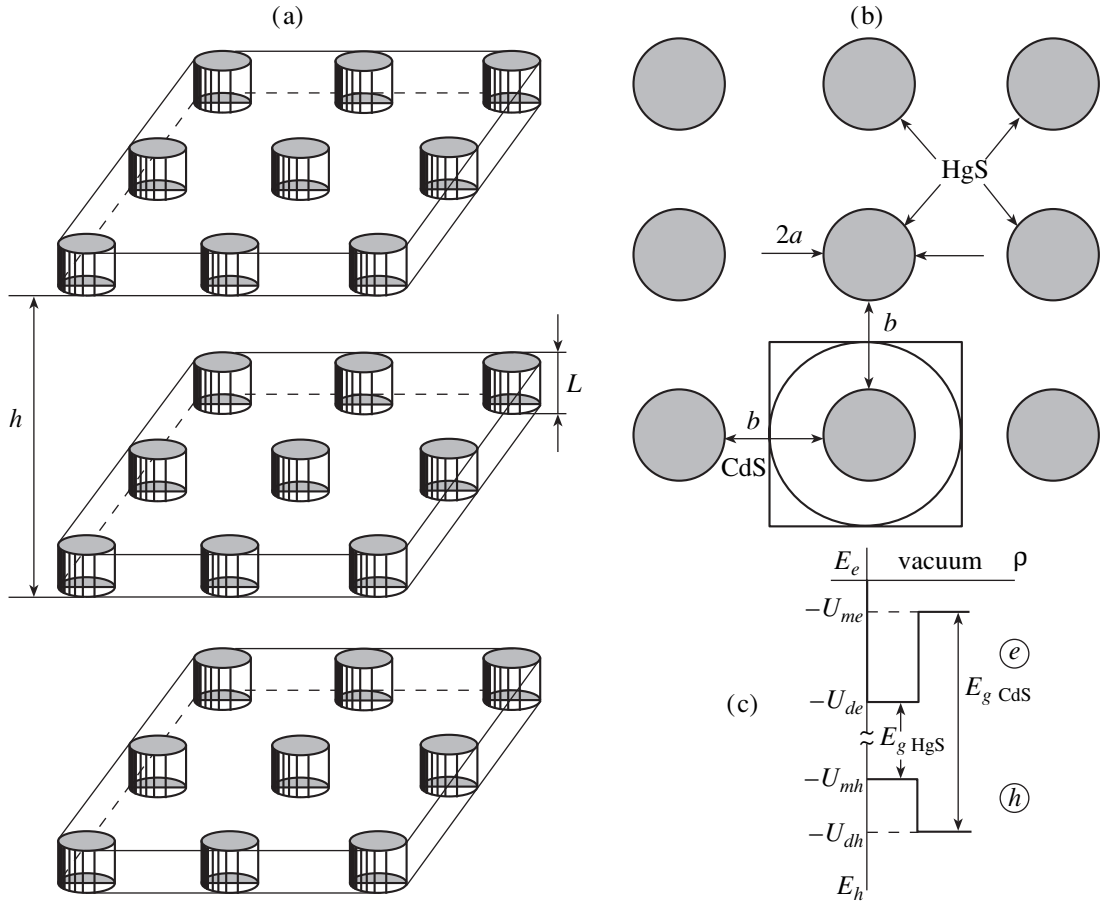

Fig. 1. (a) Schematic representation and (b) horizontal cross section of a superlattice composed of cylindrical quantum dots; (c) the dependence of electron and hole potential energies on the radius within an elementary cell of the superlattice.

Thus, we assume that the effective masses of electrons (holes) in the QD $\mu_{de}(\mu_{dh})$ and the host medium $\mu_{me}(\mu_{mh})$ are known and equal to the values characteristic of the corresponding bulk crystals. In the Cartesian coordinate system with the 0*Z* axis oriented along the symmetry axis of one of the QDs and with the *X*0*Y* plane passing through the midheight of the cylindrical QD, we have

$$\mu_{e,h} = \begin{cases} \mu_{de,dh} & \text{for} \quad x, y, z \text{ within the QD}, \\ \mu_{me,mh} & \text{for} \quad x, y, z \text{ outside the QD}. \end{cases} \tag{2}$$

The lattice constants of both crystals comprising the system are assumed to be almost identical ($a_d \approx a_m$). Therefore, we may assume that potential energies of electrons and holes are given by

$$U_{e,h} = \begin{cases} -U_{de,dh} & \text{for} \quad x, y, z \text{ within the QD}, \\ -U_{me,mh} & \text{for} \quad x, y, z \text{ outside the QD}, \end{cases} \tag{3}$$

where $U_{de,dh}$ and $U_{me,mh}$ are the potential energies of electrons and holes in the corresponding media with respect to free space (affinity) and are assumed to be known. The dielectric constants of the QD (ε_d) and of the medium (ε_m) differ from each other only slightly ($\varepsilon_d \approx \varepsilon_m$). In this situation, the self-action forces affecting the charged quasiparticles and arising owing to the presence of the boundary between the cylindrical QD and the medium can be evaluated in the following manner.

Since the potential of the self-action forces for a cylindrical QD is unknown and since the geometric parameters of a cylindrical QD are such ($L \approx a$) that this QD may be approximated by a spherical QD with a radius of $R = \left(\frac{3}{4} a^2 L\right)^{1/3}$, we may use the estimate for the self-action potential of a charged particle in a spherical QD [10], assuming that such a QD is mainly located at a distance of $R/2$ from the sphere center in a deep rectangular potential well. The polarization field with the potential [10]

$$U_p = \frac{\varepsilon_d - \varepsilon_m}{\varepsilon_d + \varepsilon_m} \frac{e^2}{\varepsilon_d \sqrt[3]{6La^2}} \left[\frac{4}{3} + \ln 3\right] \tag{4}$$

acts on a charged quasiparticle (electron or hole) in a spherical QD in the host medium.

Thus, if the geometrical parameters of a cylindrical QD (L, a) are such that the condition

$$U_p \ll U_{de,dh}, \quad U_{me,mh} \tag{5}$$

is satisfied, we may use the rectangular-potential approximation (3) to calculate the spectrum of quasiparticles.

In order to find the spectrum of excitons in the system under investigation, first of all, we have to obtain the spectra and wave functions of electrons and holes. To this end, we have to solve the Schrödinger equation

$$\mathrm{H}_{e,h}\psi_{e,h}(x,y,z) = E_{e,h}\psi_{e,h}(x,y,z) \tag{6}$$

with the Hamiltonian

$$\mathrm{H}_{e,h} = -\frac{\hbar^2}{2}\nabla\frac{1}{\mu_{e,h}(x,y,z)}\nabla + U_{e,h}(x,y,z). \tag{7}$$

Since the following consideration is completely equivalent for electrons and holes, we consider only electrons. Taking into account that we are dealing with a system with extremely weak coupling between the quasiparticles in neighboring layers, we then assume that an electron cannot leave each individual QD layer with a thickness L. The electron wave function in the Cartesian coordinate system with the $0Z$ axis being oriented along the symmetry axis of QD can be represented as

$$\psi_e(x,y,z) = \psi_\parallel(x,y)\sqrt{\frac{2}{L}}\begin{cases}\cos\dfrac{\pi n}{L}z, & n = 1,3,\ldots,\\ \sin\dfrac{\pi n}{L}z, & n = 2,4,\ldots.\end{cases} \tag{8}$$

In order to obtain the "in-plane" component of the wave function for an electron in an SL, we first separate the z component and introduce the corrected effective mass

$$\frac{1}{\bar{\mu}_e} = \frac{P_e}{\mu_{de}} + \frac{(1-P_e)}{\mu_{me}}. \tag{9}$$

Here,

$$P_e = \frac{|\mathrm{K}_m(\beta_e\rho_0)|^2\int_0^{\rho_0}|\mathrm{J}_m(\alpha_e\rho)|^2\rho d\rho}{|\mathrm{K}_m(\beta_e\rho_0)|^2\int_0^{\rho_0}|\mathrm{J}_m(\alpha_e\rho)|^2\rho d\rho + |\mathrm{J}_m(\alpha_e\rho_0)|^2\int_{\rho_0}^{\infty}|\mathrm{K}_m(\beta_e\rho)|^2\rho d\rho} \tag{10}$$

is the probability of finding an electron within an individual QD, provided that the surrounding medium has a large volume where

$$\alpha_e = \sqrt{\frac{2\mu_{de}}{\hbar^2}(V_e+E)}, \quad \beta_e = \sqrt{\frac{2\mu_{me}}{\hbar^2}E}, \qquad V_e = U_{de} - U_{me}; \tag{11}$$

and K_m and J_m are the Macdonald and Bessel functions, which are the solutions to the Schrödinger equation for the planar wave-function component in the polar coordinate system with the origin coinciding with the QD center.

According to the modified (to the case of a 2D system) method of augmented plane waves (APW) [11], the planar component of the electron wave function in the SL is then formed by a linear combination of the Bessel functions joined with the plane waves also expanded in the Bessel functions; i.e.,

$$\psi_{n\mathbf{k}_\parallel}(\boldsymbol{\rho}) = \sum_g \frac{c_{\mathbf{k}_\parallel-\mathbf{g}}}{\sqrt{\Omega}}\sum_{m=-\infty}^{\infty} i^m \exp[im(\varphi-\varphi_{\mathbf{k}_\parallel-\mathbf{g}})] \times\begin{cases}\dfrac{\mathrm{J}_m(|\mathbf{k}_\parallel-\mathbf{g}|a)}{\mathrm{J}_m(\alpha_{n,e}a)}\mathrm{J}_m(\alpha_{ne}\rho), & \rho\le a,\\ \mathrm{J}_m(|\mathbf{k}_\parallel-\mathbf{g}|\rho), & \rho > a.\end{cases} \tag{12}$$

Here,

$$\alpha_{ne} = \sqrt{\alpha_e^2 - \frac{\pi^2 n^2}{L^2}\frac{\mu_{de}}{\bar{\mu}_e}}; \quad m = 0,\pm1,\pm2,\ldots; \tag{13}$$

Ω is the volume of a planar unit cell; $\mathbf{k}_\parallel$ is the 2D wave vector of the planar reciprocal lattice; and $|\mathbf{k}_\parallel - \mathbf{g}|$ and $\varphi_{\mathbf{k}_\parallel-\mathbf{g}}$ are the polar coordinates of the vector $\mathbf{k}_\parallel - \mathbf{g}$.

The expansion coefficients $c_{\mathbf{k}_\parallel-\mathbf{g}}$ are determined from the condition for minimization of the energy functional; as a result, we obtain the system of equations

$$\left\{\frac{\hbar^2}{2\mu_{me}}(\mathbf{k}_\parallel-\mathbf{g})^2 - E + \frac{\pi^2 n^2}{L^2}\frac{\mu_{de}}{\bar{\mu}_e}\right\}c_{\mathbf{k}_\parallel-\mathbf{g}} + \sum_{\mathbf{g}'}\Gamma_{\mathbf{g}\mathbf{g}'}c_{\mathbf{k}_\parallel-\mathbf{g}'} = 0, \tag{14}$$

where

$$\Gamma^n_{\mathbf{g}\mathbf{g}'} = \frac{2\pi a}{\Omega}\left\{-\left[\frac{\hbar^2}{2\mu_{me}}(\mathbf{k}_\parallel-\mathbf{g})(\mathbf{k}_\parallel-\mathbf{g}') - E + \frac{\pi^2\hbar^2 n^2}{2\bar{\mu}_e L^2}\right]\times\frac{\mathrm{J}_1(|\mathbf{g}-\mathbf{g}'|a)}{|\mathbf{g}-\mathbf{g}'|} + \frac{\hbar^2}{2\mu_{de}}\sum_{m=-\infty}^{\infty}\exp(im\varphi_{\mathbf{g}\mathbf{g}'})\mathrm{J}_m(|\mathbf{k}_\parallel-\mathbf{g}|a) \times \mathrm{J}_m(|\mathbf{k}_\parallel-\mathbf{g}'|a)\left[\frac{d}{d\rho}\ln\mathrm{J}_m(\alpha_{ne}\rho)\right]_{\rho=a}\right\}, \tag{15}$$

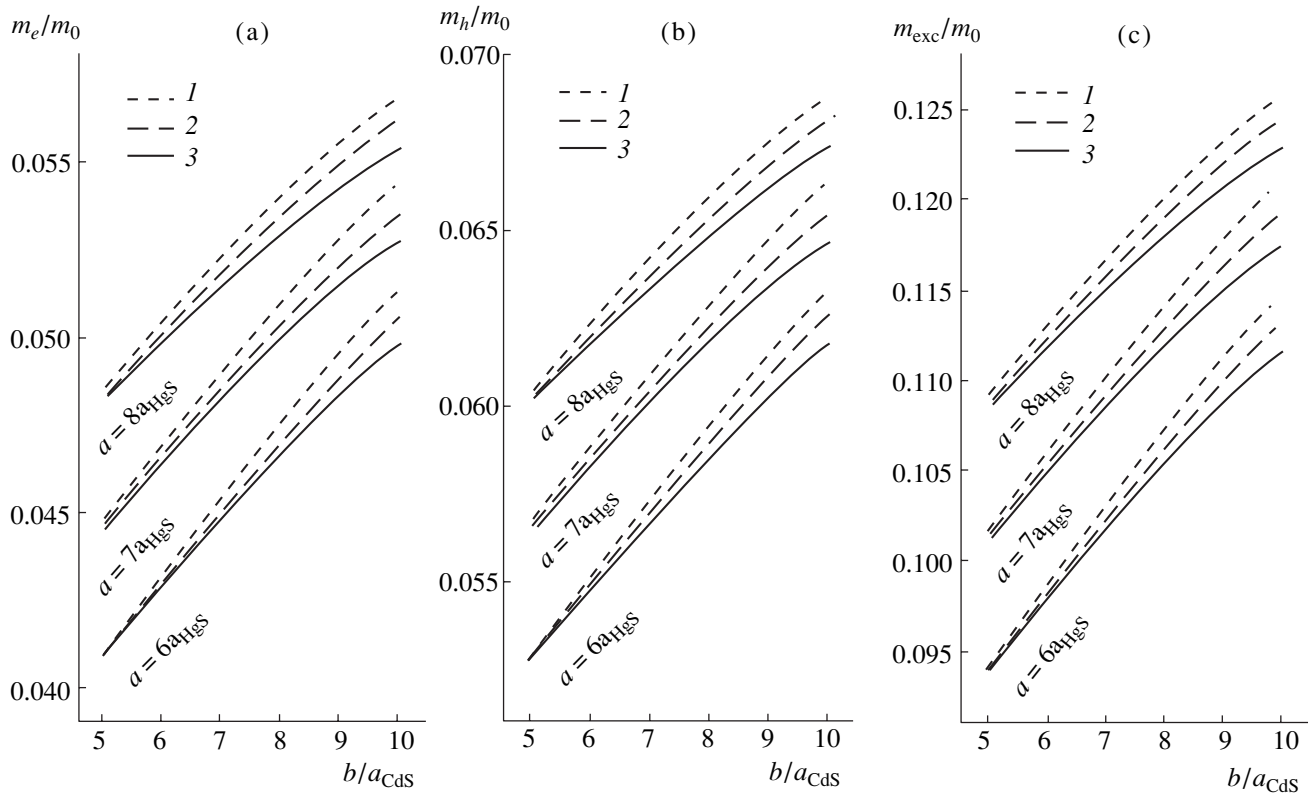

Fig. 2. Dependences of the effective masses of (a) electron m_e, (b) hole m_h, and (c) exciton m_{exc} on the distance b between the quantum dots for several values of the radius a and height L of a quantum dot. L/a_{HgS} = (*1*) 7, (*2*) 8, and (*3*) 9.

and $\varphi_{\mathbf{gg}'}$ is the angle formed by the vectors $(\mathbf{k}_\parallel - \mathbf{g})$ and $(\mathbf{k}_\parallel - \mathbf{g}')$.

The condition for nontriviality of the solution to system (14) brings about a secular equation; it is the solution to this equation that defines the energy spectrum of electrons $E_e(\mathbf{k}_\parallel)$ within the QW depth. The energy spectrum of holes $E_h(\mathbf{k}_\parallel)$ is determined similarly.

By way of example, we use the above theory to calculate and study the electron and hole spectra in an SL composed of cylindrical β-HgS QDs embedded in the β-CdS matrix in such a way that vertical coupling between QDs is weak (Fig. 1). The choice of such a system is governed by the fact that the aforementioned materials have almost the same values of the lattice constants a_{HgS} and a_{CdS} (see table); as a result, the interface between HgS and CdS is well defined and, consequently, the rectangular-potential approximation is justified. Dielectric constants of a cylindrical QD (ε_d) and the medium (ε_m) differ insignificantly.

Numerical calculation of energies of the electron $[E_e(\mathbf{k}_\parallel)]$ and hole $[E_h(\mathbf{k}_\parallel)]$ in relation to the quasi-momentum magnitude $|\mathbf{k}_\parallel|$ shows that, for the SL composed of cylindrical QDs under consideration, both $E(\mathbf{k})$ dependences can be approximated successfully by quadratic functions; i.e.,

$$E_e(|\mathbf{k}_\parallel|) = E_{0e} + \frac{\hbar^2|\mathbf{k}_\parallel|^2}{2m_e}, \quad E_h(|\mathbf{k}_\parallel|) = E_{0h} + \frac{\hbar^2|\mathbf{k}_\parallel|}{2m_h}. \tag{16}$$

Furthermore, the 2D effective masses of an electron (m_e) and hole (m_h) are given by

$$m_{e,h} = \frac{\pi^2 \mathrm{Ry} m_0}{\Delta E_{e,h}(2a+b)^2}; \quad (\Delta E_{e,h} = E_{te,th} - E_{0e,0h}), \tag{17}$$

where $\Delta E_{e,h}$ are the widths of the electron (e) and hole (h) minibands ($E_{te,th}$ and $E_{0e,0h}$ stand for the band-top and band-bottom energies, respectively), the quantities a and b are expressed in the Bohr radii, m_0 is the free-electron mass in the free space, and Ry = 13.6 eV is the Rydberg energy.

It is noteworthy that the method employed makes it possible to calculate the dispersion laws for electrons and holes in various systems, which satisfy certain conditions; however, it may so happen that the quadratic dependence of energy on quasi-momentum over the entire miniband does not hold. Physically, such a situation can arise in the systems with very small sizes (a, L, and b) involved, in which case it is necessary to take into account a great number of $\Gamma_{\mathbf{g},\mathbf{g}'}$ components in

Table

	m_e/m_0	m_h/m_0	a, Å	E_g, eV	U_e, eV	U_h, eV	ε
β-CdS	0.2	0.7	5.818	2.5	–3.8	–6.3	9.1
β-HgS	0.036	0.044	5.851	0.5	–5.0	–5.5	18.2

Eqs. (14) when calculating the energy by the APW method.

In Figs. 2a and 2b, we show the calculated dependences of effective (a) electron and (b) hole masses on the distance (b) between cylindrical QDs for several values of the QD radius (a) and height (L). It can be seen that an increase in b leads to an increase in the effective electron and hole masses for any values of a and L. This is understandable since an increase in the inter-QD distance is equivalent to an increase in the strength of the potential barrier for electrons or holes, which hampers the motion of charge carriers in a SL composed of cylindrical QDs, i.e., leads to an increase in the effective masses of these quasiparticles.

For a fixed distance b between QDs, an increase in the height (L) or radius a of the QDs causes the effective masses of quasiparticles to increase, because both factors induce an effective increase in the potential-barrier strength. Indeed, an increase in the QD size results in an increase in the QW volume; as a consequence, the energy levels are lowered. In other words, the wave functions of quasiparticles are "drawn" in the QD.

Since the effective hole mass is larger than the corresponding mass of an electron both in the QD and in the host medium, then (as can be seen from Figs. 2a, 2b) $m_h > m_e$, all other factors being the same.

3. THE SHINODA–SUGANO EXCITON IN A SUPERLATTICE COMPOSED OF CYLINDRICAL QUANTUM DOTS

It is clear from physical considerations that quasiparticles of an exciton type in an SL composed of cylindrical QDs can be described in terms of different models, depending on the relations between the geometric and physical parameters of the system. Conventionally, we can single out two groups of models.

One of the groups includes the models with extremely weak interaction between quasiparticles in different QWs (the models of isolated QWs). For such models, the main condition consists in the following:

$$h \approx b \gg \lambda_m^{(3)}, \mathrm{a}_{ex_m}^{(3)}; \tag{18}$$

i.e., all distances between QDs should exceed the free-path length ($\lambda_m^{(3)}$) and the exciton radius ($\mathrm{a}_{ex_m}^{(3)}$) in the host medium. In this situation, a free three-dimensional (3D) Wannier–Mott exciton can be formed; such an exciton has the energy

$$E_n(\mathbf{k}) = E_{gm} - \frac{\hbar^2}{2\mu_m(\mathrm{a}_{ex\,m}^{(3)})^2} - \frac{\hbar^2 k^2}{2(m_{em} + m_{hm})} \tag{19}$$

and the radius

$$\mathrm{a}_{ex\,m}^{(3)} = \frac{\hbar^2 \varepsilon_m}{\mu_m e^2} n, \quad (n = 1, 2, \ldots, \infty). \tag{20}$$

In addition, excitons of different types can exist in QWs of an SL, depending on the ratio between the geometric parameters. For example, if the geometric parameters of a QW are such that

$$L \approx a \gg \lambda_d^{(3)}, \mathrm{a}_{ex\,d}^{(3)}, \tag{21}$$

i.e., if the QD sizes far exceed the free-path length ($\lambda_d^{(3)}$) and radius ($\mathrm{a}_{ex\,d}^{(3)}$) of an exciton in the QD, a free 3D Wannier–Mott exciton can also exist in the system; this exciton has an energy and radius defined by formulas (19) and (20) with parameters corresponding to the QD medium (d).

If

$$a \gg \lambda_d^{(2)}, \quad L \approx \mathrm{a}_{ex\,d}^{(2)}, \tag{22}$$

then, since the QD is quasi-2D ($a \gg L$) and the QD radius (a) far exceeds the exciton's free-path length ($\lambda_d^{(2)}$), a free 2D Shinoda–Sugano exciton is formed in the QD medium; this exciton has the energy

$$E_n(k) = E_{gd} - \frac{\hbar^2}{2\mu_d(\mathrm{a}_{ex\,d}^{(2)})^2} - \frac{\hbar^2 k^2}{2(m_{ed} + m_{hd})} \tag{23}$$

and the radius

$$\mathrm{a}_{ex\,d}^{(2)} = \frac{\hbar^2 \varepsilon_d}{\mu_d e^2}(n + 1/2), \quad (n = 0, 1, 2, \ldots, \infty). \tag{24}$$

If

$$\lambda_d^{(2)} > a \approx L \geq \bar{\mathrm{a}}_{ex\,d}^{(2)}, \tag{25}$$

the QD is cylindrical, and a localized exciton with the radius $\mathrm{a}_{ex\,d}^{(2)}$ emerges in such a QD. In this situation, the energy of a localized excitation is controlled by the electron and hole energies in a cylindrical QD and by the energy of the Coulomb electron–hole interaction in

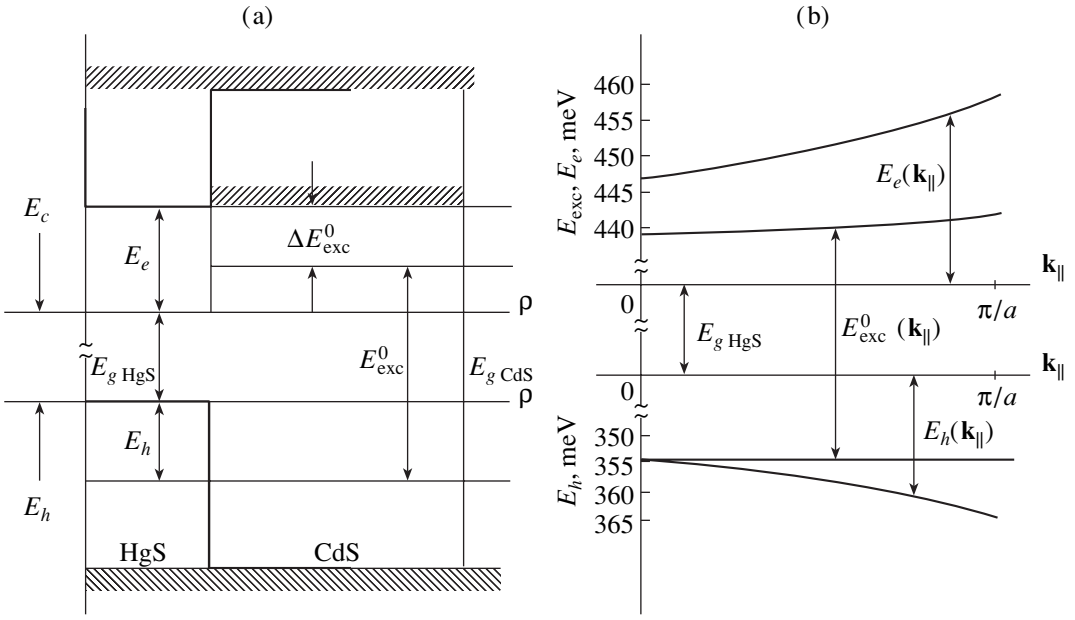

Fig. 3. (a) Schematic representation of potential energies of "two-dimensional" electron, hole, and exciton and (b) the dispersion curves for these quasiparticles.

the QD medium. The exciton radius is defined according to the laws of quantum mechanics.

If the QD size is so small that the exciton radius is on the order of several lattice constants, the models should account for the electrostatic-interaction forces, which arise owing to the presence of an interface between the QD and the host medium. If the QD size is even smaller, we should take into account the discrete structure of the medium.

The models, based on the assumption that

$$h \gg \lambda_m^{(3)},\ a, b, L, \tag{26}$$

can be referred to as the models involving interaction between QDs in quasi-planar layers.

If we have

$$a \gg b, L, \lambda_d^{(2)}, \tag{27}$$

a quasiparticle formed can be described in terms of the model of a free 2D Shinoda–Sugano exciton in the QD medium.

If

$$a \approx b \approx L \tag{28}$$

and if the condition $a + b < a_{\rm exc}$ is satisfied, a quasi-2D exciton with the radius $a_{\rm exc}$ is formed in an SL composed of cylindrical QDs; this exciton can be described in terms of the following model.

Since the electron and hole in an SL composed of cylindrical QDs with extremely weak interaction between quasiparticles in neighboring QDs are engaged in the quasi-plane motion with the quasi-momentum $\mathbf{k}_\parallel$ and have the known effective 2D masses m_e and m_h in the relevant minibands, we can determine the spectra and wave functions for the bound states of both quasiparticles.

We assume that an electron and hole have the radius vectors $\boldsymbol{\rho}_e$ and $\boldsymbol{\rho}_h$ in the $X0Y$ system (in the plane perpendicular to the QD symmetry axis) and interact with each other with the potential energy

$$V(\boldsymbol{\rho}_e - \boldsymbol{\rho}_h) = -\frac{e^2}{\varepsilon|\boldsymbol{\rho}_e - \boldsymbol{\rho}_h|}, \tag{29}$$

where

$$\varepsilon = \begin{cases} \varepsilon_d & \text{for } x, y, z \text{ within QD}, \\ \varepsilon_m & \text{for } x, y, z \text{ outside QD} \end{cases} \tag{30}$$

is the dielectric constant of an SL composed of cylindrical QDs.

It is impossible to solve the Schrödinger equation with such a complicated dependence of ε on the coordinates. Therefore, taking into account that the values of ε_d and ε_m are not much different from each other and the characteristic sizes of QDs and the inter-QD distances are comparable, we assume that an SL composed of cylindrical QDs is a continuum with a constant permittivity ($\bar{\varepsilon}$) defined as the averaged value of reciprocal permittivities of the system's components; i.e.,

$$\frac{1}{\bar{\varepsilon}} = \frac{1}{2}\left(\frac{1}{\varepsilon_d} + \frac{1}{\varepsilon_m}\right). \tag{31}$$

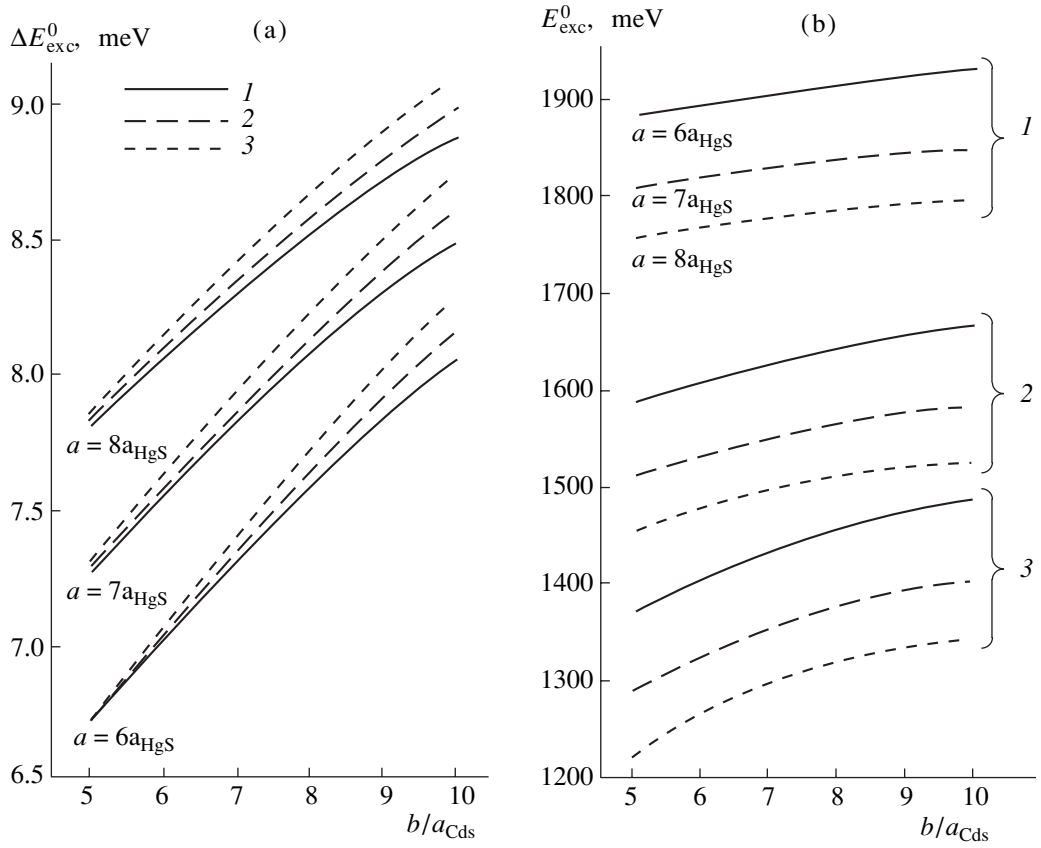

Fig. 4. Dependences of the (a) binding energy ΔE^0_{exc} and (b) formation energy E^0_{exc} of the Shinoda–Sugano exciton on the distance b between the quantum dots for several values of the radii a and heights L of the quantum dots. L/a_{HgS} = (*1*) 7, (*2*) 8, and (*3*) 9.

The Schrödinger equation for an electron and hole interacting in an SL composed of cylindrical QDs can now be written as

$$\left[\frac{\hbar^2}{2}\sum_{i=e,h}\frac{1}{m_i}\left(\frac{\partial^2}{\partial x_i^2}+\frac{\partial^2}{\partial y_i^2}\right)+\frac{e^2}{\bar{\varepsilon}|\boldsymbol{\rho}_e-\boldsymbol{\rho}_h|}-E_{ex}\right] \times F(\boldsymbol{\rho}_e,\boldsymbol{\rho}_h) = 0, \quad (32)$$

where $F(\boldsymbol{\rho}_e, \boldsymbol{\rho}_h)$ is the wave function of an electron–hole pair.

The problem of determining the energy spectrum and wave functions of a 2D exciton was solved by Shinoda and Sugano [12]. A solution to Eq. (32) defines the dispersion law for a 2D exciton; i.e.,

$$E^l_{\text{exc}}(|\mathbf{k}_\parallel|) = E^L_{\text{exc}} + \frac{\hbar^2|\mathbf{k}_\parallel|^2}{2m_{ex}}. \quad (33)$$

Here, $m_{\text{exc}} = m_e + m_h$ is the effective exciton mass; and the formation energy of exciton E^l_{exc} in the states $l = 0, 1, 2, \ldots, \infty$ is given by

$$E^l_{\text{exc}} = E_{g\text{HgS}} + E_{0e} + E_{0h} - \Delta E^l_{\text{exc}}, \quad (34)$$

where E_{0e} and E_{0h} are the energies of the electron- and hole-band bottoms (see Fig. 3);

$$\Delta E^l_{\text{exc}} = \frac{Me^4}{2\hbar^2\varepsilon^2(l+1/2)^2} \quad (35)$$

is the binding energy of a 2D exciton in the $l = 0, 1, 2, \ldots$ states; and

$$M = \frac{m_e m_h}{m_e + m_h} \quad (36)$$

is the reduced exciton mass in an SL composed of cylindrical QDs.

Specific calculations of the effective mass (m_{exc}) and the formation (E^0_{exc}) and binding (ΔE^0_{exc}) energies of an exciton in the ground state in relation to geometric parameters of an SL composed of cylindrical β-HgS QDs in the β-CdS matrix were performed numerically using a computer; the results are shown in Figs. 2c, 4a, and 4b.

Since m_{exc} is the sum of the masses m_e and m_h, the dependences of m_{exc} on a, b, and L are the same as those of m_e and m_h (Fig. 2c) and are governed by the same factors.

An increase in the distance (b) between the QDs for a = const and L = const always results in an increase in the exciton binding energy $\Delta E_{\text{exc}}^{0}$ (Fig. 4a), since an increase in b brings about an increase in the potential-barrier strength, which is conducive to a decrease in the distance between the electron and hole and to a greater degree of localization of both quasiparticles within a QW.

For fixed values of a and b, an increase in the QD height (L) or an increase in the QD radius (a), with b and L being fixed, results in an increase in the binding energy and a decrease in the exciton formation energy (Fig. 4). This is quite understandable since an increase in the QD volume is conducive to higher localization and to the closer approach of an electron and hole and also shifts the electron and hole minibands to lower energies.

In conclusion, we note that the level of a Shinoda–Sugano exciton in an SL composed of cylindrical QDs (Fig. 4) may be found quite deep in the band gap of 3D β-CdS and is very sensitive to variations in the QD height, which should clearly manifest itself in experiments.

ACKNOWLEDGMENTS

This study was supported in part by the Russian Foundation for Basic Research (project nos. 01-07-90299 and 01-07-90300) and by the "Physics of Solid-State Nanostructures" program (grant nos. 97-0003 and 97-1035).

REFERENCES

1. N. Mori and T. Ando, Phys. Rev. B **40**, 6175 (1989).
2. G. Q. Hai, F. M. Peeters, and J. T. Devreese, Phys. Rev. B **48**, 4666 (1993).
3. X. F. Wang and X. L. Lei, Phys. Rev. B **49**, 4780 (1994).
4. N. V. Tkach, Fiz. Tverd. Tela (St. Petersburg) **39**, 1109 (1997) [Phys. Solid State **39**, 995 (1997)].
5. Ch. Greus, R. Spiegel, P. A. Knipp, *et al.*, Phys. Rev. B **49**, 5753 (1994).
6. D. Schooss, A. Mews, A. Eychmuller, and H. Weller, Phys. Rev. B **49**, 17072 (1994).
7. Zh. I. Alferov, Fiz. Tekh. Poluprovodn. (St. Petersburg) **32**, 3 (1998) [Semiconductors **32**, 1 (1998)].
8. N. N. Ledentsov, V. M. Ustinov, V. A. Shchukin, *et al.*, Fiz. Tekh. Poluprovodn. (St. Petersburg) **32**, 385 (1998) [Semiconductors **32**, 343 (1998)].
9. A. D. Andreev and E. P. O'Reilly, in *Proceedings of the 3rd International Conference on Excitonic Processes in Condensed Matter (EXCON'98), 1998*, p. 272.
10. N. A. Efremov and S. I. Pokutniĭ, Fiz. Tverd. Tela (Leningrad) **27**, 48 (1985) [Sov. Phys. Solid State **27**, 27 (1985)].
11. V. N. Golovach, G. G. Zegrya, A. M. Makhanets, *et al.*, Fiz. Tekh. Poluprovodn. (St. Petersburg) **33**, 603 (1999) [Semiconductors **33**, 564 (1999)].
12. M. Shinoda and S. Sugano, J. Phys. Soc. Jpn. **21**, 1936 (1966).

Translated by A. Spitsyn

Semiconductors, Vol. 36, No. 5, 2002, pp. 519–526. Translated from Fizika i Tekhnika Poluprovodnikov, Vol. 36, No. 5, 2002, pp. 550–557.

LOW-DIMENSIONAL SYSTEMS

Evaluation of Mobility Gaps and Density of Localized Hole States in *p*-Ge/$Ge_{1-x}Si_x$ Heterostructures in the Quantum Hall Effect Mode

Yu. G. Arapov*^, O. A. Kuznetsov, V. N. Neverov*, G. I. Kharus*, N. G. Shelushinina*, and M. V. Yakunin***

** Institute of Metal Physics, Ural Division, Russian Academy of Sciences, ul. S. Kovalevskoĭ 18, Yekaterinburg, 620219 Russia*

*** Physicotechnical Research Institute, Nizhni Novgorod State University, pr. Gagarina 23/5, Nizhni Novgorod, 603600 Russia*

^ e-mail: arapov@imp.uran.ru

Submitted October 17, 2001; accepted for publication October 18, 2001

Abstract—The temperature (0.1 K $\lesssim T \lesssim$ 20 K) and magnetic field (0 T $\lesssim B \lesssim$ 12 T) dependences of the longitudinal (ρ_{xx}) and Hall (ρ_{xy}) resistivities have been studied in detail for *p*-Ge/$Ge_{1-x}Si_x$ (x = 0.07) multilayer heterostructures with hole density $p = (2.4–2.6) \times 10^{11}$ cm^{-2} and mobility $\mu = (1.1–1.7) \times 10^4$ cm^2 V^{-1} s^{-1}. The energy spectrum parameters of two-dimensional (2D) hole gas in the quantum Hall effect mode have been determined. The mobility gap W = (2–2.5) meV and the background density of localized states $g_c = (5–7) \times 10^{10}$ cm^{-2} meV^{-1} for the filling factors ν = 1 and 2. The results are discussed in terms of long-range impurity potential models for selectively doped 2D systems. © *2002 MAIK "Nauka/Interperiodica"*.

1. INTRODUCTION

The interpretation of the quantum Hall effect (QHE) is closely related to the problem of electron localization in a two-dimensional (2D) disordered system in a quantizing magnetic field. As shown by Laughlin [1] and Halperin [2], the necessary condition for QHE occurrence is the presence of narrow bands of extended states near the middle of each of the Landau subbands under the condition that all other states are localized. The density of states in the QHE mode has been determined in quite a number of works from data on heat capacity, magnetization, and thermally activated conductivity, and by spectroscopic methods for systems with *n*-type conduction (see review [3] and references therein). As shown experimentally, the density of localized states between the Landau levels is not exponentially small, and, on the whole, the density of states can be described as a series of Gaussian peaks on a constant density-of-states background. In the present study, we use the method of activated magnetoconductivity to determine the parameters of the hole spectrum in *p*-Ge/$Ge_{1-x}Si_x$ heterostructures with a complex valence band structure in quantizing magnetic fields.

2. THEORETICAL CONCEPTS

At present, it is commonly believed that the appearance of quantized plateaus in the $\rho_{xy}(B)$ dependence at infinitesimally small ρ_{xx} is due to the existence of mobility gaps in the density of states of a disordered 2D system in a quantizing magnetic field [4]. Under these conditions, the mobility edge E_c separating the localized and extended states lies near the center of a broadened Landau level. If the Fermi level lies in the range of localized states in the mobility gap, then the thermal excitation of electrons to narrow (of width γ) bands of extended states at the center of each of the Landau levels must lead to activation behavior of conductivity σ_{xx} (and also of $\rho_{xx} \propto \sigma_{xx}$).

2.1. Relations for Activated Conductivity

Following Mott [5] (see also [6, 7]), we use the Kubo–Greenwood relation for the dissipative component of conductivity:

$$\sigma_{xx} = -\int dE \frac{\partial f(E - E_F)}{\partial E} \sigma(E), \qquad (1)$$

where $f(E - E_F)$ is the Fermi–Dirac distribution function, and $\sigma(E)$ is the partial contribution of states with energy E to the conductivity. Representing the dependence $\sigma(E)$ as

$$\sigma(E) = \begin{cases} \sigma_c & |E - E_c| < \gamma/2, \\ 0 & |E - E_c| > \gamma/2, \end{cases} \qquad (2)$$

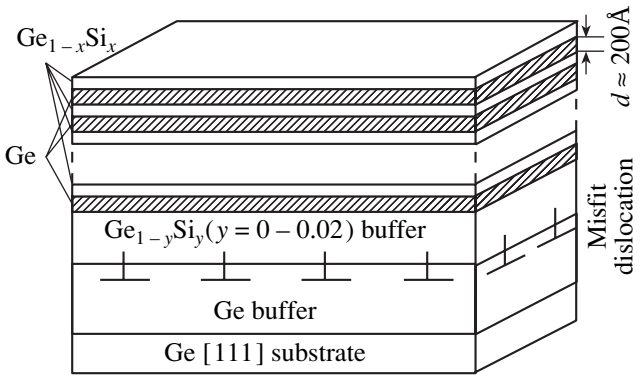

Fig. 1. Schematic of a multilayer *p*-Ge/$Ge_{1-x}Si_x$ heterostructure.

we obtain for a narrow band of extended states ($\gamma \ll kT$)

$$\sigma_{xx} = \sigma_c \frac{\gamma}{kT} F\left(\frac{E_A}{kT}\right). \quad (3)$$

Here, $E_A = |E_c - E_F|$, and

$$F(x) = \frac{\exp(-x)}{[1 + \exp(-x)]^2} = \left[4\cosh^2\left(\frac{x}{2}\right)\right]^{-1}. \quad (4)$$

At $E_A \gg kT$, from (3) follows the standard activation behavior of conductivity:

$$\sigma_{xx} \propto \exp\left(\frac{E_A}{kT}\right). \quad (5)$$

Taking into account the contribution to conductivity from two neighboring Landau levels ($E_{c1} \le E_F \le E_{c2}$), we obtain

$$\sigma_{xx} = \sigma_c \frac{\gamma}{kT}\left[F\left(\frac{E_{A1}}{KT}\right) + F\left(\frac{E_{A2}}{KT}\right)\right], \quad (6)$$

where $E_{Ai} = |E_F - E_{ci}|$ ($i = 1, 2$). In Eq. (6), we ignored the possible difference between the σ_c and γ values for different Landau levels. Here $E_{A2} = E_{c2} - E_F$ is the energy of electron activation into the nearest unoccupied band of extended states at $E = E_{c2}$, and $E_{A1} = E_{c1} - E_F$ is the energy of hole activation into a completely filled (at $T = 0$) band of extended states at $E = E_{c1}$.

It is noteworthy that the sum of activation energies for electrons and holes

$$E_{A1} + E_{A2} = W, \quad (7)$$

where $W \equiv E_{c2} - E_{c1}$ is the mobility gap width corresponding to the energy gap between the neighboring Landau levels to within the broadening γ. The maximum activation energy $E_A^{\max}$ is achieved for an integer filling factor $\nu = n/n_B$ (n is the electron density, $n_B = eB/hc$ is the degeneracy multiplicity of a Landau level), when the Fermi level lies in the middle between the Landau levels and $E_{A1} = E_{A2}$. It is in this way that the empirical estimation of the mobility gap is obtained: $W = 2E_A^{\max}$ [8–11].

2.2. Determining the Density of Localized States in the QHE Mode

With the electron density in a sample varied in a given magnetic field, E_F and, therefore, E_A are changed. Apparently, the rate of Fermi level motion in the range between the neighboring Landau levels is defined by the density of localized states $g(E)$ in the mobility gap:

$$g(E) = \frac{dn}{dE_F} \equiv \left[\frac{dE_A(n)}{dn}\right]^{-1}. \quad (8)$$

This method was used in [12] to determine the density of states in silicon MOS structures.

However, E_F is more frequently varied by changing B at n = const [8, 11, 13], rather than by altering n at constant B. In this case, the expression for the density of localized states can be represented as

$$g(E) = \frac{e\nu}{hc}\left[\frac{dE_A(B)}{dB}\right]^{-1}. \quad (9)$$

3. SAMPLE CHARACTERIZATION

Selectively doped Ge/$Ge_{1-x}Si_x$ ($x = 0.07$) multilayer heterostructures with *p*-conduction over the Ge layers were studied. The structures were grown by vapor phase epitaxy with 15–30 periods of Ge and Ge/$Ge_{1-x}Si_x$ layers of thickness $d \approx 200$ Å. The Ge layers were undoped, and GeSi solution layers were doped with boron in such a way that spacers of thickness $d_s \approx 50$ Å remained between Ge layers and the doped part of the solid solution, d_a (Fig. 1). Samples in the form of Hall bridges were used in the measurements. The growth procedure and the properties of *p*-Ge/$Ge_{1-x}Si_x$ heterostructures were described in detail in our previous reports (see [14–17] and references therein).

In this communication, we present the measurement results for Ge/$Ge_{1-x}Si_x$ samples with hole density $p = (2.4–2.6) \times 10^{11}$ cm^{-2} and mobilities $\mu = (1.1–1.7) \times 10^4$ cm^2 V^{-1} s^{-1} (at $T = 4.2$ K).

4. EXPERIMENTAL RESULTS AND DISCUSSION

The longitudinal (ρ_{xx}) and Hall (ρ_{xy}) resistivities were measured in a magnetic field B up to 12 T at temperatures T = (0.1–20) K. Well pronounced plateaus with quantized values $\rho_{xy}^i = ih/e^2$ ($i = 1$, 2, and 4) were observed in the $\rho_{xx}(B)$ dependence.

The dependences $\rho_{xx}(B)$ and $\rho_{xy}(B)$ at different temperatures are shown in Figs. 2a and 2b. An example of

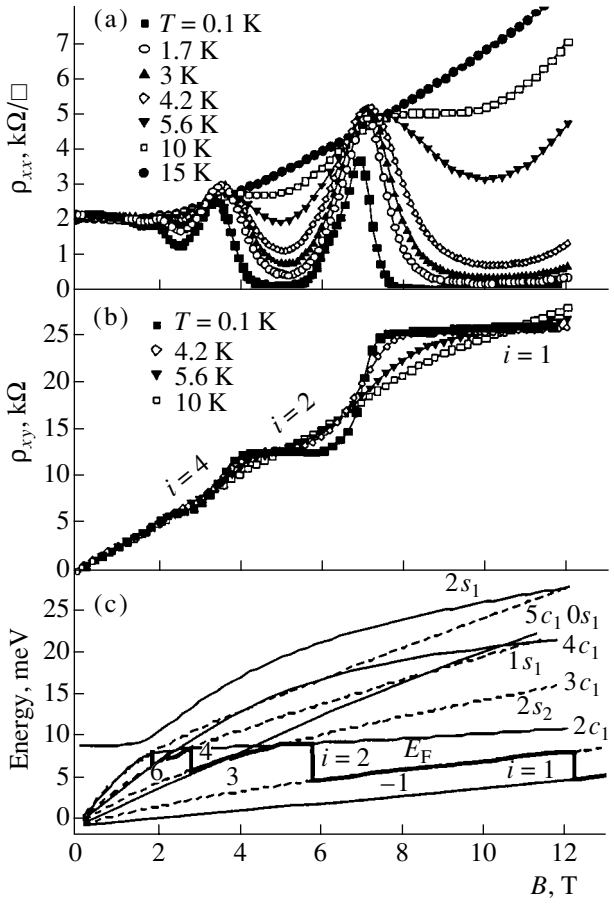

Fig. 2. (a) Longitudinal, ρ_{xx}, and (b) transverse, ρ_{xy}, resistivities vs. magnetic field for sample I; (c) calculated structure of Landau levels and the Fermi level shift in magnetic field for sample I with QW width $d \approx 200$ Å and splitting of light and heavy hole bands due to built-in uniaxial strain, $\delta = 8$ meV [15].

the temperature dependence of the conductivity σ_{xx} determined from the relation

$$\sigma_{xx} = \frac{\rho_{xx}}{\rho_{xx}^2 + \rho_{xy}^2} \qquad (10)$$

for fixed values of the magnetic field in the vicinity of $\nu = 1$ ($B_1 = 11.2$ T) is presented in Fig. 3. The dependences $\sigma_{xx}(T)$ obtained at fixed B near $\nu = 2$ ($B_2 = 5.6$ T) are similar.

The activation-type dependence of magnetoconductivity for the samples studied is observed in the temperature range $T = (3–15)$ K. Solid lines in Fig. 3 correspond to calculation by Eq. (3), with E_A and γ ($\sigma_c = 0.5e^2/h$) as fitting parameters. The deviation of experimental points from the calculated curves at $T < 3$ K is presumably due to transition to hopping conduction via localized states at the Fermi level, which commonly dominates at low enough temperatures. Figure 4 presents the activation energies found by means of fitting in relation to B (or the filling factor ν) for two samples.

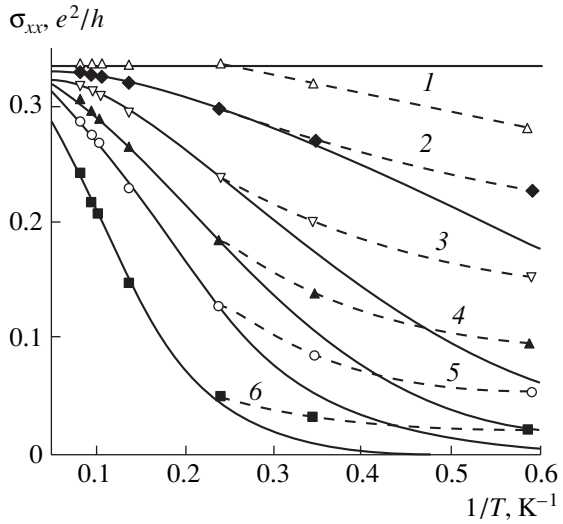

Fig. 3. Activation behavior of the conductivity tensor component σ_{xx} for sample I. *B*: (*1*) 8, (*2*) 8.2, (*3*) 8.5, (*4*) 8.8, (*5*) 9.2, and (*6*) 11.2 T. Solid curves: calculation.

4.1. Mobility Gaps

It can be seen from Fig. 4 that the activation energy reaches its maximum values $E_A^{\max}$ near integer filling factor $\nu = 1$, 2, or 4. The mobility gap estimated for the samples studied as $2E_A^{\max}$ is $W \simeq (2–2.5)$ meV for $\nu = 1$ and 2, and $W \simeq (0.5–1)$ meV for $\nu = 4$.

The W value is closely related to the energy gap between the neighboring Landau levels: $W \simeq |E_N - E_{N+1}|$ with an accuracy of about γ. For a simple parabolic band in GaAs/AlGaAs heterostructures [8, 11] or Si MOSFETs [8] with *n*-type conduction, the activation energy for integer ν virtually coincides with half the cyclotron energy: $E_A = \hbar\omega_c/2$, which assumes that the band of extended states is narrow enough. For our $Ge/Ge_{1-x}Si_x$ heterostructures with *p*-type conduction, determining the mobility gaps from the activation energy may serve as a method for reconstructing the spectrum of Landau levels in the valence band of Ge.

The combined action of quantum confinement and quantizing magnetic field on a fourfold degenerate (at $B = 0$) valence band of bulk Ge crystal gives rise to a complex spectrum of magnetic levels of a 2D hole gas [15]. An analytical solution is only possible in the weak-magnetic-field limit, when the energy of magnetic sublevels is much lower than the gap Δ_{12} between the first and second quantum confinement sublevels. In this case, the Landau levels of the ground confinement subband shift linearly with the magnetic field:

$$E^{\pm}(N) = \left\{(\gamma_1 + \gamma)\left(N \mp \frac{3}{2}\right) \pm \frac{3}{2}\varkappa\right\}\hbar\omega_0, \qquad (11a)$$

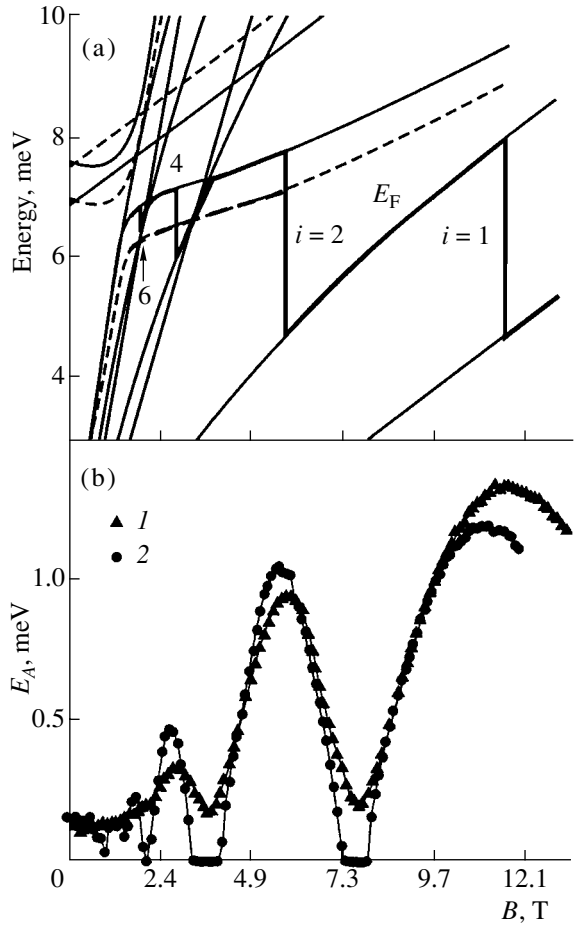

Fig. 4. (a) Calculated energy spectrum of Landau levels. Solid lines: sample II (d = 214 Å), dashed lines: sample I (d = 220 Å). (b): (*1*, *2*) activation energy vs. magnetic field for samples I and II.

where $N = -1, 0, 1\ldots$ for E^-; $N = 2, 3, 4\ldots$ for E^+; γ_1, γ and $\varkappa$ are the Luttinger parameters; and $\hbar\omega_0 = eB/m_0$, where m_0 is the free electron mass. Expression (11a) can be written in an equivalent form [18]:

$$E^{\pm}(L) = \left(L + \frac{1}{2}\right)\hbar\omega_c \pm g^*\mu_B B, \qquad (11b)$$

where $L = 0, 1, 2\ldots$ ($L = N + 1$ for E^- and $L = N - 1$ for E^+), $\hbar\omega_c = eB/m^*$, μ_B is the Bohr magneton, $m^* = m_0/(\gamma_1 + \gamma)$, and $g^* = 3\varkappa$. For Ge, $m^* = 0.054m_0$, $g^* = 10.2$, and the spin splitting is close to half the orbital splitting: $2g^*\mu_B B/\hbar\omega_c = 0.54$.

In a stronger magnetic field at $\hbar\omega_c \gtrsim \Delta_{12}$, the mixing of heavy and light hole states results in that the magnetic field dependence of the Landau levels becomes essentially nonlinear, which makes them nonequidistant and leads to the appearance of points of coincidental degeneracy (level crossover).

A typical pattern of the magnetic field dependence of Landau levels, calculated in [15] for the samples under study, is presented in Fig. 2c. The calculations were done in terms of the model of an infinitely deep square quantum well (QW), with the Luttinger Hamiltonian used for a band of symmetry Γ_8 in a magnetic field [19]. The magnetic levels in the quantum-confinement valence band form two independent sets denoted by symbols *c* and *s*. Here, we may draw an analogy with the 3D case, in which, at zero wave vector component k_H aligned with the magnetic field, levels also form two series, *a* and *b* [20]. However, since it is assumed *ab initio* in the 2D case that $k_H \neq 0$, which is necessary for establishing the boundary conditions along the magnetic field, there is no one-to-one correspondence between the sets *a* and *b*, on the one hand, and *c* and *s*, on the other. Only the lowest level (–1) has the same nature in 2D and 3D cases: *b*(–3/2) in terms of [20]. In the level designations in Fig. 2c, the digit ($N = -1, 0, 1\ldots$) before the letters *c* or *s* designates the Landau level number, and the digit ($n = 1, 2\ldots$) in the subscripts of *c* or *s*, the ordinal number of a quantum-confinement subband. Within one series (*c* or *s*), Landau levels with the same numbers *N*, belonging to different quantum-confinement subbands, are repulsed ($2s_1$ and $2s_2$ in Fig. 2c). The complication of the band structure arises from mixing of the heavy and light hole states, and also states from different quantum-confinement subbands, which occurs with increasing magnetic field. Therefore, crossover of levels belonging to the same subband occurs along with crossing of levels from different subbands.

As seen in Fig. 2c, drawing analogies with a simple parabolic band is difficult in this situation. It is not surprising, therefore, that the mobility gaps found in fields $B \simeq 10$ T are nearly an order of magnitude smaller than the formally calculated cyclotron energy $\hbar\omega_c \approx 20$ meV for $m_c = 0.054m_0$ at $B \simeq 10$ T. The relation $W \ll \hbar\omega_c$ is associated, first, with the sublinear dependence of the $2c_1$ level on *B* for $\nu = 1$ and, second, with the inclusion of the magnetic level $2s_2$ of the second quantum-confinement subband into the system of actual Landau levels across which the Fermi level moves (see Fig. 4a). Figure 4 presents in detail the results of the calculation of a system of actual Landau levels for each of the samples studied in comparison with the experimental $E_A(B)$ dependences. It is found that a relatively small (within 10%) correction of the nominally specified QW width d = 200 Å yields a precise quantitative description of the energy gaps *W* for each of the samples, W_1 and W_2 for the filling factors ν_1 and ν_2, respectively. It should be emphasized that even the observed difference between the W_1 and W_2 values, as well as the W_1/W_2 ratios for two samples with close parameters, I and II, can be described in terms of the proposed calculation model. It is the inclusion of the Landau levels of the second quantum-confinement subband into the system of actual levels that enables such a description. As seen from the scheme of quantized levels in Fig. 4a, a change in the W_1/W_2 ratio for sample I, compared with sample II, can be obtained at a certain depression of the levels in the second subband (decrease in Δ_{12}) because of an

increase in the QW width d. Owing to the strong sensitivity of the bottom of the second subband to the well width ($(\Delta_{12} \propto 1/d^2)$, the necessary corrections to d are very small: from 200 to 214 Å for sample II and from 200 to 220 Å for sample I.

4.2. Density of Localized States

Analysis of the $E_A(B)$ dependences can furnish information about the Fermi level position at a given magnetic field (filling factor), the value of the dE_F/dB ($dE_F/d\nu$) derivative, and, consequently, in accordance with (9), the density of states in the mobility gap. Figure 5 presents the density of localized states $g(E)$ in the vicinity of the filling factors $\nu = 1$ and $\nu = 2$ for one of the samples studied ($E = 0$ corresponds to the mid-distance between two neighboring Landau levels). It is seen that $g(E)$ depends on E only slightly for most of the energy interval between the Landau levels, and the "background" density of states g_c is (5–7) $\times 10^{10}$ cm^{-2} meV^{-1} for both $\nu = 1$ and $\nu = 2$. Thus, even in the middle of the mobility gap, the density of localized states is comparable with the density of states of a 2D hole gas in zero magnetic field. The density of states at $B = 0$ can be evaluated as $g_0 = m/\pi\hbar^2 = 4.4 \times 10^{10}$ cm^{-2} meV^{-1}; here we used the value of mass at the Fermi level, $m = 0.1m_0$, obtained from analysis of the Shubnikov–de Haas oscillations in the range of weak magnetic fields [16].

The presence of high, nearly energy-independent "background" density of states in the mobility gaps of a p-Ge/Ge$_{1-x}$Si$_x$ system with a complex valence band spectrum correlates qualitatively with earlier results for AlGaAs/GaAs [8, 11] and InGaAs/InP [13] heterostructures and n-Si MOSFETs [12]. As regards g_c, the values obtained here are nearly an order of magnitude higher than the corresponding densities of states in AlGaAs/GaAs [8] heterostructures with close values of effective mass and carrier density. This is undoubtedly a result of the fact that the mobility gaps W in p-type samples are narrow because of the complex valence band structure: in a given magnetic field, the same number of states n_B must be distributed within a significantly smaller energy interval.

Based on the empirical fact of relatively constant density of states, we can evaluate the number of localized states in the mobility gap W_i, i.e., in the range of filling factors from $(i - 1/2)$ to $(i + 1/2)$, as

$$n_{loc} = g_c W_i.$$

For the samples studied, we have $n_{loc} \approx (1–1.5) \times 10^{11}$ and $\approx (5–7) \times 10^{10}$ cm^{-2} for $i = 1$ and 2, respectively, which is comparable with the total number of states $n_B^{(i)} = eB_i/hc$ for $\nu = i$: $n_B^{(1)} \approx 2.5 \times 10^{11}$ cm^{-2} ($B_1 = 11.2$ T), and $n_B^{(2)} \approx 1.25 \times 10^{11}$ cm^{-2} ($B_2 = 5.5$ T). This result correlates with the concept that most of the electron states must be localized [4] in the QHE mode.

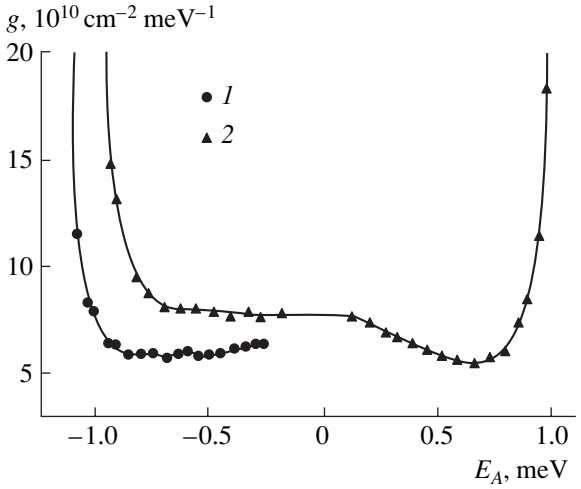

Fig. 5. Density of states vs. activation energy for sample II for filling factors ν: (*1*) 1 and (*2*) 2; $E = 0$ corresponds to the middle of the energy gap between the neighboring Landau levels.

Indeed, it is generally assumed that nearly all the states are localized by disorder in the QHE mode, with the exception of a small fraction of extended states (n_{ext}) near the center of each of the broadened Landau levels. The ratio between the fractions of localized and extended states can be evaluated empirically from the dependence $\rho_{xy}(B)$ at low temperatures T ($kT \ll W$, $kT \lesssim \gamma$) [17]:

$$\frac{n_{ext}}{n_{loc}} = \frac{\delta B}{\Delta B},$$

where ΔB and δB are the magnetic field intervals corresponding to the QHE plateau and to the transition between the two neighboring plateaus, respectively. In the samples studied, the ratio $\delta B/\Delta B$ was ≈0.1 for the 0^- peak at the lowest temperature $T = 0.1$ K; i.e., n_{ext}/n_{loc} is about 10% for $i = 1, 2$.

However, the somewhat paradoxical conclusion that nearly the entire density of states is virtually uniformly distributed within the mobility gap needs further explanation. It is noteworthy that this result is obtained only for the case when the Fermi level lies within the mobility gap.

4.3. Evaluation of Impurity Potential Parameters

In most studies devoted to the density of states in the QHE mode, attention was drawn to the impossibility of even a qualitative explanation of the obtained results in terms of the model of a uniform 2D system with short-range impurity potential. The point is that, in the quantum limit, the Landau level broadening Γ related to splitting of localized states by the short-range potential must be much less than the spacing between these levels, $\Gamma \ll W$. This strong inequality is certainly satisfied in the QHE mode, since the Shubnikov–de Haas oscil-

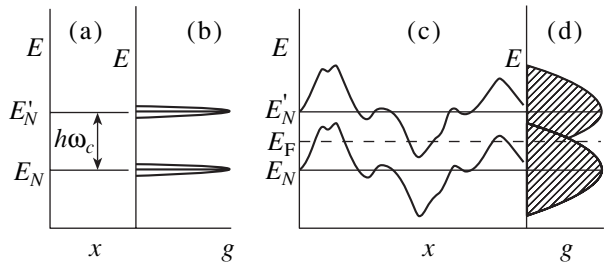

Fig. 6. (a) Coordinate dependence of the Landau level positions in a uniform medium, and (b) the corresponding energy dependence of the density of states, plotted with account of the collision broadening. (c) and (d): similar dependences for the case of long-range potential fluctuations. In (d), the range of localized states is shaded, the ranges of extended states are marked by bold lines.

lations, whose existence requires that at least the simple inequality $\Gamma < W$ be fulfilled, are clearly observed even at much lower fields $B \gtrsim 1$ T.

A reliable enough estimate of Γ can be obtained for the short-range impurity potential in the quantum limit:

$$\Gamma/W \approx (\mu B/c)^{-1/2}. \quad (12)$$

Using the experimental mobilities in a field $B = 10$ T for the samples studied, we obtain $W/\Gamma = (4–5)$. For a Gaussian shape of the density of states in the middle of the mobility gap, we have

$$g(W/2)/g_0 \propto \exp[-(W/2\Gamma)^2], \quad (13)$$

and $g(W/2)$ is 2–3 orders of magnitude smaller than the experimental g_c values.

However, the density-of-states pattern changes dramatically when the electron spectrum in a field of a random smooth potential is considered. The combination of long-range fluctuations of the impurity potential with the oscillatory dependence of the density of states on the Fermi level position (on filling factor) allows a clear physical interpretation of the observed type of density of states in the QHE mode. The idea behind this explanation was put forward by Shklovskiĭ and Efros [21] in their early work and was successfully developed further in a series of works by Efros *et al.* (see [22–24] and references therein). As shown in [21–24], the smooth long-range potential is formed owing to a random distribution of impurities in the selective doping range.

For impurity potentials $V(r)$ that are smooth on the magnetic length $l_B = (c\hbar/eB)^{1/2}$ scale, the localization in the QHE mode can be discussed in terms of the quasi-classical quantization and percolation theory (see, e.g., [25] and references therein]. Let the characteristic scale of the potential variation be $L_c \gg l_B$. In the quasi-classical approximation, the electron energy in a quantizing magnetic field can be written as

$$E_N(r_0) = (N + 1/2)\hbar\omega_c + V(r_0), \quad (14)$$

where r_0 is the coordinate of the oscillator center. Thus, the smooth potential lifts the degeneracy of states with respect to r_0, and the Landau level E_N in this approximation depends on spatial coordinates. Each Landau level is bent in space in accordance with the $V(r)$ dependence. Electron states with energy E lie on the contours of the random potential $V(r) = E$. These contours form closed trajectories corresponding to localized (within the whole sample) states for all the energies except the single energy $E = E_c^N$ for each Landau level, for which the relevant contours form an infinite cluster and percolation occurs through the random impurity potential.

It is evident that if the amplitude of the random potential $F \geq \hbar\omega_c$, there apparently exist states in between the Landau levels. In this case, the density of states integrated over the sample includes a set of extended states at $E = E_c^N$ and localized states at $E \neq E_c^N$, which is necessary for the QHE. However, the density of states remains ideal locally: the Landau level is not broadened by the smooth potential, being only bent, so that the neighboring Landau levels do not overlap at each point in space, which is also necessary for the QHE to be observed. Integrally, the role of nonoverlapping Landau levels is played by extremely narrow bands of extended states in the vicinity of the critical energy E_c^N for each of the levels (Fig. 6).

To evaluate the parameters L_c and F for our samples, we use the models proposed in [21–24]. Of the several models developed for the fluctuating impurity potential in selectively doped 2D systems, we chose the following.

(i) The model of 2D electron gas located in the $z = 0$ plane and surrounded by charged centers, which have the volume concentration N and are distributed randomly in the layer between the $z = b$ and $z = -b$ planes. For a thick layer $b \gg L$, the amplitude F of the random potential with variation scale L is [21]

$$F(L) = \beta\frac{e^2\sqrt{NL}}{\kappa}, \quad (15)$$

where β is a numerical coefficient ($\beta \approx 0.1$ [22]).

(ii) The same model with limited thickness of the impurity distribution, $b < L$, yields

$$F(L) = \beta\frac{e^2}{\kappa}\sqrt{\frac{N}{b}}\frac{L}{b}. \quad (16)$$

(iii) The model of a structure with a thick spacer, which was first developed in [22] (see also [23, 24] and references therein); i.e., a plane containing 2D electron gas and a plane with randomly distributed impurities

with surface concentration C, separated from the first plane by a distance d_s. In this case [23],

$$F(L) = \sqrt{2\pi}\frac{e^2\sqrt{C}}{\kappa}\sqrt{\ln\frac{L}{2d_s}}. \quad (17)$$

As seen from (15)–(17), in all the cases, the larger L, the higher is the amplitude of the random potential, and only screening may lead to a finite F value.

The optimal fluctuation size L_c is found from the conditions of screening of potential fluctuations via electron density redistribution. Our prime interest is the situation in the vicinity of integer filling factors. Completely filled (and, naturally, completely empty) Landau levels cannot take part in screening (at least, for weak electron–electron interaction [24, 26]), since spatial redistribution of electrons (holes) is impossible in this case. Therefore, only a small number $\delta n \ll n_B$ of carriers can be spatially redistributed in the vicinity of $\nu = i$, and we find ourselves in a situation of nonlinear screening in terms of Shklovskiĭ and Efros [27] ("threshold" screening in terms of [3]). At a precise equality $\nu = i$, the screening is due to the overlapping of the fluctuating potentials of two neighboring Landau levels; i.e., the amplitude of long-range fluctuations is on the order of the corresponding gap in the energy spectrum: $F \approx W$. The situation at $\nu = i$ strongly resembles the long-range potential screening for a completely compensated semiconductor (see [27], § 46).

For the structures we studied, $N \approx 10^{17}$ cm^{-3}, and the interimpurity distance ($N^{-1/3} \approx 200$ Å) is comparable with the 2D layer thickness $d \approx 200$ Å and with the thickness of the doped region of the sample, $d_a = 100$ Å. Therefore, the above-described models are applicable only as limiting cases.

The application of the models described in items 1 or 2 to the structures under study is justified by the fact that the nominal spacer thickness is 50 Å, which is less than the average interimpurity distance. For both cases (1 and 2), we have for the density of states in the middle of the mobility gap $W \approx 2$ meV [21]

$$g_c(W/2) = \frac{4\beta e^2 N}{\kappa W^2} \approx 7.2\times 10^{10}\ \text{cm}^{-2}\ \text{meV}^{-1}. \quad (18)$$

The optimal fluctuation size found from the condition $F \approx W$ is $L_c \approx 1000$ and 450 Å for cases 1 and 2, respectively. Since the effective thickness of the impurity layer is $b = d_a + d_s = 150$ Å, the use of model 2 for estimates is more reasonable.

Model 3, which has a thick spacer, is valid if d_s greatly exceeds both the thickness of the 2D layer and that of the doped region in a sample. This model, with $d_s = 300$ Å, was successfully used by Efros *et al.* [23] for a quantitative description of the experimental data obtained by Weiss *et al.* [8] for the density of states in GaAs/AlGaAs. If, in our case, we regard the distance between the centers of the 2D layer and the doped part of the barrier as the spacer, we obtain $d_s = 200$ Å, which is comparable with all the other dimensions, and we use model 3 at the limit of its applicability. For $W \approx 2$ meV and $C = Nd_a$, we have [23] (with an additional factor of 2, which accounts for doping of GeSi layers both above and below the given Ge layer)

$$g_c(W/2) \approx 2\frac{2}{7}\frac{\sqrt{C}}{Wd_s} = 4.6\times 10^{10}\ \text{cm}^{-2}\ \text{meV}^{-1}, \quad (19)$$
$$L_c \approx 400\ \text{Å}.$$

As seen, $g_c(W/2)$ estimates of a reasonable order of magnitude are yielded without any fitting parameters by both the model with limited spatial distribution of impurities ($d < L_c$) and that with a spacer (2D distribution of impurities). The estimated scale of fluctuations L_c = (400–500) Å, obtained using both the models, seems reliable enough. It is important that the characteristic scale of fluctuations noticeably exceeds the magnetic length ($l_B \approx 80$ Å at $B = 10$ T).

Thus, the observed density of states in the mobility gap is quite reasonably described in terms of the nonlinear screening model, when the density of screening electrons, δn, and, therefore, the Landau level broadening (integrated over the sample) depends on the filling factor. In particular, with the integer filling factor, δn is defined self-consistently by the degree of overlapping between the fluctuation potentials of the neighboring Landau levels. Consequently, the Landau levels are strongly broadened at $\nu = i$ by virtue of long-range potential fluctuations, and the density of states between the levels is high (integrated over the sample).

On the other hand, it is commonly believed that at half-integer filling, when the Fermi level lies in the range of extended states, long-range fluctuations are screened, the Landau levels are strongly narrowed (their width being on the order of the collision broadening $\hbar/\tau$), and the density of states in the mobility gap becomes exponentially small [3, 22, 23].

5. CONCLUSION

The energy spectrum of holes in a 2D Ge layer in a quantizing magnetic field has been reconstructed by analyzing the activation-type temperature dependence of the magnetoresistance in the range of QHE plateaus. The energy gaps W_1 between the Landau levels were evaluated, together with the density of localized states g_c in the mobility gaps, for integer filling factors $\nu = 1$ and 2. The obtained values $W_{1,2}$ = (2–2.5) meV are substantially less (5–10-fold) than those calculated for a simple parabolic band ($W = \hbar\omega_c$), with effective mass $m = 0.054m_0$ corresponding to the mass at the band bottom for a 2D Ge layer ($W_1 \approx 20$ meV, $W_2 \approx 10$ meV). The performed calculations of the valence band spectrum for a 2D Ge layer in a quantizing magnetic field demonstrated that both the comparatively low W values and their weak dependence on the filling factor arise from the sublinear dependence of the corresponding

Landau levels on the magnetic field. The observed complex pattern of Landau levels is a consequence of mixing between light and heavy hole states under quantum confinement conditions.

The densities of states in the mobility gaps, g_c = (5–7) × 10^{10} cm^{-2} meV^{-1}, obtained for $\nu = 1$ and 2 are nearly an order of magnitude higher than those obtained earlier for *n*-type samples with about the same carrier density. We believe that this is also a consequence of the narrow mobility gaps in *p*-type samples, which result from the complex valence band structure.

Analysis of the background density of states in the middle of the mobility gap in terms of the currently available models of impurity potential fluctuations allowed us to evaluate the scale of spatial fluctuations (nonlinear screening length). The obtained L_c = (400–500) Å greatly exceeds the magnetic length in the QHE mode ($B > 5$ T), which confirms the long-range nature of the impurity potential in the *p*-Ge/$Ge_{1-x}Si_x$ systems under study.

ACKNOWLEDGMENTS

This study was supported by the Russian Foundation for Basic Research (project nos. 99-02-16256, 01-02-17685, and 01-02-06131) and by a grant from the Ural Division of the Russian Academy of Sciences.

REFERENCES

1. R. B. Laughlin, Phys. Rev. B **23**, 5632 (1981).
2. B. I. Halperin, Phys. Rev. B **25**, 2185 (1982).
3. I. V. Kukushkin, S. V. Meshkov, and V. B. Timofeev, Usp. Fiz. Nauk **155**, 219 (1988) [Sov. Phys. Usp. **31**, 511 (1988)].
4. *The Quantum Hall Effect*, Ed. by R. Prange and S. Girvin (Springer-Verlag, New York, 1987; Mir, Moscow, 1989).
5. N. F. Mott and E. A. Davis, *Electronic Processes in Non-Crystalline Materials* (Clarendon, Oxford, 1971; Mir, Moscow, 1974).
6. S. Das Sarma and D. Liu, Phys. Rev. B **48**, 9166 (1993).
7. Y. Katayama, D. C. Tsui, and M. Shayegan, Phys. Rev. B **49**, 7400 (1994).
8. D. Weiss, E. Stahl, G. Weimann, *et al.*, Surf. Sci. **170**, 285 (1986).
9. A. Usher, R. J. Nicholas, J. J. Harris, and C. T. Foxon, Phys. Rev. B **41**, 1129 (1990).
10. R. G. Clark, Phys. Scr. **39**, 45 (1991).
11. P. Svoboda, G. Natchtwei, G. Breitlow, *et al.*, cond-mat/9612053.
12. M. G. Gavrilov and I. V. Kukushkin, Pis'ma Zh. Éksp. Teor. Fiz. **43**, 79 (1986) [JETP Lett. **43**, 103 (1986)].
13. H. P. Wei, A. M. Chang, D. C. Tsui, and M. Razeghi, Phys. Rev. B **32**, 7016 (1985).
14. V. A. Aronzon, N. K. Chumakov, J. Leotin, *et al.*, Superlattices Microstruct. **13**, 159 (1993).
15. Yu. G. Arapov, N. A. Gorodilov, M. V. Yakunin, *et al.*, Pis'ma Zh. Éksp. Teor. Fiz. **59**, 247 (1994) [JETP Lett. **59**, 268 (1994)].
16. Yu. G. Arapov, N. A. Gorodilov, O. A. Kuznetsov, *et al.*, Fiz. Tekh. Poluprovodn. (St. Petersburg) **27**, 1165 (1993) [Semiconductors **27**, 642 (1993)].
17. Yu. G. Arapov, N. A. Gorodilov, O. A. Kuznetsov, *et al.*, Fiz. Tekh. Poluprovodn. (St. Petersburg) **31**, 273 (1997) [Semiconductors **31**, 222 (1997)].
18. R. W. Martin, R. J. Warburton, R. G. Nicolas, *et al.*, in *Proceedings of he XX International Conference on Physics of Semiconductors, Thessaloniki, 1990*, p. 909.
19. J. M. Luttinger, Phys. Rev. **102**, 1030 (1956).
20. Y. Guldner, C. Rigaux, M. Grynberg, and A. Mycielski, Phys. Rev. B **8**, 3875 (1973).
21. B. I. Shklovskiĭ and A. L. Éfros, Pis'ma Zh. Éksp. Teor. Fiz. **44**, 520 (1986) [JETP Lett. **44**, 669 (1986)].
22. A. L. Efros, Solid State Commun. **70**, 253 (1989).
23. A. L. Efros, F. G. Pikus, and V. G. Burnett, Phys. Rev. B **47**, 2233 (1993).
24. A. L. Efros, cond-mat/9905368.
25. B. Huckestein, Rev. Mod. Phys. **67**, 357 (1995).
26. N. R. Cooper and J. T. Chalker, Phys. Rev. B **48**, 4530 (1993).
27. B. I. Shklovskiĭ and A. L. Efros, *Electronic Properties of Doped Semiconductors* (Nauka, Moscow, 1979; Springer-Verlag, New York, 1984).

Translated by D. Mashovets

Semiconductors, Vol. 36, No. 5, 2002, pp. 527–534. Translated from Fizika i Tekhnika Poluprovodnikov, Vol. 36, No. 5, 2002, pp. 558–564.

LOW-DIMENSIONAL SYSTEMS

Miniband Spectra of $(AlAs)_M(GaAs)_N(111)$ Superlattices

G. F. Karavaev, V. N. Chernyshov, and R. M. Egunov

Siberian Institute of Physics and Technology, Tomsk State University, Tomsk, 634050 Russia

e-mail: karavaev@elefot.tsu.ru

Submitted May 8, 2001; accepted for publication October 30, 2001

Abstract—Electron states in the conduction band of (111)-oriented $(AlAs)_M(GaAs)_N$ superlattices (SLs) with $M \geq N$ and $N < 10$ are considered. The properties of such SLs are mainly governed by the *X*-valley electrons in AlAs and the *L*-valley electrons in GaAs. The calculations are carried out using a previously developed model for the envelope-function matching at heterointerfaces. Miniband spectra, symmetry, and localization of the wave functions, as well as the probabilities of interminiband infrared absorption, are calculated and analyzed. It is shown that the absorption probabilities may be high not only for a light wave polarized along the SL axis, but also for a light wave incident normally to the surface of the structure. It is found that, for analysis of infrared absorption, it is important to take into account the contribution to the wave functions from X_5 valence-band states. © *2002 MAIK "Nauka/Interperiodica".*

1. INTRODUCTION

The energy spectra of (111)-oriented $(AlAs)_M(GaAs)_N$ superlattices (SLs) were previously studied on the basis of the empirical pseudopotential method [1, 2]. It should be noted that direct pseudopotential calculations are rather cumbersome and, therefore, have not received wide acceptance. In [2], only short-period SLs were considered; in [1], only the position of the two lowest levels in the conduction band (of types Γ and *X*, *L*) and the highest Γ-type state in the valence band were determined in relation to *M* and *N*, and the contribution of Γ, *X* and, *L* valleys to the corresponding states was analyzed. The main problem in the treatment of SL states is related to the analysis of electron scattering at heterointerfaces, while the electron behavior within the layers can be described on the basis of available bulk models. In previous papers, we developed simplified models describing Γ–*L* and *X*–*L* scattering of the conduction-band electrons by the AlAs/GaAs(111) heterointefrace [3, 4]. These models make it possible to analyze electronic characteristics of different kinds of nanostructures based on AlAs/GaAs(111).

In $(AlAs)_M(GaAs)_N(111)$ SLs, the properties of electrons in the conduction band are mostly determined by the *X*-, Γ-, and *L*-valley states in GaAs and AlAs. The values of the energy spacing $\delta_{\Gamma X}$ between the X_1 level in the AlAs conduction band and the Γ_1 level in GaAs reported so far vary from ~0.12 to ~0.3 eV (see, e.g., [1, 5]). The contributions of Γ-, *X*-, and *L*-valley states to the formation of the lower part of the miniband spectrum depend on this quantity and on the number of GaAs monolayers *N*. From pseudopotential calculations carried out for the same potentials as in [4] (with $\delta_{\Gamma X} = 0.208$ eV), we found that, for $N < 9$, the resonance energies corresponding to Γ states are higher than the energies of X_1 states in AlAs and, for $N = 9$, the Γ level is below the X_1 level in AlAs by ~0.01 eV. This means that, for $N < 10$, it is very important to take *X*–*L* scattering into account. Note that Γ–*L* and *X*–*L* electron-scattering processes at the (111)-oriented heterointerface occur at different values of the in-plane components of the wavevector. In this paper, we consider the contribution of *X* and *L* valleys of AlAs and GaAs to the miniband spectrum in the conduction band for $M \geq N$, $N < 10$.

2. CALCULATION METHOD

Let us consider a solid-state system with N_0 heterointerfaces located in the planes $z' = z'_n$ (we choose the axis *z*' along the heterostructure growth direction). In the structures with plane heterointerfaces, the wavevector component $\mathbf{k}_\parallel$ parallel to the interface is conserved. In the piecewise-continuous-potential approximation (with the potential discontinuity at the interfaces), the general solution Ψ^n to the Schrödinger equation in the *n*th layer for some energy *E* and wavevector $\mathbf{k}_\parallel$ can be expressed as

$$\Psi^n = \sum_\nu A_\nu^n \Psi_{\mathbf{k}_\nu}^n + \sum_\mu B_\mu^n \Psi_{\mathbf{k}_\mu}^n, \qquad (1)$$

where $\Psi_{\mathbf{k}_\mu}^n$ and $\Psi_{\mathbf{k}_\nu}^n$ are particular solutions for given $\mathbf{k}_\parallel$ and *E*. Here, $k_{\nu(\mu)} = \mathbf{k}_\parallel + \mathbf{k}_{\perp\nu(\mu)}^n$ ($\mathbf{k}_{\perp\nu(\mu)}^n$ is the wavevector component perpendicular to the interface in the *n*th layer). Subscript ν corresponds to the so-called "forward" states, and subscript μ, to "backward" states. The states are classified into "forward" and "backward" ones in the same way as in [6–8]. Coefficients A_ν^n and B_ν^n are determined from the wave-function matching conditions at the interfaces combined either with the

conditions at infinity (for finite systems) or by the Bloch conditions (for SLs).

Problems of this kind are commonly solved using the scattering-matrix formalism [6–8]. The scattering matrix $S(N_0)$ relates the states corresponding to a particle incident on a system with N_0 interfaces (incoming states) to the states corresponding to a particle scattered by the system (outgoing states):

$$\begin{pmatrix} A^{N_0+1} \\ B^1 \end{pmatrix} = S(N_0)\begin{pmatrix} A^1 \\ B^{N_0+1} \end{pmatrix}, \quad (2)$$

where A^n and B^n are the column vectors with the components A^n_ν and B^n_μ, respectively.

The scattering matrix contains complete information about the system. Once this matrix is calculated, one can solve various quantum-mechanical problems, in particular, determine the electron states in quantum wells (QWs) and SLs. To determine the electron spectrum in a QW (the second layer), one needs to set $A^1 = B^3 = 0$; this condition means that the incoming states (which describe particles incident on the system from the first and third layers) do not contribute to the wave function. Then, the QW spectrum $\varepsilon_j(\mathbf{k}_\parallel)$ is determined from the condition for compatibility for the equation set (2):

$$\det(S^{-1}(2)) = 0. \quad (3)$$

Considering an SL whose period consists of layers nos. 1 and 2 (the first and the third layers being composed of the same material), one can, using the Bloch theorem, demonstrate that the electron states are determined by the following set of equations [9]:

$$[S(2) - P]\begin{pmatrix} A^1 \\ B^3 \end{pmatrix} = 0, \quad (4)$$

where the matrix P has the following form:

$$P = \begin{pmatrix} P_{11} & 0 \\ 0 & P_{22} \end{pmatrix},$$

$$(P_{11})_{\nu\nu'} = \delta_{\nu\nu'}\exp[-i(k^1_{\perp\nu} - s)d], \quad (5)$$

$$(P_{22})_{\mu\mu'} = \delta_{\mu\mu'}\exp[i(k^1_{\perp\mu} - s)d].$$

Here, d is the z' component of the basic translation vector of the SL and s is the z' component of the SL-state wavevector. The electron spectrum of the SL is determined from the compatibility condition for the equation set (4).

We calculated the QW and SL energy spectra using (3) and (4), respectively, and found that the results are in good agreement with the calculations performed in terms of the envelope-function approximation considered below.

In this study, we use a simplified model [4] describing the states in GaAs/AlAs(111) heterostructures. Let us summarize briefly the principles this model is based on. The general solution to Eq. (1) can be expressed as

$$\Psi^n = \exp(i\mathbf{q}_\parallel\boldsymbol{\rho})\sum_m F^n_m(z')|K^n_{\nu_0 m}\rangle. \quad (6)$$

Here, $\mathbf{q}_{\nu(\mu)} = \mathbf{k}_{\nu(\mu)} - \mathbf{k}_{\nu_0}$, $\boldsymbol{\rho}$ is the two-dimensional radius vector in the plane of the interface, and $|K^n_{\nu_0 m}\rangle$ is the set of Bloch functions corresponding to the wavevector $\mathbf{k}_{\nu_0}$. It is convenient to choose the points $\mathbf{k}_{\nu_0}$ at the bottom of the valleys that are important for the specific problem under consideration. The functions $F^n_m(z')$ have a physical meaning of the envelope wave functions. They can be expressed as

$$F^n_m(z') = \sum_\nu A^n_\nu D^n_m(\mathbf{k}_\nu)\exp(iq_{\perp\nu}z') + \sum_\mu B^n_\mu D^n_m(\mathbf{k}_\mu)\exp(iq_{\perp\mu}z'). \quad (7)$$

The coefficients $D^n_m(\mathbf{k}_{\nu(\mu)})$ in this expansion are determined from the set of algebraic equations obtained upon substitution, for a given $\mathbf{k}_{\nu_0}$, of particular solutions $\sim\exp(iq_\perp z)$ into the conventional equations of the **kp** method.

According to [4], the matching conditions for the envelope functions at heterointerface $z' = z'_n$ (the interface between the nth and $(n+1)$th layers on the left- and right-hand sides, respectively) has the following form:

$$F^n(z'_n) = T(z'_n)F^{n+1}(z'_n), \quad T(z'_n) = \Phi^n I(z'_n)(\Phi^{n+1})^{-1}. \quad (8)$$

Here, $I(z'_n)$ ($n = 1, 2, \ldots N_0$) is the matching matrix for the functions (1) at the nth heterointerface; $F(z')$ is a column vector with the components $F_m(z')$ and $F'_m(z')$ (F'_m is the derivative with respect to z'); and Φ is a matrix with elements equal to $D_m(\mathbf{k}_\gamma)\exp(iq_{\perp\gamma}z')$ and $iq_{\perp\gamma}D_m(\mathbf{k}_\gamma)\exp(iq_{\perp\gamma}z')$ (where $\gamma = \nu, \mu$). The order of the square matrices I, Φ, and T has to coincide with the total number of arbitrary constants A_ν, B_μ in Eq. (1), and, thus, the number of the valleys taken into account in the matching equation is two times less. In each specific case, these numbers are determined by the problem under consideration.

It has already been noted that X–L scattering is important in the systems we are concerned with in this study. The points $\mathbf{k}_X = (00\bar{1})2\pi/a$ and $\mathbf{k}_L = (11\bar{1})\pi/a$ (where a is the lattice constant) of the bulk-crystal Brillouin zone are mapped onto the same point of the surface Brillouin zone, which makes X–L scattering at the interfaces possible. We found that, for the problem considered, a three-valley description of electron scattering

at the heterointerface is sufficient. X_1, X_3, and L_1 valleys of the conduction band, related to $\mathbf{k}_X$ and $\mathbf{k}_L$ points, should be taken into account. In this approximation, the order of the envelope-function-matching matrix is 6×6. In contrast to $I(z_n')$, the matrices $T(z_n')$ are virtually independent of the energy and $\mathbf{k}_\parallel$. To emphasize that the matching conditions (8) do not depend upon which order (on the left-hand or on the right-hand side of the interface) the layers of AlAs (no. 1) and GaAs (no. 2) are arranged in, we represent these conditions in a symmetric form:

$$T_1 F^1 = T_2 F^2, \tag{9}$$

where the matrix elements of T_k ($k = 1, 2$) are given in [4].

3. ELECTRON STATES IN $(AlAs)_M(GaAs)_N(111)$ SUPERLATTICES

Next, we consider electron states in $(AlAs)_M(GaAs)_N(111)$ SLs. Let us assume that $(AlAs)_M$ forms layer no. 1 of thickness d_1 and $(GaAs)_N$ forms layer no. 2 of thickness d_2. The SL period along the z' axis equals $d = d_1 = d_2$. The shape of the SL unit cell depends on whether the total number of monolayers across the SL period $N + M$ is a multiple of 3 or not. If it is, there exists a direct-lattice vector (the SL period) collinear with the z'-axis. If it is not, the true SL period is determined by a vector which has a large component (equal to d) along the z'-axis and a small component in the perpendicular direction. This distinction results in different shapes of the Brillouin zone of the corresponding SLs. The Brillouin zones for these two cases can be found in [10]. They were also presented in [1], and we reproduce them (with minor corrections) in Fig. 1. If the total number of monolayers across the SL period $N + M$ is even, the X and L points of the bulk Brillouin zone are folded into the same point of the SL Brillouin zone (points D or M in Fig. 1). If $N + M$ is odd, X and L are folded into different points of the SL Brillouin zone (D and A or M and L in Fig. 1). It has already been noted that Γ–L and X–L scattering occurs at different points in the Brillouin zone. Γ–L interaction is significant along the line ΓA (or ΓZ), and X–L interaction, along $M\bar{L}$ (or DA).

When solving the Schrödinger equation in each layer, one may consider the states related to the points $\mathbf{k}_X$ and $\mathbf{k}_L$ separately. The fact that only the contribution

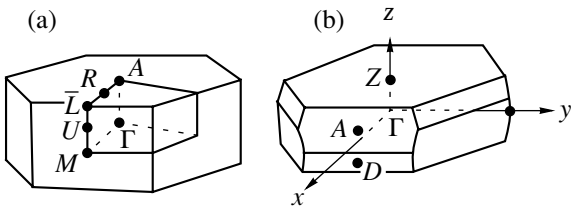

Fig. 1. The Brillouin zones of $(AlAs)_M(GaAs)_N(111)$ SLs for the two cases: (a) $(M + N)/3$ is integer and (b) $(M + N)/3$ is noninteger.

of six terms (connected to the three valleys X_3, X_1, and L_1) is taken into account in the matching conditions for the sought-for wave function does not mean, however, that only three terms should appear in the expansion (6); the reason is that the functions $\Psi^n_{\mathbf{k}_{v(\mu)}}$ and $|K^n_{v_0 m}\rangle$ are related to different energies (and different wavenumbers $\mathbf{k}_{v(\mu)}$). More than three terms may appear in expression (6), but only three envelope functions can be considered as independent and should be taken into account in the derivation of the envelope-function matching conditions; the remaining envelope functions can be expressed in terms of these three functions. Consideration of the remaining contributions is necessary to determine the energy spectrum and the wave functions more precisely.

In the vicinity of the point $\mathbf{k}_X$, in expression (6) we retain the functions corresponding to the X_3 and X_1 states from the conduction band and the X_{5x} and X_{5y} states from the valence band. In the vicinity of the point $\mathbf{k}_L$, we retain only three functions corresponding to the states L_1 from the conduction band and the two states of type L_3, nearest in energy, from the valence and the conduction bands. Thus, we express the sought-for wave function (6) (for $\mathbf{q}_\parallel = 0$) as

$$\begin{aligned}\Psi = {} & F_{X_3}|X_3\rangle + F_{X_1}|X_1\rangle + F_{X_{5x}}|X_{5x}\rangle + F_{X_{5y}}|X_{5y}\rangle \\ & + F_{L_1}|L_1\rangle + F_{L_{3c}}|L_3^c\rangle + F_{L_{3v}}|L_3^v\rangle.\end{aligned} \tag{10}$$

Within each layer, the envelope functions satisfy a coupled set of ordinary differential equations with constant coefficients. A particular solution to this set is sought for in the form of the column vector $D \propto \exp(iq_\perp z')$. After this substitution, we obtain a set of algebraic equations

$$\begin{pmatrix} E_{X_3} + E_0 w^2 - E & -iE_0 R_1^X w & iE_0 R_3^X w & iE_0 R_3^X w \\ iE_0 R_1^X w & E_{X_1} + E_0 w^2 - E & iE_0 R_2^X w & iE_0 R_2^X w \\ -iE_0 R_3^X w & -iE_0 R_2^X w & E_{X_5} + E_0 w^2 - E & 0 \\ -iE_0 R_3^X w & -iE_0 R_2^X w & 0 & E_{X_5} + E_0 w^2 - E \end{pmatrix} \begin{pmatrix} D_{X_3} \\ D_{X_1} \\ D_{X_{5x}} \\ D_{X_{5y}} \end{pmatrix} = 0 \tag{11}$$

Table 1. AlAs and GaAs band energies at the *X* and *L* points

Semiconductor	X_1	X_3	X_5	L_1	L_3^v	L_3^c
AlAs	0.2082	1.1830	–4.2429	0.8617	–2.8814	3.0654
GaAs	0.4688	0.9068	–3.8421	0.2908	–2.4515	3.3600

Note: The energies are given in eV.

Table 2. Constants appearing in Eqs. (11) and (12)

Semiconductor	R_1^X	R_2^X	R_3^X	R_1^L	R_2^L	R_3^L
AlAs	1.3308	6.0788	6.6154	0.1653	12.0022	8.8785
GaAs	1.4124	6.1004	6.5499	0.2593	11.9609	8.9620

for *X*-type envelope functions and

$$\begin{pmatrix} E_{L_1} + E_0 w^2 - E & iE_0 R_1^L w & -iE_0 R_2^L w \\ -iE_0 R_1^L w & E_{L_3^c} + E_0 w^2 - E & iE_0 R_3^L w \\ iE_0 R_2^L w & -iE_0 R_3^L w & E_{L_3^v} + E_0 w^2 - E \end{pmatrix} \begin{pmatrix} D_{L_1} \\ D_{L_3^c} \\ D_{L_3^v} \end{pmatrix} = 0 \qquad (12)$$

for *L*-type envelope functions. Here, $w = q_\perp a$, $E_0 = \hbar^2/2m_0a^2$ ($\hbar$ is Planck's constant, and m_0 is the free-electron mass), and other constants are listed in Tables 1 and 2.

From the conditions of compatibility for the sets of algebraic equations (11) and (12), the roots $w_j(E)$ are found. Among the roots, only those satisfying the conditions of applicability of Eqs. (11) and (12) are taken into account. There are four such roots if we consider the *X*-type envelope functions and two in the case of *L*-type functions. The values of $w_j(E)$ obtained in this way are very close to those determined from the calculation of the complex band structure by the pseudopotential method. Next, the general solution is written as a linear combination of exponential particular solutions. There will be a total of four arbitrary coefficients for the *X*-type envelope functions and two for *L*-type functions. Thus, the solution in each layer depends upon six arbitrary coefficients. To simplify the calculations, we locate the coordinate origin along the *z*'-axis in each layer in its midplane. With this choice of coordinate system and layer numbering adopted, the six envelope-function matching conditions at each heterointerface have the following form:

$$\begin{aligned} T_1 F^1\left(\frac{d_1}{2}\right) &= T_2 F^2\left(-\frac{d_2}{2}\right); \\ T_1 U(N) F^3\left(-\frac{d_1}{2}\right) &= T_2 U(N) F^2\left(\frac{d_2}{2}\right). \end{aligned} \qquad (13)$$

Here, $F^i(z')$ is a column $\{F_{X_3}(z'),\ F_{X_1}(z'),\ F'_{X_3}(z'),\ F'_{X_1}(z'),\ F'_{L_1}(z'),\ F'_{L_1}(z')\}$ ($i = 1, 2, 3$ is the number of the layer). $U(N)$ is a diagonal matrix of the sixth order that differs from a unit matrix by the last two elements on its main diagonal, which are equal to $(-1)^N$ because the Bloch functions of types X_j and L_j have different periods. To determine all of the envelope functions, i.e., to find 18 coefficients (6 in each layer), we need to impose six additional conditions. For an infinite SL, which we are concerned with, the Bloch theorem yields these conditions: upon a shift in space by an integer vector of the SL (which is mostly a shift along the growth axis by the SL period $d = d_1 + d_2$), the solution should change by the phase factor. This can be written as

$$F^1\left(-\frac{d_1}{2}\right) = e^{-iQd} U(M+N) F^3\left(-\frac{d_1}{2}\right). \qquad (14)$$

Here, Q is the component of the SL-state wavevector along the (111) direction (along the lines $M\bar{L}$ or DA) measured from point M (or D), which the point $X = (00\bar{1})2\pi/a$ is folded into. Conditions (13) combined with (14) form a closed set of linear equations for the coefficients in the expansion of the general solution in particular ones.

To obtain a numerical solution of the problem, for each chosen energy E we need to solve the sets of Eqs. (11)–(14) simultaneously, using the aforementioned scattering-matrix method. A set of six equations,

similar to (4), was reduced to the form that accounts for the specific choice of the coordinate system in each layer. In this case, the expressions for matrices $S(2)$ and P have only minor differences (apart from the matrix order) from those given by (4) and (5). The condition for compatibility of Eqs. (11)–(14) in the form $\det(S(2) - P) = 0$ defines the spectrum of allowed energies. From the solution of Eq. (4) supplemented by (13), coefficients A and B for each layer are determined, then the envelope functions (7) are obtained and the general solution in the form (10) is found.

4. ANALYSIS OF THE SPECTRUM AND THE WAVE FUNCTIONS

Calculations were performed for the structures $(AlAs)_M(GaAs)_N$ (hereafter denoted by (M, N)) with $N = 7$–9 and $M = 7$–11. It should be noted that the energy position of the minibands correlates well with the levels in the corresponding QWs. In Figs. 2 and 3, we plot the energy spectra of (9, 9) and (7, 7) SLs, as illustrations for the two radically distinct cases. The spectrum of the (8, 8) SL is similar to the (7, 7) spectrum, and all others are similar to (9, 9); the only difference is in the values of the energies. The energies of $Q = 0$ levels in the first two minibands and the parameters characterizing the origin of each level are summarized in Table 3. The first and the second levels, whose wave functions mainly originate from the X_1-valley states in AlAs, shift downwards in energy with an increase in the AlAs layer thickness. The energy of the third level, which mainly originates from the L_1-valley states in GaAs, decreases with an increase in the GaAs layer thickness; thus, it is this valley that is responsible for the second miniband in the (8, 9) SL. In addition to the energy level position at $Q = 0$, there is a difference in the slope of the third miniband. This is related to the evenness of the number of monolayers across the SL period (recall that the X and L points are folded into the same point of the SL Brillouin zone for $N + M$ even and into different points for $N + M$ odd). In the (7, 7) SL, the miniband energy dependence on Q is not monotonic. This is related to the fact that X_1 and L_1 minibands will cross each other if the X–L mixing at the interface is disregarded (dashed lines). With the mixing taken into account, the crossing is avoided and the minibands assume the shape shown in Fig. 3.

Figure 4 represents the net electron density averaged over bulk-crystal unit cells (electron density calculated using envelope functions) for the two lowest levels at $Q = 0$ in the (9, 9) SL. One can see that the electron density is mainly concentrated in the AlAs layer. Similar behavior is obtained for most of the other structures examined, while in the (7, 7) SL the electron density is localized within the AlAs layer for the first level and within the GaAs layer for the second. At the interface between the layers, there is a minor discontinuity in the averaged electron density. This does not mean that the current is discontinuous at the interface: the current

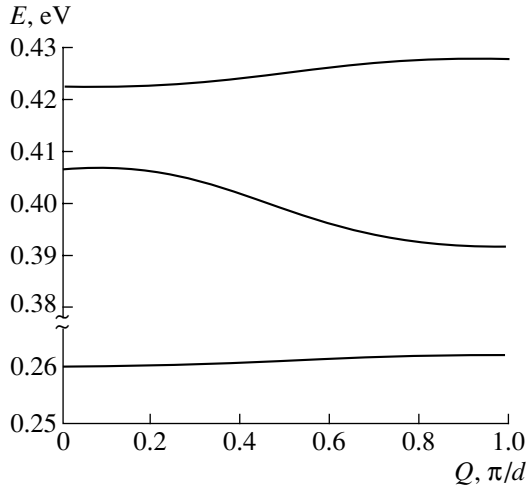

Fig. 2. The spectrum of the three lowest minibands in the $(AlAs)_9(GaAs)_9(111)$ SL.

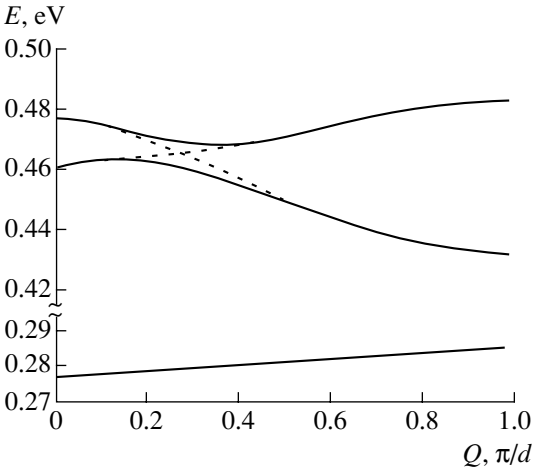

Fig. 3. The spectrum of the three lowest minibands in the $(AlAs)_7(GaAs)_7(111)$ SL.

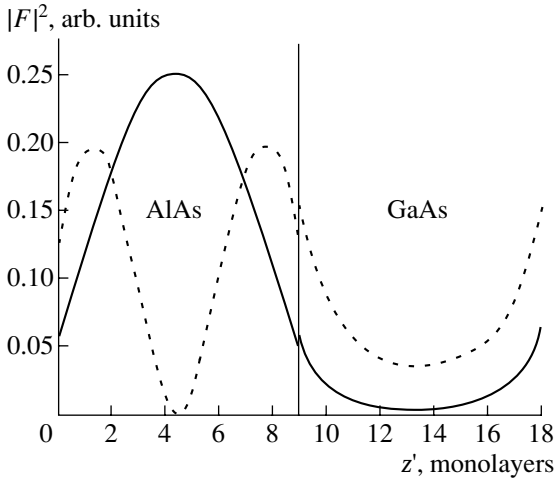

Fig. 4. The distribution of the net electron density $|F|^2$ over the period of the $(AlAs)_9(GaAs)_9(111)$ SL. The solid line corresponds to the first miniband and the dashed line, to the second.

Table 3. Energies of the two lowest levels at $Q = 0$ and the percent contribution of different valleys to the net electron density of the corresponding states

(*M*, *N*)	*E*, eV	Layer	X_3	X_1	L_1	(*M*, *N*)	*E*, eV	Layer	X_3	X_1	L_1
(9, 9)	0.260	AlAs	0.3	90.7	0.0	(7, 8)	0.278	AlAs	0.4	85.7	0.0
		GaAs	0.4	8.0	0.0			GaAs	0.5	12.7	0.1
	0.406	AlAs	1.9	61.4	0.9		0.455	AlAs	0.1	2.3	6.7
		GaAs	0.9	20.2	13.1			GaAs	0.1	1.3	89.5
(8, 8)	0.268	AlAs	0.3	88.7	0.0	(10, 9)	2.254	AlAs	0.3	92.4	0.0
		GaAs	0.5	9.9	0.1			GaAs	0.3	6.5	0.0
	0.437	AlAs	2.8	67.9	0.0		0.383	AlAs	1.9	75.1	0.1
		GaAs	1.4	25.6	0.3			GaAs	0.8	18.4	2.0
(7, 7)	0.277	AlAs	0.4	85.4	0.0	(10, 8)	0.253	AlAs	0.3	92.6	0.0
		GaAs	0.5	13.2	0.0			GaAs	0.3	6.3	0.1
	0.462	AlAs	0.0	0.3	14.9		0.386	AlAs	2.1	78.8	0.0
		GaAs	0.0	0.0	84.7			GaAs	0.9	16.4	0.0
(9, 8)	0.260	AlAs	0.3	90.9	0.0	(10, 7)	0.253	AlAs	0.3	92.4	0.0
		GaAs	0.4	7.8	0.1			GaAs	0.3	6.6	0.0
	0.409	AlAs	2.4	74.3	0.0		0.389	AlAs	2.2	79.5	0.0
		GaAs	1.1	20.3	0.1			GaAs	0.9	14.8	0.7
(8, 7)	0.267	AlAs	0.3	88.4	0.0	(11, 9)	0.249	AlAs	0.3	93.7	0.0
		GaAs	0.4	10.3	0.0			GaAs	0.3	5.3	0.0
	0.442	AlAs	2.8	66.0	0.3		0.364	AlAs	1.7	79.7	0.0
		GaAs	1.6	22.2	5.1			GaAs	0.7	15.5	0.9
(8, 9)	0.269	AlAs	0.3	88.4	0.0	(11, 8)	0.250	AlAs	0.2	93.8	0.0
		GaAs	0.5	10.1	0.1			GaAs	0.3	5.2	0.0
	0.430	AlAs	1.0	26.7	3.6		0.354	AlAs	1.8	82.2	0.0
		GaAs	0.5	12.0	55.5			GaAs	0.7	13.6	0.0

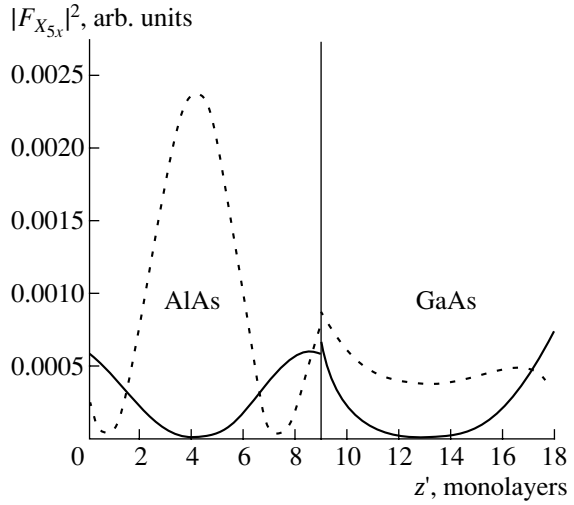

Fig. 5. The distribution of the partial electron density $|F_{X_{5x}}|^2$ over the period of the $(AlAs)_9(GaAs)_9(111)$ SL. The solid line corresponds to the first miniband and the dashed line, to the second.

(which, certainly, satisfies the continuity condition) is determined by exact wave functions (6), rather than by the envelope functions. Discontinuity of the envelope functions is due to the difference between the Bloch functions in AlAs and GaAs. Analysis of the partial contributions to the electron density in these structures indicates that, although the lowest energy minibands are mainly formed by X_1 states in AlAs, contributions of X_1 and L_1 states in GaAs are also significant. In the second level of the (7, 7) structure, the electron density is mainly determined by L_1 states in GaAs; thus, the net density is mostly concentrated in the GaAs layer. Contributions of the other states, including X_5, to the electron density are insignificant (see Fig. 5).

For all SLs considered above, we also calculated the quantity

$$\Sigma = |\mathbf{e} \cdot \mathbf{P}_{12}|^2_{(1)} + |\mathbf{e} \cdot \mathbf{P}_{12}|^2_{(2)} + |\mathbf{e} \cdot \mathbf{P}_{12}|^2_{(3)}.$$

Here, $\mathbf{P}_{12} = \langle \Psi_1(r)|\mathbf{P}|\Psi_2(r)\rangle$ is the matrix element of momentum between the wave functions of the first and the second minibands, measured in units of $\hbar/a$; **e** is the

Table 4. The values of the optical parameter Σ for different propagation directions of the incident light

(*M*, *N*)	Direction	$Q = 0$	$Q = \pi/2$	$Q = \pi$	(*M*, *N*)	Direction	$Q = 0$	$Q = \pi/2$	$Q = \pi$
(9, 9)	Normal	0.22	0.35	0.42	(8, 9)	Normal	0.12	0.17	0.48
	Oblique	0.68	0.97	1.11		Oblique	0.36	0.46	1.24
(8, 8)	Normal	0.26	0.38	0.51	(10, 8)	Normal	0.24	0.29	0.40
	Oblique	0.80	1.02	1.30		Oblique	0.70	0.82	1.05
(7, 7)	Normal	0.00	0.36	0.63	(10, 7)	Normal	0.21	0.30	0.43
	Oblique	0.00	0.98	1.59		Oblique	0.65	0.84	1.13
(9, 8)	Normal	0.25	0.31	0.45	(11, 9)	Normal	0.24	0.28	0.33
	Oblique	0.75	0.87	1.17		Oblique	0.70	0.79	0.91
(8, 7)	Normal	0.21	0.38	0.56	(11, 8)	Normal	0.23	0.28	0.36
	Oblique	0.69	1.04	1.43		Oblique	0.67	0.80	0.96

polarization vector of the light wave, chosen in such a way that the value of Σ is the largest; and the subscripts in the parentheses label one of the three possible orientations of the vectors $\mathbf{k}_X$ and $\mathbf{k}_L$ obtained from those chosen above by 120° rotations about the axis [111]. This quantity characterizes the intensity of the absorption of infrared radiation by the SL. The calculation indicated that $(AlAs)_M(GaAs)_N$ structures can effectively absorb the normally incident light. One can see from Table 4 that the value of Σ under normal incidence of light is about a factor of three lower than that under oblique incidence. Since in the former case the illuminated area may be several orders of magnitude larger than in the latter case, this is quite a satisfactory result. This interesting result requires a qualitative explanation. Our analysis revealed that small corrections to the wave function that are related to X_5 states play an important part in the effect. The contribution of these states to the electron density is shown in Fig. 5. This contribution is two orders of magnitude smaller than the net electron density, and the amplitude of the corresponding wave function is smaller by an order of magnitude. When the incident light is polarized perpendicular to the [111] axis, the leading terms in the matrix element of the momentum are of the type $\langle F_{X_{5x}}(z')|F_{X_1}(z')\rangle\langle X_{5x}|\mathbf{e}\cdot\mathbf{P}|X_1\rangle$. It was found that these terms are sufficiently large due to the large value of the matrix elements $\langle X_1|\mathbf{P}|X_5\rangle$ and $\langle X_3|\mathbf{P}|X_5\rangle$. The estimated values of $\langle F_{X_{5x}}(z')|F_{X_1}(z')\rangle$ and $\langle F_{X_{5x}}|\mathbf{e}\cdot\mathbf{P}|X_1\rangle$ (in dimensionless units) are 0.1 and 6, respectively. This is the reason why the value of Σ is so large for the case of normal incidence of light. The values of Σ in the structure (7, 7) at $Q = 0$ and in the structure (8, 9) at all Q are relatively small. This is caused by the fact that, in these SLs, the first and the second energy levels originate from different valleys.

5. CONCLUSION

We studied the miniband spectra and electron states in the conduction band of $(AlAs)_M(GaAs)_N(111)$ SLs with the number of monolayers M and N varying from 7 to 11. The analysis is carried out in the context of a previously developed model describing the X–L state mixing at heterointerfaces. We demonstrated that, for $M > N$, the two lowest minibands originate from the X_1 valley in the AlAs bulk energy-band spectrum and are separated by a gap of 0.12–0.2 eV. Since the wave functions of the two lowest minibands are mainly localized in the same layer, these SLs are promising for infrared optics. Our calculations demonstrated that the probability of the miniband absorption is fairly large not only for the incident light polarized along the SL growth axis, but also for the light propagating normally to the surface of the structure. Such SLs may be of interest for studies of photoconductivity under infrared irradiation.

ACKNOWLEDGMENTS

This study was supported by the Russian Foundation for Basic Research, project no. 00-02-17996.

REFERENCES

1. Z. Ikonic, G. P. Srivastava, and J. C. Inkson, Phys. Rev. B **46**, 15150 (1992).
2. S. H. Wei and A. Zunger, J. Appl. Phys. **63**, 5794 (1988).
3. G. F. Karavaev and S. N. Grinyaev, Izv. Vyssh. Uchebn. Zaved., Fiz., No. 9, 91 (1998).

4. G. F. Karavaev and V. N. Chernyshov, Fiz. Tekh. Poluprovodn. (St. Petersburg) **35**, 105 (2001) [Semiconductors **35**, 106 (2001)].
5. J. M. Smith, P. C. Klipstein, R. Gray, and G. Hill, Phys. Rev. B **57**, 1740 (1998).
6. D. Y. Ko and J. S. Inkson, Phys. Rev. B **38**, 9945 (1988).
7. S. N. Grinyaev and V. N. Chernyshov, Fiz. Tekh. Poluprovodn. (St. Petersburg) **26**, 2057 (1992) [Sov. Phys. Semicond. **26**, 1157 (1992)].
8. G. F. Karavaev, S. N. Grinyaev, and V. N. Chernyshov, Izv. Vyssh. Uchebn. Zaved., Fiz., No. 9, 64 (1992).
9. G. F. Karavaev, V. N. Chernyshov, and S. N. Grinyaev, in *Abstracts of Invited Lectures and Contributed Papers of International Symposium "Nanostructures: Physics and Technology", St. Petersburg, 1994*, p. 62.
10. O. V. Kovalev, *Irreducible and Induced Representations and Corepresentations of Fedorov Groups* (Nauka, Moscow, 1986).

Translated by M. Skorikov

Semiconductors, Vol. 36, No. 5, 2002, pp. 535–538. Translated from Fizika i Tekhnika Poluprovodnikov, Vol. 36, No. 5, 2002, pp. 565–568.

LOW-DIMENSIONAL SYSTEMS

Room Temperature λ = 1.3 μm Photoluminescence from InGaAs Quantum Dots on (001) Si Substrate

T. M. Burbaev, I. P. Kazakov*, V. A. Kurbatov, M. M. Rzaev, V. A. Tsvetkov, and V. I. Tsekhosh

Lebedev Physical Institute, Russian Academy of Sciences, Leninskiĭ pr. 53, Moscow, 119991 Russia

** e-mail: kazakov@sci.lebedev.ru*

Submitted October 18, 2001; accepted for publication October 30, 2001

Abstract—$GaAs/In_xGa_{1-x}As$ quantum dot heterostructures exhibiting high-intensity λ = 1.3 μm photoluminescence at room temperature have been grown on (001) Si substrate with a $Si_{1-x}Ge_x$ buffer layer. The growth was done successively on two MBE machines with sample transfer via the atmosphere. The results obtained by the study of the structure growth process by means of high-energy electron diffraction are presented. © *2002 MAIK "Nauka/Interperiodica".*

1. INTRODUCTION

Progress in information technology is largely determined by the development of optoelectronics, with the transmission capacity of communication lines raised by orders of magnitude by passing to higher signal carrier frequencies. Nowadays, SiO_2 optical fibers with zero dispersion at λ = 1.3 μm and minimum loss at λ = 1.55 μm are widely used. Light-emitting devices intended for operation at these wavelengths are being intensively developed.

The integration of optical devices for information processing into silicon integrated circuits is the most natural way of development along these lines, but the encountered technological difficulties are immense. No success has been achieved in creating light-emitting devices on the basis of silicon itself because of the "indirect" band structure of this material. Attempts to use Si–Ge nanoislands, porous Si, or Si doped with rare earths failed to yield devices owing to the unsatisfactory optical properties of these structures at room temperature.

A possible solution to this problem consists in using direct-gap III–V materials as light-emitting elements integrated on an Si substrate. Despite the evident advances in hybrid technology of integrated circuits, where finished devices, e.g., lasers, are "glued" to a silicon substrate, the structures obtained in epitaxial growth show more promise, if for no other reason than their being technologically convenient in the batch fabrication of integrated circuits. Obtaining perfect epitaxial GaAs layers on Si encounters a number of difficulties, such as a high density of dislocations and the formation of antiphase domains. At the same time, nanoisland structures of a direct-gap material on Si substrate have not been virtually studied at all. In [1], InAs nanoislands were grown directly on an Si substrate. The structures exhibited room-temperature luminescence at λ = 1.55 μm.

In the present study, a new approach is proposed consisting in that $In_xGa_{1-x}As$ quantum dots (QD) are to be formed in a GaAs matrix epitaxially grown on (001) Si substrate with $Si_{1-x}Ge_x$ buffer layers.

2. SAMPLE PREPARATION

The structures were grown using two molecular beam epitaxy (MBE) machines successively. An $Si_{1-x}Ge_x$ buffer layer was grown on a Katun machine with electron-beam evaporators, and the $GaAs/In_xGa_{1-x}As$(QD) active region, on a TsNA-25 installation with crucible molecular sources. The structure was grown on a (001) KÉF-4.5 Si (*n*-Si:P with 4.5-Ω cm resistivity) substrate 76 mm in diameter.

The pre-epitaxial treatment of a substrate in the Katun machine consisted in the oxide layer removal in an Si vapor flow at a temperature of T_s = 1000°C (as T_s readings of a thermocouple in the substrate heater are given). Then, a 1000-Å-thick Si buffer layer at T_s = 750°C and a multilayer $Si_{1-x}Ge_x$ buffer with stepwise-increasing Ge content were grown. To achieve full relaxation of the mismatch strains and to diminish the dislocation density in the buffer layer with stepwise-varying composition, we used the method proposed in [2, 3]. Figure 1 schematically shows a structure cross-section, with the composition, layer thickness, and T_s indicated. Each layer with a certain Ge content included a sublayer with a thickness of d = 500 Å grown at the lowered temperature T_s = 250°C. Further, the temperature was raised to T_s = 500°C and an additional 1500 Å of the same material was deposited. After a pause necessary for raising the Ge flux, the next layer was grown in the same way, and so on. As seen in the

GaAs, 200 Å, 650°C
InGaAs quantum dots, 650°C
GaAs, 2000 Å, 700°C
Cap Si, 50 Å, 500°C
Ge, 1500 Å, 500°C
$Si_{0.1}Ge_{0.9}$, 500 Å, 250°C
$Si_{0.38}Ge_{0.62}$, 1500 Å, 500°C
$Si_{0.38}Ge_{0.62}$, 500 Å, 250°C
$Si_{0.7}Ge_{0.3}$, 1500 Å, 500°C
$Si_{0.7}Ge_{0.3}$, 500 Å, 250°C
Si, 500 Å, 400°C
Si, 1000 Å, 750°C
Substrate Si (001)

Fig. 1. Cross section of a structure comprising InGaAs QDs on (001) Si substrate with a multilayer $Si_{1-x}Ge_x$ buffer. The thickness d and growth temperature T_s of layers are indicated.

presented scheme, the multilayer $Si_{1-x}Ge_x$ buffer contained three layers with Ge content x = 0.3, 0.62, and 1.0. To protect the top layer of Ge, a thin (d = 50 Å) Si layer was deposited onto the structure surface. Then, the structure was brought via atmosphere into the lock chamber of the TsNA-25 MBE machine, in which a vacuum with a residual pressure lower than 10^{-6} Pa was obtained in 1 h.

An SiO_2 oxide layer was removed from the structure surface in the TsNA-25 machine by heating it at T_s = 800°C in a flow of Ga. Then, the following structure was grown: a GaAs layer of thickness d = 2000 Å at T_s = 700°C, a sheet of $In_xGa_{1-x}As$ (x = 0.5) QDs at T_s = 650°C, and a GaAs protective layer of thickness d = 200 Å at T_s = 650°C. The QD sheet was grown by the cyclic deposition of pairs of InAs/GaAs layers, with each layer deposited in 2 s. The effective thickness of the QD sheet was 30 Å.

The processes of surface cleaning and heterostructure growth were monitored by the reflection high-energy electron diffraction (RHEED) method and recorded to a PC hard disk by a system for recording and processing RHEED images. Figure 2 presents RHEED patterns at several stages of heterostructure growth. After an Si substrate with $Si_{1-x}Ge_x$ buffer layers was transferred to the TsNA-25 growth chamber, the surface was covered with natural oxide (Fig. 2a). Cleaning in a weak Ga flow with simultaneous heating to T_s = 800°C removed the oxide layer, which is confirmed by the appearance of a (2 × 1) reconstruction typical of a clean Si surface (Fig. 2b). Almost immediately after the beginning of GaAs layer growth, a (2 × 4) reconstruction appeared on the structure surface. Figure 2c shows a RHEED pattern from a 2000-Å-thick (001) GaAs buffer layer grown at T_s = 700°C. The presence of elongated bars in the $\langle \bar{1}10 \rangle$ azimuth indicates the high quality of the GaAs layer. After a sheet of $In_{0.5}Ga_{0.5}As$ QDs is grown, the RHEED pattern exhibits, in addition to elongated bars, point reflections typical of crystal surfaces with three-dimensional (3D) islands (Fig. 2d). An analysis of the intensity peak positions for the bars and points yields the ratio of the InGaAs to GaAs lattice constants, a_{InGaAs}/a_{GaAs} = 1.034. This allows us to estimate the composition of the $In_xGa_{1-x}As$ solid solution to be $x \approx 0.5$, without taking into account the strains produced by the lattice mismatch between the QDs and the GaAs matrix.

The photoluminescence (PL) spectra were recorded at temperatures of 77 and 300 K with an MDR-2 monochromator. A semiconductor laser with emission wavelength λ = 0.66 μm (photon energy $h\nu$ = 1.87 eV) served as the excitation source. The maximum emission power was 70 mW, and the radiation power density incident on a sample did not exceed 4 W cm^{-2}. The emission from a sample was detected with a Ge *p–i–n* photodiode cooled with liquid nitrogen.

3. RESULTS AND DISCUSSION

PL spectra recorded at the liquid-nitrogen temperature exhibit lines associated with both the quasi-2D wetting layer (at energy $h\nu$ = 1235 meV) and 3D InGaAs QDs (line peaked at $h\nu$ = 1045 meV). At room temperature, the intensity of QD emission decreases by nearly a factor of four. In this case, the peaks shift to lower frequencies, owing to variation of the GaAs band gap with temperature. The large width of the QD emission lines (~200 meV at half-maximum) can be accounted for by nonuniformity of InGaAs islands in size and composition. Atomic-force microscopy revealed the surface relief of the Ge buffer layer and the GaAs protecting layer. This gives reason to believe that InGaAs QDs were also grown on a warped GaAs surface. A similar PL spectrum was observed in [4, 5] for samples with a mixed (2D–3D) InAs layer structure in the GaAs matrix. If we take into account the nonuniformity of the layer thickness, resulting from different inclinations of separate areas of the relief substrate surface with respect to the direction of molecular beam incidence, the (2D–3D) structure of the InGaAs layer is very likely in our samples. It is also known that the segregation in solid solutions, InGaAs included, on a relief surface gives rise to lateral nonuniformity in composition owing to different rates of surface diffusion of

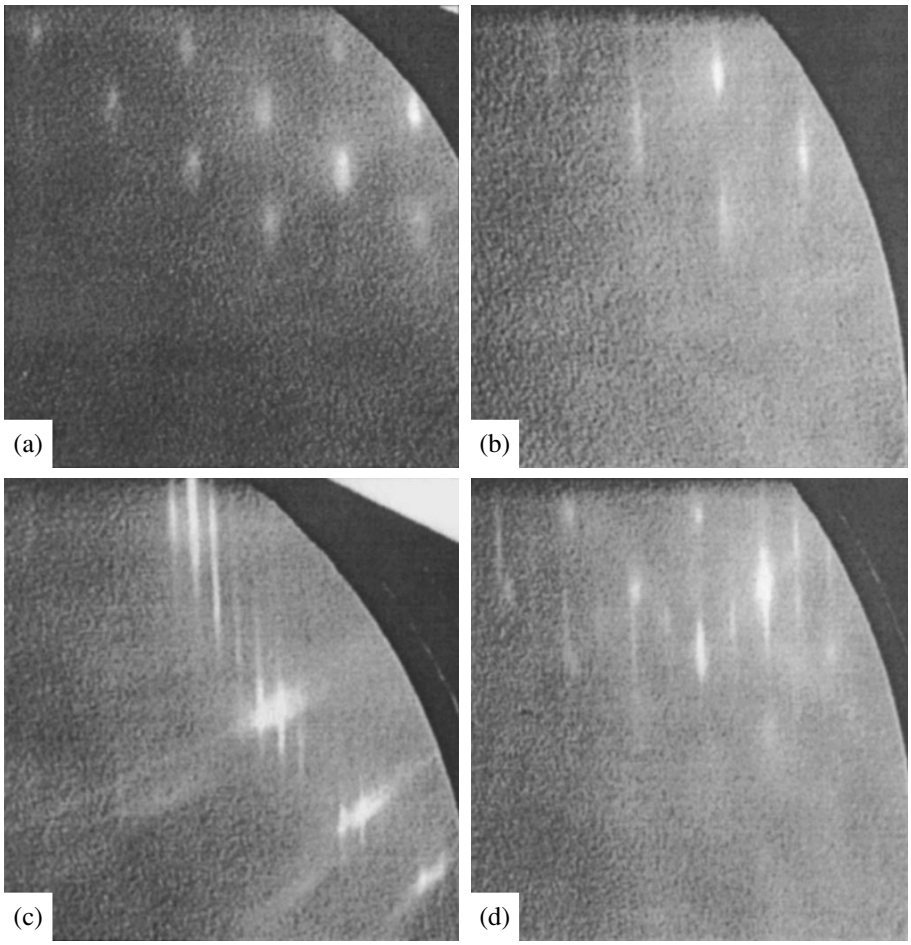

Fig. 2. RHEED patterns at different stages of heterostructure growth (electron energy 15 keV, azimuth $\langle \bar{1}10 \rangle$): (a) surface of (001) Si substrate with Si/SiGe/Ge/Si buffer layers after transfer via atmosphere from the Katun machine to the TsNA-25 growth chamber; (b) the same surface after cleaning in Ga flow; (c) surface of 2000-Å-thick (001) GaAs buffer layer; (d) change in the diffraction pattern after growth of a sheet of InGaAs QDs.

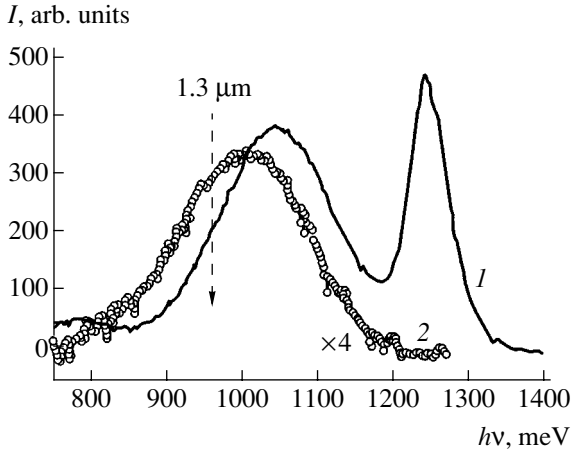

Fig. 3. PL spectra of a heterostructure with InGaAs QDs grown on (001)Si/$Si_{0.7}Ge_{0.3}$/$Si_{0.38}Ge_{0.62}$/$Si_{0.1}Ge_{0.9}$/Ge/GaAs substrate: (*1*) 77 and (*2*) 300 K.

components (adatoms) toward steps whose concentration is higher at surface areas tilted with respect to singular planes [6]. The existence of such a mixed (2D–3D) structure of the InGaAs layer is also confirmed by RHEED patterns measured *in situ* (Fig. 2d).

4. CONCLUSION

We have proposed and implemented a method for obtaining an ensemble of InGaAs QDs on a Si substrate by creating a Si/$Si_{1-x}Ge_x$/Ge/GaAs intermediate buffer layer. Structures with high-intensity room-temperate PL in the commercially important spectral range of 1.3 μm have been fabricated.

We have demonstrated that a Si/$Si_{1-x}Ge_x$ structure grown in a separate setup and transferred via the atmosphere can be used as a substrate for GaAs epitaxy.

The advantages of the proposed technique, compared with III–V QD formation directly in a silicon matrix, are as follows:

(1) The QD formation process can be flexibly controlled by varying the mismatch strain, which depends on the design of the $Si/Si_{1-x}Ge_x/Ge/GaAs$ buffer layer.

(2) The uncontrolled doping of QDs with a Si impurity from the surrounding matrix is suppressed.

(3) The structures are produced in standard MBE machines, with no special design of growth chambers with molecular sources required for obtaining III–V and $Si/Si_{1-x}Ge_x$ layers.

ACKNOWLEDGMENTS

This study was supported in part by the Russian Foundation for Basic Research (project nos. 01-02-17732, 00-02-16740), and the scientific programs "Physics of Solid-State Nanostructures" (project nos. 97-1050, 2000-2F) and "Promising Technologies and Devices of Microelectronics and Nanoelectronics" (project no. 1), and the "Scientific School" Program (grant no. 00-15-96568).

REFERENCES

1. G. E. Cirlin, V. N. Petrov, V. G. Dubrovsky, *et al.*, Pis'ma Zh. Tekh. Fiz. **24** (8), 10 (1998) [Tech. Phys. Lett. **24**, 290 (1998)].
2. H. Chen, L. W. Guo, Q. Cui, *et al.*, J. Appl. Phys. **79**, 1167 (1996).
3. C. S. Peng, Z. Y. Zhao, H. Chen, *et al.*, Appl. Phys. Lett. **72**, 3160 (1998).
4. J. M. Gerard, J. B. Genin, J. Lefebre, *et al.*, J. Cryst. Growth **150**, 351 (1995).
5. D. I. Lubyshev, P. P. Gonzalez-Borrero, E. Marega, Jr., *et al.*, J. Vac. Sci. Technol. B **14**, 2212 (1996).
6. K. Kamath, J. Phillips, J. Singh, and P. Bhattacharya, J. Vac. Sci. Technol. B **14**, 2312 (1996).

Translated by D. Mashovets

Semiconductors, Vol. 36, No. 5, 2002, pp. 539–545. Translated from Fizika i Tekhnika Poluprovodnikov, Vol. 36, No. 5, 2002, pp. 569–575.

LOW-DIMENSIONAL SYSTEMS

Resonance Tunneling and Nonlinear Current in Heterobarriers with Complex Law of Carrier Dispersion

C. S. Kim*, A. M. Satanin^, and V. B. Shtenberg****

** Applied Physics, Yale University, New Haven, Connecticut 06520-8284, USA*

*** Lobachevsky State University, pr. Gagarina 23, Nizhni Novgorod, 603600 Russia*

^e-mail: satanin@phys.unn.runnet.ru

Submitted October 16, 2001; accepted for publication November 1, 2001

Abstract—New effects in resonance electron tunneling in a GaAs/Al_xGa_{1-x}As/GaAs single-barrier heterostructure are analyzed with applied electric bias taken into account. Γ–*X* mixing of electron states at the interfaces is responsible for the Fano resonance in the barrier transmission coefficient. Trajectories of the Fano resonances and their interplay with the Breit–Wigner resonances in an electric field are studied. The current–voltage characteristic of the heterobarrier is calculated. A knowledge of the differential conductance makes it possible to obtain the Fano resonance profile and determine its parameters. © *2002 MAIK "Nauka/Interperiodica".*

1. INTRODUCTION

Studies of the electronic transport through single-barrier semiconductor heterostructures (of the GaAs/Al_xGa_{1-x}As/GaAs type) have been attracting much attention recently [1–9]. On the one hand, this is due to the possibility of applying such heterostructures for constructing resonance tunneling devices and, on the other, interesting interference phenomena leading to unusual resonance behavior of the barrier transmission are possible in multivalley heterostructures. GaAs is known to be a direct-band semiconductor with the electron energy minimum located at the Brillouin zone center (in the Γ point). When the mole fraction of Al changes (at $x > 0.45$), the Al_xGa_{1-x}As compound becomes an indirect-band semiconductor with the band minimum near the *X* point at the Brillouin zone boundary. Electrons can tunnel through the GaAs/Al_xGa_{1-x}As/GaAs structure via two intermediate states within the barrier: $\Gamma \longrightarrow \Gamma \longrightarrow \Gamma$ and $\Gamma \longrightarrow X \longrightarrow \Gamma$ channels. Mixing of states occurs at the heterointerface and is characterized by the intervalley interaction matrix element (Γ–*X* mixing) [10]. Interference of Γ–*X* states in the barrier gives rise to new coherent phenomena: the appearance of a virtual level in the *X* well and the forming of asymmetric transparence resonances (Fano resonances [11]). Participation of the *X* states in the transport through Al_xGa_{1-x}As and properties of the Fano resonances have attracted much attention [5–7, 12]. Of practical interest is that asymmetric resonances may lead to portions with a negative differential conductance in current–voltage (*I–V*) characteristics that can be used in practice.

The case when the mole fraction of Al in the barrier is such that the energy of the barrier Γ minimum is lower than the energy of the *X* valley bottom at the interface ($x < 0.63$) has been studied rather poorly. Over-barrier resonance (Breit–Wigner resonance) in $\Gamma \longrightarrow \Gamma \longrightarrow \Gamma$ tunneling is possible in this case. The interference of states inside the barrier means the effective interaction of the Fano and Breit–Wigner resonances [13, 14]. One can control the interaction between resonances and, therefore, the transmission and the tunneling current by varying the parameters of the system: barrier thickness, Al fraction (composition), pressure, electric field, etc.

In this study, we perform a detailed analysis of the behavior of the barrier transmission and properties of the Fano resonance in barriers with a complex carrier dispersion law in relation to the heterostructure geometry and Al fraction. The behavior of the asymmetric resonances in a high electric field will be studied. Since the tunneling current is integrally expressed in terms of the barrier transmission and the Fano resonance line shape strongly depends on electric field, it is necessary to determine the contribution of the resonances to the *I–V* characteristic. We are going to determine the resonance contribution to the barrier *I–V* characteristic and analyze the possibility of determining the resonance parameters from differential conductance.

2. MODEL OF THE HETEROSTRUCTURE AND METHOD FOR BARRIER-TRANSMISSION CALCULATION

Let us consider a semiconductor heterostructure like GaAs/Al_xGa_{1-x}As/GaAs, which can also include a spacer and contact layers. Let the *z* axis be chosen in the tunneling direction, while the planes bounding the Al_xGa_{1-x}As heterobarrier are defined by the conditions $z = \pm L/2$. When a bias voltage *U* is applied to the structure, the potential distribution can be found from the Poisson equation. Since we are interested in the reso-

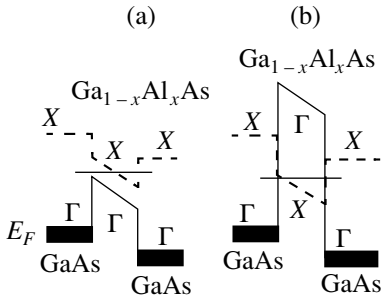

Fig. 1. Band diagram of a heterobarrier band structure in a high electric field for the Al fraction $x < 0.63$ (a) and $x > 0.63$ (b). The horizontal line shows the virtual level position in the *X* well.

nance contribution to the transmission and the *I–V* characteristics, details of the potential profile can determine only the nonresonance (potential) [15] contribution and approximation of the potential by the linear function is sufficient. We add to the equation for the envelope functions the potential of the type $V(z) = -(eU/2) - Fz$, where $F = eU/D$, and D is the thickness of the structure along with the spacers (barrier thickness is L). A band diagram of the heterostructure with the complex dispersion law put into the electric field is shown in Fig. 1. We assume that the undoped $Al_xGa_{1-x}As$ barrier is surrounded by two undoped GaAs spacer layers, which are in contact with the doped emitter and collector (n^+-GaAs).

The tunneling current can be integrally expressed in terms of the barrier transmission, which enables us to obtain information on the resonance structure. The system transmission is found by solving the Schrödinger equation in terms of the effective mass model for systems with complex carrier dispersion law. We study the simplest case, when it suffices to take into account the states of two valleys. This case is shown [1, 3] to exactly occur within a certain Al fraction range. The two-valley model approximately describes the main features of resonance tunneling through the heterobarrier.

Let the electron in the bulk be in Γ and *X* valleys and be described by the two-component wave function (ψ_Γ, ψ_X). We assume that the barrier can be described within the framework of the virtual crystal model by introducing effective masses and band parameters as functions of *z* according to [16]. Mixing of the states takes place only at interfaces, which is described by the matrix element $V_{\Gamma,X}$ [1]. The equations for the envelope functions read

$$-\frac{\hbar^2}{2}\frac{\partial}{\partial z}\frac{1}{m_\Gamma}\frac{\partial\psi_\Gamma}{\partial z} + [E_\Gamma + V(z)]\psi_\Gamma + V_{\Gamma,X}\delta(z \pm L/2)\psi_X = E\psi_\Gamma, \quad (1)$$

$$-\frac{\hbar^2}{2}\frac{\partial}{\partial z}\frac{1}{m_X}\frac{\partial\psi_X}{\partial z} + [E_X + V(z)]\psi_X + V_{X,\Gamma}\delta(z \pm L/2)\psi_\Gamma = E\psi_X, \quad (2)$$

where $m_{\Gamma,X}$ and $E_{\Gamma,X}$ are considered functions of *z*.

First, we will consider the more general situation assuming that the tunneling electron can belong both to Γ and *X* valleys. A solution in the emitter region can be written in the form

$$\psi_\Gamma(x) = a_\Gamma e^{ik_\Gamma z} + b_\Gamma e^{-ik_\Gamma z}, \quad (3)$$

$$\psi_X(z) = a_X e^{ik_X z} + b_X e^{-ik_X z}, \quad (4)$$

where $k_\Gamma = \sqrt{2m_\Gamma E/\hbar^2}$, and $k_X = \sqrt{2m_X(E - E_X)/\hbar^2}$. A solution in the collector region reads

$$\psi_\Gamma(z) = c_\Gamma e^{iq_\Gamma z}, \quad (5)$$

$$\psi_X(z) = c_X e^{iq_X z}, \quad (6)$$

where $q_\Gamma = \sqrt{2m_\Gamma(E + eU)/\hbar^2}$, and $q_X = \sqrt{2m_X(E - E_X + eU)/\hbar^2}$.

The boundary conditions can be obtained by integrating (1) over a small vicinity of the boundary (along the normal to the layer) [1]. For example, integration of (1) near $z = L/2$ gives

$$\psi_\Gamma(L/2 + 0) = \psi_\Gamma(L/2 - 0),$$

$$\psi_X(L/2 + 0) = \psi_X(L/2 - 0),$$

$$\mu_\Gamma^R\frac{\partial\psi_\Gamma(L/2 + 0)}{\partial z} - \mu_\Gamma^L\frac{\partial\psi_\Gamma(L/2 - 0)}{\partial z} = \nu\psi_X(L/2), \quad (7)$$

$$\mu_X^R\frac{\partial\psi_X(L/2 + 0)}{\partial z} - \mu_X^L\frac{\partial\psi_X(L/2 - 0)}{\partial z} = \nu\psi_\Gamma(L/2),$$

where $\mu_{\Gamma,X} = m_0/m_{\Gamma,X}$, and $\nu = (m_0/\hbar^2)V_{\Gamma,X}$; the parameters are taken on the left (subscript *L*) and on the right (subscript *R*) from the interface. The boundary conditions at $z = -L/2$ are written similarly. Mixing of the electron states at the heterointerface determines the resonance structure of the transmission.

We are interested in the multichannel transfer matrix *t*, which expresses the transmitted wave amplitudes (c_Γ, c_X) in terms of the incident wave amplitudes (a_Γ, a_X). The barrier transmission, the tunnel current, and resonance states in the barrier can be obtained from the matrix *t*. Equation (1) must be solved by taking account of the potential field inside the barrier and by satisfying the proper boundary conditions in order to calculate *t*.

We divide the heterostructure into the following regions: two contact n^+-GaAs ($j = e, c$) domains, and two undoped GaAs spacer layers adjoining the contacts and the barrier ($l = s, s$) and the $Al_xGa_{1-x}As$ ($j = I$) barrier domain (Figs. 1a and 1b). Since the potential linearly depends on *z*, the exact solution of the

Schrödinger equation at every layer can be written as a linear combination of two Airy functions

$$\psi_\Gamma^j(z) = a_\Gamma^j \mathrm{Ai}[-\xi_\Gamma^j(z)] + b_\Gamma^j \mathrm{Bi}[-\xi_\Gamma^j(z)], \quad (8)$$

$$\psi_X^j(z) = a_X^j \mathrm{Ai}[-\xi_X^j(z)] + b_X^j \mathrm{Bi}[-\xi_X^j(z)], \quad (9)$$

where

$$\xi_\Gamma^j(z) = \frac{\Delta_\Gamma^j}{(\alpha_\Gamma^j)^{2/3}} + (\alpha_\Gamma^j)^{1/3}\frac{z}{a},$$

$$\alpha_\Gamma^j = 2m_\Gamma^j a^3 F/\hbar^2,$$

$$\Delta_\Gamma^j = 2a^2 m_\Gamma^j (E - E_\Gamma^j + eU/2)/\hbar^2,$$

$$\xi_X^j(z) = \frac{\Delta_X^j}{(\alpha_X^j)^{2/3}} + (\alpha_X^j)^{1/3}\frac{z}{a},$$

$$\alpha_X^j = 2m_X^j a^3 F/\hbar^2,$$

$$\Delta_X^j = 2a^2 m_X^j (E - E_X^j + eU/2)/\hbar^2,$$

and the characteristic length a is determined by features of the emitter (or collector) according to

$$E_X^e = \frac{\hbar^2}{2m_X^e a^2}.$$

The set of coefficients in (8) is determined by a number of layers that are taken into consideration while describing the structure. If, for instance, the spacers are taken into consideration, five pairs of intermediate amplitudes must be introduced for the structure depicted in Fig. 1. The transfer matrix method establishes a relationship between the wave functions at the collector and emitter sides of the heterostructure. The wave function of the state propagating through the layer is expressed as a product of the interface matrix, which is determined by the proper boundary conditions, and the matrix describing wave propagation through the layer in the electric field. Let the amplitude vector in the emitter be chosen in the form $a = (a_\Gamma, b_\Gamma, a_X, b_X)^T$, while the amplitude vector in the collector reads $c = (c_\Gamma, 0, c_X, 0)^T$. Writing solutions in the form of (8) in the internal regions and as (3) and (5) in the external regions and using the boundary conditions at contacts and at the spacer–barrier interfaces, we obtain a linear set of equations for the amplitudes. Excluding the intermediate amplitudes, we obtain

$$\begin{aligned} \mathcal{H}a &= \mathcal{T}\mathcal{Q}c, \\ \mathcal{T} &= \mathcal{T}_{cs}\mathcal{T}_{sb}\mathcal{T}_{bs}\mathcal{T}_{se}, \end{aligned} \quad (10)$$

where $\mathcal{T}_{sc}$, $\mathcal{T}_{sb}$, $\mathcal{T}_{bs}$, and $\mathcal{T}_{se}$ are, respectively, the collector–spacer, spacer–barrier, barrier–spacer, and spacer–emitter transfer matrices that can be expressed in terms of the Airy functions and their derivatives. We have also introduced the auxiliary matrices

$$\mathcal{H} = \begin{pmatrix} 1 & 1 & 0 & 0 \\ -ik_\Gamma & ik_\Gamma & 0 & 0 \\ 0 & 0 & 1 & 1 \\ 0 & 0 & -ik_X & ik_X \end{pmatrix},$$

$$\mathcal{Q} = \begin{pmatrix} 1 & 0 & 0 & 0 \\ -iq_\Gamma & 0 & 0 & 0 \\ 0 & 0 & 1 & 0 \\ 0 & 0 & -iq_X & 0 \end{pmatrix}. \quad (11)$$

The total barrier transfer matrix $\mathcal{T}$ allows us to obtain the transmission matrix t. We introduce the matrix g for this purpose by the relation

$$\mathrm{g} = \begin{pmatrix} g_{\Gamma\Gamma} & g_{\Gamma X} \\ g_{X\Gamma} & g_{XX} \end{pmatrix}, \quad (12)$$

where

$$g_{\Gamma\Gamma} = ik_\Gamma(\mathcal{T}_{11} - iq_\Gamma\mathcal{T}_{12}) - \mathcal{T}_{21} + iq_\Gamma\mathcal{T}_{22}, \quad (13)$$

$$g_{\Gamma X} = ik_\Gamma(\mathcal{T}_{13} - iq_X\mathcal{T}_{14}) - \mathcal{T}_{23} + iq_X\mathcal{T}_{24}, \quad (14)$$

$$g_{X\Gamma} = ik_X(\mathcal{T}_{31} - iq_\Gamma\mathcal{T}_{32}) - \mathcal{T}_{41} + iq_\Gamma\mathcal{T}_{42}, \quad (15)$$

$$g_{XX} = ik_X(\mathcal{T}_{33} - iq_X\mathcal{T}_{34}) - \mathcal{T}_{43} + iq_X\mathcal{T}_{44}. \quad (16)$$

Writing the relationship between the amplitudes in the emitter and collector, we obtain

$$\mathrm{t} = \frac{2i}{(g_{\Gamma\Gamma}g_{XX} - g_{\Gamma X}g_{X\Gamma})}\begin{pmatrix} g_{XX}k_\Gamma & -g_{\Gamma X}k_X \\ -g_{X\Gamma}k_\Gamma & g_{\Gamma\Gamma}k_X \end{pmatrix}. \quad (17)$$

It is noteworthy that the expression for the transmission matrix can be simplified for the system without spacers, since elements of the matrix g read

$$\begin{aligned} g_{\Gamma\Gamma} &= -\pi[M_{21}^\Gamma - i\bar{q}_\Gamma M_{22}^\Gamma \\ &\quad - i\bar{k}_\Gamma(M_{11}^\Gamma - i\bar{q}_\Gamma M_{12}^\Gamma) + \nabla_\Gamma\nabla_X M_{12}^X], \end{aligned} \quad (18)$$

$$g_{\Gamma X} = -\pi\nabla_\Gamma(M_{22}^\Gamma - i\bar{k}_\Gamma M_{11}^\Gamma + M_{11}^X - i\bar{q}_X M_{12}^X), \quad (19)$$

$$\begin{aligned} g_{XX} &= -\pi[M_{21}^X - i\bar{q}_X M_{22}^X \\ &\quad - i\bar{k}_X(M_{11}^X - i\bar{q}_X M_{12}^X) + \nabla_\Gamma\nabla_X M_{12}^\Gamma], \end{aligned} \quad (20)$$

$$g_{X\Gamma} = -\pi\nabla_X(M_{22}^X - i\bar{k}_X M_{12}^X M_{11}^\Gamma - i\bar{q}_\Gamma M_{12}^\Gamma), \quad (21)$$

where

$$\bar{k}_\Gamma = \frac{\mu_\Gamma^e}{\mu_X^I}(k_\Gamma a)(\alpha_\Gamma^I)^{-1/3}, \quad \bar{k}_X = \frac{\mu_X^e}{\mu_X^I}(k_X a)(\alpha_X^I)^{-1/3},$$

$$\bar{q}_\Gamma = \frac{\mu_\Gamma^e}{\mu_X^I}(q_\Gamma a)(\alpha_\Gamma^I)^{-1/3}, \quad \bar{q}_X = \frac{\mu_X^e}{\mu_X^I}(q_X a)(\alpha_X^I)^{-1/3},$$

$$\nabla_\Gamma = \frac{va}{\mu_\Gamma^I}(\alpha_\Gamma^I)^{-1/3}, \quad \nabla_X = \frac{va}{\mu_X^I}(\alpha_X^I)^{-1/3}.$$

Here, we have introduced the matrices $M^{\Gamma, X}$, which are determined in terms of the Airy functions and their derivatives,

$$\begin{aligned}
M_{11}^{\Gamma, X} &= \mathrm{Ai}\left[-\xi_\Gamma^I\left(-\frac{L}{2a}\right)\right]\mathrm{Bi}'\left[-\xi_\Gamma^I\left(\frac{L}{2a}\right)\right] \\
&\quad - \mathrm{Bi}\left[-\xi_\Gamma^I\left(-\frac{L}{2a}\right)\right]\mathrm{Ai}'\left[-\xi_\Gamma^I\left(\frac{L}{2a}\right)\right], \\
M_{12}^{\Gamma, X} &= \mathrm{Ai}\left[-\xi_\Gamma^I\left(-\frac{L}{2a}\right)\right]\mathrm{Bi}\left[-\xi_\Gamma^I\left(\frac{L}{2a}\right)\right] \\
&\quad - \mathrm{Bi}\left[-\xi_\Gamma^I\left(-\frac{L}{2a}\right)\right]\mathrm{Ai}\left[-\xi_\Gamma^I\left(\frac{L}{2a}\right)\right], \\
M_{21}^{\Gamma, X} &= \mathrm{Ai}'\left[-\xi_\Gamma^I\left(-\frac{L}{2a}\right)\right]\mathrm{Bi}'\left[-\xi_\Gamma^I\left(\frac{L}{2a}\right)\right] \\
&\quad - \mathrm{Bi}'\left[-\xi_\Gamma^I\left(-\frac{L}{2a}\right)\right]\mathrm{Ai}'\left[-\xi_\Gamma^I\left(\frac{L}{2a}\right)\right], \\
M_{22}^{\Gamma, X} &= \mathrm{Ai}\left[-\xi_\Gamma^I\left(-\frac{L}{2a}\right)\right]\mathrm{Bi}'\left[-\xi_\Gamma^I\left(\frac{L}{2a}\right)\right] \\
&\quad - \mathrm{Bi}\left[-\xi_\Gamma^I\left(-\frac{L}{2a}\right)\right]\mathrm{Ai}'\left[-\xi_\Gamma^I\left(\frac{L}{2a}\right)\right].
\end{aligned} \tag{22}$$

Thus, the concrete calculation of the transmission is reduced to finding the layer transfer matrices and then obtaining the structure transmission according to (17).

3. TRAJECTORIES OF FANO AND BREIT–WIGNER RESONANCES IN AN ELECTRIC FIELD

First, we present a qualitative analysis allowing for an understanding of the transmission resonance behavior in the electric field. We consider a barrier without spacers. Let the Al fraction in the barrier be such that $E_\Gamma^I > E_X^e$ ($x > 0.63$, see Fig. 1b). In the absence of the electric field, interference of the propagating Γ state with the localized X well state leads to the Fano resonances [5–7, 12]. Now, we study zeros and poles of the scattering amplitude in the Γ–Γ channel:

$$t_{\Gamma\Gamma}(E) = \frac{2ig_{XX}(E)k_\Gamma}{\{g_{XX}(E) - g_{X\Gamma}(E)[1/g_{\Gamma\Gamma}(E)]g_{\Gamma X}(E)\}g_{\Gamma\Gamma}(E)}. \tag{23}$$

Expression (23) implies that zeros are determined by the expression $g_{XX}(E) = 0$. It is seen from (20) that the equation $g_{XX}(E) = 0$ has a real solution. Let E_0 be one of the solutions to this equation; it is related to the level in the X well. It is easy to understand that the level will move in the electric field in accordance with a change of the X well shape. Here, we assume that the electron energy and parameters of the well are such that $\bar{k}_X \gg 1$ and $\bar{q}_X \gg 1$ and the coupling parameter $\bar{v}_X \ll 1$. Then, we can retain the term with M_{12}^X in the expression for g_{XX} and the zero amplitude (level in the well) will be approximately determined by the expression

$$\begin{aligned}
M_{12}^X &= \mathrm{Ai}\left[-\xi_X^I\left(-\frac{L}{2a}\right)\right]\mathrm{Bi}\left[-\xi_X^I\left(\frac{L}{2a}\right)\right] \\
&\quad - \mathrm{Bi}\left[-\xi_X^I\left(-\frac{L}{2a}\right)\right]\mathrm{Ai}\left[-\xi_X^I\left(\frac{L}{2a}\right)\right] = 0.
\end{aligned} \tag{24}$$

Expression (8) implies that such a combination of the Airy functions is related to the condition for the existence of a level in the well with infinitely high walls in the electric field. The discarded terms obviously take into account the finiteness of the wall height and the weak interaction of states in the well with the Γ valley. They do not qualitatively change the picture of the moving of the level and, therefore, of the moving of the Fano resonance zero in the electric field. Since the Γ–X coupling parameter is small, the pole determined by the expression $g_{XX}(E) - g_{X\Gamma}(E)g_{\Gamma X}(E)/g_{\Gamma\Gamma}(E) = 0$ lies near E_0 in the complex plane; we denote such a solution as $\tilde{E} = E_f - i\Gamma_f$. It is noteworthy that the solution to the equation $g_{\Gamma\Gamma}(E) = 0$ will lie distantly in the complex plane, since it is related to the over-barrier interference in the Γ channel. Therefore, the Γ–Γ transition amplitude near the virtual level reads

$$t_{\Gamma\Gamma}(E) \propto \frac{E - E_0}{E - E_f + i\Gamma_f}. \tag{25}$$

Thus, the zero and the pole of the scattering amplitude (Fano resonance) move in the electric field. Since probabilities of reflection from the well boundaries change due to the electric field, the transmission peak magnitude decreases.

Now, we discuss possible changes due to variation of the solid solution composition (mole fraction of Al) in the barrier, when $E_\Gamma^I < E_X^e$ ($x < 0.63$, see Fig. 1a). One can see that the structure of the Fano resonances cannot essentially change, since these are related to the X well, which persists in this structure. If, however, the barrier is wide enough, the over-barrier Breit–Wigner resonances, appearing due to interference of waves in the Γ valley, can fundamentally influence the tunneling features. Such resonances are known to be sharp enough if the amplitude of reflection from the barrier edges is close to unity. The positions of resonances in the absence of the electric field are usually found as in the case for an infinitely deep well, while their widths are determined by the decay rates of these levels [17]. Let the electron energy and the barrier parameters be such that $\bar{k}_\Gamma \gg 1$ and $\bar{q}_\Gamma \gg 1$ and the coupling param-

eter $\bar{\nu}_\Gamma \ll 1$. The Breit–Wigner resonance position can be approximately determined by the condition

$$M_{12}^{\Gamma} = \mathrm{Ai}\left[-\xi_\Gamma^I\left(-\frac{L}{2a}\right)\right]\mathrm{Bi}\left[-\xi_\Gamma^I\left(\frac{L}{2a}\right)\right] - \mathrm{Bi}\left[-\xi_\Gamma^I\left(-\frac{L}{2a}\right)\right]\mathrm{Ai}\left[-\xi_\Gamma^I\left(\frac{L}{2a}\right)\right] = 0. \quad (26)$$

Resonances move in the electric field in this case according to (26). Since the barrier becomes asymmetric, tunneling probabilities will also be different, and resonance widths will increase with increasing bias.

It is evident from the foregoing that the level in the X well and the virtual level over the Γ barrier are determined by different parameters. Therefore, the crossing of these levels is possible due to varying of the barrier thickness or the electric field. An interesting situation occurs when the Breit–Wigner resonance approaches the Fano one. As was shown in [12], in the absence of an electric field, the collapse of the Fano resonance can take place.

Now, we present some numerical results demonstrating Γ–X mixing in tunneling in the electric field. The known content dependence of the $Al_xGa_{1-x}As$ material parameters [16] was used to obtain the results. The AlAs barrier transmission $T_{\Gamma\Gamma}$ as a function of energy E is presented in Fig. 2 for the case when $x = 1$ and the barrier thickness $L = 1.13$ nm (energy is measured in units of $E^* = E_X^e$). In this situation, there is a single level in the well, which leads to the Fano resonance in the transmission. It can be seen from Fig. 2 that the resonance moves in the electric field, while its amplitude decreases. In a strong field, when the X level goes to the continuum, the transmission amplitude zero goes to the complex plane. Now we consider the case when $x < 0.63$. Here, we want to demonstrate the behavior of resonances for wide barriers in order to enable collision between Fano and Breit–Wigner resonances. The results of calculations for the barrier with thickness $L = 6.22$ nm are presented in Fig. 3. Since the Breit–Wigner resonances are related to virtual levels due to the Γ barrier, while the Fano resonances are related to levels of the X well, they can cross under a bias. As is evident from Fig. 3, a collision between the Breit–Wigner and Fano resonances may occur under certain biases. The fundamental narrowing of the Fano resonance can result from this collision, which can influence the barrier I–V characteristic.

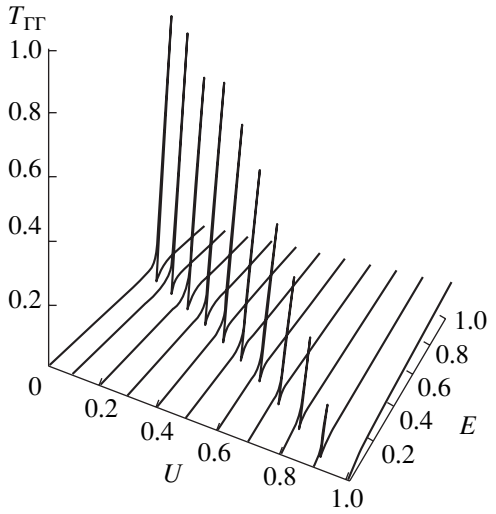

Fig. 2. Resonance transmission $T_{\Gamma\Gamma}$ of AlAs heterobarrier vs. energy E at different biases U applied to the barrier. Only a single quasi-bound state in the X well exists at the chosen barrier thickness. A change of the X well shape in the field leads to the Fano resonance moving. The energy is measured in units of $E^* = E_X^e$, and voltage, in units of $U^* = E_X^e/e$.

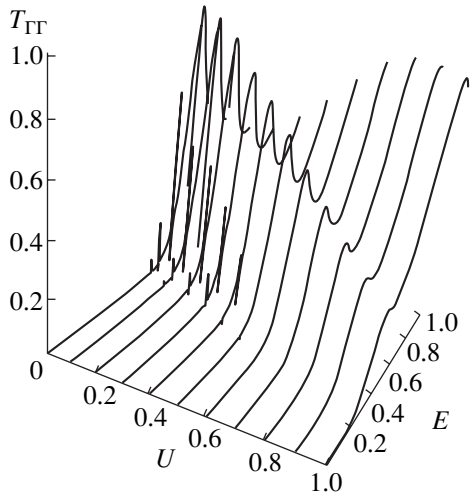

Fig. 3. $Al_xGa_{1-x}As$ ($x = 0.35$) heterobarrier transmission $T_{\Gamma\Gamma}$ vs. energy E at different biases U applied to the barrier. Four quasi-bound states exist in the X well in the absence of bias at barrier thickness $L = 6.22$ nm; they give rise to four Fano resonances. The Fano and Breit–Wigner resonances move and collision between them occurs in the electric field.

4. TUNNELING CURRENT

A method for the calculation of the tunneling current for a given barrier transmission within the framework of the one-band model was developed in [18, 19]. In generalizing this to the case of a two-valley system, possible transitions to the X valley on applying the bias U to the barrier must be taken into account. The conservation of the longitudinal momentum component must be taken into account as well. The resulting expression for the current density takes the following form:

$$J = \frac{2e}{\hbar}\int dE\{f(E) - f(E+eU)\}\int \frac{d\mathbf{q}_\parallel}{(2\pi)^2}T(E, \mathbf{q}_\parallel), \quad (27)$$

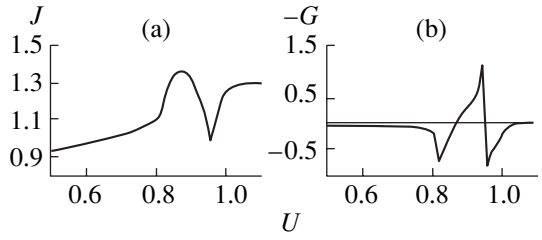

Fig. 4. Current–voltage characteristic $J(U)$ (a) and the differential conductance G (taken with opposite sign) of the barrier vs. the bias U (b). The Fano resonance peak crosses the Fermi level at $U = 0.94U^*$, and the zero does the same at $U = 0.96U^*$. The following values are chosen as measurement units for U, J, and G: $U^* = E_X^e/e$, $J^* = 10^{-4} e m_\Gamma^e (E_X^e)^2/(2\pi^2\hbar^3)$, and $G^* = 10^{-3} e^2 m_\Gamma^e E_X^e/(2\pi^2\hbar^3)$.

where $f(E)$ is the Fermi–Dirac function; the total barrier transmission is given by the expression

$$T(E, \mathbf{q}_\parallel) = (q_\Gamma/k_\Gamma)\left|t_{\Gamma\Gamma}\left(E - \frac{\hbar^2\mathbf{q}_\parallel^2}{2m_\Gamma^e}\right)\right|^2 + (q_X/k_\Gamma + k_\Gamma/q_X)\left|t_{X\Gamma}\left(E - \frac{\hbar^2\mathbf{q}_\parallel^2}{2m_\Gamma^e}, E - \frac{\hbar^2\mathbf{q}_\parallel^2}{2m_X^e}\right)\right|^2. \quad (28)$$

It is noteworthy that the longitudinal (along the field) momenta k_Γ and q_X also depend on transverse energies in, respectively, the Γ and X valleys. It is evident from the structure of (28) that the second term describing the transition Γ–X gives a rather small contribution to the total transmission, since it is proportional to $\propto v^2$. We neglect the difference of masses in this term in order to simplify calculation of the current. Then, the second term depends only on the combination $E - \hbar^2\mathbf{q}_\parallel^2/2m_\Gamma^e$, and integration over the momentum longitudinal component $\mathbf{q}_\parallel$ can be done explicitly. Assuming the temperature to be low, after integration we obtain an expression useful for calculations containing only single integration over the energy:

$$J = \frac{em_\Gamma^e}{2\pi^2\hbar^3}\int_0^{E_F} T(E_\perp)(E_F - E_\perp)dE_\perp, \quad eU \geq E_F,$$

$$J = \frac{em_\Gamma^e}{2\pi^2\hbar^3}\left[U\int_0^{E_F - eU} T(E_\perp)dE_\perp + \int_{E_F - eU}^{E_F} T(E_\perp)(E_F - E_\perp)dE_\perp\right], \quad eU < E_F. \quad (29)$$

Expression (29) was used for calculation of the tunneling current.

We assume for the concrete calculation that the donor concentration $N_D = 10^{18}$ cm^{-3} in the contact regions (corresponding Fermi energy $E_F \approx 50$ meV). The I–V characteristic and the differential conductance $G \equiv dJ/dU$ calculated in the case of $x = 1$ for the barrier with a thickness $L = 1.13$ nm are presented in Figs. 4a and 4b. The Fano resonance gives a characteristic peak of differential conductance at $U \doteq 0.94E_X^e/e$. In order to elucidate this feature, we consider the behavior of the I–V characteristic and the differential conductance as it is usually done in the case of a double-barrier structure [17]. In our case, the levels in the X well are effectively related to spreading states of the Γ valley by the Γ–X mixing matrix element. These states are small, and, therefore, the Fano resonance is well pronounced. Similarly to the case of the double-barrier structure, we assume that the voltage drop occurs mainly across the spacer levels, while the potential is constant inside the barrier. Then, the transmission for the $\Gamma \longrightarrow \Gamma$ transition can be written in the form

$$T_{\Gamma\Gamma} = (q_\Gamma/k_\Gamma)|t_{\Gamma\Gamma}|^2\Theta(E_F + eU/2 - E_\Gamma^I). \quad (30)$$

Substituting (30) into (27) and differentiating with respect to the bias U, we find that the expression for the current has the resonance term

$$dJ/dU \propto -T_{\Gamma\Gamma}(E_F + eU/2 - E_\Gamma^I) + \ldots, \quad (31)$$

where all other terms determine the nonresonance (background) contribution. This means that there exists a contribution to the differential conductance, which is proportional to the transmission peak. Thus, the differential conductance allows us to determine the shape of the resonance. Similar results take place for $x < 0.63$ as well, when collision between the Fano and Breit–Wigner resonances is possible.

5. CONCLUSION

We have studied electron tunneling in heterobarriers based on semiconductors with the complex dispersion law and have investigated coherent tunneling through the GaAs/Al_xGa_{1-x}As/GaAs heterostructure in a high electric field. Using equations for the envelope functions and taking the Γ–X mixing at the heterointerfaces into account, we have studied trajectories of the Fano resonances as a function of the applied bias to the barrier structure bias. The Γ–X interference is shown to play an important role in the forming of asymmetric resonances. Then, moving of the pole and the zero in the field and their disappearance are determined by the X well parameters. The resonance structure essentially depends on the Γ–X mixing parameter as well. In this work, the differential conductance is shown to contain information on features of the resonances. This information can be extracted by studying the differential conductance.

ACKNOWLEDGMENTS

We are grateful to E.V. Demidov, Yu.V. Dubrovskiĭ, and D.O. Filatov for useful comments and discussions of the results.

This study was supported by the Russian Foundation for Basic Research (project no. 01-02-16569). One of the authors (C.S.K.) would like to thank the Korea Research Foundation for support.

REFERENCES

1. H. C. Liu, Appl. Phys. Lett. **51**, 1019 (1987).
2. D. Y. K. Ko and J. C. Inkson, Semicond. Sci. Technol. **3**, 791 (1988).
3. T. Ando and H. Akera, Phys. Rev. B **40**, 11609 (1989).
4. E. E. Mendez, W. I. Wang, E. Calleja, and C. E. T. Goncalves da Silva, Appl. Phys. Lett. **50**, 1263 (1987).
5. T. B. Boykin and J. S. Harris, J. Appl. Phys. **72**, 988 (1992).
6. Y. Fu, M. Willander, E. L. Ivchenko, and A. A. Kiselev, Phys. Rev. B **47**, 13498 (1993).
7. R. C. Bowen, W. R. Frensley, G. Klimeck, and R. K. Lake, Phys. Rev. B **52**, 2754 (1995).
8. R. J. Teissier, J. J. Finley, M. S. Skolnick, *et al.*, Phys. Rev. B **54**, R8329 (1996).
9. J. J. Finley, R. J. Teissier, M. S. Skolnick, *et al.*, Phys. Rev. B **58**, 10619 (1998).
10. E. E. Mendez, E. Calleja, C. E. T. Goncalves da Silva, *et al.*, Phys. Rev. B **33**, 7368 (1986).
11. U. Fano, Phys. Rev. **104**, 1866 (1961).
12. C. S. Kim, A. M. Satanin, and V. B. Shtenberg, Zh. Éksp. Teor. Fiz. **118**, 413 (2000) [JETP **91**, 361 (2000)].
13. C. S. Kim, A. M. Satanin, Y. S. Joe, and R. M. Cosby, Phys. Rev. B **60**, 10962 (1999).
14. C. S. Kim and A. M. Satanin, Zh. Éksp. Teor. Fiz. **115**, 211 (1999) [JETP **88**, 118 (1999)].
15. L. D. Landau and E. M. Lifshitz, *Course of Theoretical Physics*, Vol. 3: *Quantum Mechanics: Non-Relativistic Theory* (Nauka, Moscow, 1989, 4th ed.; Pergamon, New York, 1977, 3rd ed.).
16. S. Adachi, J. Appl. Phys. **58**, R1 (1985).
17. A. S. Tager, Élektron. Tekh., Ser. Élektrn. SVCh, No. 9 (403), 21 (1987).
18. C. B. Duke, in *Tunneling Phenomena in Solids*, Ed. by E. Burstein and S. Lundqvist (Plenum, New York, 1969; Mir, Moscow, 1973).
19. R. Tsu and L. Esaki, Appl. Phys. Lett. **22**, 562 (1973).

Translated by S. Ktitorov

Semiconductors, Vol. 36, No. 5, 2002, pp. 546–551. Translated from Fizika i Tekhnika Poluprovodnikov, Vol. 36, No. 5, 2002, pp. 576–581.

LOW-DIMENSIONAL SYSTEMS

Multichannel Carrier Scattering at Quantum-Well Heterostructures

V. I. Galiev*, A. N. Kruglov*, A. F. Polupanov^*, E. M. Goldys, and T. L. Tansley****

** Institute for Radio-Engineering and Electronics, Russian Academy of Sciences, ul. Mokhovaya 11, Moscow, 101999 Russia*

*** Semiconductor Science and Technology Laboratories, Masquarie University, North Ryde 2109 NSW, Australia*

^e-mail: sashap@mail.cplire.ru

Submitted April 9, 2001; accepted for publication November 14, 2001

Abstract—An efficient combined numerical–analytical technique is developed for calculating states of the continuum spectrum in systems with quantum wells (QWs) with an arbitrary potential shape, described by a system of coupled Schrödinger equations, e.g., hole states in semiconductor QWs. Continuum-spectrum states are found exactly using the approach similar to the scattering theory. Scattering states (the *in*/*out*-solutions) and the *S*-matrix for the case of multichannel scattering in one-dimensional systems with QWs are constructed, and their symmetry is determined and analyzed. The method is applied to studying the hole scattering by GaInAs–InGaAsP QWs with strained layers. The hole transmission and reflection coefficients and the delay-time energy dependence are calculated in relation to parameters of the structures and values of the transversal momentum components. In the energy range in which the channel with heavy hole conversion into a propagating light hole is closed, scattering of the heavy hole on a QW has a resonant nature. © *2002 MAIK "Nauka/Interperiodica".*

1. INTRODUCTION

One of the most effective methods of studing the electron spectrum and the optical properties of semiconductor heterostructures (HS) with quantum wells (QW) is by the envelope function technique based on the effective-mass approximation. It well describes electron and hole subbands near the Brillouin zone center and is particularly convenient when account is to be taken of the effects of internal stresses arising from lattice mismatch or external perturbations, such as uniaxial strain, or electric and magnetic fields. Calculation of energies and wave functions of charge carriers in systems with QWs within the framework of the effective-mass approximation is reduced generically to the solving of the coupled Schrödinger equations for envelope functions. An effective combined numerical–analytical technique for calculation of confined states in systems with QWs with an arbitrary potential shape described by a coupled Schrödinger equation (such as hole states in semiconductor QWs) was developed by us in [1]. In this work, this method is generalized to the case of the continuum spectrum using results from [1] and [2]. The continuous-spectrum states are found within the scattering theory approach. Scattering states (*in*/*out*-solutions) and the *S*-matrix describing the multichannel scattering in systems with QWs are constructed, and their symmetry properties are analyzed in detail. The method has been applied to the study of the hole scattering in the GaInAs–InGaAsP QWs with strained layers.

2. GENERAL FORMULATION OF THE METHOD

Let us consider for specificity the case of a single *W* (barrier) with the potential shape $V(z)$, where z is the axis perpendicular to the structure layers. We assume that the well is located between the points $z = 0$ and $z = d$. The potential $V(z)$ breaks the translation symmetry along the z axis, but the lateral momentum components are "good" quantum numbers. Then we have the following set of the Schrödinger equations, which, as can be easily seen, is a generic form of equations for the hole envelope wave functions that can be obtained substituting $k_z \longrightarrow -id/dz$ into the effective-mass approximation Hamiltonian:

$$H\Psi = \{ad^2/dz^2 + bd/dz + c + V(z)\}\Psi(z) = E\Psi(z). \quad (1)$$

Here a, b, and c are real z-independent $n \times n$ matrices; $\Psi(z)$ is the n-component wave function; the n value is determined by the number of bands taken into consideration, while components of the matrices a, b, and c depend on the valence band parameters and lateral momentum components.

It is convenient to represent (1) as a first-order equation by writing $\Psi(z)$ in the form of a $2n$-component function $y(z) = \begin{pmatrix} \Psi(z) \\ d\Psi(z)/dz \end{pmatrix}$:

$$dy(z)/dz = A(z)y(z), \tag{2}$$

where $A(z)$ is a $2n \times 2n$-matrix function. We further assume that the potential $V(z)$ is an analytic function inside the well and that the convergence radius of the $V(z)$ power expansion exceeds d.

Evidently, if the series $A(z) = A_0 + A_1 z + A_2 z^2 + \ldots$ converges in the vicinity of the point $z = 0$, then the following series for solutions

$$y(z) = \sum_{k=0}^{\infty} y_k z^k \tag{3}$$

also converges in the same vicinity. Here A_k and y_k are, respectively, z-independent $2n \times 2n$ matrices and $2n$ vectors. Substituting (3) into (2), we obtain the following recursive relations for y_k:

$$(k+1)y_{k+1} = \sum_{l=0}^{k} A_l y_{k-l}, \quad k = 0, 1, \ldots, \tag{4}$$

where $y_0 = y(0)$. Since the potential $V(z)$ is an analytic function, (3) and (4) give exact formulas for the solution inside the well and enable us to calculate these solutions with any accuracy required by truncating the corresponding series at large enough k, determined by the prescribed accuracy.

Since $V(z) = 0$ outside the well, at $z < 0$ and at $z > d$, solutions to (2) satisfying certain conditions at $z \longrightarrow \pm\infty$ can be easily found: they are superpositions of $2n$ columns (eigenvectors of the A_0 matrix) multiplied by the exponential functions with complex arguments (eigenvalues of the A_0 matrix). In the case of the continuum spectrum states, either all eigenvalues of the A_0 matrix are imaginary or some of them have nonzero real parts and others are imaginary.

At $0 \le z \le d$, solutions are constructed as described above in the form of a power series, using the recursive relations. Certain boundary conditions are imposed on the solutions at the points $z = 0$ and $z = d$; e.g., $y(z)$ must be continuous at the interface (or more general conditions if, for example, material parameters are different in the well and in the barrier). For specificity, we now consider, but without losing generality, the case when $y(z)$ must be continuous at heterointerfaces.

2.1. Let the matrix $A_0(E)$ have $2n$ eigenvalues $i\kappa_1, \ldots, i\kappa_n, -i\kappa_1, \ldots, -i\kappa_n$ ($\kappa_i > 0$, $1 \le i \le n$) at some E belonging to the continuum spectrum. We now define the fundamental matrix of solutions to (2) at $z \le 0$ and $z \ge d$ in terms of the following $2n \times 2n$ matrix function:

$$\begin{aligned} F(z) \equiv (&\chi_1 \exp(i\kappa_1 z), \ldots, \chi_n \exp(i\kappa_n z), \\ &\chi_{n+1} \exp(-i\kappa_1 z), \ldots, \chi_{2n} \exp(-i\kappa_n z)). \end{aligned} \tag{5}$$

If λ is an eigenvalue of the matrix A_0, then the related eigenvector has the form $\chi = \begin{pmatrix} u \\ \lambda u \end{pmatrix}$ and we can conveniently consider that $u^* u = 1$. It is noteworthy that, if a, b, c, and E are real and λ is an eigenvalue, then the quantities $-\lambda$, $\bar{\lambda}$, $-\bar{\lambda}$ are also eigenvalues (the symbol * stands for Hermitian conjugation; the bar over a symbol stands for complex conjugation). We assume that the eigenvectors related to the complex conjugated eigenvalues are also complex conjugated. Using each column of the $2n \times 2n$ matrix $F(0)$ as an initial column y_0 in (4), we obtain the $2n \times 2n$ matrix function $\hat{F}(z)$, which is a solution to (2) at $0 \le z \le d$. Having calculated this matrix function at the point $z = d$, we obtain the $2n \times 2n$ matrix $\hat{F}(d)$. Since the fundamental matrix of the solutions is nondegenerate, there obviously exists such a nonsingular $2n \times 2n$ matrix Π so that $\hat{F}(d) = F(d)\Pi$. Therefore, the matrix Π is uniquely defined by the relation $\Pi = F^{-1}(d)\hat{F}(d)$). The following set of inhomogeneous linear algebraic equations will be solved in order to find a wave function describing a hole in a certain band incident on the well from the left half-space (*in*-state):

$$\Pi(e, \xi_-)^T = (\xi_+, 0)^T, \tag{6}$$

where the symbol "T" means transposition; ξ_-, ξ_+ are $2n$ coefficients to be found (the S-matrix is defined in terms of these coefficients, see Section 3 and Appendix); and $e = (0,\ldots, 0, 1, 0,\ldots, 0)$. The inhomogeneous set of $2n$ linear equations (6) for $2n$ unknown coefficients ξ_- and ξ_+ can always be solved uniquely. When set (6) is solved, we obtain the following expressions for the wave function (*in*-wave) at, respectively, $z \le 0$, $0 \le z \le d$, $z \ge d$:

$$F(z)(e, \xi_-)^T, \quad \hat{F}(z)(e, \xi_-)^T, \quad F(z)(\xi_+, 0)^T.$$

It is noteworthy that the normalization of the constructed *in*-state coincides with the one for the incident plane wave $\exp(i\kappa_s z)u_s$ (see Appendix). Constructing the wave function describing a hole incident on the well from the right half-space and of *out*-states is quite similar.

2.2. For more clarity (but without loss of generality) we consider the case of a 4×4 A_0 matrix (i.e., $n = 2$). Let $E_I < E < E_{II}$, where E_I, E_{II} are eigenvalues of the matrix c, and the eigenvalues of the matrix A_0 read as follows: $i\kappa$, λ, $-\lambda$], $-i\kappa$ (κ, $\lambda > 0$). Let us introduce the definition

$$F(z) \equiv (\chi_1 \exp(i\kappa z), \chi_2 \exp(\lambda z),$$
$$\chi_3 \exp(-\lambda z), \chi_4 \exp(-i\kappa z)).$$

As in the preceding section, we obtain $\hat{F}(d) = F(d)\Pi$. Consequently, the matrix Π is uniquely defined. In order to find a wave function for the hole in a certain band incident on the well from the left half-space, we solve the following equation:

$$\Pi(1, \eta_+, 0, \xi_-)^T = (\xi_+, 0, \eta_-, 0)^T. \quad (7)$$

These are four equations for four unknowns $\xi_\pm$, $\eta_\pm$, where ξ_- and ξ_+ are related to hole reflection and transmission. The inhomogeneous set of linear equations (7) for unknown coefficients ξ and η can always be uniquely solved. Then, we have the following expressions for *in*-waves at, respectively, $z \le 0$, $0 \le z \le d$, $z \ge d$:

$$F(z)(1, \eta_+, 0, \xi_-)^T, \quad \hat{F}(z)(1, \eta_+, 0, \xi_-)^T,$$
$$F(z)(\xi_+, 0, \eta_-, 0)^T.$$

3. *S*-MATRIX

At a given energy E, it is convenient to mark *in*/*out* states and the *S*-matrix elements by the double subscript $\alpha = (s, \tau) \equiv s\tau$, where $s = \pm$ for, respectively, particles incident from the left and from the right; and τ stands for the particle kind (e.g., light (L) or heavy (H) hole), with $-\alpha \equiv -s\tau$. Multiplying the expressions for the *in*-state wave functions by $|2\pi v_\alpha|^{-1/2}$, we obtain them normalized to $\delta_{\alpha\alpha'}\delta(E - E')$. The *S*-matrix component for the channel $\beta \longrightarrow \alpha$ has the form (see Appendix)

$$S_{\alpha\beta} = X_{\alpha\beta}|v_\alpha/v_\beta|^{1/2}, \quad (8)$$

where the matrix $X_{\alpha,\beta}$ is constructed from numbers ξ in the obvious way (e.g., $X_{-H,+H} \equiv \xi_-$), and we have $|v_\alpha| = |iu_\alpha^*(2ik_\alpha a + b)u_\alpha|$ for the group velocity.

If the *S*-matrix is known, we can find the delay time in passing the well for the $\beta \longrightarrow \alpha$ channel. Indeed, if $S_{\alpha\beta} = \rho e^{i\phi}$, then

$$t_{\text{delay}}(\beta \longrightarrow \alpha) = d\phi/dE = -i\frac{d}{dE}\left(\frac{S_{\alpha\beta}}{|S_{\alpha\beta}|}\right)\frac{|S_{\alpha\beta}|}{S_{\alpha\beta}}.$$

It is noteworthy that this value depends on the choice of the "gage" (phase) of the normalized eigenvectors of the matrix u_α. In what follows, we chose the "gage" with a positive first component of the eigenvector χ_α (or u_α).

When the *S*-matrix is determined, the hole reflection and transmission coefficients can be easily calculated:

$$P_{\alpha\beta} = |S_{\alpha\beta}|^2$$
$$= \begin{cases} \text{transmission coefficient}, & \text{sgn}(\alpha) = \text{sgn}(\beta), \\ \text{reflection coefficient}, & \text{sgn}(\alpha) = -\text{sgn}(\beta). \end{cases}$$

It is important to emphasize that it suffices to find only *in*-state solutions for holes incident on the well (barrier) from the left half-space in order to find all elements of $S_{\alpha\beta}$ and, therefore, all transmission and reflection coefficients, which follows from the symmetry relation $S_{\alpha\beta} = S_{-\beta-\alpha}$ and the unitarity of the *S*-matrix.

4. RESULTS OF CALCULATIONS AND DISCUSSION

In the axial approximation, the Luttinger Hamiltonian describing states of light and heavy holes in QWs with strained layers can be represented as

$$H = \begin{pmatrix} P + Q + \zeta + V(z) & R - iS \\ R + iS & P - Q - \zeta + V(z) \end{pmatrix}. \quad (9)$$

Here, $P = \gamma_1 k^2$, $Q = \gamma_2(k_l^2 - 2zk_z^2)$, $R = \sqrt{3}/2(\gamma_2 + \gamma_3)k_l^2$, $S = 2\sqrt{3}\gamma_3 k_l k_z$, $k^2 = k_l^2 + k_z^2 = k_x^2 + k_y^2 + k_z^2$, γ_i are the Luttinger parameters of the valence band, and ζ is proportional to the difference of the lattice constants of the well and barrier materials (see [4]). Here, the well width d and $E_d = \hbar^2/2md^2$ are used as measurement units for, respectively, lengths and energies.

The method developed was applied to calculate the hole scattering on single QWs in the case of $Ga_xIn_{1-x}As$ grown on $In_{1-x}Ga_xAs_yP_{1-y}$ lattice-matched to InP, in which hole states are described by the Hamiltonian (9). The material parameters are taken from [4]. The hole transmission and reflection coefficients and delay times for passing through a QW are calculated as functions of the over-barrier energy of the incident hole for various values of the lateral component of the momentum, well width, and alloy composition x (i.e., the internal strain associated with lattice mismatch). The most interesting results of the calculation are presented in Figs. 1–4. The calculation revealed that, within the energy range in which only a heavy hole can propagate (at nonzero lateral momentum components), i.e., in the case when the channel of conversion of a heavy hole into a propagating light hole is closed (see paragraph 2.2), the hole scattering has a resonance nature. It is noteworthy that under QW compression and in the absence of stresses, i.e., at $x \le 0.468$ [4], the results depend qualitatively only on the QW size: a resonance peak in the reflection

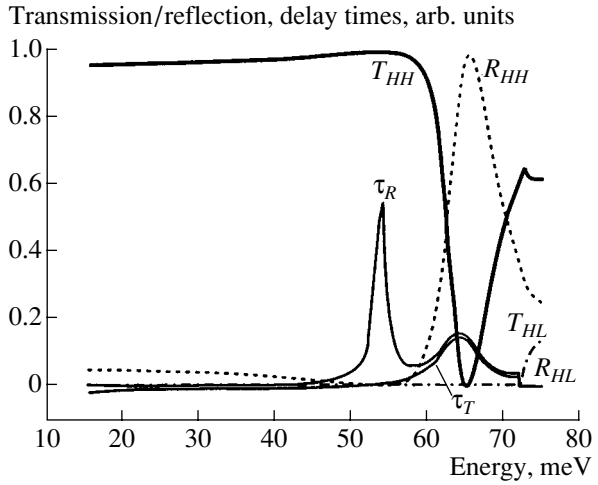

Fig. 1. Transmission (T_{HH} stands for transmission without conversion into a light hole and T_{HL}, for transmission with conversion) and reflection coefficients (R_{HH} and R_{HL}, respectively) and also delay times (τ_T and τ_R, arbitrary units) for a heavy hole incident from the left on a $Ga_xIn_{1-x}As/InGaAsP$ (InP) QW, $x = 0.468$ (unstrained lattice), of width $d = 34$ Å with the lateral quasimomentum component $k_1 = 0.03$ Å^{-1} as functions of the over-barrier energy (meV).

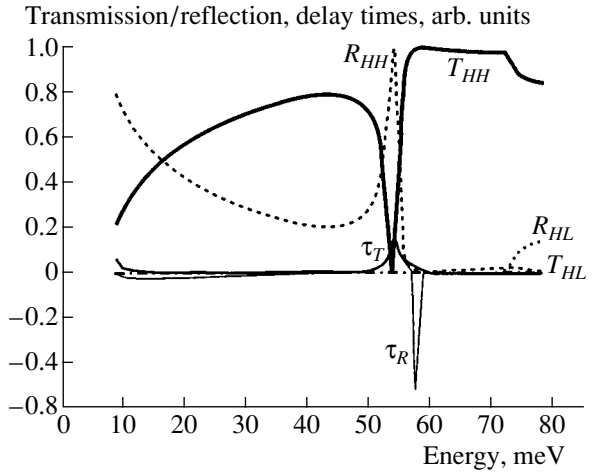

Fig. 3. The same as in Fig. 1 for $d = 48$ Å.

($R_{HH} = 1$) takes place at all QW widths, while a peak in the transmission ($T_{HH} = 1$) exists only at some QW widths, with its position relative to the reflection peak changing with increasing QW width. In the case of stretching, i.e., at $x > 0.468$, no resonance in the reflection with $R_{HH} = 1$ is observed; however, a resonance with $T_{HH} = 1$ may occur at certain well widths.

ACKNOWLEDGMENT

This study was supported in part by the Russian Foundation for Basic Research (project nos. 00-02-17429 and 00-01-00361).

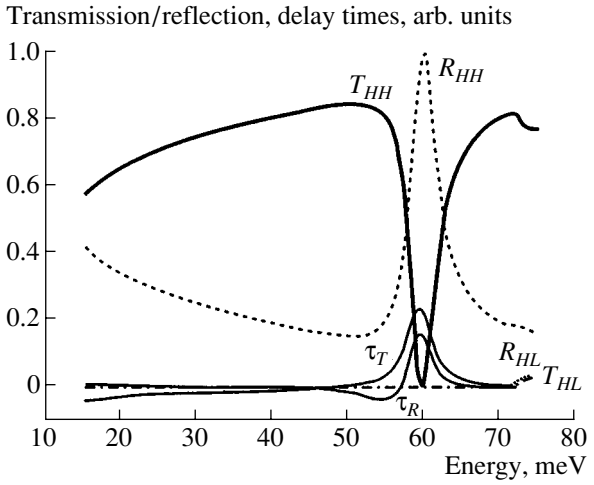

Fig. 2. The same as in Fig. 1 for $d = 42$ Å.

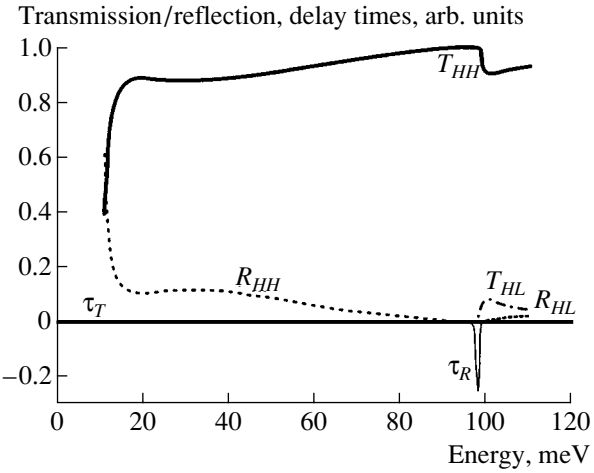

Fig. 4. The case of a strained lattice ($x = 0.69$, stretching of about 1%): $k = 0.035$ Å^{-1}, $d = 65$ Å.

APPENDIX

SCATTERING STATES AND *S*-MATRIX OF ONE-DIMENSIONAL SYSTEMS

Let us consider the Schrödinger equation (1) in the "multiwell" case, i.e., in the case when $V(z)$ is a bounded piecewise-analytic potential with a finite number of "pieces" so that

$$V(z) \sim V_1^{\pm}/z + V_2^{\pm}/z^2 + \ldots, \quad z \longrightarrow \pm\infty.$$

At $z \longrightarrow \pm\infty$, the solution $\Psi^{in}_{+\tau E}$ has the form (*in*-state wave incident from the left)

$$\Psi^{in}_{+\tau E}(z) \sim \begin{cases} e^{ik_{+\tau}z}u_{+\tau} + \sum\limits_{\tau'} X_{-\tau',+\tau} e^{ik_{-\tau'}z}u_{-\tau'}, & z \longrightarrow -\infty, \\ \sum\limits_{\tau'} X_{+\tau',+\tau} e^{ik_{+\tau'}z}u_{+\tau'}, & z \longrightarrow +\infty. \end{cases} \quad \text{(A.1)}$$

Similarly, for the *in*-state waves $\Psi^{in}_{-\tau E}$ incident from the right (in the case of $V_1^{\pm} \neq 0$), the quantities in the exponents will contain logarithmic Coulomb phases (see [2]), not given here for brevity. It is noteworthy that, if the functions $f(z)$ and $g(z)$ satisfy the Schrödinger equation (1) at the same energy E, then

$$\omega(g;\ f) \equiv g^*\left(adf/dz + \frac{1}{2}bf\right) - \left(adf/dz + \frac{1}{2}bg\right)^* f\ =\ \text{const}. \tag{A.2}$$

The group velocity $v_\alpha = idE/d\lambda$ ($\lambda = \lambda_\alpha = ik_\alpha$) can be found from the implicit n-valued function $E(\lambda)$:

$$\det(a\lambda^2 + b\lambda + c - E)\ =\ 0. \tag{A.3}$$

Indeed, it is easy to show that, if $A(t)$ is a matrix function of t, then

$$\frac{d}{dt}\det A(t) = \mathrm{tr}\left\{A^{-1}(t)\frac{dA}{dt}\right\}\det A = \mathrm{tr}\left\{A^{\vee}(t)\frac{dA}{dt}\right\}, \tag{A.4}$$

where the symbol $^{\vee}$ means an adjoined matrix: $A^{\vee} \equiv \mathrm{adj}A$. Then, from (A.4) and from the formula for the derivative of the implicit function, follows

$$v(\lambda, E)\ =\ idE/d\lambda\ =\ i\frac{\mathrm{tr}\{h^{\vee}(2a\lambda + b)\}}{\mathrm{tr}h^{\vee}},$$

where $h(\lambda, E) \equiv a\lambda^2 + b\lambda + c - E$. Let us find v at real E and $k_\alpha \equiv \lambda/i$ assuming nondegeneracy. If

$$(-ak_\alpha^2 + ibk_\alpha + c - E)u_\alpha = 0, \quad u_\alpha = u_\alpha(k_\alpha, E), \tag{A.5}$$

then $h^{\vee}\ =\ u_\alpha u_\alpha^*$ const, and, taking into account that $u_\alpha^* u_\alpha = 1$, we have

$$v_\alpha\ =\ iu_\alpha^*(2ik_\alpha a + b)u_\alpha, \quad v_\alpha\ =\ -v_{-\alpha}, \quad k_\alpha\ =\ -k_{-\alpha}; \quad u_\alpha\ =\ \bar{u}_{-\alpha}. \tag{A.6}$$

(It is noteworthy that the sign of v_α, equal to that of α, by definition, corresponds to the direction of a particle's motion; if $b \neq 0$, then it is possible that $v_\alpha < 0$ at $k_\alpha > 0$. This fact should be taken into consideration when the scattering states and the S-matrix are constructed). In addition, as seen from (A.5), the following relation holds when α and β are taken at the same energy:

$$v_\alpha\delta_{\alpha\beta}\ =\ iu_\beta^*\{i(k_\alpha + k_\beta)a + b\}u_\alpha. \tag{A.7}$$

Introducing the definition

$$S_{\alpha b}\ =\ S_{\alpha\beta}(E) \equiv X_{\alpha\beta}(E)\left|v_\alpha/v_\beta\right|^{1/2},$$

we obtain from (A.1), (A.6), and (A.7) the S-matrix satisfying the unitarity condition

$$S^*\ =\ S^{-1}. \tag{A.8}$$

If we use (A.2) for the functions $\bar{\Psi}^{in}_{\alpha E}$, $\Psi^{in}_{\beta E}$, we obtain the symmetry condition (reciprocity theorem)

$$S_{\alpha\beta}\ =\ S_{-\beta,\,-\alpha}. \tag{A.9}$$

Now, we can define

$$\Psi^{out}_{\alpha E}\ =\ \bar{\Psi}^{in}_{-\alpha E}. \tag{A.10}$$

Let us multiply *in*/*out*-state waves by $|2\pi v|^{-1/2}$. Then, applying the Sohotsky formula (excluding the energies at which the velocity vanishes), we have from (A.1)

$$\int_{-\infty}^{+\infty}\Psi^{in/out}_{\alpha E}\Psi^{in/out}_{\beta E'}dz\ =\ \delta_{\alpha\beta}\delta(E - E'),$$

$$\int_{-\infty}^{+\infty}\Psi^{out*}_{\alpha E}\Psi^{in}_{\beta E'}dz\ =\ S_{\alpha\beta}\delta(E - E'), \tag{A.11}$$

$$\Psi^{out}_{\alpha E}\ =\ \sum_\beta \Psi^{in}_{\beta E}(S^{-1})_{\beta\alpha}.$$

It is noteworthy that the relations (A.2) and (A.8)–(A.11) remain valid if we permit discontinuities of a, b, c, and Ψ, compatible with the Hamiltonian self-conjugacy, at some intermediate points between $-\infty$ and ∞. As can be easily shown, these generic properties are also valid for radial matrix Hamiltonians [2] (in this case, the constant in (A.2) vanishes because of the self-conjugacy of the radial Hamiltonian). It should be noted that an n-component problem on the interval $(-\infty, +\infty)$ is reduced to a $2n$-component problem on $(0, \infty)$, i.e., to a set of radial Schrödinger equations (see [2]).

As an example, we present formulas for the *in*-state solutions and the S-matrix in the case of $n = 1$ for the Hamiltonian

$$H\ =\ -d^2/dz^2 + V(z), \quad V(z)\ =\ \begin{cases}0, & z < 0,\\ 1, & z \geq 0.\end{cases}$$

At $0 < E < 1$, we have

$$\Psi^{in}_{+,\,E}\ =\ \pi^{-1/2}\begin{cases}p^{-1/2}\cos(pz + \theta)e^{-i\theta}, & z < 0,\\ p^{+1/2}e^{-qz - i\theta}, & z \geq 0,\end{cases}$$

where $\cos\theta = p \equiv E^{1/2}$, $0 < \theta < \pi/2$; $q \equiv |E - 1|^{1/2}$. The *S*-matrix consists of a single element $S_{-+} = e^{-2i\theta}$ at these energies. If, however, $E > 1$, then

$$\Psi^{in}_{+,E} = \pi^{-1/2}\begin{cases} \frac{p^{-1/2}}{2}\left(e^{ipz} + \frac{p-q}{p+q}e^{-ipz}\right), & z < 0, \\ \frac{p^{+1/2}}{p+q}e^{ipz}, & z \geq 0, \end{cases}$$

$$\Psi^{in}_{-,E} = \pi^{-1/2}\begin{cases} \frac{q^{+1/2}}{p+q}e^{-ipz}, & z < 0, \\ \frac{q^{-1/2}}{2}\left(e^{-iqz} + \frac{q-p}{q+p}e^{iqz}\right), & z \geq 0, \end{cases}$$

and the *S*-matrix consists of four elements:

$$\begin{bmatrix} S_{++} & S_{+-} \\ S_{-+} & S_{--} \end{bmatrix} = \begin{bmatrix} 2(pq)^{1/2} & q-p \\ p-q & 2(pq)^{1/2} \end{bmatrix}(p+q)^{-1}.$$

The scattering states also satisfy, in addition to (A.11), the completeness relation:

$$\int_0^1 \Psi^{in/out}_{+,E}(z)\overline{\Psi}^{in/out}_{+,E}(z')dE + \int_1^\infty \sum_{s=\pm} \Psi^{in/out}_{s,E}(z)\overline{\Psi}^{in/out}_{s,E}(z')dE = \delta(z-z').$$

REFERENCES

1. V. I. Galiev, E. M. Goldys, M. G. Novak, *et al.*, Superlattices Microstruct. **17**, 421 (1995).
2. V. I. Galiev and A. F. Polupanov, J. Phys. A **32**, 5477 (1999).
3. S. L. Chuang, Phys. Rev. B **40**, 10379 (1989).
4. S. L. Chuang, Phys. Rev. B **43**, 9649 (1991).

Translated by S. Ktitorov

Semiconductors, Vol. 36, No. 5, 2002, pp. 552–557. Translated from Fizika i Tekhnika Poluprovodnikov, Vol. 36, No. 5, 2002, pp. 582–586.

LOW-DIMENSIONAL SYSTEMS

Effect of Hydrogen on the Properties of Pd/GaAs/InGaAs Diode Structures with Quantum Wells

I. A. Karpovich*, S. V. Tikhov, E. L. Shobolov, and B. N. Zvonkov

Lobachevskii Nizhni Novgorod State University, pr. Gagarina 23, Nizhni Novgorod, 603600 Russia

** e-mail: fdp@phys.unn.ru*

Submitted November 26, 2001; accepted for publication November 26, 2001

Abstract—The effect of hydrogen on photoelectric properties and photoluminescence of Pd/GaAs/InGaAs diode structures with quantum wells (QWs) was investigated. The dependence of the structure characteristics on the thickness of the GaAs anodic oxide layer is revealed, and the optimum oxide thickness for the fabrication of hydrogen sensors is determined. It is established that the existence of metal bridges in a thin oxide layer has a significant influence on the *I–V* curves of the structures. It is shown that the presence of QWs leads to an increase in the structure's sensitivity to hydrogen. Using the QWs as local defect probes, formation of the defects resulting from the deposition of a Pd electrode both on natural and on anodized GaAs surface is studied. It is found that defects in the QWs of the diode structures can be passivated by introduction of atomic hydrogen through the Pd electrode upon exposure of the structures to an atmosphere of molecular hydrogen.

1. INTRODUCTION

Diode structures fabricated from Si, GaAs, and some other semiconductors with a rectifying contact made of Pd—a metal possessing high catalytic activity—are attracting much attention due to their potential as a basis for developing high-sensitivity and high-speed sensors of hydrogen [1–4]. It is known that sensor properties are manifested only in structures where the Pd contact and the semiconductor are separated by the thin layer of an insulator (native oxide is commonly used). It is believed that this layer prevents chemical interaction of Pd with the semiconductor, which results in the formation of a Pd alloy or compound with no catalytic properties. The mechanism of charge transport in diodes with a tunnel-transparent oxide layer (MOS diodes) was investigated in a number of papers [5–7].

It is of interest to examine the effect of hydrogen on Pd/GaAs diode structures with strained-layer InGaAs quantum wells (QWs) located in the contact region of GaAs, in particular, to investigate the sensor properties of such structures and the passivation of their defects by atomic hydrogen. A strained QW layer represents a potential barrier or a potential well for migrating defects and impurities, depending on whether their incorporation into the QW material increases or decreases elastic strain. It was shown [8] that InGaAs QWs located near the surface prevent the diffusion of both hydrogen and defects into the bulk of GaAs and that the presence of QWs may have a pronounced effect on the spatial distribution and the nature of the hydrogen–defect complexes formed and, thus, on the electronic properties of the structures. This can be used to enhance the structure sensor characteristics, in particular, to increase the sensitivity to hydrogen. In addition, the QWs can be used as probes sensitive to the presence of defects [9], which helps one gain insight into the interaction between Pd and GaAs.

Passivation of the defects and impurities by atomic hydrogen has been widely investigated in homogeneous semiconductors (see, e.g., the review [10]), and, in recent years, it has been studied in quantum-confinement structures [8, 11–13]. Commonly, atomic hydrogen is incorporated into semiconductor structures from gas-discharge hydrogen plasma, in which case it is difficult to avoid the generation of defects at the surface during hydrogenation. Thus, it is of interest to investigate the possibility of defect-free incorporation of atomic hydrogen from a molecular-hydrogen atmosphere using the catalytic properties of a Pd electrode.

The purpose of this study was to examine the effect of hydrogen on the properties of Pd/GaAs diode structures with a layer of anodic oxide grown on GaAs and with InGaAs QWs embedded near the GaAs surface. We investigated the photoelectric properties of these structures, their sensitivity to hydrogen, and the formation of defects and their passivation by hydrogen.

2. EXPERIMENTAL

GaAs/InGaAs QW heterostructures were grown by atmospheric-pressure gas-phase epitaxy using In and Ga metal-organic compounds and arsine (MOCVD method) on (100)-oriented *n*-GaAs substrates with an electron density $n_0 \approx 10^{16}$ cm^{-3}. Three $In_xGa_{1-x}As$ QWs ($x \approx 0.2$) were located in the space-charge region of the *n*-GaAs layer; their thicknesses were about 10, 5, and 3 nm for the first, second, and third QW from the sur-

face, respectively. The thickness of the GaAs layers separating the QWs, as well as that of the cap GaAs layer, was ~30 nm, and the thickness of the entire epilayer was 0.6 μm. Prior to Pd deposition, the cap GaAs layer was typically subjected to anodic oxidation in a 3% solution of tartaric acid with ethylene glycol (1 : 1) to a depth from 2 to 14 nm. A semitransparent Pd electrode, nominally 20 nm thick, was deposited on the structure at a temperature of 100°C by thermal evaporation in a vacuum chamber.

The effect of hydrogen on the structure characteristics was investigated either under the working conditions of a gas sensor or under the normal conditions upon thermal treatment in a hydrogen atmosphere. In the first case, we studied the changes in the characteristics of the structures at $T = 100$°C upon exposure to an air–argon mixture with the hydrogen volume content C_H from 0.2 to 4%. In the second case, we studied the changes in the room-temperature characteristics of the structures induced by short-term annealing in hydrogen at atmospheric pressure.

We measured the current–voltage characteristics $I(V)$, the open-circuit photovoltage V_{ph}, the short-circuit photocurrent I_{ph}, and the photoluminescence (PL) spectra $I_{PL}(h\nu)$; the PL spectra were measured at 77 K.

3. RESULTS AND DISCUSSION

In as-grown Pd/GaAs diode structures, the contact barrier height was $\varphi_0 = 0.8$–0.9 eV and the nonideality factor m of the forward current–voltage characteristic ($I \propto \exp(qV/mkT)$) was equal to 1.01. However, after thermal treatment of the structures at 100°C, φ_0 was reduced by 0.1 eV and m increased to 1.07; during subsequent measurements, these parameters remained virtually unchanged. Blowing of the structures by a hydrogen-containing gas mixture at 100°C led to a decrease in the barrier height, which manifested itself in a shift of the forward $I(V)$ curve to lower voltages by ΔV_I at a given current, and to a reduction in the photovoltage by ΔV_{ph}. These values were used to characterize, respectively, the current and voltage sensitivities of the structures to hydrogen.

3.1. Dependence of the Structure Characteristics on the Anodic Oxide Layer Thickness

Interest in this issue is related to the important role of the insulator layer in the operation of gas sensors. For MOS structures of the type considered in this study, there are no relevant data available.

One can see from Fig. 1 that, for small oxide thicknesses d_{ox} (up to 4 nm), the photovoltage increases with d_{ox} by approximately 1.5 times (curve *1*). This indicates that the height of the barrier in GaAs increases as a result of anodization. This is probably due to the formation of built-in negative charge in the oxide layer [14]. The sensitivity to hydrogen appears only in the structures where oxide is grown (see curves *2*, *3*), which is mainly related to the weakening of the chemical interaction between Pd and GaAs [15].

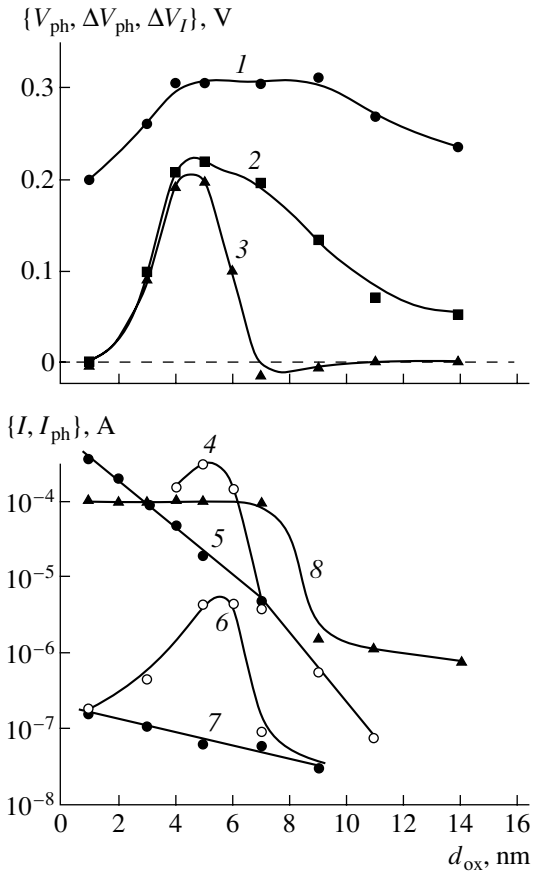

Fig. 1. Dependences of the characteristics of the diode structures on the thickness of the GaAs anodic oxide layer: (*1*) photovoltage V_{ph}, (*2*) voltage sensitivity to hydrogen ΔV_{ph}, (*3*) current sensitivity to hydrogen ΔV_I, (*4*) forward current I through the diode structure exposed to a flow of hydrogen-containing gas mixture, (*5*) forward current I through the diode structure in air, (*6*) reverse current I through the diode structure exposed to the flow of a hydrogen-containing gas mixture, (*7*) reverse current I through the diode structure in air, and (*8*) short-circuit photocurrent I_{ph}. $T = 100$°C, hydrogen content $C_H = 4$%.

When the oxide thickness exceeds ~5 nm, the sensitivity to hydrogen is reduced. The current sensitivity (given by ΔV_I, curve *3*) falls off more rapidly and virtually disappears, while the voltage sensitivity (curve *2*) decreases more slowly with increasing d_{ox}. Note that a decrease in the photovoltage is rather small even for the largest oxide thicknesses. Interestingly, an unusual drop in the forward current upon exposure to hydrogen (i.e., $\Delta V_I < 0$) is observed in a certain range of d_{ox}. It is obvious from the data represented by curves *2* and *3* that the optimum oxide layer thickness, corresponding to the highest sensitivity of the structure to hydrogen, is 4–5 nm.

The forward current (curve *5*) decreases exponentially with an increase in the oxide thickness; there is a

knee at $d_{ox} \approx 7$ nm. The dependence of the reverse current on the oxide thickness is much weaker (curve *7*). The theory of tunnel MOS diodes [7] predicts a qualitatively similar dependence of the forward and the reverse currents on the insulator thickness. However, the height of the potential barrier formed by the oxide layer, calculated in the context of this theory from the slope of the experimental dependences, appears to be extremely low: assuming a trapezoidal barrier shape, we obtain ~10 meV. Meanwhile, the actual barrier height is ~1.6 eV [16], and this discrepancy cannot be explained by theory. Furthermore, on the basis of the tunneling mechanism of the charge transport, it is difficult to explain the fact that the short-circuit photocurrent is independent of d_{ox} up to the oxide thickness of ~7 nm (see curve *8*).

We believe that these features (the relatively weak dependence of the forward current on d_{ox} and the absence of the photocurrent dependence on d_{ox}) are related to the presence of numerous microscopic Pd bridges in the thin oxide layer; they are probably formed as a result of the existence of pores in the oxide. These bridges may extend through the entire oxide layer when its nominal thickness d_{ox} is small enough; however, as d_{ox} increases, more and more of them terminate within the oxide. In such a situation, the local effective thickness of the oxide layer in those regions where the current mainly flows may be considerably smaller than the nominal thickness, when the latter is sufficiently small. This explains the deviation of the calculated tunnel-barrier height from its true value. From this point of view, in the range of small d_{ox}, an increase in its value leads to a reduction in the effective area of the diode structure. This mainly affects the forward dark current, since, under the forward-bias conditions, the internal resistance of the diode is low. At the same time, the photoactive area of the structure, which controls I_{ph}, remains unchanged and is essentially equal to the geometric area of the Pd contact. Until the resistance of the bridges becomes comparable to the internal resistance of the illuminated diode, they will control the value of I_{ph}. The presented model, explaining the special features of the oxide-thickness dependence of the electric and photoelectric properties of the diode structures, is corroborated by the fact that the nonideality factor of the *I–V* characteristic remains very close to unity for an oxide thickness no larger than ~5 nm. It should also be noted that the anodic oxide films are known to have through holes; as the film thickness increases, these holes become filled with oxide and evolve into sites of local film thinning [17].

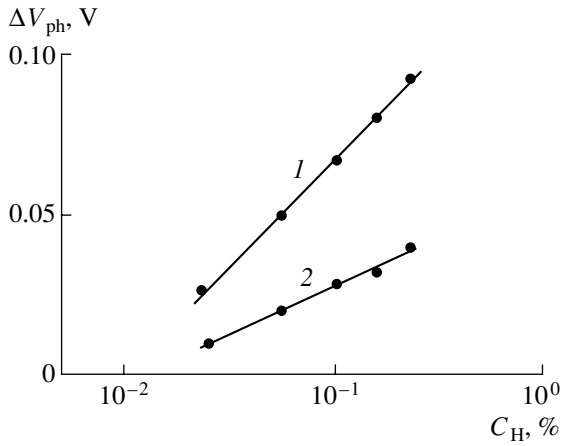

Fig. 2. Response of the diode structures (*1*) with QWs and (*2*) without QWs as a function of the hydrogen content.

In a hydrogen-containing atmosphere, a considerable increase in the forward current and a still larger increase in the reverse current take place (see curves *4*, *6*). In the structures with an oxide layer of optimum thickness (which corresponds to the peak in curve *2*), the rectification effect virtually disappears and the photovoltage decreases by a factor of three; this indicates that the barrier height in GaAs becomes drastically reduced under the effect of hydrogen. It is known that the Fermi level is pinned near the midgap at the surface of GaAs, which results in the formation of a depletion layer. The corresponding barrier height equals ~0.7 eV and is almost independent of the chemical nature of the metal in the diode structure. According to [4], the reduction of the barrier height under the effect of hydrogen is mainly related to the chemisorption of atomic hydrogen at the oxide/GaAs interface: electrons are transferred to GaAs, whereas protons remain at the interface, which leads to a decrease in the net negative charge at the surface. This model adequately explains the mechanism of the sensitivity of the diode structures to hydrogen and the sensitivity behavior as a function of the oxide thickness. A decrease in the voltage sensitivity may be ascribed to the fact that the oxide thickness becomes comparable to the hydrogen diffusion length. A sharp drop in the current sensitivity may be assumed to originate from the voltage redistribution between the barrier and the metal bridges as a result of a reduction in the internal diode resistance under the effect of hydrogen. For $d_{ox} \approx 8$ nm, metal bridges are no longer important for the process of the charge transport and the oxide layer acts as a series resistance limiting the current through the structure. In this case, the rectification effect almost disappears and the photocurrent drops by two orders of magnitude.

3.2. The Role of Quantum Wells in the Sensitivity of the Structures to Hydrogen

The response of the structures with and without QWs to the inflow of hydrogen is plotted in Fig. 2 as a function of hydrogen concentration. One may conclude that the presence of QWs near the surface of GaAs increases the structure sensitivity. This effect is especially significant in the structures with a thin oxide layer. It is reasonable to assume that the sensitivity increases because the strained-layer QWs, located in

the vicinity of the surface, prevent the diffusion of hydrogen into the bulk of GaAs [8], which increases hydrogen concentration in the oxide layer and at the oxide/semiconductor interface.

Studying the kinetics of the structure response to the exposure to hydrogen, we found that the relaxation times are nearly the same for the structures with and without QWs. When the hydrogen flow is switched on, the relaxation time is ~1 s; when it is switched off, the relaxation time is ~10 s. In the latter case, the relaxation rate increased by about an order of magnitude under the application of a reverse bias to the diode. This can be attributed to a change from the outward diffusion mechanism of relaxation to the electric-field-driven transport of protons in the oxide layer.

It should be noted that no residual effect of exposure to hydrogen under the gas-sensor operation conditions was observed in the PL of the QWs, even if the structures were cooled down in the flow of a hydrogen-containing mixture.

3.3. Defect Formation and Hydrogen-Induced Defect Passivation in the Structures under Study

The PL of QWs located close to the surface of the semiconductor is very sensitive to the processes of defect formation that occur at the surface and originate, in particular, from the chemical reactions taking place there.

Upon anodic oxidation of the GaAs surface, a damaged region is formed in the semiconductor near the interface with the oxide; its thickness is ~10 nm [9]. If this region extends to reach the QWs, their PL is quenched drastically. In the structures under study, where the thickness of the cap layer is ~20 nm, no quenching of the QW luminescence was observed when the thickness of the oxide layer was ~5 nm, which is optimal for the sensor applications (note that the thickness of the GaAs layer consumed to form the oxide is $\sim 0.65 d_{ox}$). However, when the oxide thickness approaches 12 nm, the PL of the QW closest to the surface is quenched completely.

It was found that the process of the Pd electrode deposition at 100°C also results in a considerable quenching of the PL from the QWs located below the electrode, irrespective of whether it was deposited on the natural or on the anodized GaAs surface (see Fig. 3). This effect is not related either to the optical properties of the electrode or to an increase in the recombination rate at the oxide/GaAs interface. This is shown by the fact that the PL quenching was less pronounced for the QWs farther away from the surface and was virtually not observed in the GaAs band-edge emission. Pd deposition, like anodic oxidation of the surface, leads to the formation of defects (acting as nonradiative recombination centers) in the surface region of GaAs; this corroborates the assumption about the chemical nature of the interaction between Pd and GaAs [15]. However, primary defects formed upon Pd deposition (probably, vacancies in the Ga sublattice) have a larger diffusion coefficient than those generated upon anodizing and reach, at least, the location of the third QW; i.e., they penetrate as deeply as ~100 nm from the surface.

The degree of PL quenching can be characterized by the ratio I_{PL}/I^0_{PL}, where I^0_{PL} and I_{PL} are the PL intensities before and after Pd deposition, respectively. The quenching of the PL in the first QW becomes more pronounced with increasing thickness of the Pd layer d_{Pd}; the dependence levels off at $d_{Pd} \sim 10$ nm (see Fig. 4, curve *2*). With an increase in the thickness of the oxide layer, separating the GaAs surface from the Pd layer, the effect becomes less profound (see curve *3*). For $d_{ox} = 13$ nm, the PL intensity of the first QW practically does not change upon Pd deposition, which, apparently, means that chemical interaction between Pd and GaAs vanishes completely. At the same time, the current–voltage characteristics of the diode structures with a very thin oxide layer indicate that the density of the defects introduced upon Pd deposition is not too high and the damage introduced can hardly be detected by other techniques that are less sensitive than the QW PL method.

Curve *1* in Fig. 4 shows the dependence of PL quenching on the distance to the corresponding QW. The dependence is nearly exponential. Making a reasonable assumption that it represents the spatial distribution of the defect complexes acting as quenching centers, we can determine the diffusion length L_D of the primary defects that form these complexes. The calculation yields $L_D \approx 50$ nm, which is consistent with the rough estimate given above.

Note that pronounced quenching of the PL from the first QW was also observed when the GaAs surface was coated with a layer of nickel; this was not observed upon deposition of gold. Since Pd, Ni, and Au have rather close lattice constants, we conclude that the

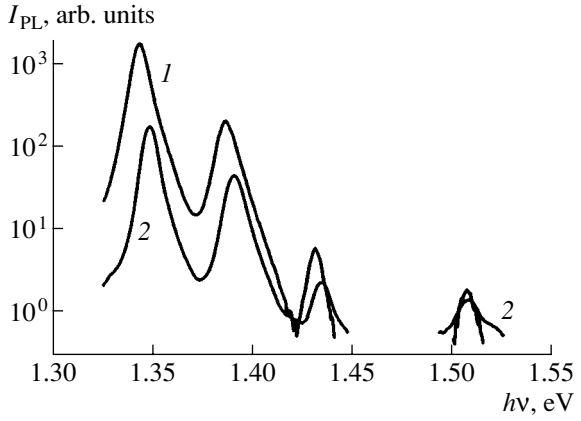

Fig. 3. The PL spectrum of a diode structure (*1*) before and (*2*) after the deposition of the Pd electrode.

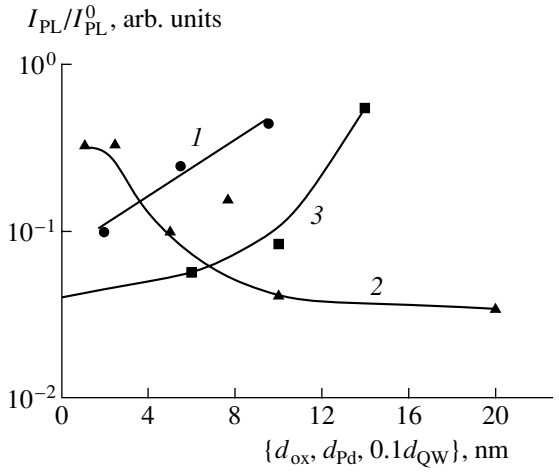

Fig. 4. Dependences of the degree of PL quenching in QWs upon the deposition of a Pd electrode on (*1*) the distance from the QW to the surface d_{QW}, (*2*) the Pd layer thickness d_{Pd}, and (*3*) the oxide-layer thickness d_{ox} (curves *2* and *3* correspond to the first QW).

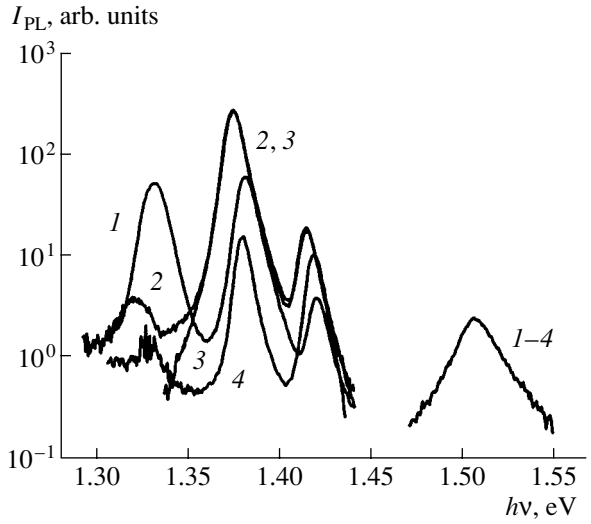

Fig. 5. The PL spectra of the diode structures with QWs after treatment in hydrogen at atmospheric pressure; the treatment temperature is (*2*) 200, (*3*) 250, and (*4*) 350°C. Curve *1* represents the PL spectrum before the treatment.

defect formation upon metal deposition has a mostly chemical origin.

Figure 5 illustrates the effect of thermal treatment of the diode structures in hydrogen at different temperatures under atmospheric pressure. The PL from the first QW becomes almost completely quenched after hydrogen treatment for all temperatures. An increase in the PL intensity, related to the defect passivation, is observed only in the second and third QWs. In the second QW, the PL intensity increases by more than an order of magnitude after thermal treatment at 200–250°C; however, with a further increase in temperature, PL quenching occurs. Only in the third QW does the passivation effect take place for all temperatures. The edge PL from GaAs remains unchanged in all cases. It should be noted that these treatments had no effect on the PL from the areas of the sample not coated with Pd. The PL quenching is probably related to the defect formation as a result of chemical interaction between Pd and GaAs. This is suggested by the observation that the sensitivity of the diode structures to hydrogen disappears after the treatment. Thus, the PL spectra in Fig. 5 illustrate the competition between the processes of defect formation and hydrogen-induced defect passivation, which occur at different distances from the contact with changing temperature.

4. CONCLUSION

The studies reported indicate that Pd/GaAs/InGaAs diode structures with quantum wells feature enhanced sensitivity to hydrogen and are promising for the development of gas sensors. It is also shown that quantum wells located in the surface region of GaAs can be used as probes that are quite sensitive to the processes of defect formation caused by surface chemical reactions, in particular, those accompanying surface oxidation and metal deposition on GaAs. It is demonstrated that defect passivation in the structures under study can be accomplished by the introduction of atomic hydrogen through the Pd electrode during the treatment of these structures in an atmosphere of molecular hydrogen.

ACKNOWLEDGMENTS

This study was supported by the Russian Foundation for Basic Research (project no. 00-02-17598) and the program “Universities of Russia” (project no. 015.06.01.37).

REFERENCES

1. A. V. Evdokimov, M. N. Murshudli, A. V. Rzhanov, *et al.*, Zarubezhn. Élektron. Tekh., No. 2, 231 (1988).
2. G. G. Kovalevskaya, M. M. Meredov, E. V. Russu, *et al.*, Zh. Tekh. Fiz. **63** (2), 185 (1993) [Tech. Phys. **38**, 149 (1993)].
3. S. V. Tikhov, V. P. Lesnikov, V. V. Podol’skiĭ, and M. V. Shilova, Zh. Tekh. Fiz. **65** (11), 120 (1995) [Tech. Phys. **40**, 1154 (1995)].
4. V. I. Gaman, M. O. Duchenko, and V. M. Kalygina, Izv. Vyssh. Uchebn. Zaved., Fiz., No. 1, 69 (1998).
5. H. C. Card and E. H. Rhoderick, J. Phys. D **4**, 1589 (1971).
6. G. Lewicki, J. Appl. Phys. **47**, 1552 (1976).
7. V. Kumar and W. E. Dahlke, Solid-State Electron. **20**, 143 (1977).
8. I. A. Karpovich, A. V. Anshon, and D. O. Filatov, Fiz. Tekh. Poluprovodn. (St. Petersburg) **32**, 1089 (1998) [Semiconductors **32**, 975 (1998)].

9. I. A. Karpovich, A. V. Anshon, N. V. Baĭdus', *et al.*, Fiz. Tekh. Poluprovodn. (St. Petersburg) **28**, 104 (1994) [Semiconductors **28**, 63 (1994)].
10. M. Stavola, Acta Phys. Pol. A **82**, 585 (1992).
11. Y.-L. Chang, I.-H. Tan, E. Hu, *et al.*, J. Appl. Phys. **75**, 3040 (1994).
12. Yu. A. Bumaĭ, B. S. Yavich, M. A. Sinitsyn, *et al.*, Fiz. Tekh. Poluprovodn. (St. Petersburg) **28**, 276 (1994) [Semiconductors **28**, 166 (1994)].
13. S. M. Lord, G. Roos, J. S. Harris, and N. M. Johnson, J. Appl. Phys. **73**, 740 (1993).
14. S. V. Tikhov, B. I. Bednyĭ, I. A. Karpovich, and V. V. Martynov, Mikroélektronika **10** (3), 250 (1981).
15. L. M. Krasil'nikova, I. V. Ivonin, M. P. Yakubenya, *et al.*, Izv. Vyssh. Uchebn. Zaved., Fiz., No. 3, 60 (1989).
16. S. V. Tikhov, V. V. Martynov, I. A. Karpovich, and B. I. Bednyĭ, Élektron. Tekh., Ser. 2 **6** (157), 18 (1982).
17. L. L. Odynets and V. M. Orlov, *Anodic Oxide Films* (Nauka, Leningrad, 1990).

Translated by M. Skorikov

Semiconductors, Vol. 36, No. 5, 2002, pp. 558–563. Translated from Fizika i Tekhnika Poluprovodnikov, Vol. 36, No. 5, 2002, pp. 587–592.

AMORPHOUS, VITREOUS, AND POROUS SEMICONDUCTORS

The Interrelation of Surface Relief of Porous Silicon with Specific Features of Raman Spectra

B. M. Bulakh[1], B. R. Jumayev[1], N. O. Korsunska[1]*, O. S. Litvin[1], T. V. Torchynska[1, 2], L. Yu. Khomenkova[1], and V. O. Yukhymchuk[1]

[1] *Institute of Semiconductor Physics, National Academy of Sciences of Ukraine, Kiev, 03028 Ukraine*

[2] *Instituto Politecnico Nacional, U.P.A.L.M., 07738, Mexico D.F.*

**e-mail: kors@lumin.semicond.kiev.ua*

Submitted June 13, 2001; accepted for publication July 11, 2001

Abstract—Structural characteristics and Raman spectra of porous silicon layers were investigated. It was demonstrated that the effect of enhancement of the signal intensity of Raman scattering from porous silicon compared with the signal intensity from the substrate is associated with the presence of micrometer-size pores in the samples. A model making it possible to explain this enhancement, the signal shape, and the coincidence of the signal from the porous layer by the shape and location with the line from the Si substrate is suggested.

1. INTRODUCTION

To elucidate the mechanism of luminescence of porous Si (*por*-Si), as well as for its practical applications, it is desirable to obtain information on its structure using nondestructive methods. For this purpose, the methods of Raman scattering [1, 2] and atomic force microscopy (AFM) [3, 4] are often used.

However, the application of these methods for *por*-Si involves certain difficulties. For AFM, they are known and are associated mainly with the resolution of the method. However, for Raman spectroscopy, the situation is not so simple. For example, a number of factors which affect the results of Raman investigations are well known. Specifically, these effects are associated with heating the sample, strains, etc. In addition to these effects, the phenomenon reported in [5] has not yet obtained an unambiguous interpretation. Specifically, in some cases, the intensity of the Raman line from the porous layer significantly (by a factor as large as 10) exceeded the intensity of the line from the substrate with the coincidence of their frequency location and shape. It was assumed [5] that the above effect was associated with the presence of a considerable amount of nanometer-sized crystallites in the *por*-Si layer, which were strictly oriented along the normal to the substrate. In this case, an increase in the intensity of the Raman signal is caused by the increasing propagation depth of light for such crystallites compared with bulk Si because of the widening of their band gap due to the quantum-mechanical size effect. Obviously, in order to verify this hypothesis and elucidate the distinctions between conventional *por*-Si layers and layers in which the amplification effect manifests itself, it is worthwhile to carry out independent investigations of their structure.

At the same time, other explanations of the increasing intensity of the Raman signal are also possible. Specifically, it can, in principle, be associated with the surface amplification (giant Raman scattering) or with resonance Raman scattering [6].

In this study, the results of the investigation of *por*-Si layers by methods of optical and scanning electron (SEM) microscopy, as well as AFM and Raman spectroscopy, were compared and an alternative explanation of the effect described above was given.

2. EXPERIMENTAL

The *por*-Si layers were obtained by anodic etching of *p*-Si(100) substrates with the resistivity $\rho = 10\ \Omega$ cm. To obtain layers with different structures, the electrolyte composition and anodizing conditions were varied. Alcohol solutions of concentrated hydrofluoric acid with various compositions were used as electrolytes. These were a water-containing solution HF : H_2O : C_2H_5OH (1 : 1 : 2) for group *A* samples and a nonaqueous solution (the same composition with proportions of 1 : 0 : 1 or 2 : 0 : 1) for group *B* samples. The anodizing current density (j_A) was varied in the range of 5–100 mA/cm^2, and the etching time (Δt_A) was varied from 5 to 40 min. All measurements were carried out at room temperature.

To investigate the structure of the layers, a NEOPHOT-21 optical microscope and a JSM-T20 (JEOL) scanning electron microscope, as well as a Nanoscope IIIa (Digital Instruments) atomic-force microscope, were used. In the last case, the measurements were carried out in the taping mode. The radius of curvature of the Si probe was 5–10 nm. In order to reveal narrow pores with a higher reliability, the mode

of varying the phase of the probe resonance vibration was used simultaneously with the mode of recording the surface topography by varying the probe vibration amplitude.

The Raman spectra were measured at room temperature using a system based on a DFS-24 spectrophotometer. The radiation of an argon laser with a wavelength of 487.9 nm was used for excitation. The power density of laser emission was no higher than 1.5 W/cm^2. The signals were detected using a cooled FEU-136 photomultiplier in the photon-counting mode.

3. RESULTS

3.1. Investigation of the Macrostructure of por-Si Layers

3.1.1. Group *A* samples. Investigations of *por*-Si layers, which were obtained by anodizing in the HF : H_2O : C_2H_5OH = 1 : 1 : 2 electrolyte, demonstrated that their macrostructure depends heavily on anodizing conditions. For short times (Δt_A) and low currents (j_A), the etched *por*-Si layers are rather homogeneous. With increasing j_A or Δt_A, grooves emerge in these layers, which separate rather large (about tens μm) homogeneous regions (islands). In this case, the grooves become threaded by micrometer-sized pores (macropores), which are separated by dividing Si walls, which are also micrometer-size (Fig. 1). It should be noted that the islands contain no such pores.

A further increase in j_A or Δt_A leads to widening of the grooves and, correspondingly, to narrowing of the islands between them. The diameter of macropores simultaneously increases, which leads, correspondingly, to a decrease in the thickness of the dividing walls between them. For a sufficiently large current or etching time, these islands can be completely removed by etching. In this case, the layer as a whole constitutes a structure threaded with macropores.

3.1.2. Group *B* samples. Upon anodizing Si in a nonaqueous etchant (HF : H_2O : C_2H_5OH = 1 : 0 : 1 and 2 : 0 : 1), the formation of macropores was not observed for any of the etching conditions used.

3.2. Investigation of the Nanostructure of por-Si Layers

Investigations of group *A* samples demonstrated that the islands between the grooves, which have no pronounced macroporous structure, and the dividing walls between the pores consist of nanometer-size hillocks (Fig 2a). These hillocks apparently correspond to the vertices of Si crystallites, whereas the hollows between them correspond to the outcrop of narrow (nanometer) pores on the surface. A similar structure is also observed at the bottom and on the walls of the macropores; i.e., the macrostructure of group *A* samples is modulated with a nanorelief.

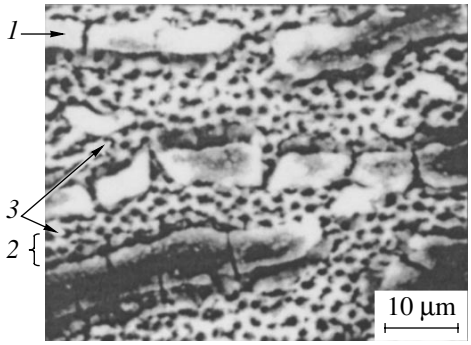

Fig. 1. SEM image of the surface of the group *A por*-Si sample anodized at j_A = 50 mA/cm^2 and Δt_A = 10 min: (*1*) Islands, (*2*) a groove with macropores, and (*3*) macropores.

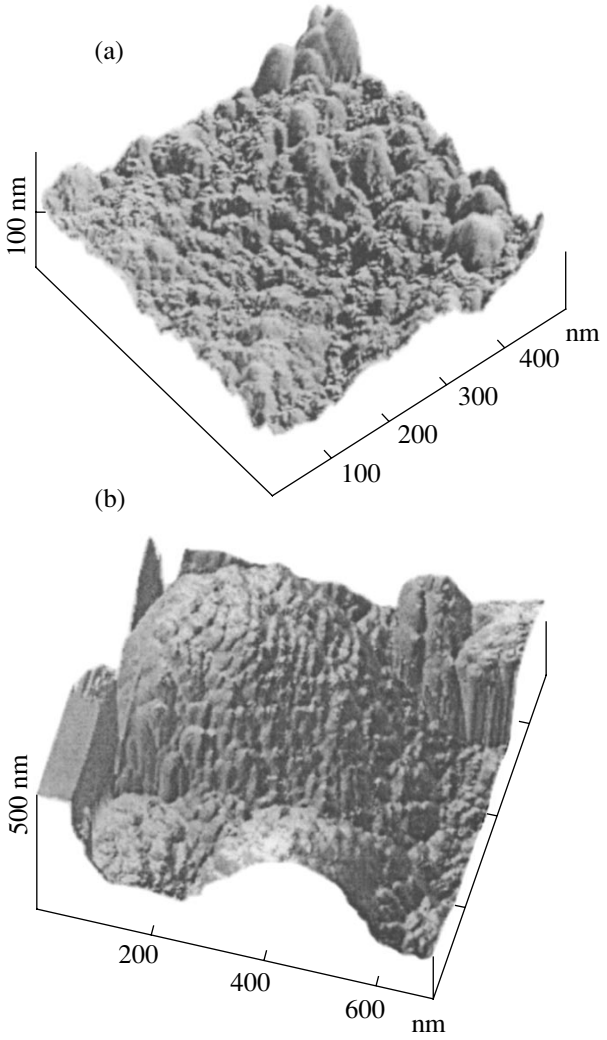

Fig. 2. AFM image of the island structure in the group *A por*-Si samples anodized at j_A = (a) 25 mA/cm^2 and (b) 100 mA/cm^2; Δt_A = 10 min.

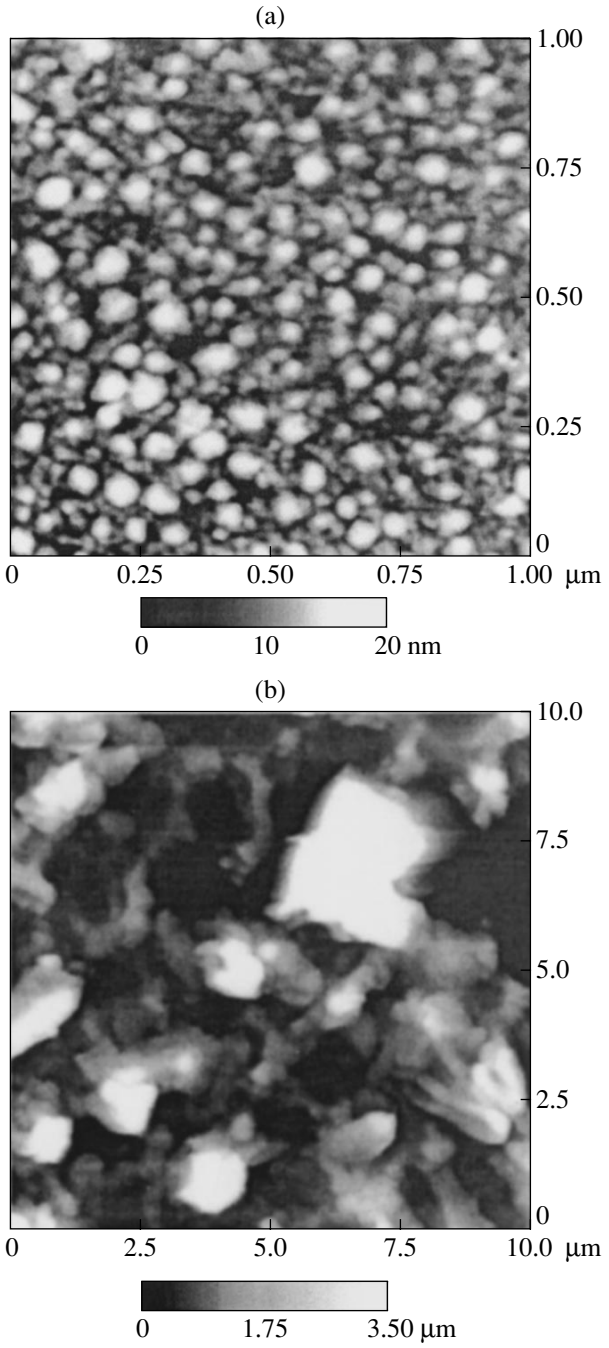

Fig. 3. AFM images of a group *B por*-Si sample anodized at j_A = 20 mA/cm^2 and Δt_A = 20 min in the HF : H_2O : C_2H_5OH = 1 : 0 : 1 electrolyte. (a) Immediately subsequent to fabrication and (b) subsequent to exposure to water for 24 h at room temperature.

For group *A* samples, the lateral dimensions of the hillocks, which were determined from transverse sections of AFM images as their largest linear dimensions at a base, are in the range of 15–150 nm. Note that in some cases, for example, for the sample obtained at j_A = 100 mA/cm^2, the structure can be more complex. It consists of very large hillocks, which include a finer relief (Fig. 2b) and which have lateral dimensions of 150–400 nm and a height of 80–250 nm. Lateral dimensions of the elements of this relief are 15–25 nm, and the height is 10–15 nm.

The AFM images of the structure of the dividing walls between the pores and the bottom of pores adjoined to walls were compared. The comparison demonstrated that, for certain group *A* samples, the horizontal dimensions of hillocks in the depth of the pores were considerably larger compared with the dividing walls.

The AFM investigations of group *B* samples demonstrate that a large number of hillocks with lateral dimensions of 15–25 nm are present in them (Fig. 3a).

Note that the actual lateral dimensions of the elements of the structure are smaller than the dimensions of the AFM images by approximately the doubled radius of the probe tip. This is associated with the effect of convolution of the shape of the probe tip with the surface features on the order of several nanometers. This means that for group B samples, the number of nanometer-sized crystallites is larger compared with group *A* samples.

3.3. Investigation of Porous Layers by Raman Spectroscopy

For group *B* samples, the intensity of Raman lines from the porous layer was comparable or lower than the intensity of the line from the substrate. In this case, two types of spectra were detected. For some samples, similarly to the data [1, 4, 7], along with the line, the location of which coincides with that of the line from the substrate, a pronounced wide shoulder was present on the low-frequency side (Fig. 4a, curve *1*). For other samples, a single broad line was observed. Its location was shifted to the lower frequencies compared with the location of the line from the substrate (curve *2*). Obviously, the first type of spectrum is caused by the superposition of the signal from the substrate, due to the fact that the excitation light propagates in the substrate.

The spectra of **group *A* samples**, which were obtained with small anodizing currents (j_A = 5–10 mA/cm^2), were similar to the spectra of group *B* samples. For the samples which were obtained by anodizing at j_A > 10 mA/cm^2, the intensity of the Raman signal from the porous layer substantially exceeded the intensity of the signal from the substrate and increased with the prolongation of the anodizing time (Fig. 4b, curves *1*, *2*). In this case, as a rule, the Raman line from the porous layer was symmetric and had the same half-width as the line from the substrate. Only in some cases this line was broadened or asymmetric at its base and could differ in its position from the line from the substrate (Fig. 4b, curve *3*).

Note that the Raman spectra, which were measured for various angles of incidence of excitation radiation, were not substantially different for all group *A* samples.

4. DISCUSSION

As can be seen from the above results, the *por*-Si layers investigated differ significantly in the macrostructure. The micrometer-size pores are present in group *A* samples, which were obtained at $j_A > 10$ mA/cm^2. For all other group *A* and group *B* samples, these pores are not observed.

The comparison of AFM images of the samples with a different macrostructure, namely, with macropores and without them, demonstrates that distinctions in their nanostructure also exist: for group *B* samples, a larger number of crystallites are detected. In addition, the nanostructures of various areas of the same sample with macropores can also differ. For example, such a difference can be seen when we compare the structures of a walls between macropores and the bottom of pores adjoining these walls. For some samples, the lateral dimensions of the nanostructure on the bottom of the pores are larger compared to those for the dividing walls between them.

An increase in the crystallite size, observed on the pore bottom, can be explained as follows. It is known that a decrease in the HF concentration should lead to an increase in the contribution of electropolishing processes, which, in turn, can cause an increase in the average crystallite size [8]. Such a process can apparently occur in the depth of macropores due to poor etchant exchange between the pores and an electrolytic cell. In addition to an increase in the crystallite size, this can also lead to a decrease in the thickness of the nanoporous layer on the macropore bottom. It follows from the aforesaid that the relationship between the processes of electropolishing and pore formation should depend on the pore width. Consequently, for a sufficiently large pore size, it is possible to expect the formation of nanometer-sized crystallites also in the pore depth.

Thus, AFM investigations reveal the presence of nanometer-sized crystallites in all layers investigated. However, because of the limited resolution of the method, which is determined by the radius of probe curvature, it seems impossible to determine the number and predominant dimensions of the crystallites.

Seemingly, information on the dimensions of Si crystallites can be obtained from Raman spectra. However, for a number of group *A* samples, only the line whose position coincides with that of the line from the substrate is observed in Raman spectra. The intensity of this line increases with increasing etching time. For this reason, it is possible to assume that, despite the coincidence noted, this line is nevertheless related to the porous layer.

The results of the investigation of the layers' macrostructure and Raman spectra were compared. Such a comparison allows one to elucidate the possible cause of this phenomenon and to suggest a model which will explain not only the intensity but also the shape of the Raman signal from *por*-Si.

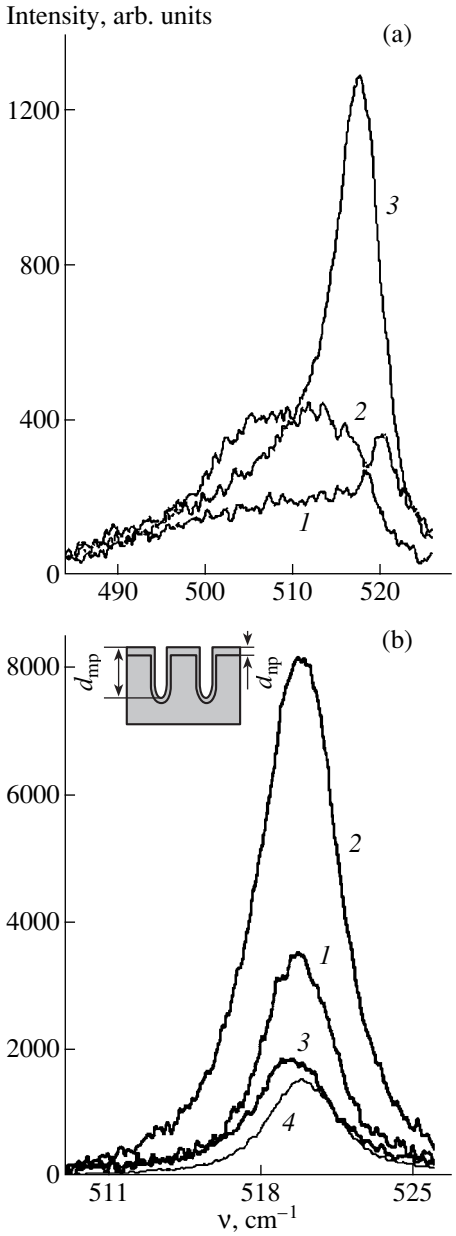

Fig. 4. Raman spectra for *por*-Si layers: (a) from group *B*, (*1*, *2*) prior to exposure to water and (*3*) subsequent to exposure; (b) from group *A*. Anodizing conditions of the layers for the spectra in Fig 4a: Δt_A = 20 min; j_A: (*1*, *3*) 10 and (*2*) 50 mA/cm^2; the anodizing electrolyte composition HF : C_2H_5OH: (*1*, *3*) 2 : 1 and (*2*) 1 : 1. Spectra in Fig. 4b: Δt_A = (*1*, *3*) 10 and (*2*) 40 min; j_A: (*1*, *2*) 50 and (*3*) 100 mA/cm^2. Curve *4* corresponds to the spectra from the Si substrate. The *por*-Si structure is schematically represented in the inset for the explanation of specific features of the spectra; d_{np} and d_{mp} stand for the thicknesses of nanoporous and macroporous layers in the sample, respectively.

As follows from Figs. 1 and 4, an excess of the intensity of the Raman signal from the porous layer over the intensity of the signal from the substrate is observed only for the samples in which macropores are detected. This permits one to associate the phenomenon

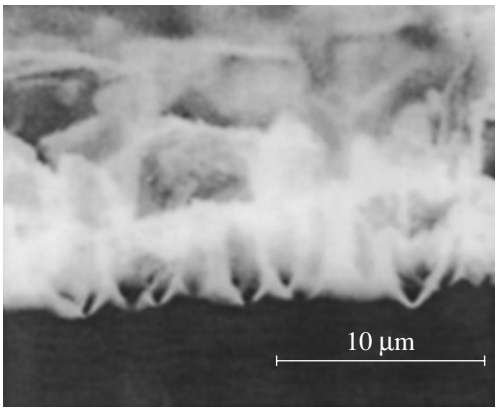

Fig. 5. SEM image of the transverse section of the group *A* *por*-Si sample anodized at j_A = 100 mA/cm^2 and Δt_A = 10 min.

observed with the presence of macropores. In order to verify this assumption, group *B* samples were kept in distilled water subsequent to the measurement of Raman spectra. It is known that this causes corrosion of the layer [9]. It turned out that such treatment simultaneously leads to the emergence of macropores (Fig. 3b) and to an increase in the intensity of the Raman signal (Fig. 4a, curve *3*). Note that the conclusion on the association of the amplification effect of the Raman signal with the presence of macropores is also consistent with the data of study [4].

The following model is suggested for the explanation of Raman spectra from *por*-Si. The Raman signal for the samples with macropores comprises the superposition of signals from the walls and the bottom of macropores and from the dividing walls between them. Consequently, the intensity of the overall signal should depend heavily on the relative contributions of these signals.

The intensity of the signal from the walls and the bottom of macropores depends heavily on their shape. Our investigations of the transverse sections of the samples using scanning electron microscopy demonstrated that this shape is close to parabolic (Fig. 5), whereas the pore diameter on the layer surface exceeds the wavelengths of excitation and scattered light. Due to such a shape, the light scattered and reflected inside the pore can be repeatedly absorbed by its walls and the bottom, and then enter the detecting system. Thus, this makes an additional contribution to Raman scattering; i.e., the area of interaction of the excitation light with the substance effectively increases due to the light of Rayleigh scattering.

Obviously, the signal from macropores should increase as their diameter and depth increase; and it should exceed the signal from separating walls. This permits one to explain the increase in the intensity of Raman signals with the emergence of macropores in group *B* samples subsequent to their exposure to water as well as in group *A* macroporous samples with increasing the anodizing time.

The shape and position of the overall Raman signal should depend on the parameters of the nanoporous layer, namely, the dimensions of Si crystallites and layer thickness, which, in principle, can differ in separating walls and in macropores. In this case, the relative contributions of the signals from the pores and separating walls are also important.

The intensity of the signal from the pores can exceed that of the signal from separating walls; i.e., the amplification effect can occur. In this case, the Raman line from the porous layer can coincide with that from the substrate in the following cases: (1) if the thickness of the nanoporous layer which contains quantum crystals (Fig. 4b, inset) is small, so that the excitation light propagates into the substrate, which determines the Raman signal; (2) or if the thickness of the nanoporous layer on the bottom is large, but there are no nanometer-sized crystallites on the surface of the macropores. If such crystallites are present and the thickness of the nanoporous layer is large enough to make a noticeable contribution to the signal, the Raman line from *por*-Si can be shifted to lower energies and be broadened (Fig. 4b, curve *3*).

Nanometer-sized crystallites can be grouped predominantly on separating walls. This is in agreement with the data of the AFM on the structure of separating walls and the bottom of macropores. If, in addition, the contribution from separating walls is noticeable enough, the position of the Raman line can coincide with the line from the substrate, but the Raman line is broadened at the base.

In conclusion, we note that if the high intensity of the Raman signal is associated with the surface amplification, then this effect should also be expected for group *B* samples. In addition, it is difficult to explain the coincidence of the position and shape of the lines from the porous layer and the substrate in this case.

5. CONCLUSION

Thus, Raman scattering, which is often used for the determination of the dimensions of nanometer-scale crystallites, can yield erroneous results in the presence of pores in the samples. For this reason, it is desirable to carry out additional structural investigations of macroporous samples using other methods.

REFERENCES

1. D. J. Lockwood and A. G. Wang, Solid State Commun. **94**, 905 (1995).
2. H. D. Fuchs, M. Stutsmann, M. S. Brandt, *et al.*, Phys. Rev. B **48**, 8172 (1993).

3. H.-J. Lee, Y. H. Seo, D.-H. Oh, *et al.*, J. Appl. Phys. **75**, 8060 (1994).
4. A. A. Filios, S. S. Hefner, and R. Tsu, J. Vac. Sci. Technol. B **14**, 3431 (1996).
5. M. E. Kompan, I. I. Novak, V. B. Kulik, and N. A. Kamakova, Fiz. Tverd. Tela (St. Petersburg) **41**, 1320 (1999) [Phys. Solid State **41**, 1207 (1999)].
6. A. Otto, in *Light Scattering in Solids IV*, Ed. by M. Cardona and G. Guntherodt (Springer-Verlag, New York, 1984).
7. H.-J. Lee, Y. H. Seo, D.-H. Oh, *et al.*, Appl. Phys. Lett. **62**, 855 (1993).
8. R. L. Smith and S. D. Collins, J. Appl. Phys. **71**, R1 (1992).
9. M. E. Kompan and I. Yu. Shabanov, Fiz. Tekh. Poluprovodn. (St. Petersburg) **29**, 1859 (1995) [Semiconductors **29**, 971 (1995)].

Translated by N. Korovin

Semiconductors, Vol. 36, No. 5, 2002, pp. 564–567. Translated from Fizika i Tekhnika Poluprovodnikov, Vol. 36, No. 5, 2002, pp. 593–597.

AMORPHOUS, VITREOUS, AND POROUS SEMICONDUCTORS

Formation of Macropore Nucleation Centers in Silicon by Ion Implantation

E. V. Astrova* and T. N. Vasunkina

Ioffe Physicotechnical Institute, Russian Academy of Sciences, ul. Politekhnicheskaya 26, St. Petersburg 194021, Russia

** e-mail: east@pop.ioffe.rssi.ru*

Submitted July 2, 2000; accepted for publication October 9, 2001

Abstract—The possibility of obtaining a regular pattern of macropore nucleation centers in Si by ion implantation, instead of using the conventional *V*-shaped nucleation pits, has been studied. It is shown that selective radiation damage or local inversion of the conduction type is sufficient for macropore nucleation in some areas and passivation of others. The obtained results may be of use for practical applications and for better understanding of pore formation in silicon. © *2002 MAIK "Nauka/Interperiodica".*

1. INTRODUCTION

Photoelectrochemical etching of (100) *n*-Si allows formation of a regular system of macropores with vertical walls and high aspect ratio [1, 2]. The diameter of cylindrical macropores lies in the range of 0.5–25 μm, and the depth may be up to 500 μm, which makes it possible to obtain through channels in Si wafers of standard thickness. Such macroporous silicon is a promising material for photonics and optoelectronics [3–6], vacuum electronics [7], solid-state electronics [8, 9], and microelectromechanics [10].

The mechanism of macropore etching in the course of Si anodizing in solutions with fluorine-containing ions is poorly understood, as is pore formation in Si in general. The existing concepts are based on the instability of a planar surface and self-organization effects [11–13]. Experiments show that a planar surface is first etched uniformly, and only after a certain time a layer is formed in which macropore nucleation centers appear that are distributed randomly but with a certain equilibrium density defined by the Si resistivity [14].

In practice, a regular macropore pattern is produced using a relief surface with *V*-shaped nucleation pits obtained by anisotropic etching in a KOH solution through an oxide or nitride mask formed by means of a standard photolithography. The electric field strength is believed to be the highest in the vertex of such an inverted pyramid, and just this fact is the reason for enhanced local etching and macropore nucleation [1]. Recent studies have shown that the nucleation pits may have other forms or are absent altogether [15]. It is known also that, to obtain a pattern of microporous light-emitting silicon on *n*-Si, it is essential to create local regions on the electrode surface with different surface potentials [16]. Then, in the course of anodizing, the selective etching of some areas and passivation of others occurs. The projection of a high-contrast optical image onto a silicon surface during etching [17] or modification of surface properties by implantation of various ions [18–21] may also serve as examples.

The present study is concerned with the possibility of using ion bombardment to produce a regular micropore pattern on a flat Si surface.

2. EXPERIMENT

Phosphorus-doped *n*-Si with a resistivity of $\rho = 15$–$20\ \Omega$ cm served as the starting material. Polished (100) wafers were 300 μm thick. A system of round holes with a diameter of 4 μm situated at vertices of equilateral triangles with sides $a = 12$ μm was used as the photomask. Two masks of the same pattern were used: those of dark- and bright-field types. Prior to ion implantation, the wafers were oxidized and photolithography on SiO_2 was performed. Boron ions with energies $E = 75$–100 keV at doses $D = 440$–500 μC cm^{-2} ($(2.75$–$3.1) \times 10^{15}$ cm^{-2}) were implanted at room temperature on a standard setup. After removing the oxide, the wafers were electrochemically etched in 4% aqueous solution of HF for 1–3 h at $U = 4$ V voltage and $j = 3$–10 mA cm^{-2} current density, with the back side of the wafer illuminated with a bandgap light. The procedure is illustrated in Fig. 1.

2.1. Unannealed Samples

In samples anodized immediately after implantation (without thermal annealing), macropores were formed in unirradiated areas. Figures 2a and 2b show, respectively, the surface and cross-section of a sample irradiated through a dark-field mask. A thin layer of microporous silicon was formed in the irradiated windows (circular gray areas), with black macropore openings around them. The macropores are preferentially

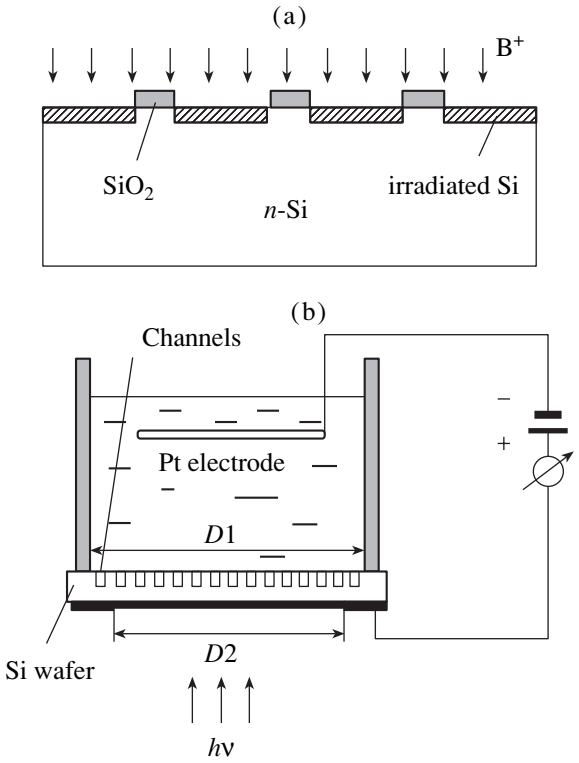

Fig. 1. Schematic of the procedure for obtaining a regular system of macropores. (a) Irradiation with boron ions through an oxide mask (irradiated areas are formed by silicon with high defect density in unannealed samples and by silicon with inverted type of conduction, p^+, in annealed samples). (b) Anodizing cell.

situated outside the areas damaged by ions, but their nucleation is random and no regular pattern is obtained.

When a bright-field mask was used, the macropores nucleated at unirradiated sections of the surface within small circular areas and a system of channels was formed (Fig. 3). The anodizing current sharply increased during the first 5–10 min, which can be accounted for by the transition of the etching front from the high-resistivity irradiated layer (occupying the major part of the surface) to the substrate. A microporous silicon layer was formed around the macropores on the implanted surface, with a macropore appearing as a crater in it (Figs. 3a, 3b). The microporous Si was removed by the short-term treatment of wafers with a 2.5% KOH solution. In the sample cross section, evenly spaced macropores of 46 μm depth can be observed. As seen in the inset of Fig. 3c, the diameter of nucleated macropores initially increases up to a steady-state value of ~7 μm, thus demonstrating the so-called bottleneck effect typical of self-born macropores [14]. A plan view obtained after removing a 6-μm-thick layer by mechanical polishing (Fig. 3d) demonstrates the formation of a regular pattern of macropores with a triangular grid of the photomask.

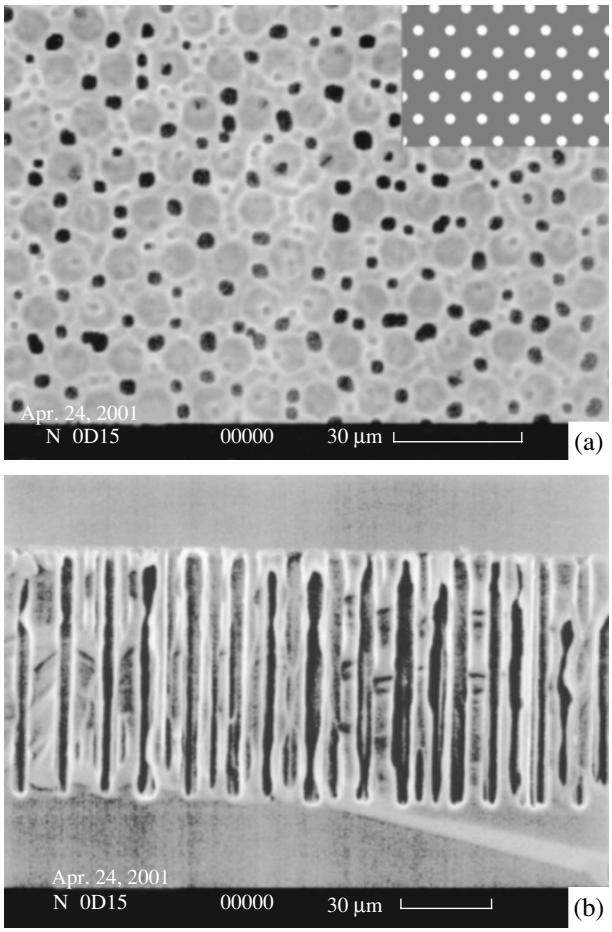

Fig. 2. (a) Plan view and (b) cross-sectional SEM images of an unannealed implanted (with a dark-field photomask, see inset) sample after anodizing. Macropores nucleated predominantly outside the irradiated circular windows (black points are macropores, ordered gray circles are areas disordered by implantation).

2.2. Annealed Samples

The second group of implanted samples was subjected, prior to anodizing, to thermal treatment in air (1050°C, 30 min.), which anneals the major part of the radiation defects and activates boron. A dark-field photomask was used in this case. As a result, islands of *p*-type conduction were formed in the areas of circular windows. After anodizing, microporous Si was formed in the irradiated windows, the window diameter increased to 11 μm, and macropores nucleated within these windows (Fig. 4). A single macropore appeared in some of the circles, and several macropores (three or four), in others. In this case, nucleation centers are situated predominantly on the irradiated part of the surface and unirradiated areas are passivated.

3. DISCUSSION

A high irradiation dose leads to pronounced disordering of the silicon substrate and the resulting substan-

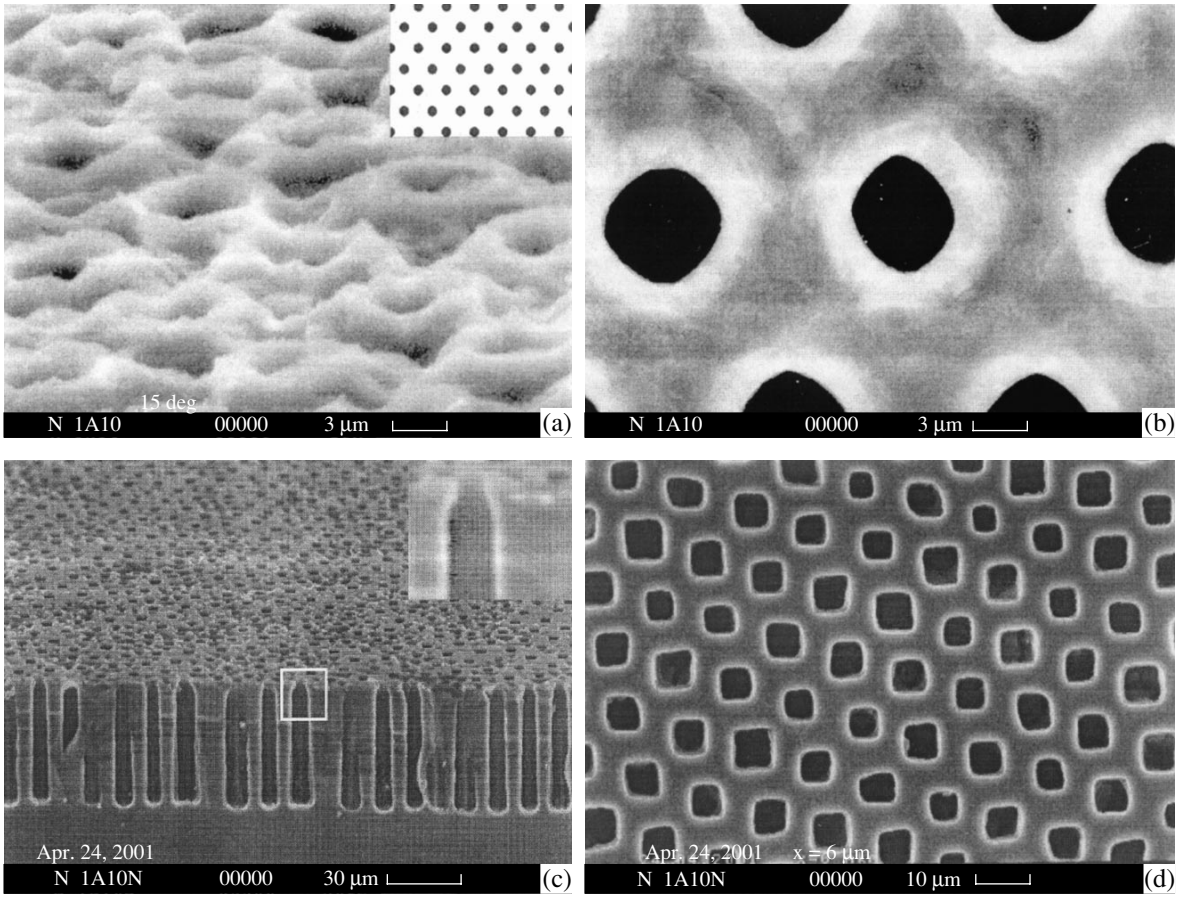

Fig. 3. SEM image of an unannealed sample implanted through a bright-field photomask (see inset in Fig. 3a) after anodization. (a) Surface covered with microporous silicon (oblique view); (b) plan view; (c) cross-sectional image and plan view of a wafer after removal of the microporous silicon layer in a 2.5% KOH solution (inset: the upper part of a macropore, the "bottleneck"); (d) plan view after removal of a 6-μm-thick top layer by mechanical polishing.

tial modification of its electrical parameters (higher resistivity, shorter lifetime of minority carriers, and lower mobility of majority carriers). The thickness of the damaged layer corresponds to the mean free path of boron ions and is about 400 nm. Thus, areas with different conductivities and surface potentials coexist on the surface. It is known that a Schottky barrier, which is reversely biased for *n*-Si, is formed at the electrolyte/Si interface. Dissolution of Si occurs as a result of the inflow of holes generated by light on the reverse side of the wafer. All these factors lead to redistribution of the anodizing current density, and the etching rates are not the same in different areas. The resulting contrast is sufficient for pores to nucleate at those areas where the etching rate is higher. The surface damaged by irradiation is not totally passivated, with a relatively thin microporous layer formed there. The observed effect correlates with the data of [18–20], where a microporous layer was formed in the course of staining and electrochemical etching in the areas not subjected to bombardment with Ga^+ and Si^+ ions, while the irradiated areas were passivated. It is noteworthy that an inverse contrast could be observed upon anodizing of unannealed samples in the breakdown mode without irradiation [16]: a thin microporous Si layer was formed in the irradiated local areas, its color differing from that of the

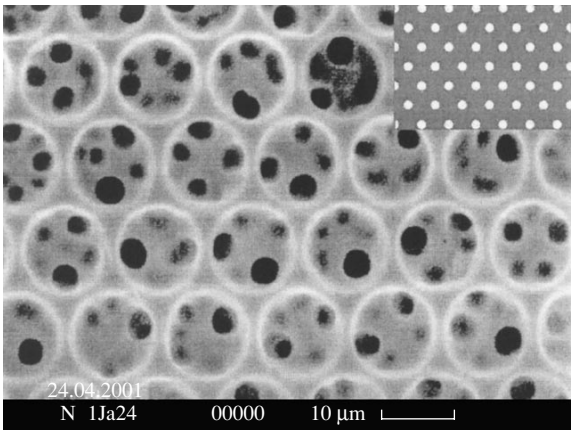

Fig. 4. SEM image of an Si surface with macropores for a sample annealed after implantation (dark-field photomask).

rest of Si owing to the faster etching of the defective layer.

In samples annealed upon implantation, the conduction type in the irradiated circular windows changed as a result of boron activation. The implantation dose was sufficient for a low-resistivity heavily doped p^+-layer to be formed. Therefore, the surface that was in contact with the electrolyte was again nonuniform. In this case, the etching rate is higher within the irradiated areas owing to the higher hole density. Initially, the etching is isotropic and microporous silicon is formed (hence, the increase in the diameter of circular windows), and then macropores nucleate essentially randomly. The preferential location of macropores inside the circular windows is presumably related to current line "focusing" and advance etching of these areas. Their density is 1.33×10^6 cm^{-2}, which is close to the equilibrium density of steadily growing macropores for the substrate material used [14]. However, the size of the fast-etched areas is somewhat larger than the average distance between the neighboring pores with equilibrium density (8.7 μm), which favors formation of several nucleation centers.

Also, the question arises as to how sharp should be the contrast in the local etching rates to ensure macropore nucleation in the desired areas. We tried to decelerate the etching outside the dark-field photomask windows by using a hardened photoresist on samples without any irradiation. Photoresist peeling started 90 min after the beginning of the process. A replica of the dark-field photomask appeared on the surface in the form of relief circles, but the macropores were randomly distributed over the wafer surface. Apparently, this method of local passivation is inefficient, in contrast to masking with silicon nitride [15].

4. CONCLUSION

Thus, it was demonstrated that nonuniformities in the planar silicon surface (selective disordering or local variation of the conduction type) lead, in the course of photoanodizing, to preferential nucleation of macropores in some areas and passivation of others. If the distance between the thus-obtained nucleation centers correlates with the substrate resistivity and the size of the nucleation areas is small enough, these areas induce the formation of a regular vertical-wall macropore structure, similar to that obtained by the standard *V*-shaped pit technology.

The use of ion implantation to generate macropore nucleation centers may be advantageous in cases where a submicrometer pattern is formed by means of a focused ion beam or with substrates having an orientation other than (100). In addition, the obtained results are of interest for a better understanding of the pore formation process in silicon.

ACKNOWLEDGMENTS

We are grateful to A. Naschekin, G. Moroz, and L. Granitsyna for SEM studies, helpful discussions, and assistance in the experiment.

This study was supported by the Scientific Program of the St. Petersburg Joint Research Center (2001), the "Scientific School" program (grant no. 00.15.96.770), and the program "Physics of Nanostructures" of the Ministry of Science of the Russian Federation (project nos. 97-1039 and 99-1107).

REFERENCES

1. V. Lehmann and H. Foll, J. Electrochem. Soc. **137**, 653 (1990).
2. V. Lehmann, J. Electrochem. Soc. **140**, 2836 (1993).
3. U. Gruning and V. Lehmann, Appl. Phys. Lett. **68**, 747 (1996).
4. S. W. Leonard, J. P. Mondia, H. M. van Driel, *et al.*, Phys. Rev. B **61**, R2389 (2000).
5. A. Chelnokov, K. Wang, S. Rowson, *et al.*, Appl. Phys. Lett. **77** (19), 2943 (2000).
6. J. Schilling, F. Muller, S. Matthias, *et al.*, Appl. Phys. Lett. **78**, 1180 (2001).
7. Ch. Beetz, R. Boerstler, J. Steinbeck, *et al.*, Nucl. Instrum. Methods Phys. Res. A **442**, 443 (2000).
8. V. Lehmann, W. Honlein, H. Reisinger, *et al.*, Thin Solid Films **276**, 138 (1996).
9. E. V. Astrova, V. B. Voronkov, I. V. Grekhov, *et al.*, Phys. Status Solidi A **182**, 145 (2000).
10. H. Ohji, P. J. Trench, and K. Tsutsumi, Sens. Actuators **82**, 254 (2000).
11. R. B. Wehrspohn, J.-N. Chazalviel, and F. Ozanam, J. Electrochem. Soc. **145**, 2958 (1998).
12. R. B. Wehrspohn, F. Ozanam, and J.-N. Chazalviel, J. Electrochem. Soc. **146**, 3309 (1999).
13. H. Foll, J. Carstensen, M. Christophersen, and G. Hasse, Phys. Status Solidi A **182**, 7 (2000).
14. M. H. Al Rifai, M. Christophersen, S. Ottow, *et al.*, J. Electrochem. Soc. **147**, 627 (2000).
15. H. Ohji, P. J. Trench, S. Izuo, and K. Tsutsumi, Sens. Actuators **85**, 390 (2000).
16. P. Schmuki, L. E. Erikson, and D. J. Lockwood, Phys. Rev. Lett. **80**, 4060 (1998).
17. V. Y. Doan and M. Y. Sailor, Appl. Phys. Lett. **60**, 619 (1992).
18. A. J. Steckl, J. Xu, H. C. Mogul, and S. Morglu, Appl. Phys. Lett. **62**, 1982 (1993).
19. J. Xu and A. J. Steckl, Appl. Phys. Lett. **65**, 2081 (1994).
20. X.-M. Bao and H.-Q. Yang, Appl. Phys. Lett. **63**, 2246 (1993).
21. S. P. Duttagupta, C. Peng, P. M. Fauchet, *et al.*, J. Vac. Sci. Technol. B **13**, 1230 (1995).

Translated by D. Mashovets

Semiconductors, Vol. 36, No. 5, 2002, pp. 568–573. Translated from Fizika i Tekhnika Poluprovodnikov, Vol. 36, No. 5, 2002, pp. 598–603.

AMORPHOUS, VITREOUS, AND POROUS SEMICONDUCTORS

X-Ray-Emission Study of the Structure of Si:H Layers Formed by Low-Energy Hydrogen-Ion Implantation

V. R. Galakhov*^, I. V. Antonova, S. N. Shamin*, V. I. Aksenova*, V. I. Obodnikov**, A. K. Gutakovskiĭ**, and V. P. Popov****

** Institute of Metal Physics, Ural Division, Russian Academy of Sciences, ul. S. Kovalevskoĭ 18, Yekaterinburg, 620219 Russia*

^ e-mail: galakhov@ifmlrs.uran.ru

*** Institute of Semiconductor Physics, Siberian Division, Russian Academy of Sciences, pr. Akademika Lavrent'eva 13, Novosibirsk, 630090 Russia*

Submitted November 13, 2001; accepted for publication November 21, 2001

Abstract—Amorphous silicon layers formed by implantation of 24-keV hydrogen ions into SiO_2/Si and Si with doses of 2.7×10^{17} and 2.1×10^{17} cm^{-2}, respectively, were studied using ultrasoft X-ray emission spectroscopy with variations in the energy of excitation electrons. It is ascertained that the surface silicon layer with a thickness as large as 150–200 nm is amorphized as a result of implantation. Implantation of hydrogen ions into silicon coated with an oxide layer brings about the formation of a hydrogenated silicon layer, which is highly stable thermally. *© 2002 MAIK "Nauka/Interperiodica".*

1. INTRODUCTION

Layers of amorphous hydrogenated silicon (*a*-Si:H) formed at the silicon surface using ion-plasma deposition or low-energy ion implantation are believed to be promising for optical applications (see, for example, [1]). Such layers have a wide band gap (2–2.1 eV) and form structures with heterojunctions; these heterostructures form the basis for the development of photosensitive elements with an efficiency as high as 18% (see, for example, [2]). However, the technology for the formation of *a*-Si:H layers is typically quite complicated. An alternative method for the formation of *a*-Si:H layers consists in the implantation of large doses of low-energy hydrogen ions [3, 4]. The objective of this study was to gain insight into the structure of *a*-Si:H layers formed by the implantation of H^+ ions (generated in a plasma source) into Si or a SiO_2/Si system and also to investigate the thermal stability of these layers.

In order to study the Si:H layers, we used ultrasoft X-ray emission spectroscopy with variations in the energy of excitation electrons. The reason for using X-ray spectroscopy for the analysis of multilayers and interfaces is based on the high sensitivity of X-ray emission spectra to chemical bonding. The X-ray Si $L_{2,3}$ emission spectrum arises owing to the transition of electrons from the 3*s* and 3*d* levels to the vacancies at the 2*p* level. As a result of the dipole selection rules, the Si $L_{2,3}$ spectra represent the partial densities of the 3*s* and 3*d* states localized at silicon atoms. In addition, a variation in the energy of excitation electrons makes it possible to vary the escape depth of the X-ray radiation. This method was used with good results to analyze the phase profile in the interface layers of silicon-based structures [5–8].

2. EXPERIMENTAL

As the starting material, we used Si(100) grown by the Czochralski method. A thermal-oxide layer with a thickness of 100 nm was grown on some of the wafers. Pulsed implantation of 24-keV hydrogen ions was performed at room temperature with the doses in the range of 1×10^{16}–3×10^{17} cm^{-2}. The range of 24-keV hydrogen ions in silicon is 0.27 μm. The ion-pulse duration was 4 μs, the pulse interval was 30 s, and the ion-current density was 40 mA/cm^2. Heat treatments of implanted wafers were performed at temperatures up to 1050°C in a nitrogen atmosphere. The heat-treatment duration ranged from 30 min to 1 h. Oxide was removed from the surface after implantation and also after each heat treatment using hydrofluoric acid. In our studies, we used secondary-ion mass spectrometry (SIMS), high-resolution transmission electron microscopy (HRTEM), and ultrasoft X-ray emission spectrometry with variable excitation-electron energy.

The spectra of the Si $L_{2,3}$ X-ray emission were measured using an ultrasoft X-ray spectrometer with the high spatial and energy resolution ($\Delta S \approx 5$ μm and $\Delta E \approx 0.4$ eV, respectively) [9]. The spectral decomposition of the X-ray emission was performed using a diffraction grating with a radius of 2 m and 600 lines/mm. Accelerating voltage applied to the X-ray tube was varied from 2 to 8 kV with the current being equal to

~130 nA. The voltage applied to the X-ray was maintained constant to within ±0.1 kV.

3. RESULTS AND DISCUSSION

3.1. Hydrogen Concentration Profiles

In Fig. 1a, we show the hydrogen concentration profiles in SiO_2/Si:H, i.e., in the samples of oxidized silicon implanted with hydrogen ions using the highest doses (~3×10^{17} cm^{-2}) and then annealed at temperatures T = 200, 500, and 1050°C; the profiles were obtained using the SIMS method. Prior to measurements, the samples were treated in hydrofluoric acid in order to remove the oxide layer from the surface. Similar concentration profiles for the Si:H samples after the hydrogen-ion implantation into Si and subsequent annealing at T = 200, 500, and 700°C are shown in Fig. 1b. The hydrogenated-layer thickness (as follows from the obtained hydrogen distributions) is 240 nm if implantation is performed through the oxide layer (SiO_2/Si:H) and 270 nm if hydrogen ions are implanted directly into silicon (Si:H).

It can be seen that, if hydrogen ions are implanted in silicon without an oxide film on the surface, the hydrogen concentration decreases as a result of annealing without an appreciable change in the hydrogenated-layer thickness. Another situation takes place in the SiO_2/Si:H system. First, a low-conductivity, ~100-nm-thick surface layer is observed immediately after implantation. The thickness and conductivity of this layer correspond to the oxide that is initially present at the wafer surface. Apparently, the properties of the oxide layer are affected by implantation of ions with large doses; as a result, this oxide cannot be removed from the surface by treating it in hydrofluoric acid.

The second specific feature in the case of SiO_2/Si:H consists in the fact that the hydrogen concentration profile shifts closer to the surface as a result of annealing (see Fig. 1a). Such behavior is not typical of hydrogen in silicon; as a rule, a decrease in the hydrogen concentration is observed without any appreciable shift of the hydrogen distribution over depth [10], as is observed in Si:H (Fig. 1b). Most probably, the unusual shift of hydrogen distributions to the surface is related to the recovery of the oxide-layer properties as a result of annealing and to removal of this layer prior to measurements. If we shift the profiles obtained in annealed samples in such a way so as to obtain a concentration decrease typical of implanted samples, we obtain the data shown in Fig. 1c. The greatest shift of the profile at the temperatures of 500 and 1050°C amounts to 100 nm, which corresponds to the initial-oxide thickness.

The third specific feature of the concentration profiles consists in the fact that the sheet hydrogen concentration changes in SiO_2/Si:H crystals to a lesser extent as a result of annealing than in the Si:H crystals. The changes in the sheet concentration in relation to the annealing temperature are illustrated in Fig. 2. It can be seen that the presence of an oxide layer at the surface diminishes to a great extent the escape of hydrogen from the crystal.

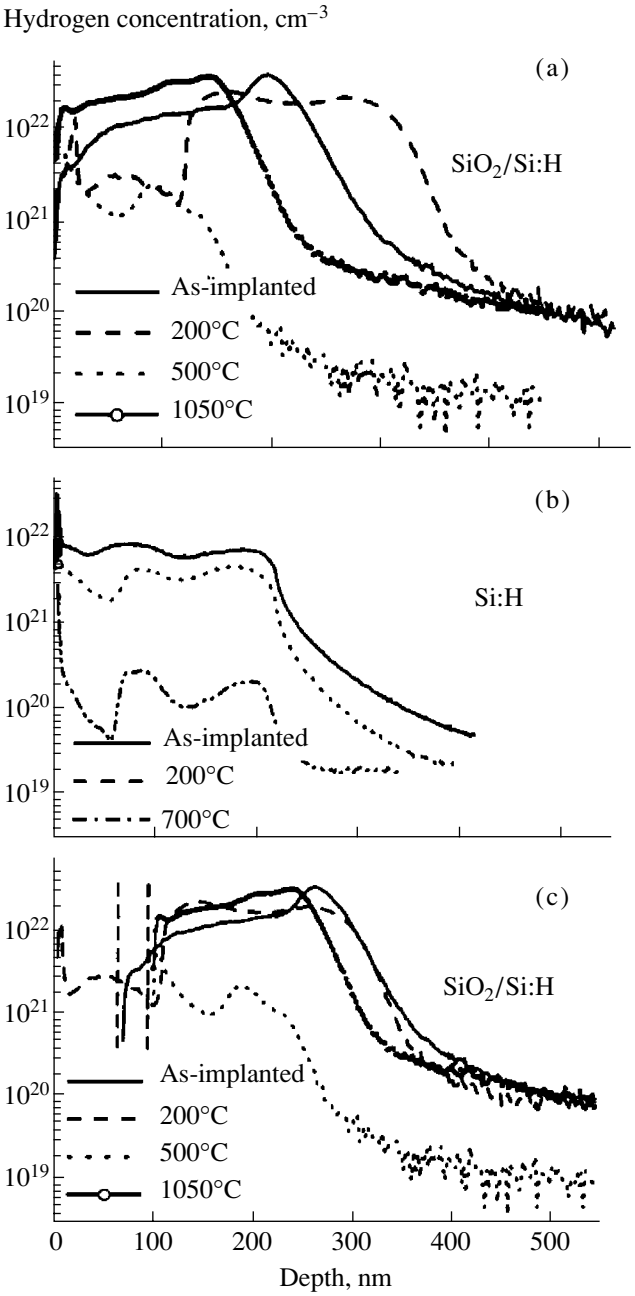

Fig. 1. The hydrogen concentration profiles in (a) SiO_2/Si:H and (b) Si:H after implantation of hydrogen ions at doses of 2.7×10^{17} and 2.1×10^{17} cm^{-2}, respectively, with subsequent annealing for 1 h, and also (c) the hydrogen concentration profiles in SiO_2/Si:H after hydrogen implantation and subsequent annealing with consideration of the shift due to removal of oxide from the surface.

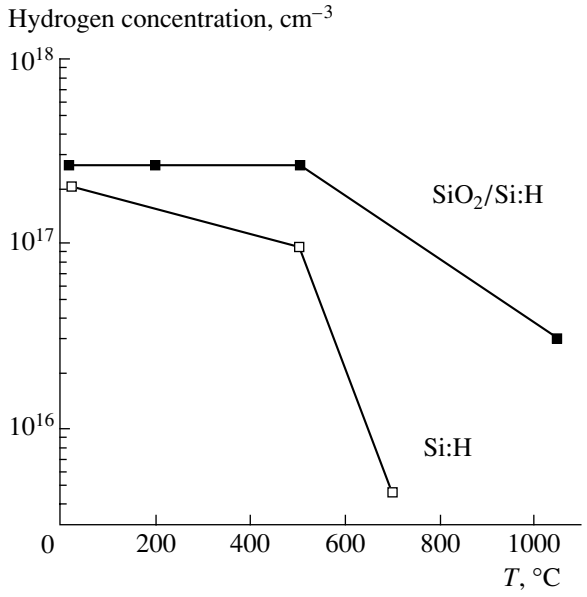

Fig. 2. The sheet hydrogen concentration in Si:H and SiO_2/Si:H as a function of annealing temperature; the SIMS data were used.

3.2. X-Ray Emission Si $L_{2,3}$ Spectra

The penetration depth of electrons into a material and, consequently, the escape depth of X-ray radiation depend on the voltage applied to the X-ray tube, i.e., on the kinetic energy of electrons E. Assuming normal incidence of the electron beam on the surface, the X-ray radiation intensity is defined by the depth distribution of electrons $\varphi(\rho z, E)$ and by the concentration of the element under investigation; i.e., we have

$$I(E) \propto \int_0^\infty \varphi(\rho z, E) c(\rho z) \exp(-\mu_m \rho z / \cos\psi) d(\rho z), \quad (1)$$

where ρ is the density of the material, ψ is the angle between the X-ray beam and the normal to the surface, and μ_m is the mass coefficient of absorption. The depth distribution function of electrons was approximated by the product of the Gaussian and exponential functions [6]. It follows from the estimations of the X-ray radiation intensity that the X-ray spectrum is formed within the 0–90-nm-thick layer for the excitation energy of 2 keV, whereas an increase in the energy to 3 keV makes it possible to increase the thickness of the analyzed layer to 180 nm.

In Fig. 3, we show the X-ray emission Si $L_{2,3}$ spectra of the SiO_2/Si:H samples annealed at temperatures of 200, 500, and 1050°C. The spectra were measured after removal of the oxide layer; the excitation energies were E = 2–8 keV. For the sample annealed at 200°C, the spectra were measured within a year following the treatment in hydrofluoric acid immediately after implantation. Repeated measurements were performed after additional treatment in hydrofluoric acid.

The spectra of the sample annealed at 200°C immediately after implantation are similar to those of SiO_2 if the excitation energies are low (2–4 keV). A characteristic feature of SiO_2 X-ray spectra at the photon energy of ~77 eV is related to the atomlike 2*s* oxygen states, which manifest themselves in the Si $L_{2,3}$ spectra owing to hybridization of the 3*s* Si and 2*s* O states. The subbands at 91 and 95 eV represent the 3*s* Si states hybridized with the O 2*p* states.

According to estimations, the thickness of the analyzed layer is about 200–250 nm for excitation energies no higher than 4 keV. As the excitation energy is increased to 6–8 keV, the shape of the spectrum changes radically. However, the spectrum becomes similar to the spectrum of crystalline Si (*c*-Si) only if the excitation energy becomes equal to 8 keV (the analyzed layer thickness is ~750 nm).

The spectra measured at low excitation energies (2–3 keV) within a year after removal of the oxide from the surface have a shape characteristic of the spectra of amorphous silicon (*a*-Si). The actual spectrum can be approximated as a superposition of the *c*-Si and *a*-Si spectra taken in the proportion of 0.68 : 0.32. The spectrum obtained in this manner closely matches the experimental spectrum measured at the excitation energy of 2 keV (see Fig. 3b). As the excitation energy is increased, the spectra become similar to those of *c*-Si.

An annealing at 500°C results in a decrease in the content of amorphous silicon: the spectrum measured for the excitation-electron energy of 2 keV can be represented as a superposition of the *c*-Si and *a*-Si spectra taken in the proportion of 0.44 : 0.56 (see Fig. 3). Amorphous silicon vanishes almost completely after heat treatment at 1050°C.

For the Si:H samples, implantation was performed directly into silicon. In Fig. 4, we show the Si $L_{2,3}$ X-ray emission spectra of the samples implanted with hydrogen ions at doses of 1.6×10^{17} and 2.1×10^{17} cm^{-2}. The latter sample was subjected to postimplantation annealing for 1 h at 500°C.

As can be deduced from the Si $L_{2,3}$ X-ray emission spectra, the surface layer of all the Si:H samples is amorphized. For the sample implanted with the lowest dose (1.6×10^{17} cm^{-2}), the surface layer is incompletely amorphized: the Si $L_{2,3}$ spectrum measured at the excitation energy of 2 keV can be represented as a superposition of the spectra corresponding to crystalline and amorphous silicon taken in the proportion of 0.31 : 0.69. An increase in the dose to 2.1×10^{17} cm^{-2} results in complete amorphization; at least, the spectrum measured at the excitation energy of 2 keV is identical to that of the *a*-Si spectrum. An annealing at 500°C only

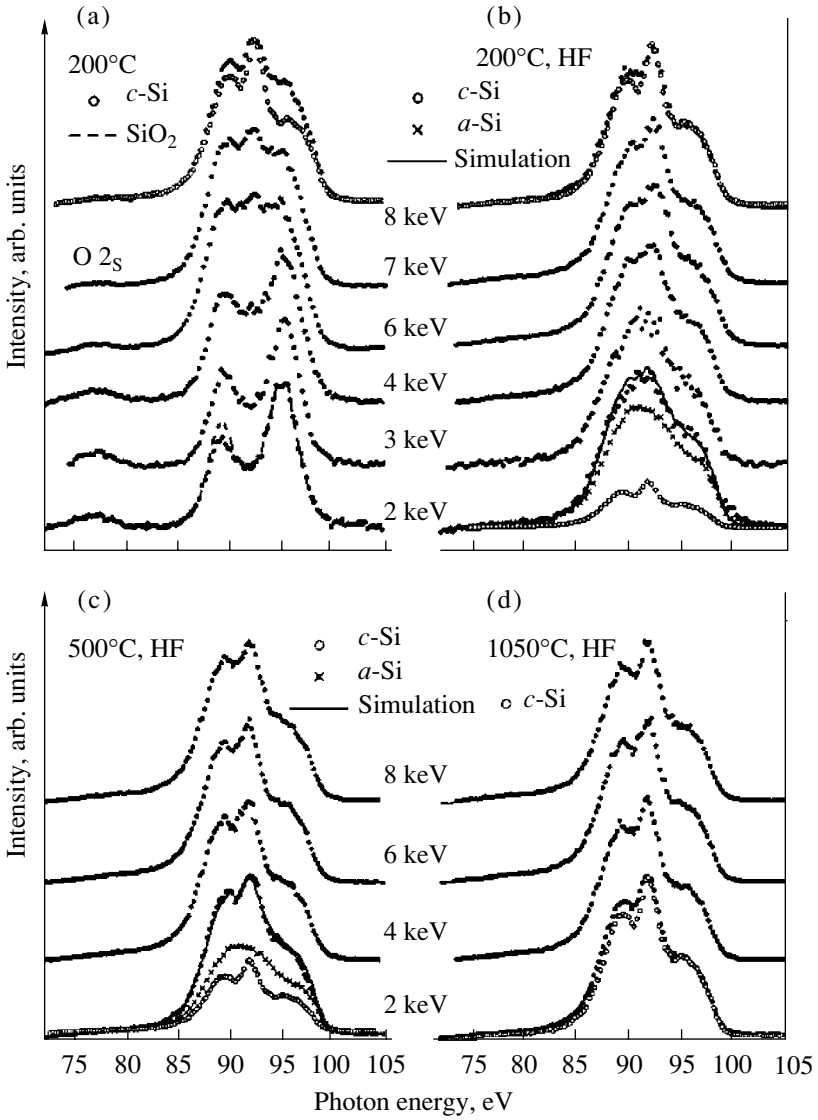

Fig. 3. The Si $L_{2,3}$ X-ray emission spectra of SiO_2/Si:H samples annealed for 1 h at the temperatures of (a, b) 200, (c) 500, and (d) 1050°C (a) before and (b–d) after removal of the oxide layer. The excitation-electron energy was 2–8 keV.

slightly affects the shape of the spectra and, consequently, the composition of the surface layers.

It is of interest to assess the composition of the layers analyzed for the excitation energies higher than 2 keV. To this end, we normalize the spectra in such a way that their integrated intensities measured at the excitation-electron energy E_i are equal to the integrals of the right-hand side of formula (1). We can then obtain the spectrum corresponding to the range Δz of the analyzed thicknesses. Such a procedure was performed for the spectra of the Si:H sample implanted at a dose of 2.1×10^{17} cm^{-2} and then annealed at 500°C (see Fig. 4c). The difference spectra for the pairs of energies are shown in Fig. 4d and are denoted by *3–2*, *4–3*, *6–4*, and *8–6*. For example, *3–2* signifies that the difference spectrum is obtained by subtracting the spectrum measured at the electron-excitation energy of 2 keV from the spectrum measured at 3 keV; this corresponds to the analyzed-depth range of 30–180 nm.

Therefore, it may be concluded that the layer of amorphized silicon in all samples has a thickness no larger than 100 nm, which is analyzed when the X-ray radiation is excited with 2-keV electrons. If the thickness is larger, the contribution of amorphous silicon vanishes almost completely. The deeper-lying layers are composed of *c*-Si.

The data on the surface-layer amorphization obtained by ultrasoft X-ray emission spectroscopy are consistent with the images obtained using high-resolution transmission electron microscopy for a Si:H sample (Fig. 5). According to the microscopy data, an amorphous layer is observed in the Si:H samples start-

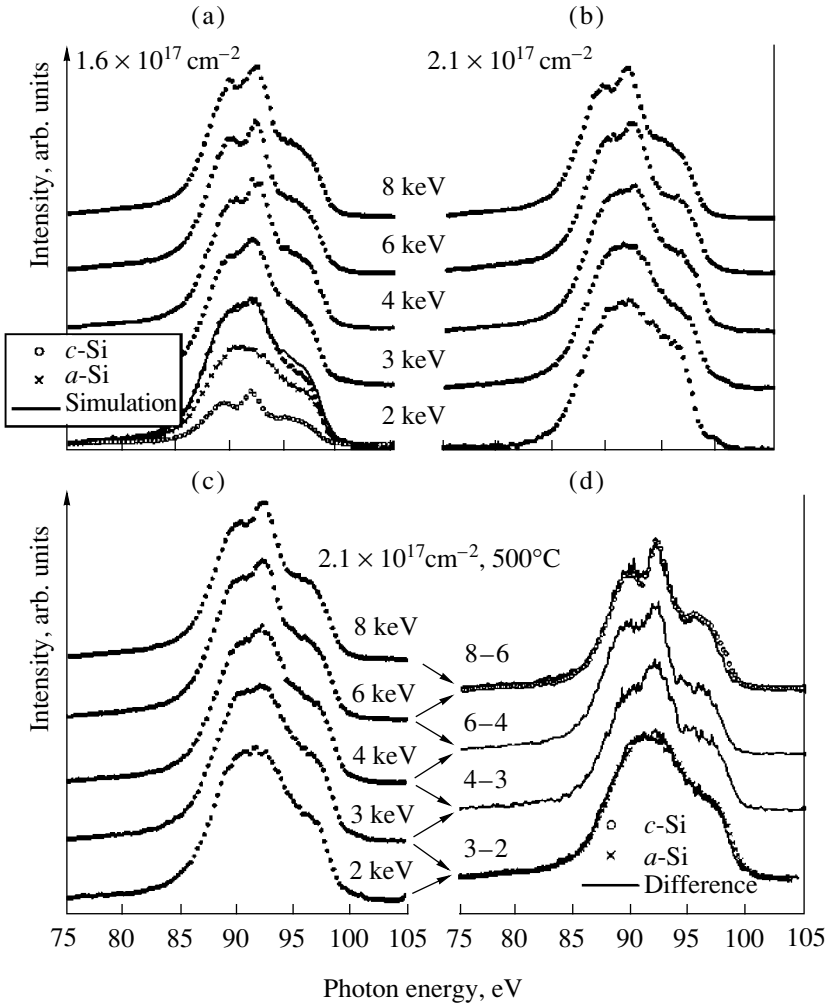

Fig. 4. The Si $L_{2,3}$ X-ray emission spectra of the Si:H samples after implantation of H^+ ions at doses of (a) 1.6×10^{17} and (b–d) 2.1×10^{17} cm^{-2}. The spectra were measured (a, b) without a postimplantation annealing and (c, d) after a postimplantation annealing for 1 h at 500°C. The curves represent the (a–c) initial and (d) difference spectra. The spectra were measured using the excitation electrons with energies of 2–8 keV. The arrows indicate the initial spectra used to obtain the difference spectra.

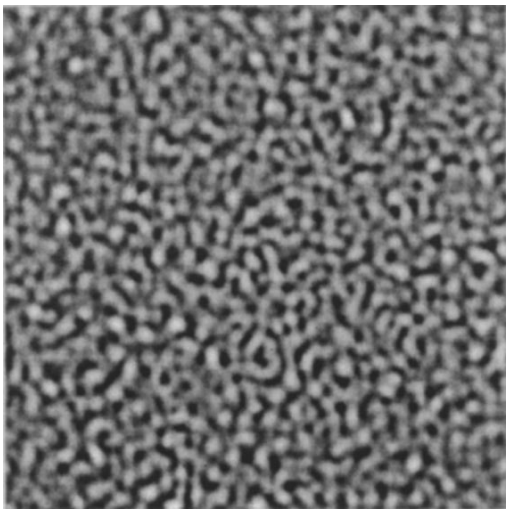

Fig. 5. The Si:H sample image obtained using high-resolution electron microscopy. The image size is 10×10 nm^2.

ing at a hydrogen dose of 1×10^{17} cm^{-2}. Amorphization is retained after the annealing of such samples at temperatures as high as 500°C. Microscopic images of the SiO_2/Si:H samples do not clearly indicate that the amorphous phase is present; rather, these images demonstrate that there are a large number of pores.

4. CONCLUSION

Thus, we used ultrasoft X-ray emission spectroscopy with a variable energy of excitation electrons to study the Si:H layers formed by implantation of hydrogen ions with energies as high as 24 keV. It is shown that hydrogen-ion implantation brings about amorphization of the surface silicon layer if the hydrogen doses are higher than 1.6×10^{16} cm^{-2}. The amorphous silicon layer is 150–200 nm thick. Implantation of hydrogen ions into silicon with an oxide film at the sur-

face results in the formation of hydrogenated silicon, which has an enhanced thermal stability compared to an Si:H layer without an oxide film at the surface. The reported results demonstrate the merits of using ultrasoft X-ray emission spectroscopy with a variable energy of excitation electrons for the analysis of the phase composition of thin-film structures.

ACKNOWLEDGMENTS

This study was supported by the Russian Foundation for Basic Research (project nos. 99-03-32503, 00-15-96575, and 01-02-16986) and by the International Science & Technology Center (grant no. 563).

REFERENCES

1. E. Edelberg, S. Bergh, R. Naone, *et al.*, J. Appl. Phys. **81**, 2410 (1997).
2. R. M. Hauser, N. Jensen, R. B. Bergman, *et al.*, Solid State Phenom. **67–68**, 551 (1999).
3. R. W. Collins, B. G. Yacobi, K. M. Jones, and Y. S. Tsuo, J. Vac. Sci. Technol. A **4**, 153 (1986).
4. I. V. Antonova, V. P. Popov, A. K. Gutakovsky, K. S. Zhuravlev, E. V. Spesivtsev, and I. I. Morosov, in *Physics, Chemistry and Application of Nanostructures*, Ed. by V. S. Borisenko (World Scientific, Singapore, 1999), p. 55.
5. E. Z. Kurmaev, S. N. Shamin, V. R. Galakhov, *et al.*, J. Mater. Res. **10**, 907 (1995).
6. V. R. Galakhov, E. Z. Kurmaev, S. N. Shamin, *et al.*, Appl. Surf. Sci. **72**, 73 (1993).
7. E. Z. Kurmaev, V. R. Galakhov, and S. N. Shamin, Crit. Rev. Solid State Mater. Sci. **23**, 65 (1998).
8. V. R. Galakhov, E. Z. Kurmaev, S. N. Shamin, *et al.*, Thin Solid Films **350**, 143 (1999).
9. E. Z. Kurmaev, V. V. Fedorenko, S. N. Shamin, *et al.*, Phys. Scr., T **41**, 288 (1992).
10. T. Hara, Y. Kakizaki, S. Oshima, and T. Kitamura, Proc.-Electrochem. Soc. **97–23**, 33 (1998).

Translated by A. Spitsyn

Semiconductors, Vol. 36, No. 5, 2002, pp. 574–580. Translated from Fizika i Tekhnika Poluprovodnikov, Vol. 36, No. 5, 2002, pp. 604–610.

AMORPHOUS, VITREOUS, AND POROUS SEMICONDUCTORS

Preparation and Study of Carbidized Porous Silicon

O. M. Sreseli^, D. N. Goryachev, V. Yu. Osipov, L. V. Belyakov, S. P. Vul', I. T. Serenkov, V. I. Sakharov, and A. Ya. Vul'

Ioffe Physicotechnical Institute, Russian Academy of Sciences, Politekhnicheskaya ul. 26, St. Petersburg, 194021 Russia

^ e-mail: Olga.Sreseli@pop.ioffe.rssi.ru

Submitted November 22, 2001; accepted for publication November 22, 2001

Abstract—Porous silicon layers with introduced carbon-containing substances (fullerenes, ultradisperse diamond, carbohydrates) have been studied. It was found that high-temperature annealing of such layers in a hydrogen atmosphere leads to substantial transformation of the photoluminescence spectra. It is assumed that this results from the formation of cubic silicon carbide crystallites and the occurrence of the quantum-confinement effect in these crystallites. © *2002 MAIK "Nauka/Interperiodica".*

1. INTRODUCTION

At present, nanocrystalline semiconductor materials are being intensively studied with the aim of using their unique properties in new optical and optoelectronic devices. A striking example of materials of this kind is porous silicon (*por*-Si) exhibiting photoluminescence (PL) in the visible spectral range, which is uncharacteristic of crystalline silicon [1–3]. However, studies of other nanocrystalline materials are largely hindered by the lack of sufficiently well-developed methods for their preparation. One of the ways to overcome this difficulty consists in the introduction of various substances, and carbon in particular, into a *por*-Si matrix. Subsequent thermal treatment of such a composition leads to the formation of silicon carbide (SiC) crystallites [4, 5]. Silicon carbide is a wide-bandgap material exhibiting blue PL and a number of properties that hold promise for device fabrication—chemical inertness, high radiation hardness, and temperature stability. Porous SiC obtained by etching of single-crystal SiC is known; its PL greatly exceeds in intensity that from bulk SiC [6, 7].

Various methods have been developed for introducing carbon into *por*-Si: deposition of diamond-like films onto *por*-Si by the chemical decomposition of carbon-containing vapor (CVD) [8, 9], carbon deposition from rf discharge plasma at room temperature [10], the introduction of ultradisperse diamond [11] or fullerenes [12] into *por*-Si, and pyrolysis of polymers introduced into *por*-Si [13].

Not all of the above-listed methods ensure deep introduction of carbon into the *por*-Si structure, especially in the case when porous silicon has mainly nanosize pores. For example, CVD leads to the deposition of carbon mainly on the surface of a porous layer [14]. The same result is obtained upon impregnation of a *por*-Si layer with polyvinyl alcohol and its subsequent thermal decomposition [13].

In the present study, the interaction of various carbon-containing substances with porous silicon was analyzed and the possibility of obtaining SiC crystallites in a matrix of partly oxidized porous silicon is demonstrated.

2. EXPERIMENTAL

2.1. Preparation of Porous Silicon Samples

Two kinds of *por*-Si were used in experiments: mesoporous (characteristic cross-sectional size of crystallites 10–100 nm), possessing no PL in the visible, and nanoporous (with a crystallite size of several nanometers), with PL peaked in the red-orange spectral range. *por*-Si layers were obtained on silicon substrates by electrolytic etching of single-crystal silicon in a 1 : 1 mixture of 50% hydrofluoric acid and ethanol. Mesoporous *por*-Si was obtained on heavily doped *p*-type Si (0.005 Ω cm) at high current densities (J = 100 mA cm^{-2}) without substrate illumination in the course of electrolysis. Nanoporous Si was prepared on Si substrates of both *p*- and *n*-types (2–5 Ω cm) at J = 10 mA cm^{-2} and high-intensity substrate illumination.

2.2. Methods of por-Si Carbidization

Three different methods of *por*-Si carbidization were used, with introduction of ultradisperse diamond, fullerene molecules, carbohydrate molecules, and subsequent high-temperature annealing in all cases.

An aqueous suspension of ultradisperse diamond (UDD) synthesized by the procedure described in [15, 16] was deposited onto the surface of mesoporous silicon and kept there for 2–5 min, after which the samples were dried at a temperature of about 50°C. Fullerene molecules were also introduced into *por*-Si from the liquid phase—a solution of fullerenes in orthoxylene. Preliminarily, *por*-Si samples, both mesoporous and

nanoporous, were kept for about 24 h in a straight orthoxylene solution to improve wetting and ensure penetration of C_{60} molecules into the pores of *por*-Si. A disadvantage of these techniques is that the introduced amounts of UDD and fullerenes widely vary between different samples. The problem consists in that, although a UDD cluster is about 60 Å in size, aggregates comprising a large number of clusters are actually present in solution. The size and number of these aggregates depend on quite a number of parameters and are, therefore, difficult to control.

We have developed a new method for *por*-Si carbidization based on the introduction of carbohydrate solutions into its matrix. The choice of this class of carbon-containing compounds was governed by the possibility of their subsequent thermal decomposition to give carbon with the liberation of only water vapor ($T_{dec} \approx 200$°C). Carbohydrates are not volatile, and, consequently, the entire amount of carbon contained in them must remain in substrate pores upon annealing. It was assumed that an appropriate carbohydrate must have the lowest atomic mass and, consequently, the smallest molecular size. Our experiments demonstrated, however, that the best results are achieved with more complex molecules of saccharose (M = 342.3), rather than with one of the simplest carbohydrates—glucose (M = 180.16). The mentioned carbohydrates are easily soluble in water. However, it is known that water poorly wets the *por*-Si surface and has difficulty penetrating inside its porous structure [17]. Previously, we showed that such solvents as ethanol and acetone are advantageous in this respect [18]. Since the solubility of saccharose in ethanol is low (~0.9%), several percent water was added to ethanol to improve the saccharose solubility. Impregnation of *por*-Si in such a solution was commonly done within 1 to 24 h. Samples were then rinsed with water to remove the saccharose solution from their surface and dried in air at room temperature.

The samples were annealed in a quartz reactor with external heating in a flow of hydrogen preliminarily passed through a palladium filter. Samples were charged into a cold reactor, heated to an annealing temperature of 1000°C, kept under isothermal conditions for 15 min, and then cooled in the switched-off-heater mode. The time of heating up to a prescribed temperature was 2h, and the time of cooling, 3 h. Samples with deposited fullerene molecules were covered with crystalline silicon wafers in view of the high volatility of fullerene molecules.

In accordance with published data [4], silicon carbide is formed at these temperatures.

2.3. Morphological Studies

The sample morphology was studied by atomic-force microscopy (AFM) [19, 20]. Samples for these measurements were fabricated by a special procedure. An approximately 500-nm-thick layer of fullerene molecules was deposited onto a polished (100) surface of crystalline silicon, and then annealing was done at a temperature of 1000°C for 15 min, following the procedure described above.

AFM images were obtained using a Burleigh Instruments ARIS-3500 atomic-force microscope (USA) with an ARIS-3005 scanning unit. In the employed constant-force mode (needle load of 5 nN), its vertical and horizontal resolution was about 0.1 and 1 nm, respectively.

The composition and thickness of the layers were also studied by the methods of Rutherford backscattering (RBS) and particle-induced X-ray emission (PIXE) [21].

2.4. Photoluminescence and Raman Spectroscopy

PL spectra were measured on computerized setups based on MDR-2 and DFS-24 monochromators with various photomultipliers under pulsed PL excitation (λ = 337.1 nm, τ = 10 ns) in two modes: at the peak of a laser pulse (so-called fast PL) and with a delay of ~3 μs. In the latter case, the PL spectra can be considered quasi-stationary.

The Raman spectrum of an annealed sample was measured with the 488-nm line of the argon-ion laser used for excitation.

3. RESULTS AND DISCUSSION

3.1. Sample Surface Morphology

The AFM method was applied to study samples annealed at 1000°C (described in Section 2.3).

Figure 1a presents an AFM image of the surface of one of the samples. It can be seen that crystallites with a cross-sectional size ranging from 100 to 300 nm and a height not exceeding 100 nm lie on the planar surface of silicon. For the most part, the shape of these crystallites is trihedral pyramidal truncated from above. A special study of the height profiles along lines intersecting the crystallites along lines *1–3* in Fig. 1a demonstrated that the faces of some crystallites make angles of 52–54° with the basal plane (100) of silicon (see curves *1–3* in Fig. 1b). These data indicate that the crystals grown belong to a cubic crystal system. In the given case, this is most likely silicon carbide 3C-SiC.

3.2. RBS and PIXE Studies

The RBS method was used to study mesoporous samples before and after deposition of carbon in order to find out whether particles (UDD clusters and fullerene molecules) penetrate deep inside pores. Figure 2a presents spectra of a porous silicon sample before and after deposition of a UDD film onto it (both spectra measured in the “random” orientation mode).

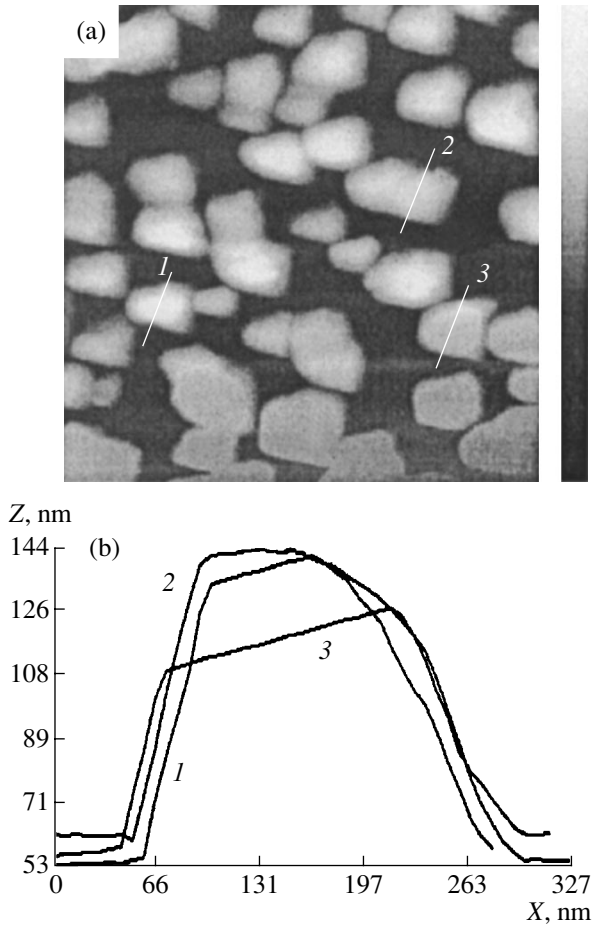

Fig. 1. (a) AFM image of an annealed structure ⟨polished silicon + fullerene⟩. Field dimensions 1.7 × 1.7 μm; relief scale at the right from 0 (black field) to 150 nm (white field). (b) Structure profile along cut lines *1*, *2*, and *3* in Fig. 1a.

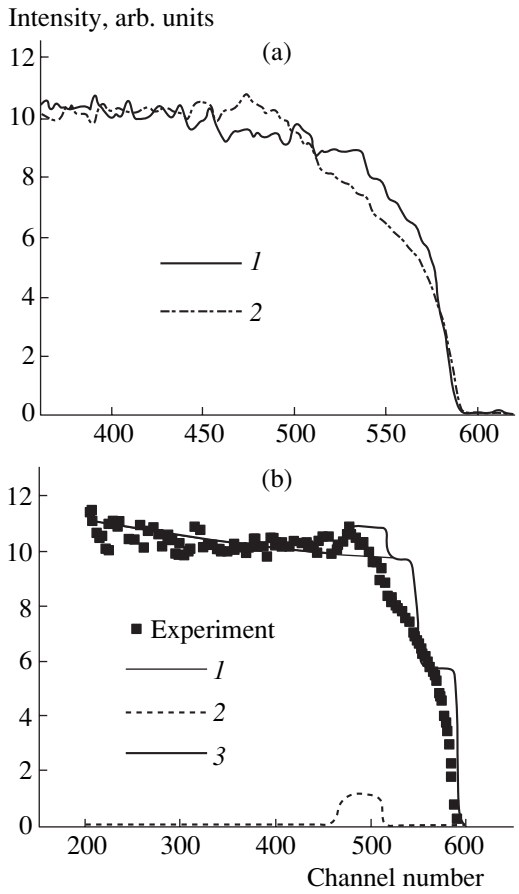

Fig. 2. (a) RBS spectra of a mesoporous silicon sample (*1*) before and (*2*) after carbon deposition, before annealing. (b) Comparison of experimental points in curve *2* of Fig. 2a with calculated content of elements in a film after carbon deposition. (*1* and *2*) Partial curves for silicon and carbon, calculated for relative content: Si 0.5 and C 0.5; (*3*) sum of curves *1* and *2*.

Probing was done with 190-keV protons; scattered ions were detected at an angle of 120°.

The edges of both spectra in the region of channel nos. 580–590 correspond to reflections from the crystalline silicon surface. The "bevels" observed in the spectra at channel nos. 500–580 arise from the fact that a considerable part of the flux of probing ions fall into pores, which diminishes the backscattering signal from the surface layers of a sample. The coincidence of the leading edges of the spectra (channel nos. 580–590) indicates that carbon clusters are within pores, rather than on the surface of single-crystal parts of the sample. Otherwise, the edge of spectrum *2* would be shifted relative to that of spectrum *1* because of the coating of the silicon surface with carbon. The same conclusion follows from the difference between the spectra in the "bevel" region: changing the pore filling leads to a change in the backscattering signal. The increase in the signal for curve *2* at channel nos. in the vicinity of 510 corresponds to the signal appearing from carbon, and its spread (from channel 510 to 460) makes it possible to find the thickness of the layer containing ultradisperse diamond. In the given case, this thickness was found to be 26 nm. Figure 2b shows the experimental points belonging to curve *2* of Fig. 2a and calculated curves coinciding with it to the maximum extent and allowing calculation of the content percentage of silicon and carbon in the layer. In this figure, *1* and *2* are partial curves for silicon and carbon calculated for their relative content (Si 0.5 and C 0.5); curve *3* is a sum of curves *1* and *2*.

The samples were annealed at 1000°C. The annealed samples were studied by two methods: RBS and PIXE. Both these techniques demonstrated the presence of a SiO_2 layer with a thickness of 30 nm or more on the sample surface. The presence in the layer of a large amount of oxygen can be attributed to the use of liquid-phase (with water) methods both in preparing *por*-Si layers and in the subsequent introduction of carbon. The presence of a large amount of silicon oxide in

annealed samples, revealed by RBS studies, is confirmed by optical measurements and suggests that the introduction of carbon into our samples is accompanied by their partial oxidation. No signal from carbon could be revealed in RBS spectra of the annealed samples, which, in our opinion, is accounted for by the insufficient sensitivity of the method to light element impurities. According to our estimates, the carbon detection threshold is about 10% relative to the amount of silicon atoms.

Thus, it was demonstrated that carbon clusters are introduced into *por*-Si even in the case of deposition of UDD, having the form of rather coarse aggregates (up to 50 nm in size). With fullerene or carbohydrate solutions used for *por*-Si carbonization, a considerable amount of carbon is found in the *por*-Si bulk—up to 50% relative to the silicon content of the layer (Fig. 2).

3.3. Photoluminescence

The PL from the samples was studied immediately after porous layer preparation (in the case of nanoporous silicon), after deposition of carbon-containing solutions and drying, and also after the final procedure of high-temperature annealing.

The PL spectra of the initial nanoporous silicon are typical of this material. The main PL band lies in the red-orange part of the spectrum and is characterized by slow (microseconds) rise and decay kinetics. The fast (nanoseconds) PL band is very weak. After introduction of carbon-containing compounds (molecules of fullerene, glucose, saccharose) into *por*-Si, the intensity of the fast band increases. This is accounted for by the partial oxidation of *por*-Si in the course of carbon introduction into *por*-Si, especially in water-containing solutions, which leads to the formation of oxygen bonds changing somewhat the nature of PL from *por*-Si.

Changes caused by carbon introduction before annealing were also followed for the example of PL spectra of nanoporous *por*-Si films with UDD. As mentioned above, the initial (without UDD) spectra of two samples (Fig. 3, curves *1*, *2*) are typical of *por*-Si. Spectra *1*' and *2*' show the PL from the same samples after UDD deposition. Curve *3* is the emission spectrum of an UDD layer deposited on a polished Si surface. It is noteworthy that the amount of UDD deposited onto samples nos. *1* and *2* is, respectively, two and three times smaller than that deposited onto the polished surface (curve *3)*. The UDD film deposited onto the polished silicon surface is characterized by a broad PL band peaked around 500 nm with short radiative times. The PL spectra of *por*-Si samples with UDD look like a superposition of the PL spectrum of UDD on the spectrum of *por*-Si. An analysis of time-resolved PL spectra shows that the short-wavelength part of the spectrum is associated with emission from the deposited UDD, and the long-wavelength part, with emission from *por*-Si nanocrystallites lying under the UDD film.

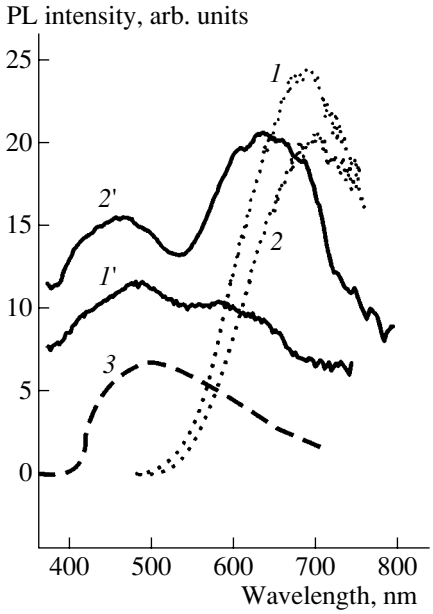

Fig. 3. Steady-state PL spectra of two nanoporous silicon samples before and after deposition of a film of ultradisperse diamond (*1*, *2* and *1*', *2*', respectively). (*3*) PL spectrum of UDD film on polished silicon surface.

Mention should be made of certain specific features of the presented spectra. In the first place, this is the shift of the long-wavelength peak (i.e., the peak associated with *por*-Si proper) to shorter wavelengths. This shift is characteristic of the partial oxidation of *por*-Si and is related to the decreasing size of *por*-Si nanocrystallites. Second, we have an increase in the intensity of PL from UDD with the decreasing thickness of its film. A dependence of this kind may occur if the emission comes only from the surface, rather than from the entire volume of the UDD films. Indeed, the real surface area of the UDD films increases markedly on passing from a polished silicon substrate to *por*-Si, and then, with the UDD film becoming thicker, its surface is gradually smoothed.

After being annealed at 1000°C, all the samples are characterized by bright white-blue PL. One of the main distinctions of the spectra of annealed samples from those of the initial samples consists in the short (tens of nanoseconds) radiative times characterizing the PL in the former case. Figure 4 presents the kinetics of a PL pulse at a wavelength of 494 nm at 300 K. The relaxation time of the PL pulse is about 30 ns. These times exceed the decay time constant of fast PL from *por*-Si, which is commonly not longer than 10 ns.

Several typical PL spectra of annealed samples are presented in Fig. 5. Irrespective of the method of carbon introduction, two broad bands peaked at 400–410 and 500–520 nm can be distinguished in the PL spectra, with a superimposed finer structure. The intensity of PL bands varies between samples, as do the relative inten-

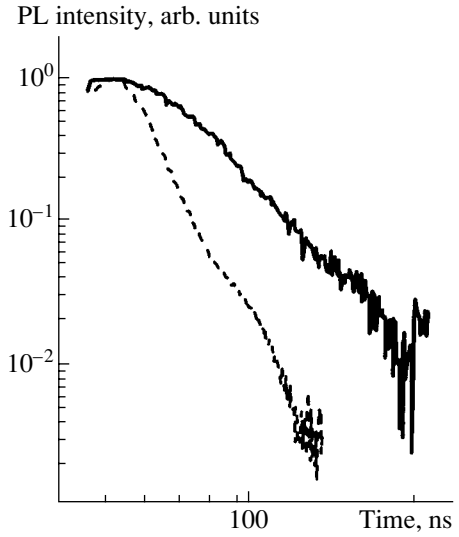

Fig. 4. PL kinetics for an annealed nanoporous silicon sample with fullerene. The wavelength of the excitation pulse is 325 nm, that of detected emission, 494 nm. Dashed line shows the shape of the laser pulse.

sities of the main peaks. Samples with a predominating long-wavelength PL band were obtained by treating porous silicon with a solution containing fullerene molecules. The intensity of the short-wavelength band grows with increasing the time of keeping *por*-Si in carbon-containing aqueous solutions.

The nature of the short-wavelength band is, in our opinion, associated with the large amount of oxygen in samples subjected to liquid-phase treatment. Subsequent annealing leads to partial oxidation of *por*-Si. It was also noted in [22] that introduction of fullerene molecules through compounds containing OCH_3 groups makes higher the intensity of lines attributed to Si–O–Si vibration modes in Fourier-transform IR spectra. At the same time, there is no way of knowing whether this band is fully analogous to the fast PL band in *por*-Si because of the different times of PL relaxation.

We relate the second, longer-wavelength PL band in annealed samples to the formation of silicon carbide. The energy gap of 3C-SiC is 2.36 eV (4.2 K) [23], which is somewhat lower than the values obtained in this study (2.4–2.5 eV at room temperature); i.e., a certain short-wavelength shift of the PL peak occurs. A shift of this kind is possible as a result of the quantum-confinement effect with a sufficiently small size of the forming SiC crystallites. At the same time, the PL band under consideration may also be due to the formation of amorphous silicon carbide. For example, it was noted in [24] that, depending on preparation conditions, hydrogenated amorphous silicon may have an energy gap in the range from 1.8 to 2.8 eV. The fact that cubic silicon carbide is revealed by the AFM of similarly treated polished samples of silicon with fullerene can serve as evidence in favor of the cubic modification of the obtained carbide. In [4], *por*-Si samples treated with a fullerene

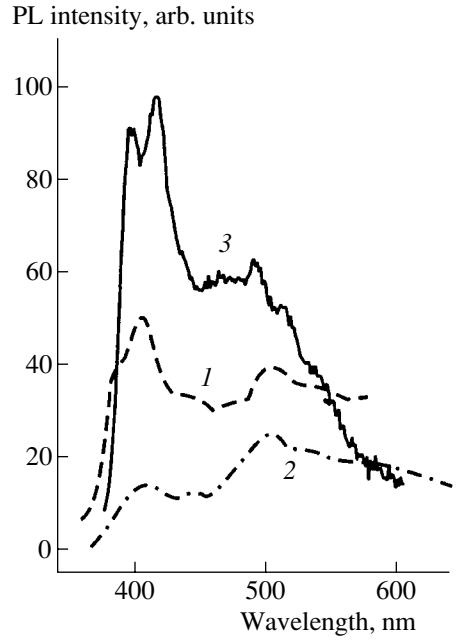

Fig. 5. PL spectra of annealed porous silicon samples. (*1*) mesoporous sample with introduced UDD, (*2*) nanoporous sample with introduced fullerene, and (*3*) nanoporous sample impregnated with carbohydrate (saccharose).

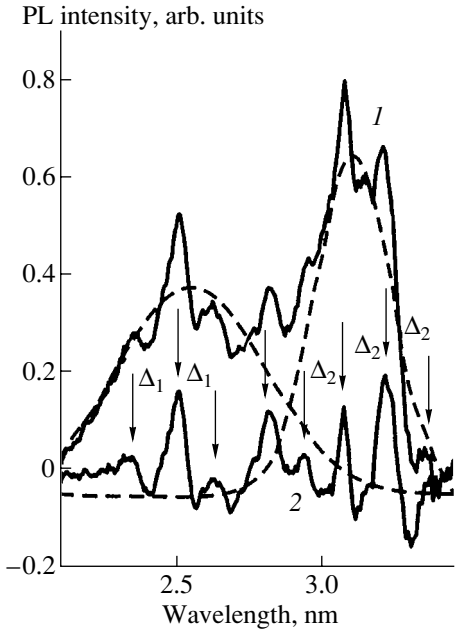

Fig. 6. (*1*) PL intensity vs. energy of emitted quanta for annealed nanoporous silicon sample impregnated with saccharose. (*2*) Difference between curve *1* and two Gaussians shown by dashed lines. Δ_1 = 0.16 eV (1280 cm^{-1}), Δ_2 = 0.136 eV (1090 cm^{-1}).

solution and subsequently annealed at 1000°C were studied and the observed PL spectrum was interpreted as a superposition of two bands peaked at 380 and 454 nm. The first of these was attributed, as in the present study, to defects (oxygen vacancies in silicon oxide formed upon annealing), and the second, to particles of 3C-SiC silicon carbide. Thus, the formation of silicon carbide nanocrystallites, including those with quantum confinement, is more probable, in our opinion, under the conditions of interaction of adsorbed carbon atoms with silicon nanocrystallites.

Attention should be paid to the characteristic structure of the PL spectra of carbidized *por*-Si (Fig. 6). This structure is manifested in spectra of all nanocrystalline samples in the present study fabricated on the basis of *n*- and *p*-type silicon. The effect is observed both in thin carbidized (tenths of a micrometer) layers of *por*-Si, having a mirror-smooth surface, and in thick (several micrometers) *por*-Si samples, with a rough coarse-grained surface, and also in samples with an irregular interface between *por*-Si and the *n*-type silicon substrate. The position of additional peaks is also independent of the angle between the sample plane and the optical axis of the setup. All these data make it impossible to attribute the additional PL peaks to interference phenomena.

Figure 6 shows a PL spectrum of an annealed sample measured with a DFS-24 double monochromator and plotted as a function of the energy of detected quanta. The spectrum can be decomposed into two Gaussians (dashed lines) peaked at 3.1 and 2.55 eV. Equidistant peaks are observed around each peak, spaced by 0.135 eV around the higher frequency peak and 0.16 eV in the vicinity of the lower frequency peak. A similar discrete sequence of additional peaks was observed in PL spectra in [25, 26] when studying porous silicon oxide. In these studies, the fine structure was attributed to the interaction between electron transitions in various surface compounds and the vibration modes of these compounds in the ground electronic state. For example, the authors attributed one of the observed progressions with a step of 630 cm^{-1} (~0.08 eV) to Si–H bonds on the surface of silicon oxide nanocrystallites.

Taking into account the large surface area of the porous material and the great number of surface compounds in carbidized silicon, we can make an attempt to relate the fine structure of our spectra to the vibration modes of various surface bonds. In particular, the energy spacing of 0.136 eV, corresponding to 1080 cm^{-1}, is most frequently attributed to stretched vibrations of Si–O–Si bonds in oxidized *por*-Si [27]; although there are studies [28] in which a closely lying line (1095 cm^{-1}) is related to C–O bonds. At the same time, M. Cardona *et al.* [29] attributed the broad line at about 1000 cm^{-1} to rotation vibrations of CH_n.

The second equidistant series around the peak at 3.55 eV, with a spacing of 0.16 eV corresponding to 1280 cm^{-1}, may be related to carbon compounds. In [24, 29], the absorption peak at 1250 cm^{-1} is attributed to the symmetric bending mode of Si–CH_3 (1288 cm^{-1} according to [30]). This confirms the assumption of the carbide nature of the peak at 3.55 eV (454 nm).

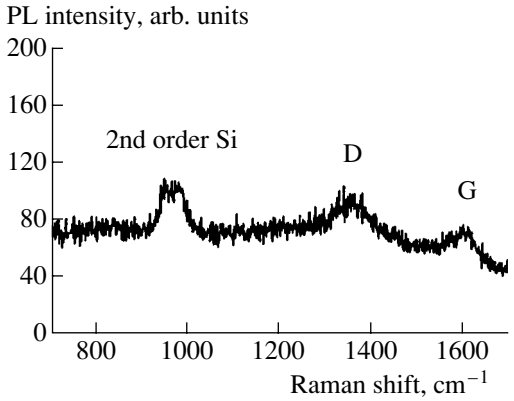

Fig. 7. Raman spectrum of annealed structure (polished silicon + fullerene). The wavelength of the exciting light is 488 nm. Bands D and G of the sp^2 state of carbon are clearly seen.

3.4. Raman spectra

The Raman spectrum of an annealed sample is presented in Fig. 7. It can be seen that bands at 1350 and 1600 cm^{-1}, associated with scattering on carbon in the sp^2-hybridized state, are present in the Raman spectra, in addition to the second-order scattering band of silicon at 930–1000 $cm^{-1.}$ Amorphous carbon appears as a result of the thermal decomposition of carbon-containing compounds and represents that part of the carbon material which has not reacted with the substrate to form silicon carbide. It may be assumed that a thin layer of amorphous carbon covers the silicon substrates and silicon carbide crystallites grown on the substrate. Bands corresponding to cubic silicon carbide are not observed, which is presumably accounted for by the insufficient sensitivity of the method to minor amounts of C-SiC crystallites formed on the surface.

4. CONCLUSION

Thus, the interaction of various carbon-containing substances with a porous silicon matrix has been studied and it was shown that high-temperature annealing of porous silicon samples containing introduced carbon molecules leads to a strong transformation of their PL spectra. It is assumed that the annealing leads to the formation of silicon carbide crystallites of cubic modification. The energy position of the PL peak, exceeding the energy gap of cubic silicon carbide, can be attributed to the quantum-confinement effect in crystallites.

ACKNOWLEDGMENTS

We thank V.G. Melekhin for Raman measurements and V.N. Afanas'ev for his help in the AFM studies.

This study was supported in part by the following programs: "Physics of Solid-State Nanostructures" (project "Plenka-2"), "Low-Dimensional Quantum Structures" of the Presidium of the Russian Academy of Sciences, and "Scientific Schools" of the Russian Foundation for Basic Research (grant no. 00-15-96750).

REFERENCES

1. L. T. Canham, Appl. Phys. Lett. **57**, 1046 (1990).
2. A. G. Cullis, L. T. Canham, and P. D. J. Calcott, J. Appl. Phys. **82**, 909 (1997).
3. D. Kovalev, H. Heckler, G. Polisski, and F. Koch, Phys. Status Solidi B **215**, 871 (1999).
4. L. Moro, A. Paul, D. C. Lorents, *et al.*, J. Appl. Phys. **81**, 6141 (1997).
5. X. L. Wu, G. G. Siu, M. J. Stokes, *et al.*, Appl. Phys. Lett. **77**, 1292 (2000).
6. V. Petrova-Koch, O. Sreseli, G. Polisski, *et al.*, Thin Solid Films **225**, 107 (1995).
7. S. Kim, J. E. Spanier, and I. P. Herman, Jpn. J. Appl. Phys. **39**, 5875 (2000).
8. A. A. Kulkarni, S. V. Bhoraskar, S. B. Ogale, *et al.*, J. Phys. D **28**, 1400 (1995).
9. Y. Liao, F. Ye, Q. Y. Shao, *et al.*, Thin Solid Films **368**, 211 (2000).
10. A. G. Rozhin, N. I. Klyuĭ, Yu. P. Piryatinskiĭ, and V. A. Semenovich, Pis'ma Zh. Tekh. Fiz. **25** (8), 27 (1999) [Tech. Phys. Lett. **25**, 304 (1999)].
11. A. N. Obraztsov, I. Yu. Pavlovsky, and V. Yu. Timoshenko, Diamond Relat. Mater. **6**, 1629 (1997).
12. F. Yan, X. Bao, X. Wu, and H. Chen, Appl. Phys. Lett. **67**, 3471 (1995).
13. V. Baranauskas, M. C. Tosin, A. C. Peterlevitz, *et al.*, Thin Solid Films **377-378**, 315 (2000).
14. V. Baranauskas, B. B. Li, A. C. Peterlevitz, *et al.*, Thin Solid Films **356**, 233 (1999).
15. A. I. Lyamkin, E. A. Petrov, A. P. Ershov, *et al.*, Dokl. Akad. Nauk SSSR **302**, 611 (1988) [Sov. Phys. Dokl. **33**, 705 (1988)].
16. A. E. Aleksenskiĭ, M. V. Baĭdakova, A. Ya. Vul', and V. I. Siklitskiĭ, Fiz. Tverd. Tela (St. Petersburg) **41**, 740 (1999) [Phys. Solid State **41**, 668 (1999)].
17. L. T. Canham and A. Groszek, J. Appl. Phys. **72**, 1558 (1992).
18. D. N. Goryachev, O. M. Sreseli, and L. V. Belyakov, Pis'ma Zh. Tekh. Fiz. **23** (1), 58 (1997) [Tech. Phys. Lett. **23**, 35 (1997)].
19. D. C. Chang, V. Baranauskas, I. Doi, and T. Prohaska, J. Porous Mater. **7**, 349 (2000).
20. G. J. Adriaenssens, V. Yu. Osipov, O. M. Sreseli, and A. Ya. Vul', in *Abstracts of the 20th Fullerene General Symposium, Japan, 2001*, p. 93.
21. V. V. Afrosimov, G. O. Dzyuba, R. N. Il'in, *et al.*, Zh. Tekh. Fiz. **66** (12), 76 (1996) [Tech. Phys. **41**, 1240 (1996)].
22. X. L. Wu, S. J. Xiong, D. L. Fan, *et al.*, Phys. Rev. B **62**, R7759 (2000).
23. H. Morkoc, S. Strite, G. B. Gao, *et al.*, J. Appl. Phys. **76** (3), 1363 (1994).
24. Y. Tawada, K. Tsuge, M. Kondo, *et al.*, J. Appl. Phys. **53**, 5273 (1982).
25. Yu. D. Glinka, S. H. Lin, and Y. T. Chen, Appl. Phys. Lett. **75**, 778 (1999).
26. Yu. D. Glinka, S. H. Lin, L. P. Hwang, and Y. T. Chen, Appl. Phys. Lett. **77**, 3968 (2000).
27. P. Gupta, A. C. Dillon, A. S. Bracker, and S. M. George, Surf. Sci. **245**, 360 (1991).
28. Z. Sun, X. Shi, X. Wang, and Y. Sun, Diamond Relat. Mater. **8**, 1107 (1999).
29. H. Wieder, M. Cardona, and C. R. Guarnieri, Phys. Status Solidi B **92**, 99 (1979).
30. L. Little, *Infrared Spectra of Adsorbed Species* (Academic, London, 1966; Nauka, Moscow, 1972).

Translated by M. Tagirdzhanov

Semiconductors, Vol. 36, No. 5, 2002, pp. 581–587. Translated from Fizika i Tekhnika Poluprovodnikov, Vol. 36, No. 5, 2002, pp. 611–617.

PHYSICS OF SEMICONDUCTOR DEVICES

Shallow *p–n* Junctions Formed in Silicon Using Pulsed Photon Annealing

S. T. Şişianu, T. S. Şişianu, and S. K. Railean

Technical University of Moldova, Chisinau, MD2012 Moldova

e-mail: sisianu@mail.utm.md

Submitted August 21, 2001; accepted for publication October 9, 2001

Abstract—Shallow and ultrashallow *p–n* junctions were formed in Si by stimulated diffusion of P from phosphosilicate glass and B from borosilicate glass under pulsed photon annealing. Electrical, photoelectric, and optical properties of these junctions were investigated. Special features of stimulated diffusion of P and B in surface layers of Si under pulsed photon annealing were revealed. The obtained results are discussed in terms of *kick-out*, pair vacancy–interstitial, and dissociative diffusion mechanisms. The features of the dopant concentration profiles are explained in terms of the vacancy–interstitial mechanism and the stimulated diffusion model with allowance made for the time dependence of the dopant surface concentration and the concentration dependence of the diffusivity. *© 2002 MAIK "Nauka/Interperiodica".*

1. INTRODUCTION

There is much interest in using shallow and ultrashallow p^+–n and n^+–p junctions in Si to increase the integration scale, operating speed, and reliability of integrated circuits (ICs), microelectronic devices, and self-assembled microstructures and nanostructures of different types [1–3]. This is especially urgent now, considering that very large-scale integrated circuits (VLSICs) with a device dimension of 0.18 μm are presently manufactured, and future reduction of the device dimension is expected: to 0.13 μm in 2004, 0.10 μm in 2007, and 0.07 μm in 2010. In addition to this, as shown in [1], ultrashallow diffusion *p–n* junctions can be successfully used to form superlattices of different types, self-assembled microresonators and quantum wells, one-electron memory cells, and other nanoelectronic devices.

A number of methods are used to form ultrashallow *p–n* junctions: planar diffusion via fluxes of excess vacancies or self-interstitials generated at the Si–SiO_2 interface [4, 5], low-energy B implantation [6], dual implantation of B^+ and Si^+, amorphization of Si by BF_2 implantation [7], proton implantation [8], and ion implantation through a thin silicide film [9]. Preamorphization of Si is most often used. However, when using this technique, it is very difficult to optimize the conditions of postimplantation annealing, which is necessary to activate dopant atoms, remove radiation defects, and retard the diffusion. Thus, alternative techniques should be looked for.

There is much interest in diffusion stimulated by laser annealing [10], different types of radiation (e^-, α, β, γ) [11], combined radiation and electric field [12], and combined radiation, implantation, and photon annealing [2, 13]. However, more and more interest is being shown in doping Si with the use of diffusion caused by pulsed photon annealing (PPA) or rapid thermal annealing (RTA) (which is widely used for thermal treatment of ion-implanted semiconductors [2–5, 14–16]) as an alternative technique for forming ultrashallow *p–n* junctions. Commonly, diffusion of either B from borosilicate glass (BSG) or P from phosphosilicate glass (PSG) is used. As shown in [2–5, 14, 15], this technique makes it possible to form ultrashallow (10–30 nm) *p–n* junctions in Si with higher concentration gradients of B and P, compared with *p–n* junctions formed by ion implantation. With the use of secondary-ion mass spectrometry (SIMS) and relevant calculations, it was shown [14] that the diffusivity of B in a BSG–SiO_2–Si system subjected to RTA exceeds the conventional diffusivity by a factor of 9–10.

Different stimulating effects can be used in this technology. These include fluxes of excess nonequilibrium vacancies and interstitials generated at the Si–SiO_2 interface; excitation of the electron subsystem and charge exchange between dopant atoms, caused by PPA; and other effects related to the nonequilibrium stimulated diffusion. However, to date, many of these effects have not been adequately investigated and opinions differ as to the mechanism and model of the stimulated diffusion of B and P in Si [17]. Thus, additional basic and applied research is necessary for widespread implementation of this technology.

In this paper, we report the results of the investigations of shallow and ultrashallow *p–n* junctions formed in Si by stimulated diffusion of P from PSG and B from BSG using PPA. We measured the depth of n^+–p and p^+–n junctions, the sheet resistance of diffusion layers, the current–voltage characteristics of junctions, and we

Table 1. Values of n^+–p junction depth (L) and sheet resistance (ρ) for layers formed in Si by stimulated diffusion of P under PPA at different temperatures T and annealing times (t)

T, °C	460	700	850*	900*	950*	1000	1050*	1080	1120	1180	1200
t, s	4	6	25	25	25	8	25	10	12	14	16
L, μm	0.14	0.2	0.03	0.07	0.2	0.25	0.33	0.3	0.38	0.46	0.54
ρ, Ω/□	420	400	300	80	30	–	12	–	–	–	–

Note: Astericks denote the annealing temperatures for which the data were taken from [15].

Table 2. Values of the depth of p–n junctions (L) formed in Si by stimulated diffusion of B under PPA at different temperatures T and annealing times (t)

T, °C	400	500	700	950*	1000*	1050*	1080	1120	1150	1200
t, s	2	4	6	60	60	60	10	12	14	16
L, μm	0.13	0.18	0.2	0.1	0.2	0.33	0.32	0.36	0.4	0.51

Note: Astericks denote the annealing temperatures for which the data were taken from [14].

also studied the optical properties of junctions used in optoelectronic sensors. Different mechanisms and models of stimulated diffusion in surface layers of Si are considered.

2. EXPERIMENTAL

Shallow n^+–p and p^+–n junctions in Si were formed in Si by stimulated diffusion of P from PSG and B from BSG using PPA. Phosphosilicate glass was deposited on the surface of p-Si by the method of anodic oxidation from a dilute solution of H_3PO_4 or from a gaseous medium at low (450°C) or high (1000°C) temperatures. The low-temperature deposition was carried out in a commercial HPCVD (high-pressure chemical vapor deposition) reactor in gaseous mixtures of O_2, SiH_4, and PH_3. Nitrogen was used as the carrier gas. The thickness of the deposited film was ~1 μm. Borosilicate glass was deposited on a surface of KÉF-03(111) wafers (i.e., n-Si:P(111), with the resistivity of 0.3 Ω cm) at 850°C in production conditions. The thickness of the BSG film was ~1.3–2 μm.

After the deposition of PSG (or BSG) films, the samples were subjected to PPA in an inert gas atmosphere (Ar, N_2). The PPA was conducted in a present-control setup using halogen lamps in the pulsed mode. The PPA system made it possible to control the temperature in the processing chamber in the range of 300–1200°C with an accuracy of ±1°C. The pulse duration ranged from 1 to 100 s. The heating rate was in the range of 180–200 K/s.

After the annealing, the samples were etched in order to remove the glass and then ohmic contacts were deposited on them.

The samples with n^+–p and p^+–n junctions were studied using different methods, including GDOES (glow-discharge optical emission spectroscopy) [18]. Other electrical, photoelectric, and optical measurements were also carried out.

3. RESULTS

3.1. Junction Depth and Sheet Resistance

At the first stage, we studied the effect of the PPA conditions (temperature and pulse duration) on the junction depth and the sheet resistance of the diffusion layers. The relevant data are given in Tables 1 and 2. The results obtained in other studies [14, 15] are also included.

As can be seen, the increase in the temperature and pulse duration under PPA (or RTA) results in an increase of the junction depth and a decrease in the sheet resistance. For the junctions formed by diffusion of P, the junction depth increased from 0.03 μm at 850°C to 0.54 μm at 1200°C, and the sheet resistance decreased from 300 Ω/□ at 850°C to 12 Ω/□ at 1050°C. For the junctions formed by the diffusion of B, the junction depth L increased from 0.1 μm at 950°C to 0.51 μm at 1200°C. It is worth noting that the diffusion depth of P and B, $L(t)$, and the sheet resistance, $\rho(t)$, change with time more rapidly than proportionally to $\sqrt{t}$. The same effect was observed in [14]. Simplified estimations using the data from Tables 1 and 2 show that under PPA the diffusivities of P and B ($D = x^2/30t$) in the surface layer of Si are 1–2 orders of magnitude higher and the activation energy is lower than the relevant parameters for conventional diffusion.

3.2. Concentration Profiles of P and B in Si after PPA

The concentration profiles of dopant atoms in structures used in semiconductor devices govern to a great extent the device parameters. In addition to this, the shape and other characteristics of the concentration

profiles provide valuable data on the diffusion mechanism and special features of interaction between diffusing dopants and the semiconductor lattice.

Figure 1 shows the concentration profiles of P measured by GDOES of Si samples in which diffusion of P from PSG was carried out using PPA. As can be seen, the concentration profiles are complex, have a two-step shape, and, therefore, cannot be described by the conventional functions erfz or erfcz. This indicates that the mechanism of diffusion of P in the surface layer of Si is rather complex and cannot be described in terms of the conventional model of substitutional or interstitial impurity atoms.

3.3. Current–Voltage Characteristics of Junctions

Figure 2 shows the current–voltage characteristics of n^+–p junctions in the process of their formation by using PPA. As can be seen, an increase in the number of pulses (the pulse duration and the sample temperature within each pulse were 20 s and 1000°C, respectively) changes the current–voltage characteristic from a nearly linear one (after two pulses) to a stable rectifying characteristic (after six pulses). The junctions formed in this manner had good rectifying properties.

3.4. Photoelectric Properties

Figure 3 shows the spectral characteristics of photodiodes formed by diffusion under PPA (curve *1*) and by conventional diffusion (curve *2*). The junction depths were 0.15 μm and 0.4 μm, respectively. In accordance with this, the spectral characteristic of shallow junctions (*1*) is slightly broader than that of deeper junctions (*2*); the latter are characterized by a greater energy loss in the short-wavelength region due to absorption in the surface layer.

The optical properties of the junctions and the efficiency of conversion of the energy of light to electrical energy were also studied. It was found that an increase in the number of annealing pulses from two to ten results in improvement of the efficiency of solar cells simultaneously with the improvement of their rectifying properties. The conversion efficiency and the fill factor increased from 1.7% after two annealing pulses to 5.9% after six to eight pulses. These parameters are lower compared with those of silicon solar cells formed by conventional diffusion, for which the values in the range of 8–12% are commonly obtained. We attribute this to the poor quality of contacts.

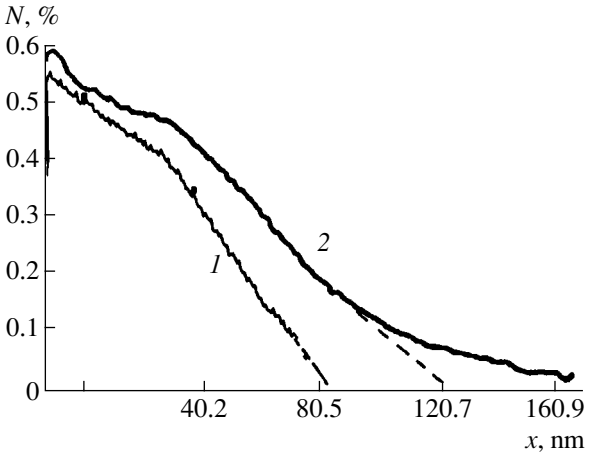

Fig. 1. Concentration profiles of P in Si after stimulated diffusion under PPA for 16 s at 900°C (*1*) and 1000°C (*2*).

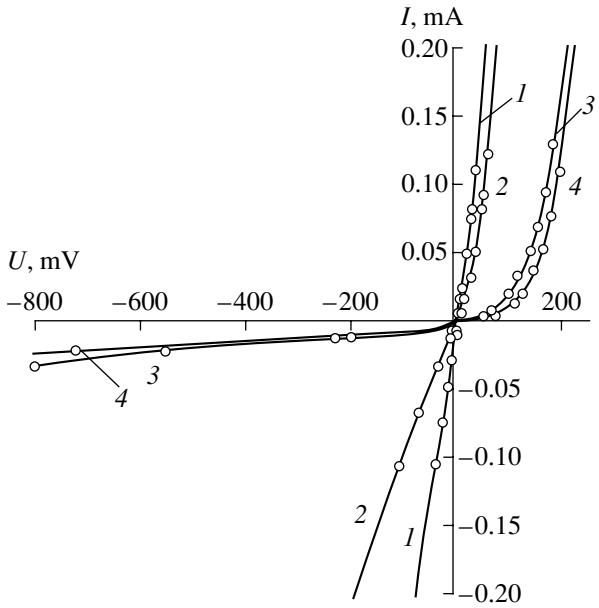

Fig. 2. Current–voltage characteristics of n^+–p junctions formed by using (*1*) 2, (*2*) 4, (*3*) 6, and (*4*) 8 annealing pulses.

4. DISCUSSION

4.1. Main Features of Diffusion of P and B in Si under PPA

As the experimental data show, the formation of shallow and ultrashallow junctions by diffusion under PPA has a number of interesting features:

(1) Phosphorus diffuses from PSG into the surface layer of Si under PPA much faster than in the case of conventional diffusion. Simplified estimates show that the stimulated diffusivity in the surface layer is one to two orders of magnitude higher than in the case of conventional diffusion;

(2) The shapes of P concentration profiles are complex and cannot be described by the conventional error functions erfz or erfcz; the diffusion depth $L(t)$ and sheet resistance $\rho(t)$ change with time faster than proportionally to $\sqrt{t}$. This indicates that, in the surface layer of Si, the stimulated diffusion of P proceeds via a

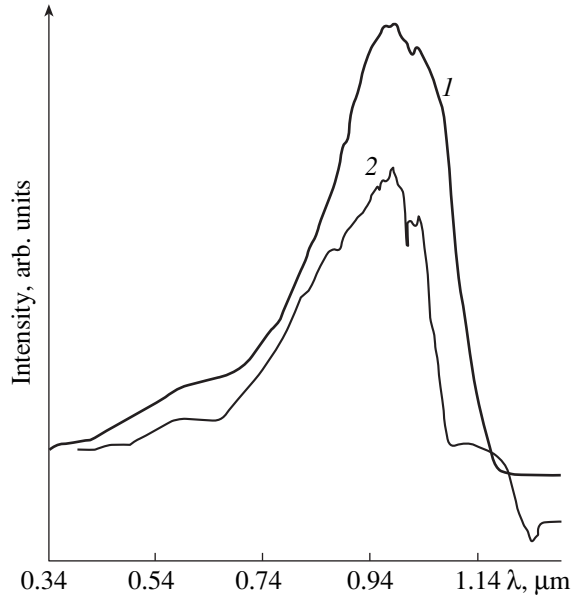

Fig. 3. Spectral characteristics of photodiodes formed using PPA (*1*) and conventional diffusion (*2*).

more complex mechanism than the substitutional and interstitial mechanisms;

(3) It was observed in many experiments that the stimulation (enhancement) effect manifests itself to a greater extent under a short-time anneal or at the initial stage of an anneal with longer duration. This indicates that the stimulated diffusion is related to the interaction between nonequilibrium defects and dopant atoms;

(4) The stimulation (enhancement) effect manifests itself to a greater extent when the heated samples are exposed to light during annealing.

We took into account all these features when generalizing the mechanisms and models of stimulated diffusion of P and B in Si.

4.2 Mechanisms of Stimulated Diffusion of P and B in PSG–Si and BSG–Si Systems

In order to explain the obtained results, we will consider the most plausible mechanisms of stimulated diffusion of P and B in PSG–Si and BSG–Si systems, respectively.

4.2.1 Kick-out and dissociative–vacancy diffusion mechanisms. Even in earlier studies [19–21], it was shown that, when silicon is oxidized, the diffusion of B from BSG and P from PSG proceeds much faster than in the case when there is no oxidation. The enhancement effect is attributed to the interaction of Si interstitials (Si_i) with impurity atoms (*kick-out* mechanism) or to the interaction of vacancies V_{Si} with dopant atoms (dissociative–vacancy mechanism) [4, 5, 19–21]. In the case of the *kick-out* mechanism, the following reactions accompanied by the recharge of diffusing B atoms occur [4, 5]:

$$(B_iV_{Si})^- + Si_i^+ \longrightarrow Si_i^0 + B_S^0; \tag{1}$$

$$\begin{aligned} &2(e+h) + B_S^0 + Si_i^0 \\ &\longrightarrow (B_iV_{Si})^- + Si_i^+ + e + h \longrightarrow B_S^0 + Si_i^0. \end{aligned} \tag{2}$$

Here, B_i denotes a B interstitial and B_S denotes a substitutional B atom.

In accordance with these reactions, it is Si interstitials and recharged B ions that mainly contribute to the exchange interaction. Their charge state and the recombination of excited charge carriers via diffusing atoms (Auger process) govern this interaction. It has been found that the B_iV_{Si} complex is a center of symmetry C_{3v}, which is formed mainly along the [111] axis, and enhances the diffusion in this direction. This is experimentally confirmed in [4, 5].

In the case of the dissociative–vacancy mechanism, B atoms interact with vacancies. This interaction can be described by the following reactions [5]:

$$B_S^- + V_{Si}^+ \longrightarrow V_{Si}^0 + B_S^0, \tag{3}$$

$$\begin{aligned} &B_S^0 + V_{Si}^0 \longrightarrow (B_iV_{Si})^- + V_{Si}^0 + h \\ &\longrightarrow (B_iV_{Si})^- + V_{Si}^+ \longrightarrow V_{Si}^0 + B_S^0. \end{aligned} \tag{4}$$

In accordance with [5], the vacancies V_{Si}^+ are centers of symmetry D_{2d}, move mainly along the [100] axis, and enhance the diffusion of B in this direction. This is also confirmed experimentally [5].

4.2.2 Dissociative diffusion mechanism. The dissociative diffusion mechanism is based on the concept of simultaneous interaction of substitutional atoms, interstitial atoms, and vacancies with each other. Let their concentrations be N_S, N_i, and N_V, respectively. The diffusion equations for these components in the general case are given in [22] and can be written, using N_i as an example, as

$$\begin{aligned} \frac{dN_i}{dt} &= \frac{d}{dt}\left[D_i\left\{\frac{dN_i}{dx} \pm ZN_iE\right\}\right] \\ &+ [K_1N_S - K_2N_iN_V] - K_i(N_i - N_{i0}), \end{aligned} \tag{5}$$

where D_i is the diffusion coefficient, Z is the charge of a diffusing atom, K_i is the coefficient accounting for the change in the concentration of interstitial atoms, N_{i0} is the initial concentration of interstitial atoms, and E is the electric-field strength. The terms in the braces in Eq. 5 account for diffusion (gradient) and drift flows, the terms in the square brackets account for the dissociation (generation) and association (recombination) flows of diffusing particles, and the terms in parenthe-

ses account for the drain of diffusing particles due to lattice defects.

Equations similar to (5) imply that the diffusion rate can be governed not only by temperature (T), concentration gradient (dN/dx), and electric field (E), but also by the dissociation (generation) and association (recombination) rates of diffusing particles via the effect of other factors, such as light ($h\nu$), radiation (α, β, γ), and ion implantation [2, 13]. The excitation of the electron subsystem and the recharging of substitutional atoms, interstitials, and vacancies play an important role in this case. The model based on the dissociative diffusion mechanism was used to explain the main features of the gradient diffusion and stimulated diffusion of different impurities in Si, GaAs, InP, and other semiconductors [2, 12, 13].

5. MODELS OF STIMULATED DIFFUSION OF P AND B IN PSG–Si AND BSG–Si SYSTEMS

Different diffusion models have been developed on the basis of the mechanisms considered above [2, 12, 13, 19–25]. However, concerning the experimental results we obtained, two models are the most appropriate, namely, the pair vacancy–interstitial diffusion model [24] and the diffusion model with variable parameters [2].

5.1 Pair Vacancy–Interstitial Diffusion Model

In order to explain the experimental data on the diffusion of P in Si, we use the pair vacancy–interstitial diffusion model suggested in [24, 25] with the following effective diffusion coefficients:

$$D^{\text{eff, eq}}_{\text{P}^+, I} = D_{(\text{P}I)^0}(k^f_{\text{P}/I}/k^b_{\text{P}/I})^i C_I^{\text{eq}, i}\exp(\eta - \eta^i)(1 + A), \quad (6)$$

$$D^{\text{eff, eq}}_{\text{P}^+, V} = \{D_{(\text{P}V)^0} + D_{(\text{P}V)} - \exp[\eta + (\varepsilon_c - \varepsilon_{(\text{P}V)^-})/kT]\} \times (k^f_{\text{P}/I}/k^b_{\text{P}/I})^i C_V^{\text{eq}, i}\exp(\eta - \eta^i)(1 + A). \quad (7)$$

Here, $D^{\text{eff}}_{\text{P}^+}$, $D^{\text{eff}}_{\text{P}^+, V}$ and $D^{\text{eff}}_{\text{P}^+, I}$ are the effective diffusion coefficients of (P atom)–vacancy (P–V) and (P atom)–interstitial (P–I) pairs, respectively; C is the concentration of defects denoted by the relevant subscripts; $A = C_{\text{P}^+}/\sqrt{C^2_{\text{P}^+} + 4n_i^2}$ is the parameter that evaluates the effect of the internal electric field on the diffusion; n_i is the intrinsic concentration of charge carriers; $D_{(\text{P}I)^0}$ and $D_{(\text{P}V)^0}$ are the equilibrium diffusion coefficients of (P atom)–defect pairs (defects are denoted by the relevant subscripts); $D_{(PV)}$ is the diffusion coefficient of (P atom)–vacancy pairs in the nonequilibrium state; $k^f_{\text{P}/I}$, $k^b_{\text{P}/I}$, $k^f_{\text{P}/V}$, and $k^b_{\text{P}/V}$ are the relevant recombination- and generation-rate constants; $\eta = (\varepsilon_\text{F} - \varepsilon_c)/kT$, where ε_F and ε_c are the Fermi level and the bottom of the conduction band, respectively; $\varepsilon_{(\text{P}, V)^-}$ is the energy level of the $(\text{P}V)^-$ complex; and η^i is the reduced Fermi level in intrinsic Si. The subscripts "eq" and "i" stand for the equilibrium state and intrinsic Si, respectively. The concentration profiles $C(x)$ were calculated in [24] for four different models of pair diffusion: diffusion by dopant–vacancy pairs, diffusion by dopant–interstitial pairs, intrinsic diffusion, and diffusion under oxidation.

Comparison of the calculated profiles reported in [24] with the experimental profiles shown in Fig. 1 indicates that there is better agreement with the first model, which accounts for the interaction of diffusing dopants with nonequilibrium vacancies. In addition to this, as follows from expressions (6) and (7), diffusion can be governed not only by temperature, but also by other factors caused by PPA, which affect the Fermi level, recharging of diffusing particles, and generation (recombination) rates.

Thus, we may conclude that the stimulated diffusion of P in the PSG–Si system subjected to PPA proceeds via the dissociative mechanism with generation of nonequilibrium vacancies in the surface layer of Si. This diffusion can be described by the model of the vacancy–impurity interaction [24] taking into account (i) the decrease in the formation energy of vacancies at high dopant concentrations, $\Delta E^f_{V^-} = (b_V C_{\text{P}^+})^2$, where b_V is the coefficient of proportionality; (ii) the change in the generation and recombination rates of substitutional atoms and vacancies, $k^f_{\text{P}/V}$ and $k^b_{\text{P}/V}$; and (iii) the change in the Fermi level position $\eta = (\varepsilon_\text{F} - \varepsilon_c)/kT$ due to the effect of heat and light.

5.2 Diffusion Model with Variable Parameters

It has been found experimentally that the diffusion of P and B in PSG–Si and BSG–Si systems under conditions of short-time annealing proceeds with variable parameters [2, 14]. This was demonstrated most clearly by the precision SIMS measurements [14]. In particular, it was shown that diffusion of B in a BSG–SiO_2–Si system under RTA is characterized by a time dependence of the surface concentration $N_0(t)$ and by a concentration dependence of the diffusion coefficient $D(N)$.

We simulated the diffusion of B in Si by numerically solving the diffusion equation, taking into account the above-mentioned special features. We used different functional dependences: $N_s = N_1\exp(a\sqrt{t})$ and $D = D_1\exp(1 - x/x_0)$, where N_s is the surface concentration. Some of the calculated diffusion profiles, which will be compared with the experimental data from [14], are

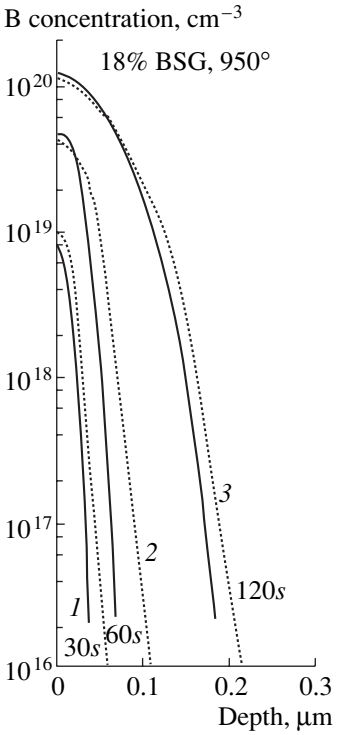

Fig. 4. Experimental [14] (solid lines) and calculated (dotted lines, curves *1*–*3*) diffusion profiles of B in Si. The calculations were performed assuming that $N_s(t) = N_1 \exp(a\sqrt{t})$ and $D(N) = D_1 \exp(1 - x/x_0)$.

shown in Fig. 4 (dotted lines, curves *1*–*3*). The experimental and calculated data are in good agreement, especially for high dopant concentrations (curve *3*).

6. CONCLUSION

(i) Shallow and ultrashallow p^+–n and n^+–p junctions were formed in Si by the diffusion of P from PSG and B from BSG under PPA with the use of halogen lamps. The electrical, photoelectric, and optical measurements point to the good quality of the junctions. However, the efficiency of photocells based on these junctions depends to a great extent on the diffusion modes and the quality of ohmic contacts.

(ii) Some features of stimulated diffusion of P and B in PSG–Si and BSG–Si systems were revealed. The main features are the increase in the diffusivity by one to two orders of magnitude compared with conventional diffusion, the complex shapes of concentration profiles $N(x,t)$, the time dependence of the surface concentration $N_s(t)$, and the concentration dependence of the diffusion coefficient $D(N)$.

(iii) The most probable models and mechanisms of stimulated diffusion in the surface layer of Si in PSG–Si and BSG–Si systems subjected to PPA are considered. For the diffusion of P, it is the vacancy–interstitial pair model [24] based on the dissociative diffusion mechanism. For the diffusion of B, it is the model that takes into account the time dependence of the surface concentration of B $N_s(t)$ and the concentration dependence of the diffusion coefficient $D(N)$ or the $D(1 - x/x_0)$ dependence.

(iv) The mechanisms of diffusion of P and B in PSG–Si and BSG–Si systems subjected to PPA are rather complex and require further investigation.

ACKNOWLEDGMENTS

We are deeply grateful to the reviewer of the first variant of the manuscript, whose helpful remarks considerably improved it.

REFERENCES

1. N. Bagraev, A. D. Buravlev, D. K. Klyachkin, *et al.*, Fiz. Tekh. Poluprovodn. (St. Petersburg) **34** (8), 725 (2000) [Semiconductors **34**, 971 (2000)].
2. S. T. Şişianu, *Tehnologii neconvenţionale in microelectronică cu tratament fotonic şi difuzie stimulată* (Tehnica U.T.M., Chisinau, 1998).
3. M. Drăgănescu, in *Proceedings of the 20th International Semiconductor Conference, Sinaia, Romania, 1997.*
4. N. T. Bagraev, D. K. Klyachkin, and V. L. Sukhanov, Pis'ma Zh. Tekh. Fiz. **17** (2), 42 (1991) [Sov. Tech. Phys. Lett. **17**, 55 (1991)].
5. A. A. Andronov, N. T. Bagraev, D. K. Klyachkin, *et al.*, Fiz. Tekh. Poluprovodn. (St. Petersburg) **33** (1), 58 (1999) [Semiconductors **33**, 51 (1999)]; Fiz. Tekh. Poluprovodn. (St. Petersburg) **32** (2), 137 (1998) [Semiconductors **32**, 124 (1998)].
6. A. Bousetta, J. A. van der Berg, D. Armour, and P. C. Zalm, Appl. Phys. Lett. **58** (15), 1626 (1991).
7. L. V. Dokukina and S. I. Kondratenko, Élektron. Prom-st, No. 1, 62 (1992).
8. A. Yu. Kuznetsov, M. Janson, A. Hallin, *et al.*, Nucl. Instrum. Methods Phys. Res. B **148**, 279 (1999).
9. H. B. Erzgreber, P. Zaumseil, E. Bugiel, *et al.*, J. Appl. Phys. **72** (1), 73 (1992).
10. T. D. Dzhafarov, *Light-Induced Atomic Processes in Semiconductors* (Énergoatomizdat, Moscow, 1984).
11. D. C. Schmidt, B. G. Svensson, J. L. Lindstrom, *et al.*, Mater. Sci. Eng. B **57**, 161 (1999).
12. I. K. Sinishchuk, G. E. Chaĭka, and F. S. Shishiyanu, Fiz. Tekh. Poluprovodn. (Leningrad) **19** (4), 674 (1985) [Sov. Phys. Semicond. **19**, 415 (1985)].
13. T. S. Shishiyanu, I. K. Sinischiuk, and S. T. Shishiyanu, Int. J. Electron. **78** (4), 699 (1995).
14. M. Miyake, J. Electrochem. Soc. **138** (10), 901 (1991).
15. B. Hartiti, A. Slaoni, I. C. Muller, *et al.*, J. Appl. Phys. **71** (11), 5474 (1992).
16. O. I. Velichko and V. A. Labunov, Mikroélektronika **14** (6), 542 (1985).

17. Ad. Agarwal, D. H. Eaglesham, H. J. Gassmann, L. Pelaz, S. B. Herner, D. C. Jacobson, and T. E. Haynes, Lecture Tu-1430, *Modeling Enhanced Diffusion of Implanted Dopants*, http://www.ihp-microelectronics.com/chipps/Djpg/Agarwal.html.
18. I. M. Dharmadasa, M. Ives, J. S. Brooks, *et al.*, Semicond. Sci. Technol. **10**, 369 (1995).
19. S. M. Hu, J. Appl. Phys. **45**, 1567 (1974).
20. R. B. Fair and J. C. C. Tsai, J. Electrochem. Soc. **124**, 1107 (1977).
21. R. B. Fair, Diffus. Defect Data **37**, 1 (1984).
22. M. R. Pinto, D. M. Baulin, C. S. Rafferty, *et al.*, in *Technical Digest of the International Electron Devices Meeting, IEDM-92, 1992*, p. 923.
23. M. Uematsu, Jpn. J. Appl. Phys. **38**, 6188 (1999).
24. M. Yoshida, M. Morooka, M. Takahashi, and H. Tomokage, Jpn. J. Appl. Phys. **39**, 2483 (2000).
25. M. Yoshida, M. Takahashi, and H. Tomokage, Jpn. J. Appl. Phys. **38**, 36 (1999).

Translated by Yu. Sin'kov

Semiconductors, Vol. 36, No. 5, 2002, pp. 588–591. Translated from Fizika i Tekhnika Poluprovodnikov, Vol. 36, No. 5, 2002, pp. 618–621.

PHYSICS OF SEMICONDUCTOR DEVICES

Simulation of Avalanche Multiplication of Electrons in Photodetectors with Blocked Hopping Conduction

S. P. Sinitsa

Institute of Semiconductor Physics, Siberian Division, Russian Academy of Sciences, pr. Akademika Lavrent'eva 13, Novosibirsk, 630090 Russia

e-mail: IFP@isp.nsc.ru

Submitted May 31, 2001; accepted for publication October 20, 2001

Abstract—The avalanche electron multiplication in a silicon structure with blocked hopping conduction is simulated for the photon-counting mode. The acceleration of an electron in an electric field that is linearly dependent on the coordinate, the elastic scattering of electrons by longitudinal acoustic phonons, the inelastic scattering of electrons by intervalley phonons, and the ionization of impurity centers are taken into account when considering the motion of an electron. A simple algorithm making it possible to calculate directly the coordinates of all ionized centers in an avalanche and the probability of N electrons leaving the avalanche if a single electron has entered the multiplication region is suggested. It is shown that this probability is at its maximum in the vicinity of $\langle N \rangle$ (the mean value of the leaving-probability function), which is consistent with experimental data. © *2002 MAIK "Nauka/Interperiodica".*

1. INTRODUCTION

The Si:As- and Si:B-based blocked impurity band (BIB) structures [1–3] have found wide application in photodetector arrays designed for the wavelength range of 5–40 μm and in photon counters. When designing the corresponding photocells for the photodetector arrays and photon counters, different requirements are imposed on the arrays and counters with respect to both the physical parameters and the modes of their operation. Thus, in a detector array, all the active components operate at the same read-out voltage; therefore, their structure ensures a high uniformity of photoelectric conversion with an ultimately high efficiency of this conversion. This is attained owing to the fact that the mode of avalanche multiplication is typically not used in photodetector arrays and the quantum efficiency is in the range of 50–80%. In order to obtain an electric pulse, which can be isolated from the preamplifier noise in the photon counters, one has to attain a photoelectric-conversion efficiency that is much greater than unity. Because of this, the avalanche-multiplication mode is used in the BIB counters, with the multiplication factor being equal to $M = 3 \times 10^4$. To this end, the concentration of the compensating (in the case under consideration, acceptor) impurity is increased in the photoactive layer of a BIB structure. This increases the electric field in the space-charge region and makes it possible to attain the required values of the multiplication factor.

The experimental study of Si:As-based BIB structures, operating in the photon-counting mode, demonstrated interesting and important special features of avalanche processes in these structures [4]. It was ascertained that large values of the multiplication factor ($M > 10^4$) can be easily obtained in these structures. It was also found that the variance of charge in the BIB-structure avalanche initiated by a single photon is much smaller than the corresponding variance in the avalanches in p–n junctions. Thus, the variance (D) of the probability function for N electrons leaving the avalanche region [$W(N)$] if a single photogenerated (or thermally generated) electron has entered this region is equal to $D < \{\langle N \rangle\}$, which [5, 6] is not observed in the p–n-junction avalanches in which the variance $D \gg \{\langle N \rangle\}$.

The result of measuring the noise factor in a BIB counter is also consistent with the aforementioned special feature; this result shows that the noise factor is equal to unity within the experimental accuracy [7]. The results of measuring the illuminance–current sensitivity in the linear photodetector arrays based on Si:As BIB structures in the mode of avalanche amplification are also consistent with this special feature [8].

The study of the avalanche statistics in a p–n junction [9, 10] showed that the function $W(N)$ features a maximum at $N = 1$. This position of the maximum is based on the assumption that there is a Poisson distribution of the number of ionization events in the avalanche region. The corresponding expression for $W(N)$ (in an electron avalanche) is written as

$$W(N) = \exp(-N\langle P \rangle)[\exp\langle P \rangle - 1]^{(N-1)}, \qquad (1)$$

where $\langle P \rangle = \ln\langle N \rangle$ is the mean number of ionization events executed by a single charge carrier in the multiplication layer.

1063-7826/02/3605-0588$22.00

Previously [4], the function $W(N)$ for a BIB structure was determined from the solution to the Kolmogorov–Smoluchowski–Chapman equation; i.e.,

$$W(N) = (1 - 1/\langle N\rangle)^N/(\langle N\rangle - 1). \quad (2)$$

Both expressions (1) and (2) yield the same result with a maximum at $N = 1$; this is not surprising since the Poisson distribution is one of the solutions to the Kolmogorov–Smoluchowski–Chapman equation and is not consistent with experimental data for a BIB structure.

It was assumed [4] that the special features of the avalanche statistics in a BIB structure were related to the non-Markovian process of the avalanche development; the corresponding calculations were performed. The $W(N)$ function was reconstructed using its first four moments determined from the probability function for distribution of the path lengths (l) between the ionization events $W(l)$. The latter function was determined by numerical integration of the avalanche-ionization process. The function $W(N)$ determined in this manner indicated that the assumption concerning the non-Markovian character of the avalanche multiplication in a BIB structure is correct.

At the same time, the assumption that there is a constant electric field in a BIB structure (this assumption was used previously [4] when simulating the function $W(l)$) is inconsistent with an actual BIB structure and can result in uncontrollable systematic errors in determination of $W(N)$ using its first four moments.

Taking the above into account, it is expedient to perform a direct simulation of the avalanche electron multiplication in a silicon BIB structure in the photon-counting mode taking into account the linear dependence of the electric field on the coordinate. In this case, the function $W(N)$ can be calculated using the direct simulation of the avalanche development and employing averaging over a number of avalanches. When considering the motion of an electron, its acceleration in an electric field, its elastic scattering by longitudinal acoustic phonons, its inelastic scattering by intervalley phonons, and ionization of neutral impurity centers are taken into account. A simple algorithm is suggested that makes it possible to calculate both the coordinates of all ionized centers in an avalanche and the function $W(N)$ describing the probability that N electrons leave the multiplication region if a single electron has entered this region.

2. DESCRIPTION OF A BIB-STRUCTURE MODEL

The motion of an electron was simulated in the six-dimensional coordinate and momentum space. The scattering mechanisms resulting in the most intense interactions in n-Si at the liquid-helium temperature were taken into account [11]. This corresponds to the operation of an actual BIB structure as a component of both the photodetector array and as the photon counter. Elastic scattering of an electron by longitudinal acoustic phonons is taken into account if the electron energy $E < 47$ meV. For the electron energy in the range of 47 meV $< E <$ 81 meV, scattering by the $f2$ intervalley phonons is considered. The value of $E = 81$ meV is taken as the threshold ionization energy $E_{av} = (3/2)E_d$, where $E_d = 54$ meV is the optical ionization energy of an As atom in Si, for the random distribution of energy $E = E_{av} - E_d$ between two electrons after ionization. It was assumed that, when the electron energy becomes as high as the ionization threshold, the ionization event occurs; simultaneously, the coordinate Z_I along the axis parallel to the electric field F was recorded. It is assumed that electrons do not recombine in the space-charge region.

The non-Markovian nature of the avalanche ionization is taken into account in simulation by introducing the probability of scattering for each of the aforementioned mechanisms as a function of electron energy and also by the law of conservation of this energy in the course of inelastic scattering (with allowance made for the phonon energy). Consideration of the probability of electron scattering is consistent with the accepted procedures and with the known constants and functions for silicon, which were reported in detail in [11].

The algorithm for calculating both ionization sites Z_I in an avalanche and the function $W(N)$ involves the following. A vector is formed, the components of which are the coordinates of ionization sites Z_I in the order of their appearance when the first electron moves in the multiplication layer. Once the first electron has left the multiplication layer, the first component Z_I is treated as the starting point Z_0 for the motion of the second electron and is removed from the vector. The second electron performs ionization during its motion and supplements the vector with the components Z_I, whereas the third electron (like the second one) reduces the vector by one (the second) component. It is easy to verify that this process, if included in the corresponding cycles, makes it possible to trace all the avalanche branches without omitting even a single branching point.

3. RESULTS AND DISCUSSION

A typical dependence of the electron energy on the coordinate parallel to the electric field is shown in Fig. 1. It can be seen that elastic scattering represented in Fig. 1 by the condensation of points lying along the monotonic segments ($E \propto Z^2$) can only prolong the process but does not control the important features of this process. The determining factor is the ratio between the probability of generation of intervalley phonons and the probability of ionization. It can also be seen that the BIB-structure region with a lower electric field (the first 5 μm) is only slightly involved in the avalanche formation and can extend the probability function to longer electron-path lengths.

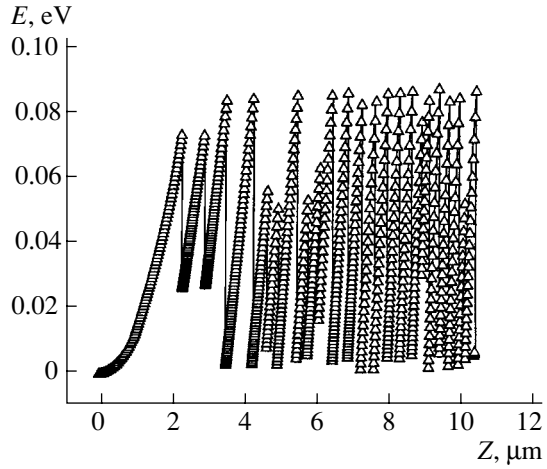

Fig. 1. Typical dependence of the electron energy on the coordinate along the electric field in a BIB structure. The following values of the parameters were used: the concentration of compensating acceptors $N_a = 3 \times 10^{13}$ cm^{-3}, the blocking-layer thickness $b = 4$ μm, $T = 10$ K, and the bias voltage $V_b = 2.8$ V.

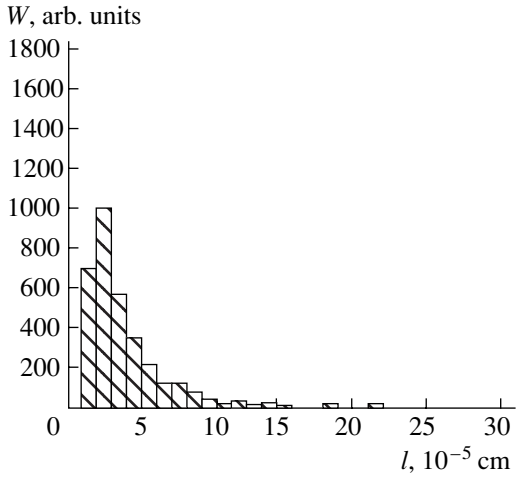

Fig. 2. Typical function for the probability of the free-path length between the impact-ionization events $W(l)$. The parameters are $N_a = 2 \times 10^{13}$ cm^{-3} and $V_b = 2.0$ V.

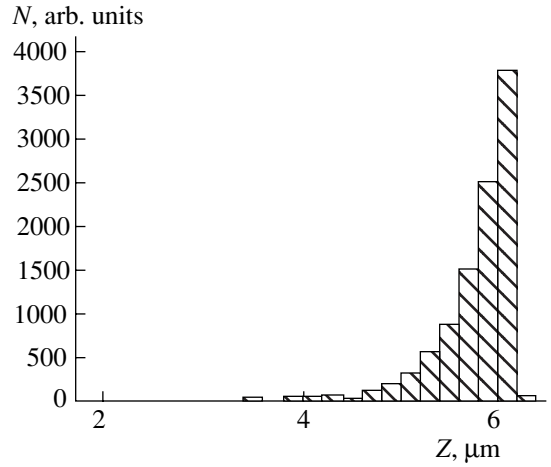

Fig. 3. Distribution of ionized centers along the avalanche in a BIB structure.

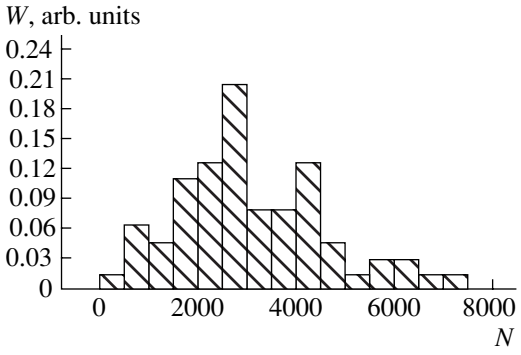

Fig. 4. The probability function for the N electron leaving the avalanche if a single electron enters the multiplication region. The parameters are $N_a = 5 \times 10^{13}$ cm^{-3} and $V_b = 2.8$ V. Averaging was performed over 64 avalanches.

The calculated probability of the path length of a primary electron $W(l)$ as a function of the distance between the successive ionization points l is shown in Fig. 2. Averaging was performed over 300 primary electrons. The form of the function $W(l)$ is qualitatively consistent with the results reported previously [4]. However, it is easy to verify that the obtained dependence is appreciably more extended to the region of large values of l, which is primarily related to the linear dependence of the field on the coordinate and corroborates the assumption about the significant effect of the linear electric-field dependence on the coordinate.

The calculated distribution of ionized centers in an avalanche N_I along the coordinate Z is shown in Fig. 3; this distribution was averaged over a number of avalanches. It can be seen that the charge, which is generated in the avalanche owing to ionized impurities, is formed in the photoactive layer within a micrometer distance from the blocking layer. This charge becomes included in the negative feedback of the steady-state avalanche process and can give rise to an additional (with respect to the mechanism for the decrease in the potential in the avalanche region) limitation of the avalanche and its fluctuations, which was considered by Shadrin *et al.* [12]

Figure 4 displays the function $W(N)$, determined using the direct calculation of the number of electrons in the avalanches. For the chosen values of N, this function features a maximum located in the vicinity of $\langle N \rangle$ and has the variance $D \propto \langle N \rangle$.

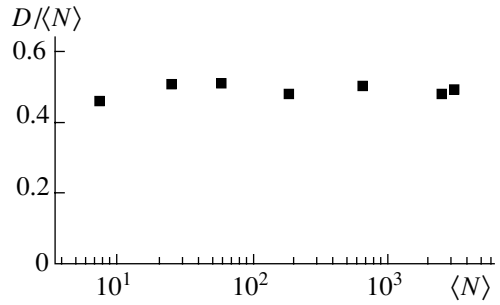

Fig. 5. Ratio between the distribution variance D and the mean number of electrons $\langle N \rangle$ that left the avalanche. The parameters are $N_a = 5 \times 10^{13}$ cm^{-3} and $T = 10$ K.

The ratios $D/\langle N \rangle$ for the range of $\langle N \rangle$ of interest are shown in Fig. 5. It can be seen that this ratio is smaller than unity in the entire range under consideration. It is convenient to express the noise factor in terms of variance, i.e.,

$$F_N \equiv \langle N^2 \rangle / \langle N \rangle^2 = 1 + D/\langle N \rangle^2. \quad (3)$$

It can be seen from formula (3) that, within the accuracy of observation, the noise factor F_N is equal to unity for $\{\langle N \rangle\} > 10$. It is only in a completely determinate avalanche, in which $D = 0$, that F_N is exactly equal to unity. This result also accounts for the absence of additional noise as the readout voltage increases and as the elements of a linear photodetector array are transferred to the avalanche-multiplication mode [8].

The above results demonstrate that the avalanche formation in a BIB structure is more determinate compared to a Markovian process; the latter is defined in terms of two probability functions and ranks next to purely stochastic processes. The fact that the avalanche process is substantially non-Markovian may be caused by a longer (by nearly an order of magnitude) free-path time between ionization events in a BIB structure compared to the corresponding time in a *p–n* junction. This difference is related to a much higher electron energy in the *p–n*-junction avalanches. As the interval between ionization-inducing collisions increases, the processes involving electrons within this interval affect more and more the ionization probability. The situation then resembles that for such a typically non-Markovian process as the branching process of growth of a biological population; the non-Markovian nature of the latter process is related to the dependence of the fission probability on the age of a species.

4. CONCLUSION

(i) The avalanche electron multiplication in a BIB structure was simulated for the photon-counting mode with allowance made for the actual dependence of the electric field on the coordinate along the structure axis. The calculations were performed for the six-dimensional space of coordinates and momenta. The major mechanisms of electron interaction with the lattice and impurities in *n*-Si at $T = 10$ K were taken into account.

(ii) The results of calculations show that, in a BIB structure, the probability of electrons leaving the avalanche $W(N)$ has a maximum located near the mean value $\langle N \rangle$ for all actual values of the multiplication factor M in the range of $M = (1–3) \times 10^4$; it is also shown that the variance $D < \{\langle N \rangle\}$ and the noise factor is nearly equal to unity. This makes it possible to appreciably increase the signal-to-noise ratio both in the BIB-based photon counters and in the elements of photodetector arrays by increasing the bias voltage.

(iii) A simple algorithm for the direct evaluation of the avalanche process is suggested; this algorithm makes it possible to calculate the function $W(N)$, its variance, and the noise factor for an avalanche of charge carriers with a like sign using a computer with moderate memory size and speed.

REFERENCES

1. R. A. Noel, Proc. SPIE **1685**, 250 (1992).
2. J. E. Huffman, Proc. SPIE **2274**, 157 (1994).
3. M. Atac, J. Park, D. Cline, *et al.*, Nucl. Instrum. Methods Phys. Res. A **314**, 54 (1992).
4. R. A. LaViolette and M. G. Stapelbroek, J. Appl. Phys. **65** (2), 830 (1989).
5. M. C. Teich, K. Matsuo, and B. E. A. Saleh, IEEE J. Quantum Electron. **QE-22**, 1184 (1986).
6. N. Z. Hakim, B. E. A. Saleh, and M. C. Teich, IEEE Trans. Electron Devices **ED-37**, 599 (1990).
7. J. Kim, Y. Yamamoto, and H. H. Hogue, Appl. Phys. Lett. **70** (21), 2852 (1997).
8. D. G. Esaev and S. P. Sinitsa, Fiz. Tekh. Poluprovodn. (St. Petersburg) **35** (4), 474 (2001) [Semiconductors **35**, 459 (2001)].
9. R. J. MacIntire, IEEE Trans. Electron Devices **ED-13** (1), 164 (1966).
10. A. S. Tager and V. M. Val'd-Perov, *Avalanche Transit-Time Diodes* (Sov. Radio, Moscow, 1968).
11. V. M. Ivashchenko and V. V. Mitin, *Simulation of Kinetic Phenomena in Semiconductors. The Monte Carlo Method* (Naukova Dumka, Kiev, 1990).
12. V. D. Shadrin, V. T. Coon, and I. K. Blochin, J. Appl. Phys. **74** (11), 6972 (1993).

Translated by A. Spitsyn

Semiconductors, Vol. 36, No. 5, 2002, pp. 592–598. Translated from Fizika i Tekhnika Poluprovodnikov, Vol. 36, No. 5, 2002, pp. 622–628.

PHYSICS OF SEMICONDUCTOR DEVICES

Spectral Line Width of the Current-Tunable Lasers on the Base of InAsSb/InAsSbP at Low Temperature

A. N. Imenkov*, N. M. Kolchanova*, P. Kubat, S. Tsivish**, and Yu. P. Yakovlev***

** Ioffe Physicotechnical Institute, Russian Academy of Sciences, Politekhnicheskaya ul. 26, St. Petersburg, 194021 Russia*

*** Y. Heyrovský Institute of Physical Chemistry, Academy of Sciences of the Czech Republic, Dolyš kova 3, 18223 Prague 8, Czech Republic*

Submitted October 24, 2001; accepted for publication October 30, 2001

Abstract—Current-tunable diode lasers with a narrow emission line (7–10 MHz) were designed on the basis of a InAsSb/InAsSbP heterostructure for low-temperature (15–60 K) operation within the range of 3.2–3.4 μm. It is shown that the fast modulation of radiation frequency can be attained only if the current far exceeds the threshold value. This is due to the fact that a smooth optical waveguide can be formed only if the concentration of nonequilibrium charge carriers at the lateral edges of the cavity is in sufficient excess over the threshold. It is noted that the current-induced increase in the hole concentration near the *p* region due to a reduction in the effective lifetime of the carriers in the lasing mode additionally extends the frequency tuning range. The absorption spectrum of ammonia is presented within the range from 3232 to 3237 cm^{-1} as measured with the use of the laser developed. © *2002 MAIK "Nauka/Interperiodica".*

INTRODUCTION

Current-tunable diode lasers hold much promise for various branches of modern science and technology. One of the most advanced up-to-date fields of application is the detection of the absorption spectra in gases with the aim of revealing harmful gas present in the atmosphere, as well as the study of the vibration–rotation spectra of gas molecules [1–9]. The diode laser is a valuable tool of molecular spectroscopy, since it facilitates the determination of low concentrations of gases due to its high selectivity and detectivity. Along with the output intensity, tuning range, and the speed of response, the spectral line width is one of the most important parameters of tunable lasers. In our previous studies [10–12], we proposed a technique for the determination of the lasing line width in current-tunable lasers and presented the results obtained for the InAsSb/InAsSbP-based lasers operating at 60–80 K. The line width of lasers with a smooth waveguide induced by the action of the laser radiation is determined. In lasers of this type, the concentration of nonequilibrium carriers increases from the midline of the waveguide towards its edges, thus forming a smooth waveguide where the light propagates from one cavity wall to another along the active region width. The line width of lasers with a smooth waveguide was estimated at 10–30 MHz. This narrow range of spectral line widths Δf obtained for different types of lasers suggests that the frequency noise, which broadens the lasing line, is caused by the phenomena connected with the interaction between radiation and nonequilibrium carriers rather than by the defects existing in the crystal or in the structure. Fluctuations in the density of nonequilibrium charge carriers and the related variations of the refractive index influence the natural frequency of the cavity and, therefore, the spectral line width. The dependence of the lasing line width on the laser parameters was analyzed with regard for the special features of lasers with a smooth waveguide. Based on the expressions derived in [10–12], the calculation of the line width yields values from 3 to 10 times greater than those predicted by Henry [13] and Yamada [14]. Consideration of the physical processes taking place in the tunable lasers with a smooth waveguide of different geometric parameters suggests a heavy dependence of the lasing line width on both the concentration of nonequilibrium charge carriers N and the volume of the active region [11]. In this study, we measured the lasing line width for lasers operating at cryogenic temperatures (from 15 to 60 K) and determined the parameters of lasers which provide minimal line width in the temperature range specified.

EXPERIMENTAL

Most of the diode laser structures based on InAsSb/InAsSbP double heterostructure were grown by liquid-phase epitaxy [10–12] on *p*-InAs crystals doped with Zn to a density of holes as high as 10^{19} cm^{-3}. The geometrical parameters of the structures and the carrier densities in the layers were chosen in such a way so as to prevent the freezing-out of the carriers and ensure laser operation at low temperatures. The narrow-gap active region with the band gap of 0.4 eV at $T = 77$ K

1063-7826/02/3605-0592$22.00 © 2002 MAIK "Nauka/Interperiodica"

and a thickness of 1.1–1.5 μm formed a type-I heterojunction confined by two InAsSbP layers (2-μm-thick each) with a band gap of 0.6 eV at $T = 77$ K. The electron density in the undoped region amounted to $(2–4) \times 10^{16}$ cm^{-3}. The hole density in the Zn-doped *p*-InAsSbP boundary layer adjacent to the substrate was ~10^{19} cm^{-3}, and the electron density in the Sn-doped *n*-InAsSbP was $(6–8) \times 10^{18}$ cm^{-3}. The upper 0.5-μm-thick layer was doped with Si to an electron density of 10^{19} cm^{-3}. After the epitaxial growth, the substrate was thinned down to 100 μm. Double-grooved mesa-chips with 16-μm-wide stripes spaced at 500 μm were lithographically formed. Diode lasers with a 200- to 500-μm-long Fabry–Perot resonator were produced by cleaving. Laser chips were mounted on the surface of a special copper holder [15, 16], which allowed the diode to be installed into the pumped-out helium cryostat.

The spectral characteristics of the laser structures were measured, and the dependence of the lasing line width on the injection current was studied. The experiments were carried out in the temperature range between 15 and 80 K with the use of a diode laser spectrometer described in the previous papers [15, 16]. The laser under study was placed into a Dewar pumped-out closed-cycle laser vessel (Laser Photonics, model L573) functioning in the temperature range from 12 to 100 K. The temperature and the power output were monitored using the Laser Photonics systems, models L5820 and L571. A parabolic mirror focused the laser beam onto the entrance slit of a grating monochromator used to separate the laser mode to be studied. After leaving the monochromator, the beam propagated through a cell with an absorbing gas (e.g., NH_3) or through the Fabry–Perot air etalon, whose natural wave numbers were spaced 0.026 cm^{-1}. The beam then passed a KBr window and entered a 40-cm-long cell filled with the studied gas under a pressure of 1–3 Torr. The radiation emitted by the current-tunable laser was detected by an InSb photodiode cooled by liquid nitrogen. The electric signal from the photodiode was amplified by a broadband amplifier.

The absorption spectra were measured as a function of the injection current being varied linearly for the time $t = 1$ min. The range of current from 50–100 to 300 mA was divided in intervals of 50 mA each. The supply current was modulated by a small sinusoidal signal with a frequency of 1 kHz. The constantly varying second derivative of the signal with respect to the time was recorded using a computer and an SP-530-type recorder with a lock-in amplifier. The bandwidth of the photodetecting amplifier ranged from 50 to 80 kHz.

To measure the lasing line width, the tunable laser was energized by a direct current modulated by a sawtooth current with a modulation depth of 3–10 mA and frequency of 200 Hz. The signal from the photodetecting amplifier *U* entered the channel of a Le Croy 9361

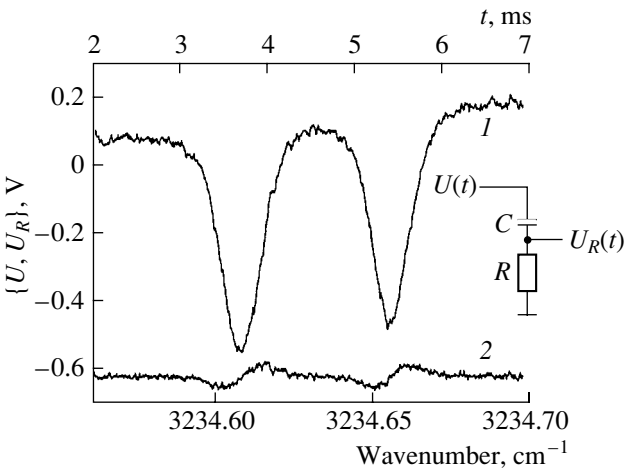

Fig. 1. Oscillograms of (*1*) $U(t)$ signal representing the absorption spectrum of NH_3 and (*2*) the $U_R(t)$ signal after an *RC* filter. The inset shows the schematic circuit diagram of the *RC* filter.

digital oscillograph (Fig. 1, curve *1*). This signal was fed into the differentiating *RC* circuit with the time constant of 20 μs. The signal taken from the resistor U_R arrived at the other channel of the oscillograph (Fig. 1, curve *2*). The oscillograph detected the mean signal $\bar{U}_R$ averaged over at least 100 values and its standard deviation $\langle U \rangle$ in the extremes of the signals. Two photodetecting amplifiers with bandwidths from 10 Hz to 300 kHz and from 50 Hz to 80 kHz were also used.

Let us now dwell on the technique of measuring the lasing line width and formulate the conditions for its applicability. The technique utilizes the narrow lines present in the absorption spectra of the reference gases and makes use of the capability of the *RC*-circuit to differentiate the low-frequency part of the signal and transmit its high-frequency part without distortions. The *RC*-circuit output voltage U_R is related to the input voltage *U* by the expression

$$U' = U'_R + U_R/\tau, \tag{1}$$

where $\tau = RC$ is the time constant of the *RC* circuit. The lasing frequency *f* can be represented as the sum of f_0, which continuously varies with the current, and the term corresponding to the random deviations of the frequency μ due to the variations in current. The random deviations of the frequency μ are responsible for the effective width of the lasing line. In view of the Lorentzian shape of the lasing line [13], its full width at the half-maximum Δf can be found as the doubled standard deviation of the lasing frequency

$$\Delta f = 2\langle \mu \rangle. \tag{2}$$

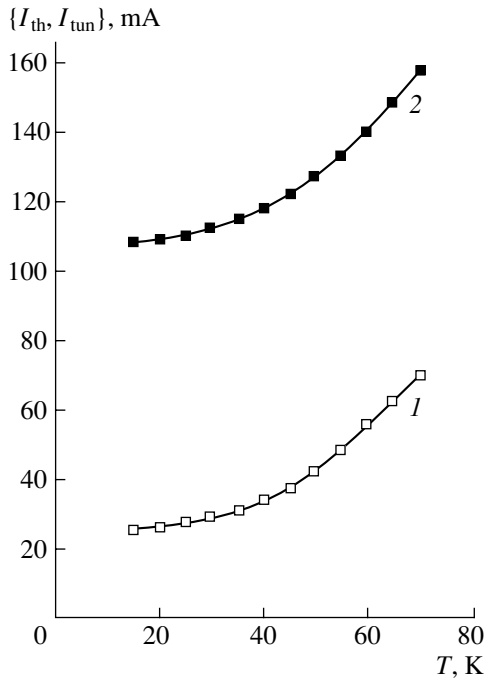

Fig. 2. Temperature dependences of (*1*) the lasing threshold current I_{th} and (*2*) the current giving rise to a tunable line I_{tun}.

The resistor voltage U_R also contains the average component $\bar{U}_R$ and the random quantity U_μ, which allows us to make the following rearrangement of expression (1):

$$\frac{dU}{df}[(df_0/dt) + (d\mu/dt)] = (d\bar{U}_R/dt) + (dU_\mu/dt) + (\bar{U}_R/\tau) + (U_\mu/\tau). \quad (3)$$

When averaging the U_R signal at extreme points, the $d\bar{U}_R/dt$ value may be considered as zero. Since the result of averaging random quantities is always zero, we obtain

$$\bar{U}_R = \tau(df_0/dt)(dU/df). \quad (4)$$

The signals with frequencies below $1/2\pi\tau$ are suppressed by the *RC* circuit. Therefore, the term U_μ/τ may be omitted from the dU/dt signal in the presence of components with much higher frequencies. Then, for the random components, we obtain the equation

$$dU_\mu = (dU/df)d\mu, \quad (5)$$

which, after integrating and finding the standard deviation $\langle\mu\rangle$, allows the determination of the $\langle U_\mu\rangle$ value. We have

$$\langle U_\mu\rangle = (dU/df)\langle\mu\rangle. \quad (6)$$

Substituting expressions (6) and (4) into (2), we obtain the expression for the lasing-line width in terms of $\bar{U}_R$, $\langle U_\mu\rangle$, and df_0/dt in the form

$$\Delta f = 2\tau(df_0/dt)\langle U_\mu\rangle/\bar{U}_R. \quad (7)$$

In order to eliminate the influence of the amplitude fluctuations, the standard deviation U_R was measured not only at the extreme points (s) but also away from them (s_0), where $U_R = 0$. The sought-for quantity $\langle U_\mu\rangle$ was calculated as

$$\langle U_\mu\rangle = (s^2 - s_0^2)^{0.5}. \quad (8)$$

To determine Δf with a high accuracy requires that there should be only a few suppressed frequencies included in the U_R signal. In other words, the range of the reproduced frequencies should be considerably wider than the range where the roll-off of the frequencies is observed. It is required that the lowest frequency of the amplifier be an order of magnitude lower than $1/2\pi\tau$, lest differentiating by the *RC* circuit be affected. Frequencies below $1/2\pi\tau$ are suppressed by the circuit itself. The frequency cutoff of the amplifier should be abrupt and exceed $1/2\pi\tau$ by more than an order of magnitude. When the standard deviation is determined, the strobe-pulse width should be at least an order of magnitude smaller than τ, lest the deviations U_μ from the average $\bar{U}_R$ be underestimated. When determining the df_0/dt value, we used the known doublet lines of absorption (Fig. 1), as well as the Fabry–Perot etalon resonator.

RESULTS

With respect to the lasing spectra, the lasers fall into two categories: tunable (where the frequency of lasing depends on the injection current I) and nontunable (where the wavelength is fixed). Frequency spectra of nontunable lasers include up to ten lines corresponding to the longitudinal cavity modes and nearly the same number of lines related to the transverse spatial modes. The dominance of the long-wavelength modes over the short-wavelength ones increases with current. In nontunable lasers, the cavity length (300–500 μm) is statistically larger and the active region thickness (0.8–1.1 μm) is smaller than those in the tunable ones (200–300 μm and 1–1.5 μm, respectively). In the frequency spectrum of tunable lasers, a set of emitted lines can only appear at small (from one to three times) or, in contrast, large (above five times) excess of current over the threshold I_{th}. At moderate currents, only one tunable line prevails. This line is shifted to the shorter wavelengths with respect to that prevailing at low currents by five to seven intermode intervals. The threshold current giving rise to the tunable line I_{tun} shows a relatively weaker increase with temperature (Fig. 2, curve *2*) than the lasing threshold current I_{th} (Fig. 2, curve *1*). When $I \approx I_{tun}$, the tunable-line intensity increases due to the attenuation of the fixed lines. Figure 3 shows the intensity of radiation that passed through the external Fabry–Perot cavity versus the current. Harmonic oscillations are not observed for the current ranging from I_{th} to I_{tun}. This indicates that there is no frequency tuning at low

currents. A harmonic signal appearing in the range from I_{tun} to (2–3)I_{tun} indicates that the frequency tuning of the prevailing short-wavelength line does actually take place. Increasing the off-axis tilt of the external cavity results in a shift of sinusoids to the right on the screen of the oscillograph, which indicates that the radiation wave number increases with current. The maximal tuning range (up to 6 cm^{-1}) is attained at the temperatures T = 15–20 K, which is consistent with the formulas derived in [10]. With increasing temperature, the tuning range narrows, which is largely due to the recommenced generation of the long-wavelength lines. At T > 70–80 K, single-mode tunable lasing is usually observed for only the short saw-tooth pulses with a duration <20 μs and an off-duty factor >50, when heating of the laser is moderate.

Figure 4 presents the ammonia spectrum doubly differentiated with respect to the wave number and measured at 17.5 K for the current ranging from 110 to 350 μ. Wave numbers of the bands identified are plotted versus the current in Fig. 5. The resulting calibration dependence is nearly linear. The same bands were used to measure the lasing line width. In the experiments involving amplifiers with different high-frequency cutoffs (80 and 300 kHz), the line width obtained at equal currents is the same within experimental error (Fig. 6); this indicates that the error which the amplifier introduces into the signal measurement is fairly small. Therefore, the points obtained in the experiments with either of the two amplifiers can be connected by a single curve. The resulting curve represents a polynomial of the second degree, with a minimum at 270 mA corresponding to the half-width of 7 MHz, which is smaller than that observed previously with similar lasers at 60 K by a factor of 1.5. Compared to the lasers under study, the lasers considered previously were characterized by a lower density of acceptors in both the substrate and the boundary layer and by a thinner active region. Their lasing line width was measured at higher temperatures (T = 60–70 K).

Thus, a rise in the density of holes in the boundary p layer and an increase in the active layer thickness provided a single-mode frequency tuning and a narrow lasing line at lower temperatures than those at which these were attained before.

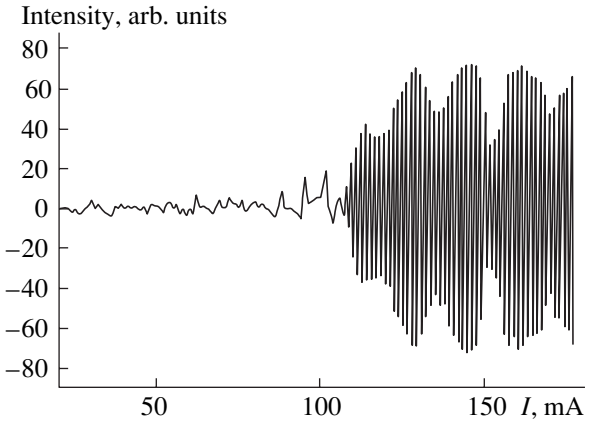

Fig. 3. The intensity of radiation passed through the external Fabry–Perot resonator versus the current.

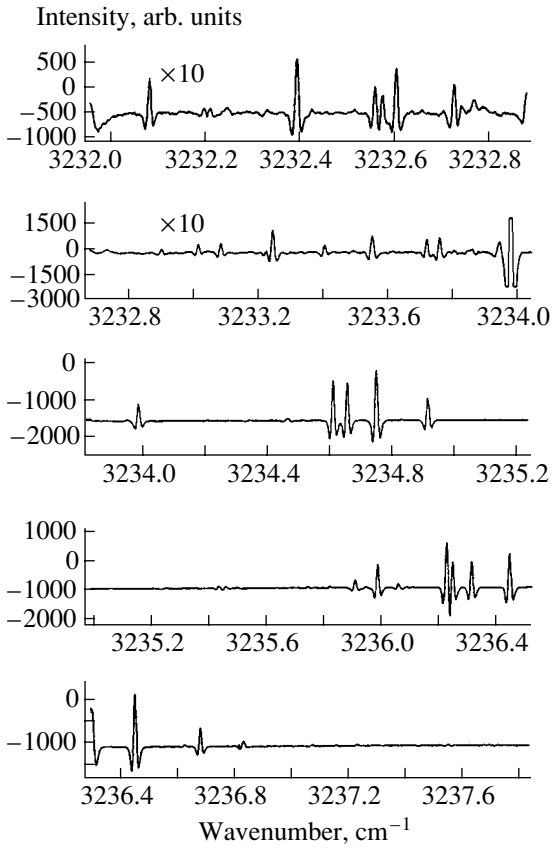

Fig. 4. Doubly differentiated spectrum of absorption in NH_3 measured at 17.5 K.

DISCUSSION

According to our experimental results, when the current slightly exceeds the threshold, both the tunable and the fixed-wavelength lasers generate a variety of lines corresponding to the longitudinal and transverse electromagnetic waves. It was also shown that, with an increase in the cavity length, not only the new longitudinal but also the transverse modes appear. The most favorable cavity length for both the longitudinal and the transverse modes to appear together was determined to be 500 μm. In this case, the modes are spaced at 24 Å. With the stripe width of 16 μm, the first transverse modes are shifted with respect to the longitudinal ones by the same margin. As a result, the transverse and the longitudinal modes are generated at the same wavelength and with equal probability. The transverse modes hinder the formation of a smooth concentration

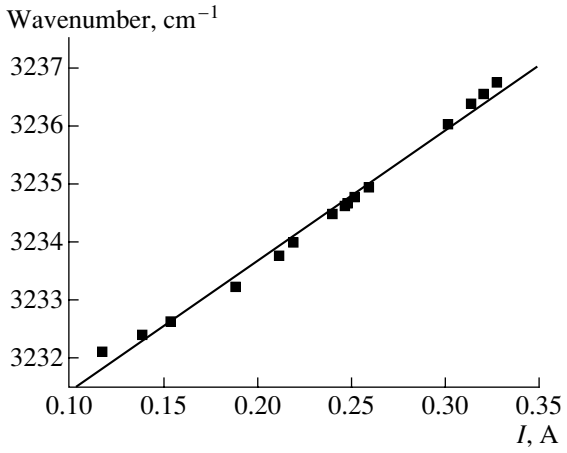

Fig. 5. Wave number of the laser radiation versus the current as obtained on the base of the lines identified in the NH_3 absorption spectrum (see Fig. 4).

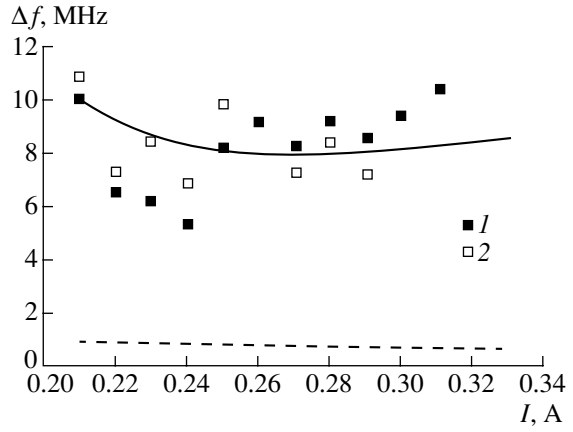

Fig. 6. Spectral line width versus the current as measured in the experiments with two amplifiers with a high-frequency cutoff at (*1*) 300 and (*2*) 80 kHz. Solid curve represents the values calculated according to (13) and the dashed curve, the result predicted by the Yamada theory [14].

waveguide, since they do not lower the density of carriers at the central part of the waveguide. Because of this, it is highly unlikely that the lasers with a cavity length of 500 μm can be tunable. Due to the nonlinear scattering of radiation by the waves of electron density produced by the lasing mode, the amplification grows at the long-wavelength and weakens at the short-wavelength side of each of the lasing modes [17]. In this situation, an increase in the current gives rise to modes with progressively larger wavelengths, while the short-wavelength modes are still produced as before. As a result, several tens of modes support one another.

At a cavity length between 200 and 300 μm, the transverse and longitudinal modes are separated by half of the intermode interval. When the amplification peak coincides with the longitudinal mode, generation of the transverse modes is hampered because of insufficient amplification. A smooth concentration waveguide appears, where the lateral travelling of light entirely suppresses the transverse modes. For such a laser, there should be a range of currents ensuring the single-mode operation. The lasing frequency is bound to increase with current due to an increase in the density of the charge carriers towards the edges of the waveguide, where the intensity of lasing is low. Low-intensity long-wavelength modes appearing at large currents may be connected with heating, which causes a distortion of the waveguide profile.

Since the jump experienced by the density of nonequilibrium charge carriers at the cavity edges (which is a necessary condition for the formation of a smooth waveguide) is nearly temperature independent and the threshold density increases with temperature (Fig. 2), the temperature dependence of I_{tun} should be weaker than that of the threshold current I_{th}, which is consistent with the experimental data (Fig. 2). When the current driving a tunable laser exceeds the threshold, the density of nonequilibrium carriers N increases with current rather than remaining at its threshold value N_{th}. It is the increasing density of the charge carriers that leads to a decrease in the refractive index n, since $\partial n/\partial N < 0$, and to the corresponding increase in the eigenfrequencies of the laser cavity. These considerations allow an approximate representation of N in terms of variation of the lasing frequency δf:

$$N = N_{th} - \frac{(\delta f/f)n}{\partial n/\partial N}. \qquad (9)$$

At the same time, fluctuations of N entail fluctuations of the eigenfrequencies of the laser cavity and, thus, broaden the lasing line Δf. With allowance made for the radiation-induced smoothing of fluctuations in N, the lasing line width can be expressed as

$$\Delta f = (\tau_L/\tau_0)(f/n)|\partial n/\partial N|(8N/V)^{0.5}, \qquad (10)$$

where τ_L/τ_0 is the ratio between the carrier lifetimes for small deviations of N from the equilibrium with (τ_L) and without (τ_0) the laser radiation and V is the volume of the active region. Here, the τ_L/τ_0 ratio is also N-dependent. At low temperature, an intermediate excitation level is realized, since the densities of equilibrium and nonequilibrium carriers are close to each other. For any level of excitation in the active region of the p-type,

$$\tau_L/\tau_0 = I_{th}(N - N_0)(2N_{th} + N_d)/\{IN_{th}(N_{th} + N_d) \times [1 + I_{th}(N - 2N_0 - N_0N_d/N)/IN_{th}(N_{th} + N_d)]\}, \qquad (11)$$

where N_0 is the inverted density of nonequilibrium charge carriers for the mode generated and N_d is the density of donors. The quantity in brackets is close to

unity with an accuracy of several percent. Let it be denoted by B.

For any level of excitation, $\partial n/\partial N$ can be approximated by the formula

$$\partial n/\partial N = -1.15cAT^{0.5}(F_i/kT)^{0.5}/[6\pi^2 f(N_d + N_i)], \quad (12)$$

where c is the speed of light; $A = 186$ cm^{-1} K$^{-0.5}$ is the coefficient characterizing the slope of the absorption edge in the material of the active region; F_i and N_i are the Fermi level and the density of nonequilibrium charge carriers in the conduction band at the population inversion threshold, respectively; and 1.15 is the coefficient accounting for the contribution of the plasma oscillations to the refractive index. Combining formulas (10)–(12) yields the lasing line width in the form

$$\Delta f = 1.15cAT^{0.5}(8NF_i/kTV)^{0.5}I_{\text{th}}(N - N_0) \times (2N_{\text{th}} + N_d)/[6\pi^2 n(N_d + N_i)IN_{\text{th}}(N_{\text{th}} + N_d)B]. \quad (13)$$

Let us turn to an analysis of formulas (11)–(13). It follows from formula (11) that $\tau_L/\tau_0 = 1$ at $I = I_{\text{th}}$ and decreases with current, thus promoting the damping of the random fluctuations of the density of nonequilibrium carriers and smoothening the fluctuations of the refractive index. Formula (12) implies a decrease in $\partial n/\partial N$ with the donor concentration because F_i increases slower than N_d. As a result, the presence of donors narrows the range of the lasing frequency modulation. Expression (13) suggests that there are two main causes for the decrease in Δf with the lowering of temperature: one is the decrease in N, and the other is an increase in I/I_{th} in the frequency tuning mode. The latter statement requires special comment. According to our results [18–20], fast frequency tuning requires the formation of a smooth waveguide, which appears owing to the accumulation of nonequilibrium charge carriers at the cavity edges. To a first approximation, the excess of additional concentration over the threshold one is temperature-independent. Hence, it follows that, since N_{th} decreases with cooling, the attainment of this value at lower temperatures requires a greater relative excess of current over the threshold than that demanded at higher temperatures. In fact, with a small excess of current over the threshold, there is no frequency tuning of the modes generated (see Fig. 3). The tuning sets in at a fourfold excess of current over the threshold at $T = 17.5$ (Figs. 2, 3). The considerations presented above also explain the decrease in this excess with temperature (Fig. 2).

For the NH_3 spectra recorded (Fig. 4), the excess of current over the threshold was found to range between $4I_{\text{th}}$ and $13I_{\text{th}}$, which, according to expression (6), allows highly accurate detection of the absorption lines. Based on these lines, the calibration dependence of the wave number on the current was plotted (Fig. 5). The experimental Δf values (Fig. 6) appeared to be in close correlation with those calculated from (13) (solid curve) and are an order of magnitude greater than those following from the Yamada theory [14] (dashed curve).

The tendency of Δf to decrease with current at small currents ($I < 270$ mA) is probably connected with a reduction in the differential lifetime of the charge carriers τ_L. The tendency of Δf to increase with current in the opposite case ($I > 270$ mA) may be attributed to the growth in N, which was previously noted as a typical feature of the frequency tunable lasers.

We note that an increase in the thickness of the active region not only favors the narrowing of the lasing line due to the growing volume of the waveguide but also promotes the extension of the lasing frequency modulation range. This may be explained as follows. In the spontaneous mode, the diffusion length of the electron–hole pairs is comparable with the thickness of the active region, whereas, in the lasing mode, it decreases with current and becomes thinner than the active region, thus causing a change in the concentration of nonequilibrium charge carriers throughout the thickness of the waveguide. Because of the significantly lower mobility of holes than electrons, there is an increase in the concentration of nonequilibrium charge carriers near the p region and a reduction near the n region with respect to its value in the center of the active region, with the magnitude of the former being considerably greater than the latter. The resulting increase in the average density of nonequilibrium carriers entails an additional lowering of the effective refractive index with a corresponding increase in the lasing frequency with the current. No mention of this phenomenon was made previously. Another consequence it implies is the reduction in the losses of radiation in the boundary layers due to the increasing optical-confinement coefficient, which contributes to the lowering of the threshold current and the narrowing of the lasing line.

CONCLUSION

Thus, a change in the geometrical parameters of the structure and the concentration of charge carriers in the layers prevents freezing-out of the carriers and ensures the operation of the laser at low temperatures. Cooling of the current-tuned diode laser structure down to 17 K made it possible to reduce the lasing line width to 7 MHz. It is demonstrated that the fast frequency modulation of radiation takes place with a considerable excess of current over the threshold, when the change in the concentration of carriers is sufficient to give rise to a smooth waveguide. The fast frequency tuning of the laser is conditioned by the concentration-related smooth optical waveguide appearing both along and across the structure. An increase in the concentration of holes near the p region because of a decrease in the effective lifetime of the carriers with current in the lasing mode results in an additional extension of the frequency tuning range.

ACKNOWLEDGMENTS

We are grateful to V.V. Sherstnev for growing the laser structures.

This study was supported by the Academy of Sciences of the Czech Republic (grant no. A-4040708), and the Russian Foundation for Basic Research (project no. 99-02-18019).

REFERENCES

1. V. G. Avetisov, A. N. Baranov, A. N. Imenkov, *et al.*, Pis'ma Zh. Tekh. Fiz. **16** (14), 66 (1990) [Sov. Tech. Phys. Lett. **16**, 549 (1990)].
2. J. C. Comparo, Contemp. Phys. **26**, 443 (1985).
3. A. I. Nadezhdinskii, R. Grisar, H. Schmidtke, *et al.*, in *Proceedings of the Freiburg Symposium, 1991* (Kluwer, Dordrecht, 1992), p. 155.
4. V. G. Avetisov, Yu. V. Kosichkin, V. I. Malakhova, *et al.*, Kvantovaya Élektron. (Moscow) **20**, 839 (1993).
5. C. E. Wiemann and L. Hollberg, Rev. Sci. Instrum. **62**, 1 (1991).
6. K. B. MacAdam, A. Steinbach, and C. Wiemann, Am. J. Phys. **60**, 1098 (1992).
7. J. Gea-Banacloche, Y. G. Li, S. Z. Jin, and M. Xiao, Phys. Rev. A **51**, 576 (1995).
8. M. Xiao, Y. G. Li, S. Z. Jin, and J. Gea-Banacloche, Phys. Rev. Lett. **74**, 666 (1995).
9. R. V. Martinelli, Laser Focus World **3**, 77 (1996).
10. A. N. Imenkov, N. M. Kolchanova, P. Kubat, *et al.*, Fiz. Tekh. Poluprovodn. (St. Petersburg) **34** (12), 1468 (2000) [Semiconductors **34**, 1406 (2000)].
11. A. N. Imenkov, N. M. Kolchanova, P. Kubat, *et al.*, Fiz. Tekh. Poluprovodn. (St. Petersburg) **35**, 375 (2001) [Semiconductors **35**, 360 (2001)].
12. A. N. Imenkov, N. M. Kolchanova, P. Kubat, *et al.*, Rev. Sci. Instrum. **72** (4), 1988 (2001).
13. C. N. Henry, IEEE J. Quantum Electron. **18**, 259 (1982).
14. M. Yamada, IEEE J. Quantum Electron. **30**, 1511 (1994).
15. A. Popov, V. Sherstnev, Yu. Yakovlev, *et al.*, Spectrochim. Acta A **54**, 821 (1998).
16. A. A. Popov, V. V. Sherstnev, Yu. P. Yakovlev, *et al.*, Pis'ma Zh. Tekh. Fiz. **23** (22), 72 (1997) [Tech. Phys. Lett. **23**, 890 (1997)].
17. A. P. Bogatov, P. G. Eliseev, and P. N. Sverdlov, Kvantovaya Élektron. (Moscow) **1** (10), 2286 (1974).
18. A. P. Danilova, T. N. Danilova, O. G. Ershov, *et al.*, Fiz. Tekh. Poluprovodn. (St. Petersburg) **32** (3), 373 (1998) [Semiconductors **32**, 339 (1998)].
19. A. P. Danilova, T. N. Danilova, A. N. Imenkov, *et al.*, Fiz. Tekh. Poluprovodn. (St. Petersburg) **33** (8), 1014 (1999) [Semiconductors **33**, 924 (1999)].
20. A. P. Astakhova, T. N. Danilova, A. N. Imenkov, *et al.*, Fiz. Tekh. Poluprovodn. (St. Petersburg) **34** (9), 1142 (2000) [Semiconductors **34**, 1100 (2000)].

Translated by A. Sidorova-Biryukova

Semiconductors, Vol. 36, No. 5, 2002, pp. 599–604. Translated from Fizika i Tekhnika Poluprovodnikov, Vol. 36, No. 5, 2002, pp. 629–634.

PHYSICS OF SEMICONDUCTOR DEVICES

Generation of Microwave Oscillations in a No-Base Diode

S. A. Darznek, S. K. Lyubutin, S. N. Rukin*, and B. G. Slovikovskiĭ

Institute of Electrophysics, Ural Division, Russian Academy of Sciences, Yekaterinburg, 620016 Russia

** e-mail: rukin@iep.uran.ru*

Submitted November 1, 2001; accepted for publication November 12, 2001

Abstract—The GHz-frequency microwave oscillations of voltage in a no-base p^+–p–n^+ silicon diode driven by reverse current with a pulse duration of ~300 ns and a current density of several kA/cm^2 were experimentally observed for the first time. The mechanism of initiation of these oscillations was theoretically considered. The frequency and the modulation percentage of the microwave oscillations were shown to depend on the current density and dopant-concentration gradient in the p–n-junction plane. © *2002 MAIK "Nauka/Interperiodica".*

Microwave radiation sources using a reverse-biased semiconductor diode as the operating element have been known since the late 1950s [1]. Among devices of this type, the widest acceptance has been gained by the avalanche transit-time diodes (ATTDs) and their modification—the trapped plasma avalanche transit-time diodes (TRATTDs), which are widely used for generating microwave oscillations in the range from several GHz (TRATTDs) to tens of GHz (ATTDs). The operation mechanism of such oscillators is based on the phenomenon of ionization breakdown of a semiconductor induced by an intense electric field and the formation of a current–voltage phase difference during the drift of charge carriers in the transit region, which provides a negative resistance of the diode. A distinguishing feature of the principle of operation of these devices consists in the fact that an external overvoltage pulse is necessary for initiating the ionization breakdown. In the ATTDs, a high-frequency electric field is used for this purpose. In combination with the constant-bias field, the high-frequency field gives rise to the breakdown of the diode at each period of oscillations of the external field. In the TRATTDs, the ionization breakdown occurs when the triggering pulse, which is generated by an external resonator circuit, arrives at the diode. Notably, the current flows through both an ATTD and a TRATTD in the pulse mode, and the current-pulse duration is shorter than one half-period of generated oscillations.

However, the high-frequency oscillations can also be observed in the diodes which were not specially designed for this purpose. For example, in study [2], the authors observed the relaxation microwave oscillations of voltage with a frequency of ~0.3 GHz in the case of the breakdown of abrupt-recovery drift diodes at the stage of generation of a reverse-voltage pulse.

In this study, we discovered continuous microwave oscillations of voltage with a GHz frequency in a silicon no-base diode. The oscillations arose when the reverse current, with a duration of hundreds of nanoseconds and with a density of several kiloamperes per square centimeter, flowed through this diode. In this case, the internal processes in the diode generating oscillations are independent of feeding external voltage pulses into the diode and depend only on the reverse-current magnitude.

In this experiment, we used a diode assembly containing four series-connected silicon p^+–p–n^+ structures produced by diffusion technology from lightly doped n-Si with a resistivity of 50 Ω cm. The length of each semiconductor structure was equal to L = 270 μm, the cross-sectional area was 0.26 cm^2, and the p–n-junction depth amounted to 135 μm. In this structure, the p^+, p, and n^+ regions were formed by diffusion of boron, aluminum, and phosphorus, respectively. Distributions of these dopants in the structure are illustrated in Fig. 1.

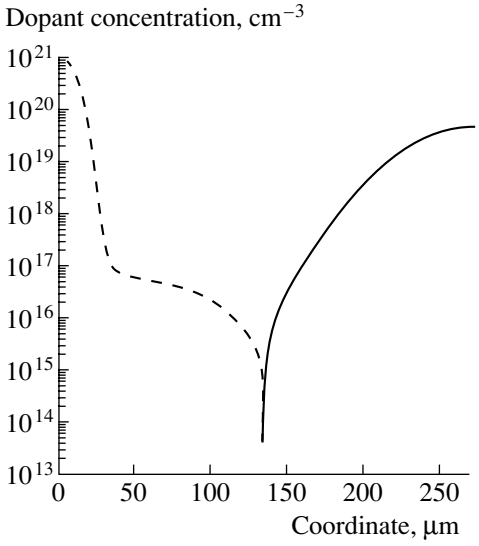

Fig. 1. Dopant profile of the semiconductor p^+–p–n^+ structure. The solid curve represents the donor distribution, and the dashed curve represents the acceptor distribution.

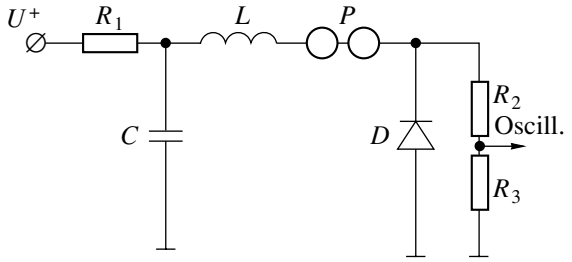

Fig. 2. Experimental circuit.

The key feature of this structure is the lack of a lightly doped base with a constant dopant concentration. In such a structure, the uncompensated-dopant distribution near the *p*–*n* junction is almost linear with the high concentration gradient (for the structure shown in Fig. 1, it is 8×10^{18} cm^{-4}). As a result, the breakdown voltage is much lower in this structure than in conventional diodes with a lightly doped base and amounts to ~300 V per *p*–*n* junction; the depletion-region width is ~10 μm.

The experimental circuit is shown in Fig. 2. The preliminarily charged capacitor *C* with a capacitance of 20 nF was discharged through the inductance *L* of 0.4 μH and the spark gap *P*; the resulting reverse-current pulse was fed to the diode *D*. The current-pulse parameters were specified by values of *L* and *C* in the circuit and were close to the short-circuit mode because the reverse resistance of the diode *D* was much lower than the wave impedance $\sqrt{L/C} \approx 4.5\ \Omega$ of the circuit. The initial capacitor voltage varied from 2 to 12 kV, and the current pulse through the diode was sinusoidal with a half-period of approximately 290 ns and with an amplitude ranging from 400 A to 2.2 kA. The highest reverse-current density in the diode was as high as 8.8 kA/cm^2.

The diode voltage was measured by a broadband resistive voltage divider R_2/R_3 with a rise time shorter than 200 ns. The broadband characteristic of the divider was provided by the partial shielding of the resistor R_2 [3]. The resistor R_3 was represented by 50-Ω input resistance of the broadband signal attenuator. For recording the pulse shape, we used a Tektronix TDS-684B digital oscillograph with a bandwidth of 1 GHz and the highest sampling rate f_d = 5 GHz (5 pixel/ns). The current through the diode was detected using a 0.55-Ω low-inductive resistive shunt with an inherent rise time of 2 ns (the shunt is not shown in Fig. 2).

In the experiments, we found that the high-frequency oscillations of voltage across the diode were observed if a current flowed through the reversely connected diode. A diode-voltage pulse duration coincided with the first half-period of current and amounted to ~290 ns. Typical oscillograms of pulses of voltage across the diode *D* are shown in Fig. 3 for various time sweeps and a current amplitude of 2.2 kA. The general shape of the diode voltage for the first half-wave of current is shown in Fig. 3a. In this oscillogram, the high-frequency oscillations are represented in the form of chaotic noise at the quasi-flat part of the voltage pulse owing to an insufficiently high sampling rate (1 GHz) of the oscillograph. In Figs. 3b and 3c, we show the oscillograms at the time sweeps which provide the highest sampling rate (5 GHz) for this type of oscillograph. As can be seen from these oscillograms, the shape of the oscillations is almost sinusoidal. The greatest span in the observed oscillations amounted to ~370 V, and the period was nearly 860 πs.

In order to explain the discovered effect, we consider the processes occurring in the semiconductor structure (see Fig. 1) when a reverse current flows through it. For describing the dynamics of motion for electrons and holes, we use the particle-balance equations

$$\frac{\partial n}{\partial t} + \frac{\partial s_n}{\partial x} = G, \quad \frac{\partial p}{\partial t} + \frac{\partial s_p}{\partial x} = G, \tag{1}$$

where *t* is the time; *x* is the coordinate along the diode axis; *n* is the electron concentration; *p* is the hole concentration; s_n and s_p are the electron and hole fluxes, respectively; and *G* is the bulk rate of generation of carriers.

With allowance made for diffusion and drift in the electric field, the expressions for s_n and s_p have the form

$$s_n = -D_n\frac{\partial n}{\partial x} - V_n(E)n, \quad s_p = -D_p\frac{\partial p}{\partial x} + V_p(E)p, \tag{2}$$

where D_n = 40 cm^2/s and D_p = 12 cm^2/s are the diffusivities, while $V_n(E)$ and $V_p(E)$ are the drift velocities of carriers in the electric field *E*.

The dependences $V_n(E)$ and $V_p(E)$ must account for the saturation effect for the drift velocities in high electric fields. In this study, we used the interpolation formulas for $V_n(E)$ and $V_p(E)$ in silicon taken from [4]; i.e.,

$$V_n(E) = V_{ns}\frac{E/E_{ns}}{\left(1 + (E/E_{ns})^{\beta_n}\right)^{1/\beta_n}},$$
$$V_p(E) = V_{ps}\frac{E/E_{ps}}{\left(1 + (E/E_{ps})^{\beta_p}\right)^{1/\beta_p}}, \tag{3}$$

where V_{ns} = 107 μm/ns and V_{ps} = 83 μm/ns are the saturation velocities for electrons and holes, E_{ns} = 7 kV/cm and E_{ps} = 18 kV/cm are the field strengths above which the constant-mobility approximation ceases to be true, and β_n = 1.11 and β_p = 1.21 are the fitting coefficients.

The volume rate of generation of carriers depends on the ionization processes

$$G(E) = \alpha_n(E)n|V_n(E)| + \alpha_p(E)p|V_p(E)|, \tag{4}$$

where

$$\alpha_n(E) = A_n \exp(-B_n/|E|),$$
$$\alpha_p(E) = A_p \exp(-B_p/|E|), \quad (5)$$

are the coefficients of ionization by electrons and holes; and $A_n = 7.4 \times 10^5$ cm^{-1}, $B_n = 1.16 \times 10^6$ V/cm, $A_p = 7.25 \times 10^5$ cm^{-1}, and $B_p = 2.2 \times 10^6$ V/cm are the approximation parameters [5].

The electric field in the p–n-junction plane was calculated from the equation for the total current $j(t) = j_d + j_c$, where $j(t)$ is the current density flowing through the diode, $j_d = \varepsilon \partial E/\partial t$ is the displacement-current density, $j_c = e(s_p - s_n)$ is the conduction-current density, $\varepsilon = 1.0 \times 10^{-12}$ F/cm is the permittivity of silicon, and e is the elementary charge. Outside the p–n junction, we used the Poisson equation for calculating the field

$$\varepsilon \partial E/\partial x = \rho(x) = e[p(x) - n(x) + N(x)], \quad (6)$$

where $\rho(x)$ is the space charge; $N(x) = N_D(x) - N_A(x)$; and $N_D(x)$ and $N_A(x)$ are the donor and acceptor concentrations, respectively. Equation (6) was solved using direct integration with respect to the coordinate x, and the field at the p–n junction calculated by the above method was chosen as the starting value.

In what follows, it is shown that nonequilibrium plasma exists only near the p–n junction and does not extend from it by more than several tens of micrometers (see Figs. 6–8) if the reverse-current densities are on the order of several kA/cm^2 for the parameters of the semiconductor structure shown in Fig. 1. For this reason, we chose a narrow region, $x_1 < x_{p-n} < x_2$, around the p–n junction, where x_{p-n} is its coordinate and the electron–hole plasma is considered to be in equilibrium outside this region.

The voltage across the p^+–p–n structure was determined from the formula

$$U_{p-n} = U_{cont} + \int_0^{x_1} E(x)dx + \int_{x_1}^{x_2} E(x)dx + \int_{x_2}^{L} E(x)dx, \quad (7)$$

where $U_{cont} = U_T \ln[N_D(L)N_A(0)/n_i^2]$ is the contact potential difference, $U_T = 26$ mV is the thermal potential, $n_i = 1.4 \times 10^{10}$ cm^{-3} is the intrinsic carrier concentration in silicon, and L is the structure length. The electric field in the highly doped regions 0, x_1, and x_2, L, was calculated from the current-flow condition in the equilibrium p^+–p–n^+ structure with allowance made for only the drift component of the current, while we used the exact solution for the set of Eqs. (1)–(6) in the x_1–x_2 region. The total diode voltage was calculated by multiplying the number k of series-connected structures by the voltage $U_d = kU_{p-n}$ across each of them.

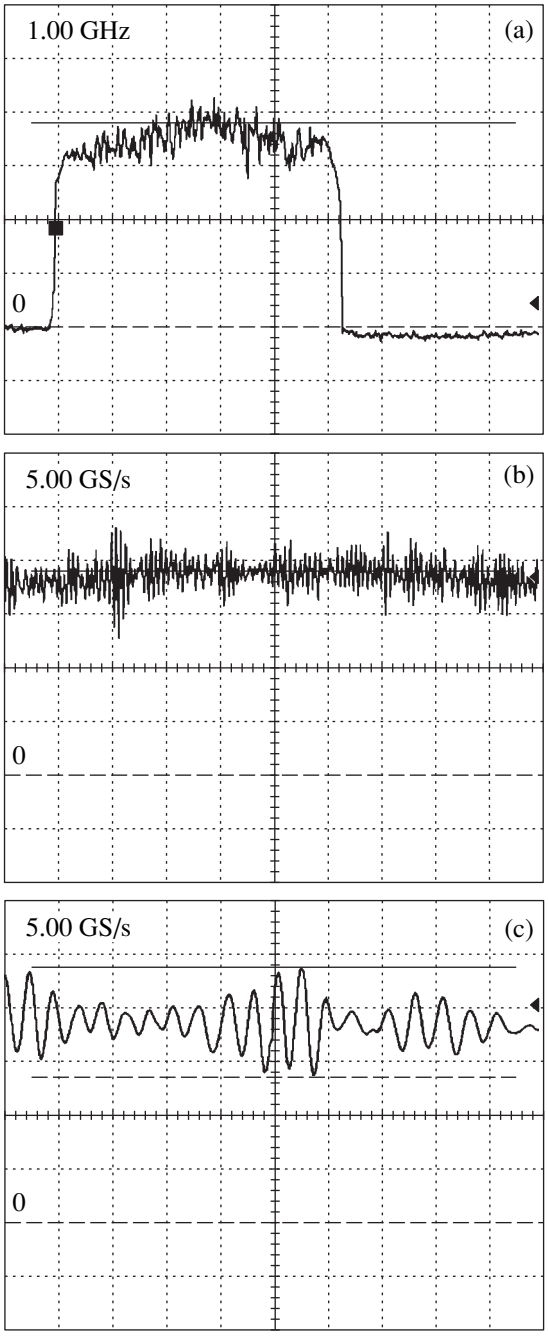

Fig. 3. Oscillograms of voltage across the diode D with various time sweeps and sampling rates: (a) 50 ns/division, 1 GHz; (b) 10 ns/division, 5 GHz; and (c) 2 ns/division, 5 GHz. The vertical sweep is 185 V/division.

The current flow in the electric circuit was calculated on the basis of a set of the Kirchhoff equation

$$LdI/dt = U_C - U_d(I, t), \quad CdU_C/dt = -I. \quad (8)$$

The calculations were carried out for the above values of capacitance and inductance of the circuit and for an initial capacitor voltage equal to 6 kV. The results of solving the complete set of Eqs. (1)–(8) are shown in

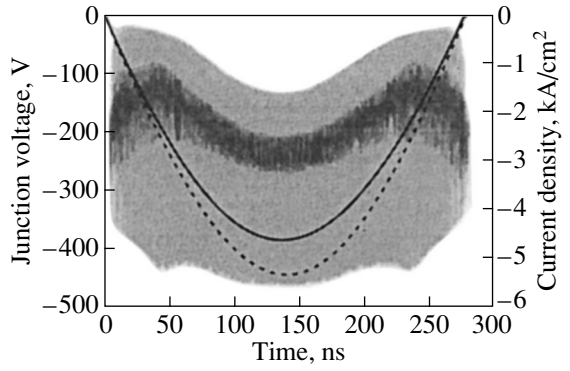

Fig. 4. Calculated time dependence of the voltage across the semiconductor structure (the light gray curve) and the current density through this structure (the solid black curve). The dashed curve represents the short-circuit current density. The dark gray curve represents the voltage calculation with allowance made for the oscillograph bandwidth of 1 GHz and the sampling rate f_d = 5 GHz.

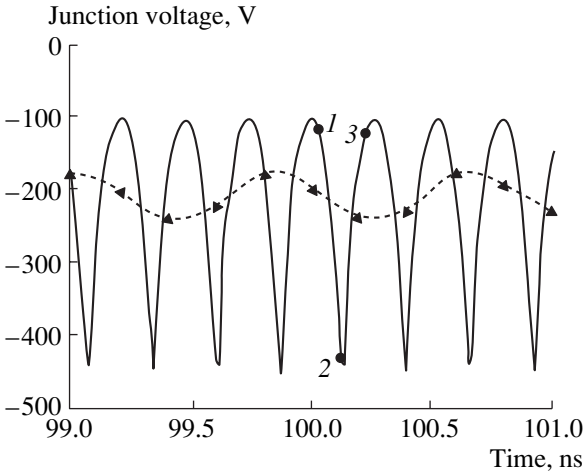

Fig. 5. Time-extended calculated dependence of voltage across the semiconductor structure (the solid line). The dots in the curve and the numbers near these dots denote the moments of time for which the spatial distributions of the electric field and the concentrations of electrons and holes in the structure are shown in Figs. 6–8. The dashed line represents the voltage calculated with allowance made for the oscillograph bandwidth of 1 GHz and the sampling rate f_d = 5 GHz. The triangles in this curve correspond to the moments of time at which the signal is sampled by the oscillograph.

Figs. 4–8. We show the general pattern of oscillations of the diode voltage in Fig. 4 and several periods on an enlarged scale in Fig. 5. As a whole, the process of generation of voltage oscillations appears as follows. Near the lowest voltage (dot *1* in Fig. 5), the p^+–p–n^+ structure is filled by a residual electron–hole plasma. The reverse current flowing through the diode removes the plasma from the structure, and the field amplitude rises near the *p*–*n* junction (Figs. 6, 7).

When the field strength exceeds the ionization threshold $E_{br} \approx 300$ kV/cm, the local breakdown of the semiconductor occurs. The field-rise time up to the breakdown can be estimated from the following reasoning. After the *p*–*n* junction becomes free of plasma, only the displacement current flows through the junction and determines the rate of the field increase $dE/dt = j/\varepsilon \approx -4 \times 10^{15}$ V/cm s. For such rates of increase, the electric field attains the ionization threshold in a time

$$\tau_1 = \varepsilon E_{br}/|j| \approx 100\ \pi\text{s}. \qquad (9)$$

Estimate (9) is somewhat low because the time necessary for removing the plasma from the *p*–*n* junction is ignored; however, formula (9), as a whole, adequately yields an order of magnitude of the value τ_1 (see Fig. 5).

Up to the moment of the onset of intense-ionization (Fig. 7), the region to the right of the *p*–*n* junction turns out to be free of the electron–hole plasma. To the left of the junction, in the *p*-region, the concentration of carriers becomes appreciably lower than the equilibrium one. Therefore, the space charge near the *p*–*n* junction is primarily formed by charged impurities. Because the dopant profile is almost linear (with the field $dN/dx(x_{p-n}) = 8 \times 10^{18}$ cm^{-4} for the p^+–p–n^+ structure shown in Fig. 1) in the region of the *p*–*n* junction, the field near this junction is given by

$$E(\Delta x, \Delta t) = -E_{br} + [j\Delta t + 0.5(\Delta x)^2 edN/dx(x_{p-n})]/\varepsilon, \qquad (10)$$

where $\Delta x = x - x_{p-n}$ is the distance from the *p*–*n* junction, and Δt is the time elapsed from the onset of the avalanche ionization. From (10), we can obtain the following estimate of the depletion-region width:

$$\Delta x_{br} = \sqrt{\frac{2\varepsilon E_{br}}{edN/dx(x_{p-n})}} \approx 10\ \mu\text{m}.$$

In this case, the structure voltage amounts to the value $\sim E_{br}\Delta x_{br} \approx 300$ V, which is much lower than the breakdown voltage for conventional diodes with base ~1 kV.

As time elapses, the avalanche-ionization region expands at a velocity whose value can be obtained from (10) as

$$\left|\frac{dx_{fr}}{dt}\right| = \sqrt{\frac{|j|}{2tedN/dx(x_{p-n})}},$$

where $x_{fr}(t)$ is the position of fronts of the avalanche-breakdown region. The velocity dx_{fr}/dt decreases gradually and becomes equal to the carrier saturation drift velocity of ~100 μm/ns within ~20 ns. By this time, the ionization region increases up to a size of $2x_{fr} \approx 6$ μm. Thus, at the initial stage of the avalanche development, the breakdown dynamics is close to the TRAPATT (trapped plasma avalanche triggered transit) operation mechanism and to the mode (the so-called trapped-plasma mode [1]) when the generated electrons and

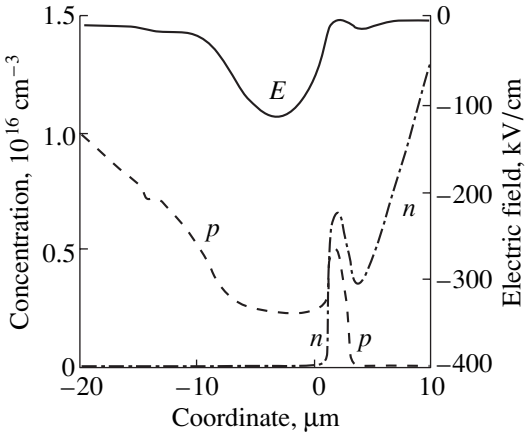

Fig. 6. Distribution profile for the electric-field strength (the solid curve), the hole concentration (the dashed line), and the electron concentration (the dot-and-dash line) for t = 100.02 ns (dot *1* in Fig. 5). In this and the next figures, the origin of the coordinates along the abscissa axis coincides with the position of the *p*–*n* junction.

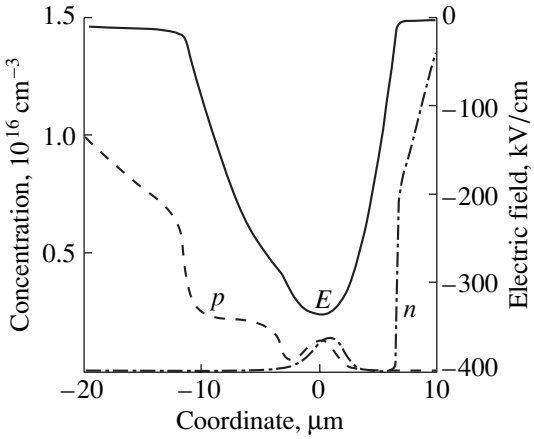

Fig. 7. Distribution profile for the electric-field strength (the solid line), the hole concentration (the dashed line), and the electron concentration (the dot-and-dash line) for t = 100.13 ns (dot *2* in Fig. 5).

holes have no time to leave the rapidly expanding ionization region.

After completion of the intense-ionization phase, the diode passes to the stage of removal of the nonequilibrium carriers from the breakdown region. Because the ionization region is shifted towards the n^+ region (Fig. 7), the drift-stage duration depends on the transit time of holes through the space-charge region of ~10 μm (Fig. 8). This time is independent of the value of the flowing current because the carriers move with the saturation velocities, and, by its order of magnitude, it is equal to the ratio between the drift-region size and the particle velocity, which amounts to $\tau_2 \approx 100$ πs. It should be noted that weakly mobile and almost quasineutral plasma is generated in the ionization region and is removed from the diode at the field-increase stage (Figs. 6, 7). As a whole, the process of plasma outflow to the highly doped regions of the p^+–p–n^+ structure is similar to the passage of carriers through the drift region of the avalanche transit-time diode.

After removal of the carriers, the electric field in the vicinity of the *p*–*n* junction begins to increase and the process is repeated. As a result, continuous oscillations of voltage arise in the diode with the period $\tau = \tau_1 + \tau_2$, which steadily decreases with increasing current density. The characteristic oscillation frequency $f = 1/\tau$ amounts to several GHz: for the current density j = –26 kA/cm^2 (for τ = 50 ns) (see Fig. 4), f = 2.2 GHz, while f = 3.8 GHz for j = –4.3 kA/cm^2 (for f = 100 ns).

Using the above characteristic values for the field and the oscillation frequency, we can estimate the power of the microwave component of the signal. In our case, the power associated with pulsations of electromagnetic-field energy $V_E\partial(\varepsilon E^2/2)/\partial t$, where $V_E \approx 10^{-4}$ cm^3 is the volume of the region occupied by the electric field in the structure, amounts to ~10 kW per *p*–*n* junction. For comparison, it should be noted that the most powerful TRATTDs irradiate power on the order of 0.2 kW per *p*–*n* junction [6] with an efficiency of 25%. It should also be noted that high values of the voltage modulation percentage are characteristic only of the structures with higher doping gradients in the region of the *p*–*n* junction. The calculations performed for the structures with lower gradients show that the breakdown voltage grows and the modulation percentage of the microwave oscillations decreases when the gradient decreases. This is associated with the fact that the region of localization of the nonequilibrium carriers in the structure with a sloping dopant profile increases, and the plasma generated as a result of ionization has no time to flow out into heavily doped regions of the

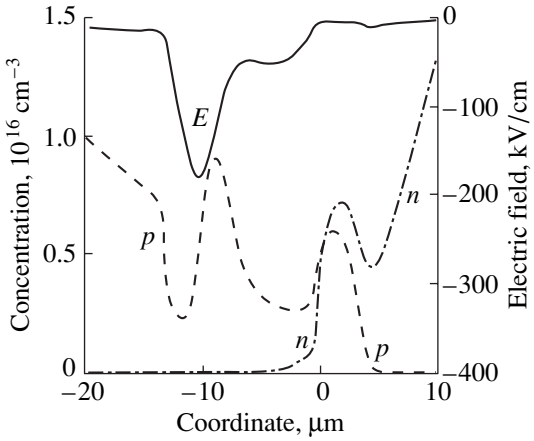

Fig. 8. Distribution profile for the electric-field strength (the solid line), the hole concentration (the dashed line), and the electron concentration (the dot-and-dash line) for t = 100.23 ns (dot *3* in Fig. 5).

diode. As a result, the carrier profile begins to resemble the distribution of electrons and holes for the case of steady-state breakdown upon which a weak modulation wave is superimposed. In other words, a decrease in the doping gradient of the structure leads to formation of the modulated-breakdown mode in the diode and to suppression of the microwave component in the signal.

Because we used a measuring circuit with a bandwidth of 1 GHz and a sampling rate f_d = 5 GHz in the experiment for detecting the high-frequency signal, the measured signal considerably differs from the calculated one (Fig. 3 and 4). To estimate the effect of measuring equipment on the microwave component of the signal, the calculated signal was transmitted through a numerical low-frequency filter with a transfer function of the *L*–*R*-chain type and a bandwidth corresponding to that of the oscillograph (1 GHz). The results of such a simulation are shown in Figs. 4 and 5. It can be seen from these figures that the measuring circuit reduces the amplitude of the microwave signal by a factor of approximately four. In addition, the finite sampling rate leads to an appreciable distortion in the carrier frequency of the high-frequency oscillations. Such an effect is the consequence of the frequency-superposition principle: the observed frequency $f_m = \mathrm{mod}[f/(0.5f_d)] = 1.3$ GHz for a signal frequency of 3.8 GHz and the sampling rate of 5 GHz (Fig. 5). As a whole, the results of simulating the detection system yield values of voltage amplitude of microwave oscillations (~100 V per *p*–*n* junction) and the signal frequency (~1 GHz) that correspond to those obtained in the experiment. However, for the precise measurement of the frequency and the amplitude of the oscillations, it is necessary to use measuring equipment with a better time resolution.

Thus, in this study, we discovered continuous microwave oscillations driven by reverse-current flow through a silicon no-base diode. The major distinction of the mechanism of these oscillations from that of the generation of microwave oscillations in known semiconductor oscillators based on avalanche transit-time diodes and their modifications consists in the following. For the ATTDs, the physical factor initiating the mechanism of avalanche ionization is the field of the external microwave. In the TRATTDs, an external voltage pulse is also used to induce ionization breakdown. In our case, the mechanism for generating oscillations requires no external factors. The factor determining the most important parameters of the high-frequency oscillations—the frequency and the modulation percentage—is the reverse-current density.

REFERENCES

1. M. Shur, *Physics of Semiconductor Devices* (Prentice-Hall, Englewood Clifs, 1990; Mir, Moscow, 1992), Vol. 2, Chap. 6.
2. V. A. Kozlov, A. F. Kardo-Sysoev, and V. I. Brylevskiĭ, Fiz. Tekh. Poluprovodn. (St. Petersburg) **35** (5), 629 (2001) [Semiconductors **35**, 608 (2001)].
3. V. S. Belkin and G. I. Shul'zhenk. Preprint No. 91-51, IYaF SO AN SSSR (Budker Inst. of Nuclear Physics, Siberian Division, Academy of Sciences of USSR, Novosibirsk, 1991).
4. *Landolt-Börnstein: Numerical Data and Functional Relationships in Science and Technology, New Series* (Springer-Verlag, Berlin, 1982), Vol. 17a.
5. I. V. Grekhov and Yu. N. Serezhkin, *Avalanche Breakdown of p–n Junction in Semiconductors* (Énergiya, Leningrad, 1980).
6. S. Sze, *Physics of Semiconductor Devices* (Wiley, New York, 1981; Mir, Moscow, 1984), Vol. 2, Chap. 10.

Translated by V. Bukhanov